NADZEYA KHINEVICH

TWO-DIMENSIONAL STRUCTURES OF NANOPARTICLES FOR ELEMENTS OF SURFACE-ENHANCED RAMAN SCATTERING SUBSTRATES

DOCTORAL DISSERTATION

Kaunas
2024

KAUNAS UNIVERSITY OF TECHNOLOGY

NADZEYA KHINEVICH

TWO-DIMENSIONAL STRUCTURES OF NANOPARTICLES FOR ELEMENTS OF SURFACE-ENHANCED RAMAN SCATTERING SUBSTRATES

Doctoral dissertation
Natural Sciences, Physics (N 002)

2024, Kaunas

This doctoral dissertation was prepared at Kaunas University of Technology, Institute of Materials Science during the period of 2018–2023.
The doctoral right has been granted to Kaunas University of Technology together with the University of Southern Denmark.

Scientific Supervisor:
Prof. Dr. Hab. Sigitas TAMULEVIČIUS (Kaunas University of Technology, Natural Sciences, Physics, N002).

Edited by: English language editor Dr. Armandas Rumšas (Publishing House *Technologija*), Lithuanian language editor Aurelija Gražina Rukšaitė (Publishing House *Technologija*).

The official defence of the dissertation will be held at 1 p.m. on 31 May 2024 at the public meeting of the Dissertation Defence Board of Physics Science Field in the Rectorate Hall at Kaunas University of Technology.

Address: K. Donelaičio 73-402, LT-44249 Kaunas, Lithuania.
Phone (+370) 608 28 527; email doktorantura@ktu.lt

The doctoral dissertation was sent out on 30 April 2024.
The doctoral dissertation is available on the internet at http://ktu.edu and at the libraries of Kaunas University of Technology (Gedimino 50, LT-44239 Kaunas, Lithuania) and University of Southern Denmark (Campusvej 55, Odense M, DK-5230, Denmark).

KAUNO TECHNOLOGIJOS UNIVERSITETAS

NADZEYA KHINEVICH

DVIMATĖS NANODALELIŲ STRUKTŪROS PAVIRŠIAUS STIPRINAMOS RAMANO SKLAIDOS PADĖKLŲ ELEMENTAMS

Daktaro disertacija
Gamtos mokslai, fizika (N 002)

2024, Kaunas

Disertacija rengta 2018–2023 metais Kauno technologijos universiteto Medžiagų mokslo institute.
Doktorantūros teisė Kauno technologijos universitetui suteikta kartu su Pietų Danijos universitetu.

Mokslinis vadovas:
prof. habil. dr. Sigitas TAMULEVIČIUS (Kauno technologijos universitetas, gamtos mokslai, fizika, N002).

Disertaciją redagavo: anglų kalbos redaktorius dr. Armandas Rumšas (leidykla „Technologija“), lietuvių kalbos redaktorė Aurelija Gražina Rukšaitė (leidykla „Technologija“).

Fizikos mokslo krypties disertacijos gynimo taryba:
prof. dr. Diana ADLIENĖ (Kauno technologijos universitetas, gamtos mokslai, fizika, N002) – **pirmininkė**;
prof. dr. Ramūnas ALEKSIEJŪNAS (Vilniaus universitetas, gamtos mokslai, fizika, N002);
doc. dr. Jacek FIUTOWSKI (Pietų Danijos universitetas, Danija, gamtos mokslai, fizika, N002);
doc. dr. Ieva PLIKUSIENĖ (Vilniaus universitetas, gamtos mokslai, chemija, N003);
prof. dr. Rolandas TAMOŠIŪNAS (Vilniaus universitetas, gamtos mokslai, fizika, N002).

Disertacija bus ginama viešame Fizikos mokslo krypties disertacijos gynimo tarybos posėdyje 2024 m. gegužės 31 d. 13.00 val. Kauno technologijos universiteto Rektorato salėje.

Adresas: K. Donelaičio g. 73-402, LT-44249 Kaunas, Lietuva.
Tel. (+370) 608 28 527; el. paštas doktorantura@ktu.lt

Disertacija išsiųsta 2024 m. balandžio 30 d.
Su disertacija galima susipažinti interneto svetainėje http://ktu.edu, Kauno technologijos universiteto (Gedimino g. 50, LT-44239 Kaunas, Lietuva) ir Pietų Danijos universiteto (Campusvej 55, Odense M, DK-5230, Danija) bibliotekose.

CONTENTS

LIST OF TABLES

LIST OF FIGURES

LIST OF ABBREVIATIONS AND DEFINITIONS

2NT – 2-naphthalene thiol;
AgNCs – silver nanocubes;
AgNPs – silver nanoparticles;
CAPA – capillary assisted particle assembly;
CHEM – chemical;
CT – charge-transfer;
D – diameter;
DL – detection limit;
DMF – dimethylformamide;
DO – dipolar oscillation;
EF – enhancement factor;
E_f – Fermi level;
EL – edge length;
EM – electromagnetic;
Ex – excitation;
FCC – face-centered cubic structure;
FEM – finite element method;
FWHM – full width at half maximum;
HF – hydrofluoric acid;
HOMO – highest occupied molecular orbital;
ICP – inductively coupled plasma;
IR – infrared;
LSPR – local surface plasmon resonance;
LUMO – lowest unoccupied molecular orbital;
MeNPs – metal nanoparticles;
NC – nanocube;
NP – nanoparticle;
OD – optical density;
PDMS – polydimethylsiloxane;
PML – perfectly matched layers;
PR – plasmon resonance;
PS – porous silicon;
PVP – polyvinylpyrrolidone;
Q-factor – quality factor;
QO – quadrupole oscillation;
RI – refractive index;
RIE – reactive ion etching;
SAM – self-assembled monolayer;
SD – standard deviation;
SEM – scanning electron microscope;
SERS – surface-enhanced Raman scattering;
SF_6 – sulfur hexafluoride;

SIS – polystyrene–polyisoprene–polystyrene;
SLR – surface lattice resonance;
SM – single molecule;
SPP – surface plasmon polariton;
SPR – surface plasmon resonance;
TA – tannic acid;
TAS – transient absorbance spectroscopy;
TC – trisodium citrate;
TEM – transmission electron microscopy;
UV– ultraviolet;
VIS – visible;
XRD – X-ray diffraction;
ΔA – differential absorption.

INTRODUCTION

The fields of application of *Surface-enhanced Raman Scattering* Spectroscopy (SERS) are very numerous, ranging from environmental studies, forensic science and pharmacology to biomedicine. Biotechnology is currently a field that is rapidly expanding, and the constant pursuit of smaller, more efficient, and compact devices stimulates the ever-growing interest of the research community. Biosensors are selective and sensitive to biological substances. One of the interesting fields of the application of the biosensor is SERS, which provides quantitative and qualitative analyses of biological materials. The use of nanostructured materials for the biosensor design is attractive because of their unique optical, chemical, and physical properties. Today, active research is being conducted in pursuit of developing metal nanoscale structures demonstrating plasmonic properties for the application as SERS active substrates. Unfortunately, SERS spectroscopy has not found wide practical application as an analytical method yet, despite significant progress in the formation and study of nanosized metal structures. The development of an inexpensive technology for manufacturing SERS-active substrates, which would combine both a high signal enhancement factor ($>10^8$) and high reproducibility of the signal across the surface (Signal variation < 10%), is still an ongoing challenge. In this regard, the task of studying not only the physical aspects of the phenomenon of SERS but also the development and research of new materials and technologies for the formation of substrates for SERS spectroscopy will make it possible to apply this method of spectroscopy in practice to solve applied problems.

Metalized porous silicon (PS) structures have already been shown to offer a wide practical use for biosensing by SERS. The prospects for PS use are associated with the characteristics of its structure, biocompatible, optical, and surface properties, which can be easily varied by selecting the parameters of the initial monocrystalline silicon and the modes of formation of porous layers. However, there is no systematic study of the PS formation without a 'bottleneck' surface layer that can be used as a template to produce the highly ordered set of silver nanoparticles (AgNPs) divided by silicon walls of nanoscaled thickness. This structure demonstrates the prospect of generating an extremely intensive electromagnetic (EM) field in the spots of AgNPs and silicon wall contact because of the plasmonic coupling between metallic NPs and semiconductors.

The other way to achieve the maximum SERS enhancement factor (*EF*) is to tune the plasmon resonance to the laser wavelength excitation that is used for measurements. The plasmonic periodic array of NPs has proven itself as a structure in which the geometry of the particle arrangement affects the position of the absorption peak of the structure as well as its intensity. The position of the absorption peak can be easily adjusted by changing the geometry depending on the needs.

Lithography techniques are widely used to produce an array of NPs with defined sizes and distances between them, but they incur limitations in nanoscale resolution and require expensive equipment and time to produce a large area of around 1 cm^2. *Capillary-Assisted Particle Assembly* (CAPA) is a method of nanoparticle deposition

on a substrate with a pattern that allows the production of a large area with a controllable number of NPs per unit and can be considered as an alternative method to lithography.

However, it is important to study the optomechanical modes of AgNPs as they can also influence the results of SERS measurements because different relaxation times of excited electrons on crystallite boundaries do not convert into thermal dissipation, which causes NPs heating those transfers to the molecules and degrading them.

In this thesis, we shall mainly focus on the realization and application of SERS substrates based on the array of NPs implemented in pores of nanostructured silicon, in which the SERS enhancements factor can be improved due to plasmonic coupling in the metal-semiconductor interaction and based on a periodic array of NPs whose sensitivity is increased due to tunable plasmonic properties to the target excitation laser wavelength.

I. GENERAL DESCRIPTION OF THE DISSERTATION

1.1. The Aim of the Research

The research aim is to develop extremely sensitive SERS-active substrates using chemically synthesized AgNPs deposited randomly or in a regular way on different substrates by a capillary-assisted particle deposition method.

1.2. Research Tasks

1. To chemically synthesize spherical AgNPs, investigate the effect of the concentration of the surfactants on the size of the NPs, produce monodispersed AgNPs, and study their ultrafast optomechanical properties.
2. To develop an irregular structure based on PS fabricated by electrochemical etching followed by reactive ion etching (RIE) and investigate their morphological, structural, and optical properties.
3. To fabricate regular and randomly structured SERS active substrates by a capillary-assisted technique by using prepared templates and synthesized AgNPs.
4. To investigate the SERS sensitivity of the developed SERS active substrates by using the organosulfur compound as a target molecule.

1.3. Scientific Novelty

1. The optimal conditions for the formation of monodispersed spherical AgNPs chemically synthesized by applying the seed growth method have been defined.
2. Investigation of ultrafast charge carrier relaxation on grain boundaries in chemically synthesized AgNPs has been performed, thereby showing the role of crystallinity on the electron-phonon interaction.
3. Systematic studies of the influence of the HF concentration in the electrolyte and the current density applied during PS formation by electrochemical etching on the morphology of the pore-open PS structure after RIE-treatment have been performed, demonstrating the use of the designed structure as a template for plasmonic NP array formation and perspective application as a SERS substrate.
4. Fabrication, investigation, and application of the wavelength-tailored SERS active substrate based on a periodic array of plasmonic NPs with a controlled number of hot spots enabled by the SLR has been performed for the first time.

1.4. Key Statements

1. The seed-growth method can be used to synthesize monodispersed AgNPs with the required diameter.
2. Ultrafast carrier relaxation in polycrystalline AgNPs can be investigated by transient absorption spectroscopy.

3. Electrochemical etching followed by reactive ion etching can be a useful method for producing controllable open-pore nanostructured silicon.
4. Capillary-assisted particle deposition can be used to assemble NPs into a periodic/non-periodic lattice controlling their number in the unit cell.
5. Variation of the NPs sizes tailors the wavelength of SLR.
6. SERS substrates with a tailored SLR to the excitation wavelength and hot spots to the periodic unit cells show extremely high sensitivity surpassing the currently existing SERS substrates with random distribution of nanoparticles.

1.5. Structure of the Dissertation

The dissertation is mostly based on the results which were published in the articles prepared by the author and co-authors during the author's PhD study. The contents of the dissertation are grouped and compiled according to the defined research tasks. The main body of the dissertation consists of five chapters: an introduction and a general description of the dissertation, a review of the recent description of research, experimental techniques and simulations, results and discussion, and conclusions. In the first chapter, the introduction to Raman scattering spectroscopy and ways of scattered signal enhancements leads to the formulation of the aim and the objectives of the research. Chapter 2 is a literature review of the recent research in the field of plasmonic structure fabrication providing enhancement of the Raman scattering signal of organic molecules covering the materials and methods of plasmonic structure formation, followed by the description of their advantages and limitations in practical application and commercialization. Chapter 3 presents the experimental techniques and optical properties simulations used in this thesis. Chapter 4 provides the results obtained and presented in the published papers. In the final chapter, the conclusion is given where the implementation of the research objectives and the achieved scientific novelty is highlighted.

This is followed by a list of cited references and copies of the scientific papers on which the dissertation is based. Finally, the *curriculum vitae*, lists of scientific papers and conferences related to the topic of the dissertation, and acknowledgements are presented.

The volume of the dissertation is 164 pages, including 28 figures, 5 tables, 8 numbered equations and 150 references.

1.6. Author's Contribution

The results of the research presented in the dissertation were achieved by conducting the research at the Institute of Materials Science of Kaunas University of Technology, as well as at South Denmark University in Sondenburg during the Erasmus+ Internship, and at Life Sciences Center of Vilnius University.

Nadzeya Khinevich independently planned and conducted most of the experiments and measurements; the author also prepared preliminary analyses and graphical visualizations.

The present dissertation is based on 4 research papers which feature most of the results received during the study, marked with the letter [A] in the list of the published

articles. The scientific contribution to the articles of the doctoral candidate and each co-author is as follows:

A1: Khinevich, N., Bandarenka, H., Zavatski, S., Girel, K., Tamulevičienė, A., Tamulevičius, T., Tamulevičius, S. Porous Silicon – A Versatile Platform for Mass-Production of Ultrasensitive SERS-Active Substrates. *Microporous and Mesoporous Materials, 323*, 111204 (2021). DOI: 10.1016/j.micromeso.2021.111204.

Nadzeya Khinevich (corresponding author) provided a formal analysis, collected the data, summarized the reviewed articles, prepared the visualization part, and wrote the original draft, prepared, and submitted the final manuscript. Dr. Hanna Bandarenka (Belarusian State University of Informatics and Radioelectronics) assisted with summarizing the reviewed articles, and conceptualized, reviewed, and edited the draft. Dr. Siarhei Zavatski (Swiss Federal Institute of Technology, Lausanne), Dr. Kseniya Girel (Belarusian State University of Informatics and Radioelectronics), Dr. Asta Tamulevičienė (Kaunas University of Technology) and Dr. Tomas Tamulevičius (Kaunas University of Technology) contributed to the conceptualization and editing of the manuscript. Supervisor Prof. Sigitas Tamulevičius (Kaunas University of Technology) came up with the idea, conceptualized, supervised, reviewed and edited the manuscript.

A2: Khinevich, N., Peckus, D., Tamulevičienė, A., Klimaitė, G., Henzie, J., Tamulevičius, T., Tamulevičius, S. Size and Crystallinity Effect on the Ultrafast Optical Response of Chemically Synthesized Silver Nanoparticles. *Journal of Materiomics* (2023). DOI: 10.1016/j.jmat.2023.08.009.

Nadzeya Khinevich conducted the chemical synthesis of monodispersed AgNPs, XRD and UV-vis measurements, implemented data analysis, prepared the illustration, and wrote the original draft. Dr. Domantas Peckus (corresponding author) conducted the transient absorbance spectroscopy, analyzed the data, wrote the draft of the manuscript, prepared a graphical visualization, and finalized and submitted it. Dr. Asta Tamulevičienė (Kaunas University of Technology) reviewed and edited the manuscript. Dr. Joel Henzie (International Center for Materials Nanoarchitectonics, Japan) conducted silver nanocube synthesis and edited the manuscript. Dr. Tomas Tamulevičius (Kaunas University of Technology) designed the TAS measurement setup and reviewed and edited the manuscript. Prof. Sigitas Tamulevičius (Kaunas University of Technology) came up with the idea, designed the TAS measurement setup, and conceptualized, supervised, reviewed, and edited the manuscript.

A3: Khinevich, N., Juodėnas, M., Tamulevičienė, A., Bandarenka, H., Tamulevičius, S. Tailoring Mesoporous Silicon Surface to Form a Versatile Template for Nanoparticle Deposition. *Coatings*, *11*(6), 699 (2021). DOI: 10.3390/coatings11060699.

Nadzeya Khinevich (corresponding author) came up with the idea, fabricated and investigated nanostructured silicon with open-pore morphology, performed SEM

measurements, analyzed the data, conducted AgNPs deposition into the pore of nanostructured silicon, prepared the graphical visualization, wrote the original draft, prepared and submitted the final manuscript. Dr. Mindaugas Juodėnas (Chalmers University of Technology; Kaunas University of Technology) designed the self-assembly setup and assisted with the reactive ion etching process. Dr. Asta Tamulevičienė (Kaunas University of Technology) consulted regarding the chemical synthesis of NPs and conceptualized and edited the manuscript. Dr. Hanna Bandarenka (Belarusian State University of Informatics and Radioelectronics) assisted with the method development of the open-pore process and investigation of pore morphology and reviewed and edited the manuscript. Prof. Sigitas Tamulevičius (Kaunas University of Technology) supervised, conceptualized, and edited the manuscript.

A4: Khinevich, N., Juodėnas, M., Tamulevičienė, A., Tamulevičius, T., Talaikis, M., Niaura, G., Tamulevičius, S. Wavelength-Tailored Enhancement of Raman Scattering on a Resonant Plasmonic Lattice. *Sensors and Actuators B: Chemical*, *394*, 134418 (2023). DOI: 10.1016/j.snb.2023.134418.

Nadzeya Khinevich (corresponding author) came up with the idea, synthesized AgNPs, conducted capillarity-assisted AgNPs deposition on a PDMS template, measured the optical properties, performed the modelling, SEM images, analyzed the data, summarized the EM enhancement factor calculations, prepared the visualization part and wrote the original draft, finalized, and submitted the manuscript. Dr. Mindaugas Juodėnas (Chalmers University of Technology) designed the self-assembly setup, provided supervision and guidance for the modelling, and conceptualized, reviewed, and edited the draft of the manuscript. Dr. Asta Tamulevičienė (Kaunas University of Technology) consulted with the chemical synthesis of NPs, and conceptualized and edited the manuscript. Dr. Tomas Tamulevičius (Kaunas University of Technology) designed the self-assembly and UV-VIS measurement setups and contributed to the conceptualization and editing of the manuscript. Dr. Martynas Talaikis (Vilnius University) and Dr. Gediminas Niaura (Vilnius University) conducted SERS measurements, evaluated SERS substrate sensitivity, and edited the manuscript. Prof. Sigitas Tamulevičius (Kaunas University of Technology) supervised the paper, analyzed the data, conceptualized and edited the manuscript.

All in all, the author has published 6 research papers in scientific journals indexed in the *Web of Science* database, has taken part in 18 scientific conferences, and has done 7 conferences presentations in person.

II. REVIEW OF THE RECENT RESEARCH

This chapter presents the analysis of the main steps in the scientific development of SERS spectroscopy and the formation of the SERS substrates. Sections 2.1–2.3 are devoted to the history of the discovery of the effects of Raman scattering and SERS, as well as to the studies of the mechanisms of amplification of the Raman scattering signal. In Section 2.4, the localized and lattice surface plasmon resonances (LSPR and SLR) are considered in detail. In Section 2.5, the development of SERS substrates based on LSPR and SLR is considered, describing their advantages and disadvantages, and some unresolved issues, including the review part published by the author of the thesis in [**A1**] are outlined.

2.1. Raman Spectroscopy

With the discovery of the Raman effect by the physicist Venkata Raman in 1928 [1], it became one of the most commonly used vibrational methods for material structure analysis, complementing *Infrared Spectroscopy* (IR). The *Raman spectroscopy* is a light scattering technique which is based on the interaction of light with chemical bonds. Scattered light typically includes elastic scattering (Rayleigh), which has the same wavelength as the incident light and inelastic scattering (Raman) at a different wavelength [2] (**Figure 1**). The scattered wavelength, which differs from the initial one, is explained by molecule release from the excited virtual energy state to the vibrational energy level with an increase or decrease in the photon frequency ($\nu_{ex} \pm \nu_{vib}$). The difference in the frequencies is a characteristic of a substance that is equal to the frequencies of natural oscillation bonds of its molecules, and it appears as a peak on the two sides of the Rayleigh scatter in the spectra (Stokes and Anti-Stokes scatter).

Depending on the energy level where the molecule was before the interaction with the light, the sign in the expression for the frequency $\nu_{ex} \pm \nu_{vib}$ is determined.

In Raman spectroscopy, the Anti-Stokes transition is less used as it necessarily requires the molecule to be on the excited vibrational energy level before the photon interaction. This condition is less common than the initial stage and the peak intensity is lower relative to the Stokes scatter signal.

Raman spectroscopy is a non-destructive method which provides substance identification, a study of the dynamics of the crystal lattice, the determination of chemical bonds and groups in molecules, the study of isomerism, phase transitions in samples, adsorption, and the detection of microimpurities.

Since the Raman signal is quite weak as only one out of 10^8 exited photons is scattered with a changed frequency [2], it becomes unsuitable for studying substances at low concentrations. One of the ways to enhance the intensity is through Surface-Enhanced Raman Scattering spectroscopy.

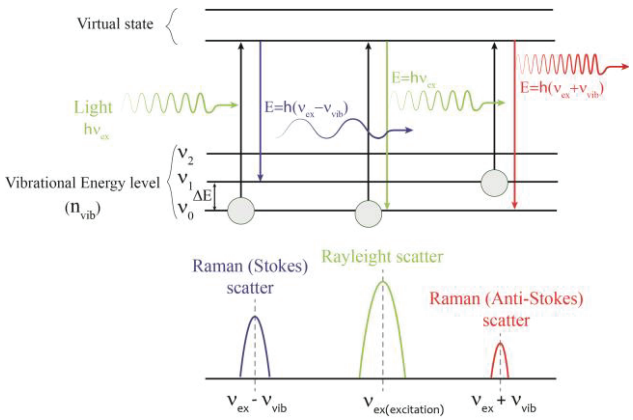

Figure 1 – Energy level diagram demonstrating Stokes Raman scatter, Rayleigh scatter, Raman Anti-Stokes scatter (top). The resulting spectrum (indicated with a peak) of Raman Stokes and Anti-Stokes scattering is relative to Rayleigh

2.2. Surface-Enhanced Raman Scattering (SERS) Spectroscopy

Today, SERS spectroscopy is a commonly used sensing technique where the number of photons scattered after an interaction with a molecule is greatly enhanced (more than 10^8 times), and it enables the detection of a single molecule (SM). Mainly, SERS makes possible the structural fingerprinting of substances in a low concentration due to the enhancement of EM fields by plasmon excitation or chemical enhancement.

The SERS effect was first observed during the Raman spectrometry experiment with a solution of pyridine molecules in the presence of a rough silver electrode – enhancement of Raman spectra of pyridine was induced by increasing the efficiency of light scattering. Initially, the observed increase in the signal was attributed to a higher number of adsorbed molecules on the metal surface due to its roughness followed by an increase in the surface area, but later it was identified as arising from surface enhancement [3].

Almost all early studies of the SERS effect were carried out by using rough silver electrodes. The development of nanotechnologies over the past 50 years has led to the possibility of manufacturing and adapting nanostructures from gold, copper, aluminum, platinum, palladium and many other metals, as well as from their combinations, which are commonly called SERS-active substrates, to solve the problems of Raman spectroscopy [4–6]. The discovery of the SERS effect brought forward research in the classical electrostatic and electromagnetism theory, especially in relation to NPs, in solving problems of radiating multipoles near metal surfaces, in the optics of nanostructures and the generation of surface plasmons. The number of theoretical and experimental studies on the optical properties of metallic structures and molecules located next to them has increased significantly. In addition, the discovery of SERS interaction with light helped to bring together, in a single area of research, such effects as an increase in photoemission due to the resonant coupling of

optical energy with the surface waves on a grating substrate [7,8], light radiation from metal particles excited by inelastic tunnelling of electrons [9], anomalous absorption of light in island films [10], as well as excitation of surface plasmons [11]. The SERS effect is based on basic enhancement mechanisms due to the interaction of electromagnetic fields, plasmon excitation, and chemical enhancement.

2.3. SERS Enhancement Mechanisms

As the fundamental aspects of SERS, researchers have been considering two types of SERS enhancement mechanisms: electromagnetic (EM) enhancement mechanisms, and chemical (CHEM) enhancement. SERS specialists agreed that both mechanisms contribute to the enhancement of SERS, as it is experimentally not possible to separate and determine their individual contributions [12].

In turn, CHEM enhancement relates to molecular polarity amplification and implies three mechanisms: (1) Enhancement due to chemical interactions in the ground state between a molecule and NP, which is not related to any excitations of the NP-molecule system; (2) Resonance Raman enhancement with the excitation wavelength being resonant with a molecular transition; and (3) Charge-transfer (CT) resonance Raman enhancement with the excitation wavelength being resonant with NP–molecule CT transitions [12] (**Figure 2**). The main requirement to achieve CHEM enhancement stems from the fact that the molecule must be in direct contact with the metal surface. This mechanism depends on factors such as the measurement site, the arrangement in which molecules are bonded, and the energy states of these molecules.

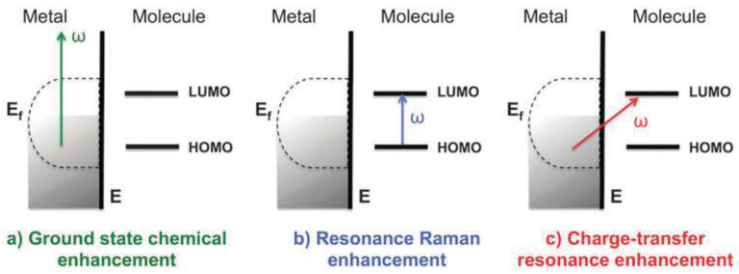

Figure 2 – Illustration of the three different types of chemical enhancement mechanisms in SERS. (a) Ground state chemical enhancement; (b) resonance Raman enhancement; (c) charge-transfer resonance enhancement. (HOMO – highest occupied molecular orbital; LUMO – lowest unoccupied molecular orbital; E_f – Fermi level) [13]

EM is associated with EM field density amplification near a rough metal surface. This provides specific optical properties of highly dispersed metal suspensions (for example, colloidal solutions of gold and silver). In the EM theory of the acting field, the presence of geometrically limited metal nanostructures on the surface or in the volume of substrates is the key factor determining the SERS effect and EM enhancement which is directly related to the metal surface roughness [14]. A rough metal surface can be converted to nanostructured metal particles, for example,

in the form of ellipsoids (or spheroids), randomly distributed over the metal surface, having different sizes but smaller than the light wavelength excitation. When light excites the metal nanostructure, the conductive electrons show up as a collective oscillation, which causes the EM field to strike around the metal nanostructures. Such collective oscillations of electrons (or, usually, it is represented as a free electron gas) are called plasmons. If the frequency excitation light is resonant with the electron oscillation, then the EM field and the Raman scattering of the adsorbed molecule on the metal surface are enhanced [15]. The effect of resonant wavelength excitation is called *Plasmon Resonance* (PR). For planar structures with propagated or standing waves, the effect is termed the *Surface Plasmon Polariton* (SPP), or simply surface plasmons (**Figure 3a**), for nanostructured metal particles, the effect is referred to as *Localized Surface Plasmon Resonance* (LSPR) (**Figure 3b**), and, for periodic metal nanostructures, the effect is named *plasmonic Surface Lattice Resonance* (SLR).

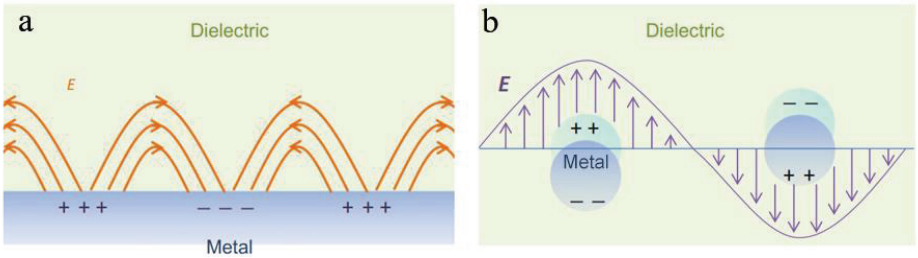

Figure 3 – Schematic of surface plasmon polariton (a); and localized surface plasmon resonance (b) [16]

The EM mechanism contributes the most strongly to the enhancement of SERS and is related to the plasmon excitations in metal nanostructures whose plasmon characteristics strongly depend on the density of electrons, the effective electron mass, the shape, and the size of charge distribution [17]. The causes of plasmon resonance and its variations will be discussed in the following section.

2.4. Surface Plasmon Resonances

2.4.1. Localized surface plasmon resonance (LSPR)

Localized surface plasmon resonance is conducted by UV-vis light interaction with metal NPs (MeNPs) which have a nanosized dimension that is significantly smaller than the wavelength of the incoming light. Incident light collectively excites electrons of a conduction band of MeNPs, which leading to coherent localized plasmon oscillations characterized by a resonant frequency. MeNPs show strong EM near-field enhancement and appear as the sharp absorption or scattering peak. The resonant frequency strongly depends on the type of the metal, the size of MeNPs, their geometry, the dielectric environment and the particle-particle distance [18–21]. SPR is called localized as it occurs at specific locations on the surface of metal nanoparticles, rather than propagating across the entire surface (see **Figure 5**).

The optical properties of plasmonic spherical NPs were described by the Mie theory and characterized by the absorption and scattering parameters which are contributed by dipole oscillation and presented as extinction and scattering cross-section parameters [22]:

$$\sigma_{ext} = \frac{18\pi\varepsilon_m^{3/2}V}{\lambda} \frac{\varepsilon_2(\lambda)}{[\varepsilon_1(\lambda)+2\varepsilon_m]^2+\varepsilon_2(\lambda)^2}, \quad (1)$$

$$\sigma_{sca} = \frac{32\pi^4\varepsilon_m^2V^2}{\lambda^4} \frac{(\varepsilon_1-\varepsilon_m)^2+(\varepsilon_2)^2}{(\varepsilon_1+2\varepsilon_m)^2+(\varepsilon_2)^2}, \quad (2)$$

where V is the volume of the sphere; λ is the light wavelength; ε_1 and ε_2 are the real and imaginary parts of the metal-dielectric constant; ε_m is the dielectric constant of the surrounding medium [22].

Absorption and scattering have the resonant maximum when the denominator tends to zero. Subject to $\varepsilon_1 = -2\varepsilon_m$, the enhanced EM field and the peak on the optical absorbance spectra correspond to the LSPR of the metallic sphere. **Figure 4a,b** presents the real and imaginary parts of Au and Ag. According to the condition of the extinction maximum, for gold NPs (AuNPs) in water (ε_m=1.7), the LSPR peak is observed at a wavelength of around 520 nm. The sensitivity of the NPs to ε_m is defined by the slope of the real component of the dielectric function. The imaginary part also plays a role in plasmonic properties and is related to the broadening of the LSPR peak [22].

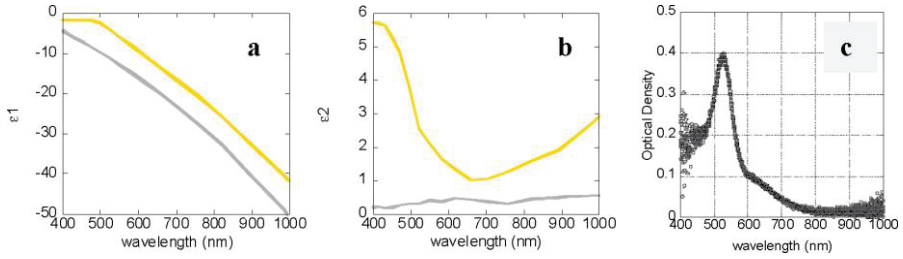

Figure 4 – Real (a) and imaginary (b) parts of the complex dielectric functions of Au (yellow line) and Ag (grey line). (c) The absorption spectrum of gold colloid solution [22]. Reprinted with permission from [21]. Copyright 2023 *American Chemical Society*

According to the Drude model of the electronic structure of metals, the dielectric permittivity can be a function of frequency [23]:

$$\varepsilon_1 = 1 - \frac{\omega_p^2}{\omega^2+\gamma^2}, \quad (3)$$

where ω_p is the plasma frequency of the bulk metal, and γ is the damping parameter of the bulk metal. For visible and near-infrared frequencies when $\gamma \ll \omega_p$, Eq. 3 will take the following look:

$$\varepsilon_1 = 1 - \frac{\omega_p^2}{\omega^2}, \quad (4)$$

By applying the resonant condition, the ω_{max} (LSPR peak frequency) value can be calculated from:

$$\omega_{max} = \frac{\omega_p}{\sqrt{2\varepsilon_m + 1}}, \quad (5)$$

Converting the frequency to the wavelength and the dielectric permittivity to the *Refractive Index* (RI) ($\varepsilon_m = n^2$), the λ_{max} (LSPR peak wavelength) can be found from the following Equation:

$$\lambda_{max} = \lambda_p \sqrt{2n_m^2 + 1}, \quad (6)$$

where n_m is the refractive index of the surrounding medium, and λ_p is the wavelength corresponding to the plasma frequency of the bulk metal.

Thus, the LSPR peak wavelength depends on the refractive index and can be tuned in dependence of the surrounding medium. It has been reported that covering with a material with a higher RI than the medium results not only in LSPR peak position tuning, but also enhances the EM field and shows a higher stability of NPs [24–26].

In case two NPs are placed at a distance of 2–10 nm from each other, the plasmons of these particles can couple with each other. This coupling thereby leads to a significant increase of the EM field density in the space between NPs and their so-called hot-spot. The SERS signal can be increased by 10^9–10^{12} by placing it in hot spots, and it rapidly decays with an increasing distance [27]. Furthermore, the correlation of the LSPR peak position linearly with the size has been reported [28,29].

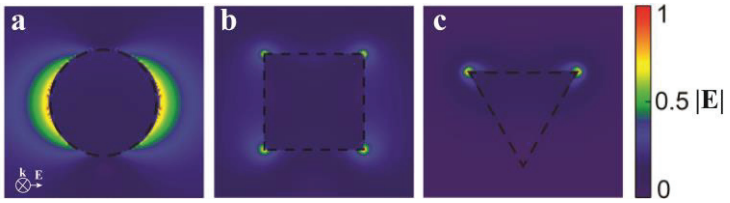

Figure 5 – Normalized electric field (|E|) distribution of nanosphere (a); nanocube (b); and nanotriangle (c); demonstrating highly localized enhancement [30]

For the calculation of the extinction cross-section of nonspherical NPs, the extended Mie theory to prolate and oblate ellipsoids by adding depolarization factors is used [31]. Usually, EM remains highly localized in specific areas, such as edges, tips, or gaps along the boundary between the metallic surface and the dielectric material [32–34] (**Figure 5**).

Different types of NPs can be synthesized, such as cubes, nanorods, triangles, nanobars [35–41], and nanobranches demonstrating greater sensitivity to the RI of the

medium [42]. It has been reported that their shape affects the LSPR properties. For example, in the case of nanorods, bipyramids due to their elongated shape or emanating from their tips, an additional electron oscillation mode was observed [35]. In this case, the LSPR peak divides into two peaks related to dipolar (DO) and quadrupolar (QO) oscillations whose positions depend on the geometry of the NPs [35] (**Figure 6**).

NPs characterized by LSPR properties (silver, gold, copper, nickel, palladium, platinum, iron and their alloys) found application not only in SERS but also in photocatalysis [43,44] solar cells [45,46], and biosensing [47]. SERS preferably use Ag structures because of their higher plasmon quality in comparison to gold and copper, and gold because of its superior chemical stability.

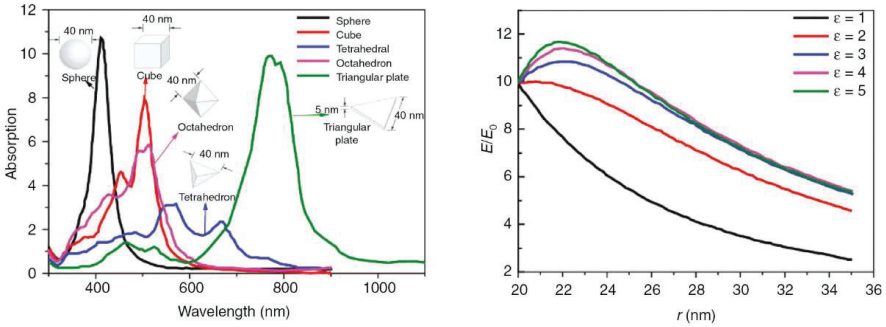

Figure 6 – Absorption bandwidth of different shapes of AuNPs and localized EM field enhancement at different dielectric constants of the surrounding medium [48]

2.4.2. Plasmonic surface lattice resonance (SLR)

The variation of LSPR is a *plasmonic Surface Lattice Resonance* (SLR) effect which is represented in a 1D or 2D metal NP array with a period comparable to the wavelength and appears as a sharp dip or a peak in transmittance or absorbance spectra, respectively [49–51]. The physical principle behind SLR includes the far-field interaction of LSPR which occurs through the in-plane diffraction waves (*Rayleigh Anomaly* (RA)) interfering with light scattered by NPs in symmetric media (**Figure 7**).

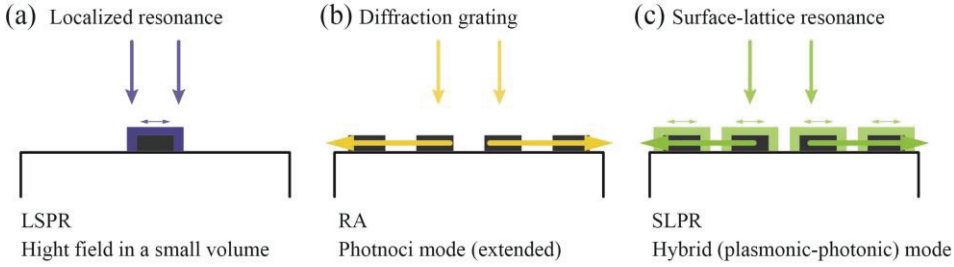

Figure 7 – Localized surface plasmon resonance under the incident excitation (vertical arrows) (a); scattered incident wave (horizontal arrows) by diffraction gratings (b) enhanced radiative coupling of LSPR through diffraction gives rise to SLR (c)

The quality factor (Q-factor) of the SLR peak generated by a regular array experiences a significant increase and can reach as high a value as 330 [52]. That is much higher compared to the Q-factor of the LSPR peak characterized by a value of 10–20. When the position of LSPR is determined by the optical properties of NP, such as the size, the shape, and the composition, the position of the pitch of the RA depends on the array pitch (Λ) and the medium refractive index (n) which follows the relationship $\lambda_{\mathrm{RA}} = \Lambda n$. Theoretical and experimental investigations have been reported on the influence of the pitch of metal NP, the properties of the surrounding media, and the thickness of materials on the optical response of SLR [53–55].

Nowadays, several periodic lattice geometries have been reported, such as the square, rectangular, 45-rotated square, honeycomb, hexagonal, and Lieb lattice which demonstrate SLR [56]. Spherical NPs, nanocubes, triangles, rods, nanodisks, V-shaped metal structures, and NPs clusters as active metal structures have been reported [57–59].

Recently, it has been found that nanoholes in thin metal films can demonstrate a similar effect [60].

Structures exhibiting lattice resonance are used in a wide range of applications, including resonators [61,62], sensing devices [63,64], and nanolasers [65,66]. Metal periodic arrays show a significant promise, particularly in SERS applications, due to the tunability of plasmon properties [67].

Since the EM mechanism mainly contributes to the enhancement of the Raman signal, the diversity of the SERS substrates is driven by materials selection for plasmon resonance optimization.

2.5. SERS-Active Substrates

2.5.1. Basic concept of SERS-active substrates

Various SERS-active substrates based on the LSPR effect for the single- or multianalyte studies have been reported. Conventionally, regarding the type of substrate, they can be divided into two groups:

(i) liquid substrates – colloidal solutions of metallic NPs (MeNPs);

(ii) solid substrates – metallic nanostructures immobilized on the surface of the solid plates, membranes, polymers, etc. [**A1**].

MeNPs with different shapes (spheres, cubes, triangles, plates, nanostars, core shells) and sizes [68–70] can be fabricated by chemical synthesis. The control of the component concentration, the temperature, the reduction time, and the stirring rate during the synthesis process allows easy manipulation in MeNPs forms, thereby tuning the LSPR and enabling better SERS at a specific wavelength [71,72]. SERS measurements with MeNPs can be carried out directly in a solution [73–75], or NPs mixed with analyte can be deposited on a solid support [76]. NPs aggregation in solutions leads to an increase in the number of hot spots, which greatly improves SERS, but non-controlled aggregation tends to NPs sedimentation, and, as a consequence, to high spatial SERS signal fluctuation. The presently mentioned disadvantages of liquid SERS substrates, such as a non-reproducible SERS signal and

bad stability, as well as the impossible application for quantitative analysis, lead to limitations in their use.

The solid substrates with ordered assembling of MeNPs are preferable in practical terms as they demonstrate good signal reproducibility, stability, and a long shelf life. Along with this SERS substrate, the SERS enhancement factor (*EF*) and detection limit (*DL*) are crucial parameters used for the evaluation of the analytical performance of the substrates.

EF is a ratio of the SERS intensity contributed by each molecule adsorbed on the surface to the Raman intensity of free molecules. This parameter is calculated according to the following formula [68]:

$$EF = \frac{I_{SERS}/N_{SERS}}{I_{Raman}/N_{Raman}}, \quad (7)$$

where N_{Raman} and N_{SERS} are the molecule numbers in the Raman and SERS measurements; I_{Raman} and I_{SERS} are the normalized intensity values of the detected molecule characteristic band for the Raman and SERS measurements.

DL is characterized as the minimum amount of molecules (or their concentration) present in a solution; they are absorbed onto the metal surface of the SERS substrate and become detected and distinguishable within the SERS spectrum.

Overall, while both liquid and solid substrates have their merits and drawbacks, solid substrates offer superior analytical performance, which makes them preferable for various applications in SERS-based sensing and analysis. Further research and development in this field will continue to refine and optimize SERS substrates for enhanced performance and broader practical applications.

2.5.2. Solid base of SERS active substrates

A great choice of rigid SERS-active substrates based on paper, polymers (polydimethylsiloxane (PDMS) [77], polystyrene – polyisoprene – polystyrene (SIS) [78]), plants [79], fibres [80], dielectrics (glass [81], porous aluminium oxide [82]) and semiconductors [83]) have been described [**A1**]. According to a recent review, the most popular solid substrates are paper, nanostructured silicon, and polymer [**A1**]. Despite the popularity of cheap paper substrates, they are unlikely to be implemented in practice due to their rapid degradability. Nanostructured silicon (e.g. silicon nanowire ensembles, nanoporous silicon sponges, porous silicon nanoplates, quasi-ordered arrays of branched or smoothed nano- and micropore channels in silicon) templates have also been investigated as the SERS-substrate since they provide a greater contribution to the enhancement of Raman signals [84] and a longer shelf-life [85][**A1**]. As a result of its high surface area and good biocompatibility nanostructure, silicon-based SERS substrates increase the number of adsorbed molecules, which leads to a rise in *DL*. Recently, some outstanding performances have been reported, such as *DL* being able to reach 10^{-18} M [86] and a shelf life of up to 3 years [87]). A detailed review of the varieties of nanostructured silicon, its methods of manufacturing, and its application have been considered [**A1**].

Polymer substrates rank third in popularity for their use as templates for SERS substrates due to the low cost and easy fabrication of the required geometry (in case of need) obtained by using the soft lithography technique [88] or by stretching followed by plasma treatment [89]. It should be noted that, in the case of soft lithography, the same reproducing patterns in solid materials like silicon molds can be used an unlimited number of times for substrate fabrication, which increases its reproducibility from sample to sample [90–94].

In addition, the potential of material elasticity for tuning the optical properties of metal structures after their fabrication on the surface has been demonstrated [95,96].

All in all, the diverse range of SERS-active substrates, combined with the controllable assembly of NPs on solid substrates, provides researchers with versatile options for tailored SERS applications.

2.5.3. Controllable assembly of nanoparticles (NPs) on a solid substrate

During the last decade, in the process of immobilization of MeNPs on the solid substrate surface, researchers have been pursuing the goal of increasing the efficiency of the active SERS substrate by the fabrication of well-defined structures with a high density of hot spots [97–103].

Several simple methods of immobilization of MeNPs on solid surfaces such as spontaneous (immersion) deposition [104,105], electrodeposition, vacuum methods (electron beam, focused ion beam, and photon lithography) [99,106–108], deposition of MeNPs from colloidal solutions have been reported. The first three approaches can be used to fabricate large areas of nanoscale patterns. These advantages sound promising for the development of SERS active substrates; nevertheless, spontaneous deposition and electrodeposition incur difficulties in the fabrication of well-defined structures, while vacuum techniques suffer from limitations in metal structure production with a gap of 2–5 nm, as well as due to having a low fabrication speed and a high production cost.

The techniques of immobilization of MeNPs from colloids deserve special attention as they are usually simpler and more cost-effective than the use of lithography methods [99,107,109,110], Langmuir-Blodgett [111], Langmuir-Schaefer [112], electrophoretic deposition [113], liquid/liquid (liquid/air) [114,115] interface self-assembly techniques realize the assembly of NPs into an ordered array. Such layers of NPs are characterized by evenly distributed hot spots and demonstrate good signal reproducibility to a signal standard deviation of less than 10% [114]. Additionally, in order to produce the controllable assembly of NPs and the distance between them, some ligands (antibodies, polymers, organic molecules) are used. These molecules are strongly adsorbed on MeNPs, which prevents the target molecule from going to the hot spot. The required cleaning process includes harsh substances that can partially or completely destroy the structure.

An alternative method to high-order MeNPs assembly fabrication is convective flows or *Capillarity-Assisted Particle Assembly* (CAPA). In addition, these methods are called template-assisted fabrication methods when a patterned substrate is used

[93]. The manipulation of key parameters, such as the substrate temperature, the contact angle, and the particle concentration achieve the process speed and yield, while also enabling the ability to switch from one force to another. The compatibility of the convective and capillary assembly along with the use of different materials and sizes of NPs and variations in the trap shapes and depths provides a single or multiparticle array for multiple applications (memory cells, transistors, plasmon-guiding structures) [116–118].

The ongoing advancements in both substrate materials and assembly techniques promise continued improvements in sensitivity, reproducibility, and practicality for addressing diverse analytical challenges.

III. EXPERIMENTAL TECHNIQUES AND SIMULATIONS

This chapter describes the materials and experimental techniques, reported in **A2-A4**, used for fabricating periodic and random (nonperiodic) arrays of AgNPs on solid templates demonstrating plasmonic properties.

3.1. Silver Nanoparticles Fabrication

Monodispersed AgNPs (diameter SD<10%) were synthesised by using the seeded-growth method [28] in which a complex of tannic acid (TA) ($C_{76}H_{52}O_{46}$, *Sigma-Aldrich*, China), trisodium citrate (TC) ($C_6H_5Na_3O_7$*$2H_2O$, *Fluka*, Belgium) and silver nitrate ($AgNO_3$, *Sigma-Aldrich*, USA) were used. The synthesis process consisted of two steps: the synthesis of Ag seeds followed by their growth.

Synthesis of Ag seeds. An aqueous solution (100 ml) containing 5 mM of TC and 0.0125 mM – 2.5 mM of TA was heated at 100°C degrees for about 15 min under vigorous stirring. Subsequently, 1 ml of $AgNO_3$ solution (25 mM) was injected. The synthesis lasted for 70 min.

Growth of Ag NPs. 19.5 ml of seeds was mixed with 16.5 ml of water and heated under 90°C, 0.033–0.347 mM of TC, 0.008–0.1mM of TA, and 0.083–0.7 mM of $AgNO_3$ were sequentially injected. After 30 min of heating, 1 ml of aliquots was extracted for further characterization. The produced solution was used as the seed solution for the next synthesis step. The growth process was repeated five times. The aliquots were centrifuged at a set rate from 4000 rpm to 12000 rpm (depending on the size of the NPs).

AgNPs were functionalized with PVP (Polyvinylpyrrolidone, average MW ~55,000, *Sigma-Aldrich*, USA) for better stabilization during CAPA deposition. Before deposition, the concentration of the NPs was increased by up to 10 times, and the solvent was exchanged and mixed with ethanol and dimethylformamide (DMF) at a 1/2 ratio [**A2**].

3.2. Template Fabrication

3.2.1. Porous silicon template fabrication

Antimony-doped Si wafer (100) (*Siegert Wafer*, Germany) with a resistivity of 0.008–0.02 Ohm·cm was used for PS formation. Before etching, native silicon dioxide was removed in a low concentration (4 wt.%) hydrofluoric acid solution (*Fluka*). Electrochemical etching for PS formation was carried out in an aqueous HF solution at different concentrations (5, 10, and 20 wt.%) for 90 s. The current density (j) varied from 20 mA/cm^2 to 200 mA/cm^2. Removal of the parasitic surface layer was performed by using RIE for 5 min in a 50 scm gas flow of SF_6 at 20 mT pressure, 40 V bias voltage and 500 W ICP (inductively coupled plasma) coil power (*Vision LL-ICP*, Sweden). After the RIE process, all PS samples were cleaned in an ultrasonic bath in chloroform for 5 min in order to remove the oil that was used to bond them to a carrier wafer. Just before characterization, the PS layers were treated with diluted HF solution for a few seconds to remove the oxidized areas [**A3**].

3.2.2. Polymer template fabrication

The polymer template with the periodic structure for CAPA deposition was made of (PDMS) by replicating a 20x20 mm^2 Si mold while using the soft-lithography technique. The Si-mold was fabricated by using electron-beam lithography (*eLine plus*, *Raith*, Germany) and RIE (*Vision LL-ICP*, *Plasma-Therm*, USA). The pattern consisted of a square array of 180 nm in diameter, 100 nm tall, and 330 nm centre-to-centre spaced round pillars. The Si mold was functionalized with trichloro-(1H,1H,2H,2H-perfluorooctyl)-silane (*Alfa Aesar*, Germany) to prevent bonding with PDMS in subsequent soft-lithography replication cycles. 20 ml drop of 10:1 mixture of polymer base and a curing agent (*Sylgard 184*, *Dow-Corning*, USA) was dispensed on the Si mold and covered with a glass coverslip. The sample was cured at 100°C for 35 min in the oven. After cross-linking, the glass coverslip with a patterned PDMS film was separated from the mold [119] [**A4**].

3.2.3. Capillarity-assisted particle deposition

Open-pore PS and PDMS patterns were used as a template for *Capillarity-Assisted Particle Assembly* (CAPA) deposition. CAPA was performed by using a custom setup equipped with a motorized linear precision translator (*LS-110*, *PI miCos*, Germany), a temperature control system (*TEC-1090*, *Meerstetter Engineering GmbH*, Germany) and an optical microscope system (*BX51*, *Olympus*) with a CCD camera (*QImaging*, *Micropublisher 3.3*) [120]. The PS and PDMS templates were placed on the moving stage, and 100 µl of AgNPs solution was dispended and confined by a fixed microscope slide. A drop of the solution moved along the surface, thus forming a meniscus. Evaporation-induced flux and the contact angle led to AgNPs accumulating at the edge of the meniscus and going into the pores/traps. The temperature of the sample holder was controlled by the thermoelectric controller [**A4**].

3.3. Analysis Methods

3.3.1. Optical spectroscopy

The *UV-Vis* absorbance spectra of the synthesized NPs were registered by using a fiber-optic spectrometer *AvaSpec-2048* (*Avantes*, the Netherlands) with a 1.2 nm resolution in the 400–800 nm spectral range [**A2**].

Transient Absorption Spectroscopy (TAS) was used to study the ultrafast electron dynamics of Ag NPs. The TAS spectra were recorded by using a *HARPIA* spectrometer (*Light Conversion*, Lithuania). The experimental setup involved an excited system with an ultrafast 290 fs pulse length and 1030 nm wavelength Yb:KGW laser *Pharos* (*Light Conversion*, LT) with a regenerative amplifier at a 66.7 kHz repetition rate. A collinear optical parametric generator *Orpheus* and a harmonic generator *Lyra* (*Light Conversion*, LT) were used to tune the pump beam wavelength to 350 nm with an excitation intensity of 29 µJ/cm^2, and the pulse width at about 290 fs. The samples of Ag NPs were probed with a white-light supercontinuum generated by using a 2 mm thick sapphire plate excited with the

second harmonic (515 nm) of fundamental laser wavelength. The spectral range of the supercontinuum probe, as well as the detection range of the TAS signal relaxation dynamics, spanned wavelengths from 370 to 674 nm. The excitation beam was focused on a ca. 700 μm diameter spot, and the diameter of the supercontinuum probe was approximately 500 μm [**A2**].

3.3.2. SEM, TEM and XRD

Scanning electron microscopy (*Quanta 200 FEG*, *FEI*) at a low vacuum in a water vapor atmosphere was used for the imaging of NPs on insulating PDMS substrates. The electron gun voltage was 10 kV, WD 8.6–8.7 mm, and the spot size was 3.

Transmission electron microscope Tecnai G2 F20 X-TWIN (*FEI*, the Netherlands) with an FE source operated at 200 kV was used for the visualization of Ag NPs. 20 mL of the precipitates after centrifugation was dropped onto a TEM copper mesh and left to dry at room temperature. Meanwhile, Ag NCs were inspected with 2100F (JEOL) TEM operating at 200 kV.

The XRD method was used to analyze the crystalline structure of synthesized Ag NPs. *8 Discover* diffractometer from *Bruker AXS GmbH* was used, which uses Cu $K\alpha_1$ radiation with a wavelength of 0.154 nm as the radiation source. The experiment used a parallel beam focusing geometry, and the peak intensities were measured within the 30–90° 2θ range with a step size of 0.012°. Analysis of the diffraction data was performed by using the *DIFFRAC.EVA* software, and Rietveld refinement was performed by using the *X'pert HighScore Plus* software to determine the crystallite sizes and lattice parameters [**A3**].

3.4. SERS Measurements

SERS measurements were performed by using a multiwavelength Raman microscope (*Renishaw*, Wotton-under Edge, UK) equipped with a thermoelectrically cooled CCD detector. Samples were excited and spectra were collected by using the following combinations of laser wavelengths and gratings: 442 nm (2400 lines/mm), 532 nm (1800 lines/mm), 633 nm (1800 lines/nm), 785 nm (1200 lines/nm), and 830 nm (830 lines/mm). The 30×30 μm^2 surface area was mapped with a step size of 1.5 μm. A 50×/0.75 NA (*Leica*) objective lens focused the laser light to a ca. 0.8–1.4 μm size spot on the surface depending on the wavelength used. The organic molecule 2-Naphthalenethiol (2NT) (*Sigma-Aldrich*, Belgium) was chosen as the target molecule for the substrate's SERS-activity investigation because of its self-assembling monolayer ability.

The intensity of SERS was determined by averaging all the acquired spectra on a selected map and then calculating the intensity at 1377 cm^{-1} by fitting the obtained spectrum with the Gaussian-Lorentzian shape component. To determine the enhanced Raman intensity, 2.5 mM of 2NT solution in ethanol was measured in a 1 cm thick quartz cell by using a 5×/0.12 NA (*Leica*) objective lens. The method of calculating *EF* was detailed in [121]. We assumed that the surface of the AgNP array was fully

covered with a monolayer of 2NT when one 2NT molecule occupies 34.9 $Å^2$ surface area ($Å^2$/molecule) [122] [**A4**].

3.5. Modelling

Finite element method (FEM) modelling was performed by using *COMSOL Multiphysics* while employing the wave optics module. Real samples were modelled by building the unit cell based on the basis of SEM measurements. Floquet boundary conditions were applied to hexagonal and square patterns. The array was illuminated from the upper port positioned above the nanoparticle, with varying incidence wavelength, while a secondary port below collected the transmitted light, resulting in transmittance spectra. A spherical computational domain with perfectly matched layers (PML) was implemented for isolated nanoparticle calculations, and a background field was designed as a plane wave. The far-field border layer was defined as the boundary separating the physical dielectric domain from the perfectly matched layer. The optical constants of Ag were taken from [123] [**A4**].

IV. RESULTS AND DISCUSSION

4.1. Synthesis and Characterization of NPs

4.1.1. Chemical synthesis of silver nanoparticles (AgNPs) (TA effect on seeds and further growth)

The influence of the components used for the chemical synthesis of AgNPs was investigated. The purpose of this research part was to develop a methodology for the fabrication of AgNPs with the required size and its size distribution by using the seeds-mediated method. Trisodium citrate (TC) is a popular component which plays multiple roles (as a reductant and stabilizer) used in nanoparticle synthesis. Even so, a single use of TC in the growth procedure provides a slow reduction of Ag ions, causes the new nucleation process arises together with the growth and leads to inhomogeneous nanoparticle formation [124]. Bastus et al. reported the possibility of kinetically controlling the reduction of Ag ions by the use of TA in the reaction [28]. Adding TA in a low concentration, which acts primarily as a reducer, makes it possible to speed up the formation of particles and promotes fast reduction of Ag ions, thereby preventing additional nucleation. However, at high concentrations of TA, it forms the complex [Ag_2^+-TA] and causes the slowdown of particle formation, which, in turn, forms large and polydisperse AgNPs. A detailed description of Ag ions reduction in the presence of TA can be found in [28,125].

By varying the concentration of TA in the AgNPs formation process, it is possible to increase or decrease the speed of nucleation and reduction processes, thereby influencing the homogeneity of nanoparticles [125].

As a method for the synthesis of monodisperse nanoparticles of the required size, a seed process was chosen, which consists of two parts: Ag seed formation in the solution, followed by Ag reduction on the surface of the already formed silver seeds/particles, inducing consistent AgNPs growth. First, we studied the influence of TA concentration on the NPs size and distribution in seed solutions. **Figure 8** presents absorbance spectra showing the mean sizes and SD of seeds prepared by using 0.1 mM (*Set a*), 0.5 mM (*Set b*), 1 mM (*Set c*), 1.5 mM (*Set d*) and 2.5 mM (*Set e*) concentrations of TA (corresponding to TA/TC ratios 0.02; 0.1; 0.2; 0.3; 0.5). It is evident that an increase in TA concentration leads to an increase in AgNPs size from 24 nm to 61 nm, which is confirmed by the shift of the SPR peak (λ_{SPR}) from ~406 to ~430 nm. Additionally, a high TA concentration changes the degree of monodispersity where the SD size varies from ±4 nm to ±13 nm, as can be observed by analyzing SEM pictures (**Figure 9**).

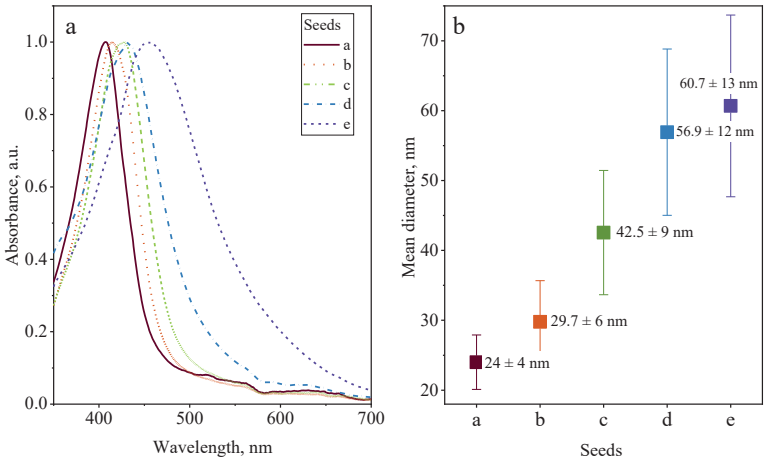

Figure 8 – Absorbance spectra (a) and the mean diameter (b) of seeds solution prepared by using different concentrations of TA: a – 0.1 mM; b – 0.5 mM; c – 1 mM; d – 1.5 mM; e – 2.5 mM

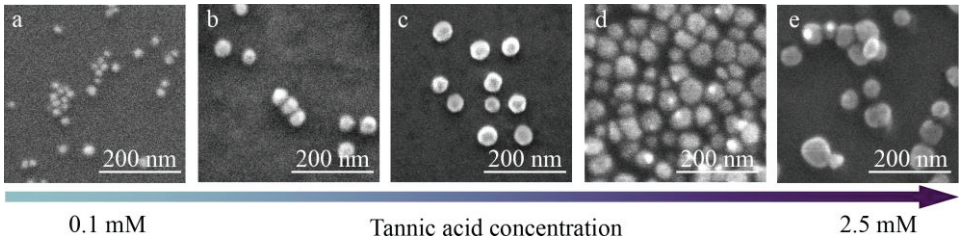

Figure 9 – SEM images of seeds prepared at different concentrations of TA: a – 0.1 mM; b – 0.5 mM; c – 1 mM; d – 1.5 mM; e – 2.5 mM

The results of the remaining five steps of seed growth are shown in **Figure 10**. The mixtures of growing NPs were identical and contained 0.347 mM of TA, 0.1 mM of TC, and 0.7 mM of $AgNO_3$. The shift of the SPR peak for each *set* (**Figure 10**) identifies the increase in the NPs size. Interestingly, seeds with ~24 nm (referred to as *Set a*, **Figure 10a,b,c**) exhibit a more gentle growth curve related to the speed of growth per cycle of the subsequent growth for five series (NPs size changed from ~24 nm to ~70 nm) than the growth curve observed for ~61 nm in diameter (referred to as *Set e*, **Figure 10d,e,f**), where NPs increased from ~61 nm to ~276 nm. In the latter case, an inhomogeneous growth of NPs is observed, where, after the first growth cycle, a nonspherical shape of NPs appears, with triangles or hexagonal nanoplates getting formed after the fifth stage.

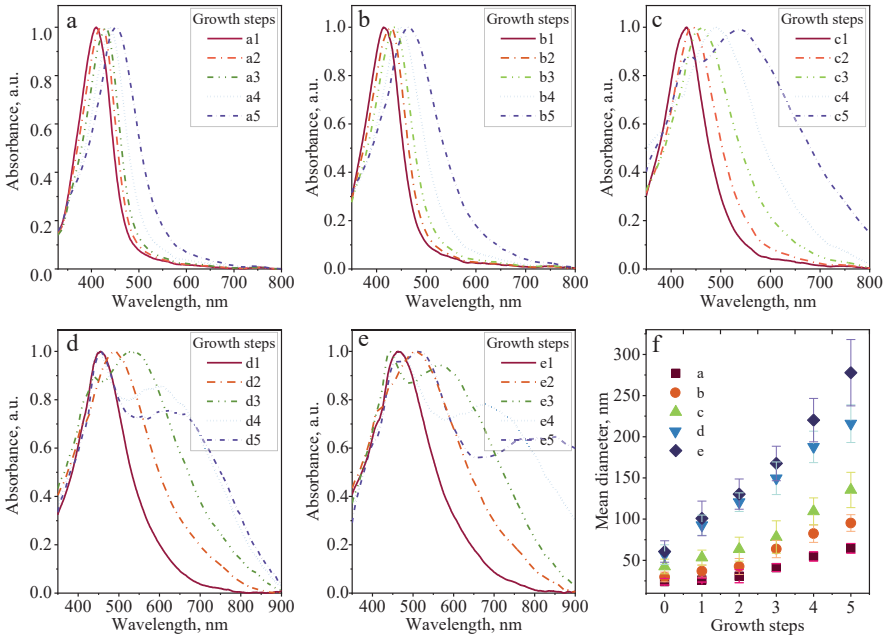

Figure 10 – Absorbance spectra of AgNPs chemically synthesized by growing seeds prepared by using different TA concentrations (a–b): a – 0.1 mM; b – 0.5 mM; c – 1 mM; d – 1.5 mM; e – 2.5 mM. The mean diameter of prepared NPs (f)

The approach of using seeds with the diameter above 40 nm for the synthesis of NPs with the target size of around 200 nm in diameter cannot be implemented as its results in polydisperse NPs. Whereas, the use of ~24 nm seeds demonstrated a promising potential in the formation of monodisperse nanoparticles (**Figure 11**); however, the NPs size can be roughly tuned. All optical and morphology characteristics of the NPs are presented in **Table 1**.

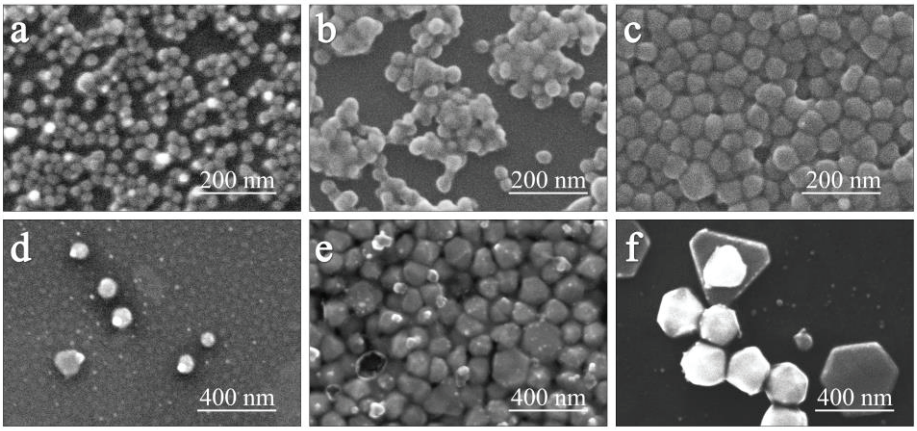

Figure 11 – SEM images of NPs prepared with TA concentration (a–b) 0.1 mM and (d–c) 2.5 mM in seeds solution after 1st (a,d), 3rd (b,e) and 5th (c,f) times growth process repetition

Table 1 – Average and standard deviations of AgNPs measured from SEM Images and SPR of samples shown in **Figure 8** and **Figure 10**

Growth steps	SPR dipolar	SPR quadrupolar	Mean diameter	SD, nm
Set a (TA concentration 0.1 mM)				
0 (seeds)	~406 nm	---	24.4 nm	3.9
1	~409 nm	---	27.8 nm	4.1
2	~419 nm	---	36.6 nm	7.9
3	~429 nm	---	43.7 nm	4.8
4	~438 nm	---	65.1 nm	5.6
5	~451 nm	---	70.4 nm	5.9
Set b (TA concentration 0.5 mM)				
0 (seeds)	~415 nm	---	29.7 nm	5.9
1	~416 nm	---	35.8 nm	7.4
2	~426 nm	---	42.5 nm	9.8
3	~435 nm	---	63.1 nm	10.6
4	~448 nm	---	83.2 nm	10.7
5	~466 nm	---	99.7 nm	10.1
Set c (TA concentration 1 mM)				
0 (seeds)	~424 nm	---	42.6 nm	8.9
1	~429 nm	---	53.3 nm	9.1
2	~444 nm	---	63.5 nm	14.5
3	~463 nm	---	78.2 nm	13.9
4	~415 nm	~490 nm	109.4 nm	16.3
5	~431 nm	~534 nm	135.4 nm	21.4
Set d (TA concentration 1.5 mM)				
0 (seeds)	~427 nm	---	57.1 nm	11.9
1	~455 nm	---	98.1 nm	12.3
2	~489 nm	---	120.2 nm	11.3
3	~443 nm	~528 nm	149.6 nm	19.8
4	~459 nm	~590 nm	187.7 nm	19.04
5	~463 nm	~621 nm	215.9 nm	22.9
Set e (TA concentration 2.5 mM)				
0 (seeds)	~430 nm	---	60.7 nm	13.1
1	~465 nm	---	100.8 nm	21.1
2	~435 nm	~507 nm	130.4 nm	18.4
3	~447 nm	~563 nm	167.6 nm	20.9
4	~474nm	~676 nm	218.1 nm	26.4
5	~508 nm	~815 nm	275.5 nm	40.3

Reducing the concentration of components utilized during the NPs growth process results in a slight increase to 5 nm particle size after each growth cycle. This is attributed to the reduced amount of silver available for reduction on the surface of the already formed particles, thereby slowing down the rate of successive growth over multiple cycles and inducing precise control over the size and uniformity of the NPs. For this purpose, the TA concentration in the seeds solution was decreased to

0.0125mM, thus making the TA/TC ratio equal to $2.5x10^{-3}$. Consistent growth of AgNPs was carried out by using 0.033 mM TC, 0.008 mM TA, and 0.083 mM $AgNO_3$ in growth solutions, which is almost three times lower than the values used in the previous experiments (0.347 mM of TA, 0.1 mM of TC, and 0.7 mM of $AgNO_3$).

After each growth step, a shift of the SPR peak by a few nanometers was introduced, which corresponds to a slight increase in the size of the NPs (**Figure 12**). After 21 successive growth procedures, the mean diameter was raised from ~20 nm to ~88 nm, with SD at around 4–5 nm (**Table 2**).

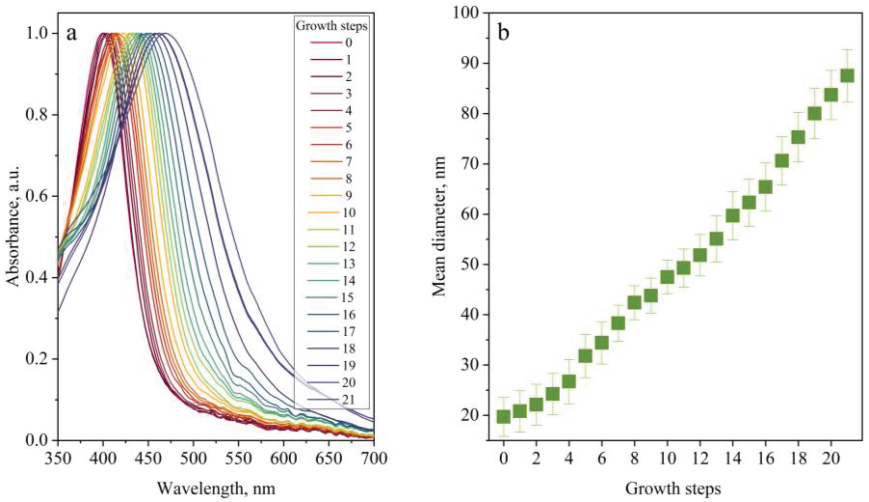

Figure 12 – Absorbance spectra of seeds obtained using 0.0125 mM of TA and 20th consistent grow AgNPs obtained using 0.033 mM TC, 0.008 mM TA and 0.083mM $AgNO_3$ in growth solutions (a); mean diameter of obtained AgNPs (b)

The growth process presented in the description of the method enables control over the nucleation, growth and stabilization processes, thereby leading to reproducible monodisperse spherical AgNPs with a diameter of 20–90 nm and SD lower than 10%. The faster AgNPs formation occurs at a lower concentration of TA (0.0125 mM in the seeds solution and 0.008 mM in the growth solution) which was being used for the experiments, because of the strong ability of TA to stabilize intermediate forms of Ag ions (as supported by the findings of [126]), which results in producing small nuclei, which further grow homogeneously. The growth mechanism enabled the formation of NPs with a controlled crystallite size, which is important in the quantitative studies of electron-phonon scattering, when investigating the effects of electron scattering in grain boundaries.

Table 2 – Average and standard deviations of AgNPs measured from SEM Images and SPR of Samples Shown in **Figure 12**

Growth steps	Mean diameter	SD, nm	SPR peak
0 (seeds)	19.7 nm	3.9	~399 nm
1	20.8 nm	4.1	~401 nm
2	22.1 nm	4.1	~403 nm
3	24.2 nm	4.1	~405 nm
4	26.7 nm	4.4	~407 nm
5	31.8 nm	4.3	~409 nm
6	34.4 nm	4.2	~411 nm
7	38.3 nm	3.6	~414 nm
8	42.4 nm	3.4	~417 nm
9	43.8 nm	3.5	~421 nm
10	47.5 nm	3.4	~429 nm
11	49.3 nm	3.8	~431 nm
12	51.9 nm	4.1	~434 nm
13	55.1 nm	4.6	~437 nm
14	59.7 nm	4.8	~439 nm
15	62.3 nm	4.7	~443 nm
16	65.4 nm	4.8	~445 nm
17	70.6 nm	4.8	~451 nm
18	75.3 nm	4.9	~457 nm
19	80.1 nm	5.1	~462 nm
20	83.7 nm	4.9	~463 nm
21	87.5 nm	5.2	~467 nm

4.1.2. Crystallite structure of AgNPs

The size of NPs is important in quantitative studies of *electron-phonon* scattering, in terms of elucidating the effects of electron scattering in grain boundaries. AgNPs formed after the 4^{th}, 6^{th}, 9^{th} and 13^{th} steps of consistent growth when using 0.0125 mM of TA in the seeds solution and 0.008 mM in the growth solution (from **Table 2**) were chosen for the crystalline structure and ultra-fast relaxation dynamics study. The polycrystallinity of AgNPs was defined by TEM images (**Figure 13, top**) and the monocrystalline silver nanocubes (NCs) are presented at the bottom in **Figure 13** for comparison. The linear dimension (diameter (D); edge length (EL)) was determined by TEM and presented in **Table 3**. XRD patterns of two types of NPs (spherical and cubes) (**Figure 14**) show the diffraction peaks at $2\Theta = 38.2°$, 44.5°, 64.6°, and 77.6°, 81.7°, which corresponds to the planes (111), (200), (220), (311) and (222), respectively, of the face-centered cubic (FCC) NPs structure, according to the standard powder diffraction card Joint Committee on the *Powder Diffraction Standards* (JCPDS), NPs file No. 04-0783.

The crystallite size of spherical nanoparticles was calculated by using the Scherrer formula [127], and the results are presented in **Table 3**. It can be seen that the size of the AgNPs crystallite increases together with the diameter (**Table 3**), and this is in good agreement with the applied synthesis approach.

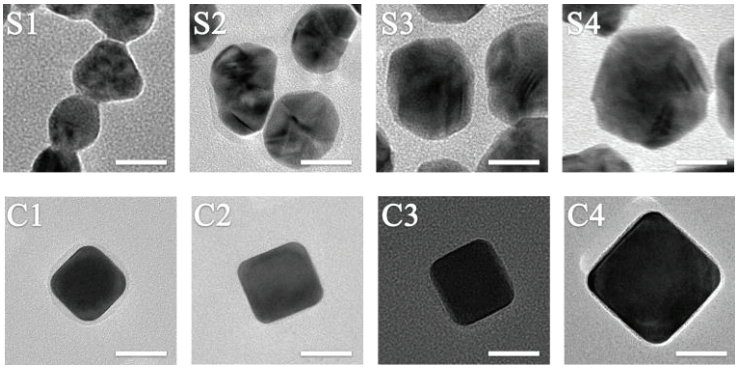

Figure 13 – TEM analysis of Ag NPs (S1-S4) and AgNCs (C1-4). The scale bar is 25 nm

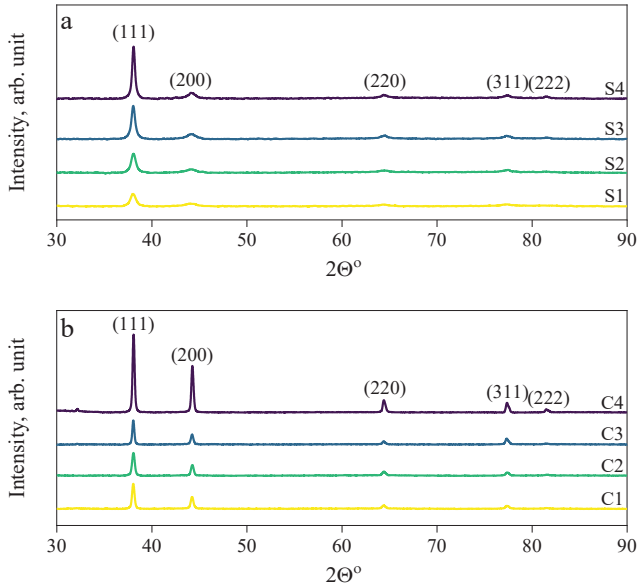

Figure 14 – XRD patterns of AgNPs (a) and AgNCs (b). The peaks are assigned to diffraction from planes (111), (200), (220), (311), and (222) of AgNPs (the spectra are offset for clarity) [**A2**]

Table 3 – Mean sizes of Ag NPs (S1-4) and AgNCs (C1-4) based on TEM analysis, crystallite size based on XRD data, *e-ph* coupling time constant $\tau_{e\text{-}ph}$ from TAS data [**A2**]

Sample	Diameter /Edge length (nm)	Crystallite size (nm)	Crystallite size/Diameter	(Crystallite size/Diameter)^2	$\tau_{e\text{-}ph}$ (ps)
S1	27.8±4.1	9.8	0.349	0.1218	0.96±0.02
S2	35.7±4.9	10.5	0.310	0.0961	0.90±0.002
S3	44.8±4.4	13	0.291	0.08468	0.77±0.003
S4	56.3±5.6	15	0.272	0.07398	0.69±0.02
C1	31.3±1.72	27.1	0.8686	0.7545	0.86±0.04
C2	35.1±1.70	27.8	0.7920	0.6272	0.94±0.01
C3	37.2±2.17	30.9	0.8306	0.6899	0.85±0.01
C4	55.8±3.62	32.1	0.5753	0.3310	0.85±0.02

4.1.3. Optomechanical characterization of AgNPs

TAS measurements were conducted for AgNPs S1–S4 (as described in Section 4.1.2) to explore ultrafast processes occurring in them, including defectiveness and the structure on them.

The measured AgNP solutions demonstrated the TAS signal oscillations that are typical of monodisperse-sized NPs [128] (**Figure 15e,f,g,h**) and become clearer with an increase in the size of the NPs.

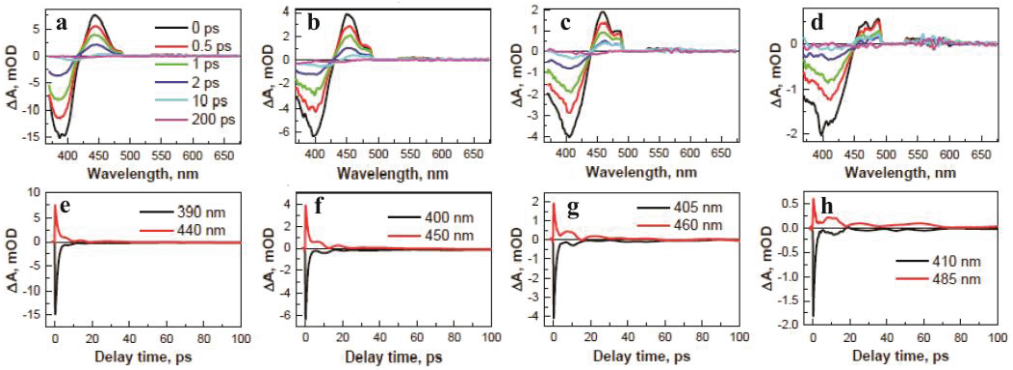

Figure 15 – TAS spectra and traces of S1 (a,e), S2 (b,f), S3 (c,g), S4 (d,h) samples [**A2**]

Electron-phonon coupling (*e-ph*, τ_1) and *phonon-phonon* (*ph-ph*, τ_2) scattering time constants were calculated from the TAS signal decay traces, measured at different probe wavelengths and different pump excitation intensities (**Figure 16**) by fitting traces at the negative and positive peaks of the TAS spectra by using the exponential decay function with one or two components (Eq. 8) [129,130]:

$$I(t) = A_1 e^{-\frac{t}{\tau_1}} + A_2 e^{-\frac{t}{\tau_2}} + I_0, \quad (8)$$

where τ_1 and τ_2 are time constants of decay; A_1 is the amplitude of the τ_1 decay component; A_2 is the amplitude of the τ_2 decay component; while I_0 represents the background of the TAS signal [131]. The fitting results for AgNPs are summarized in **Table 4**.

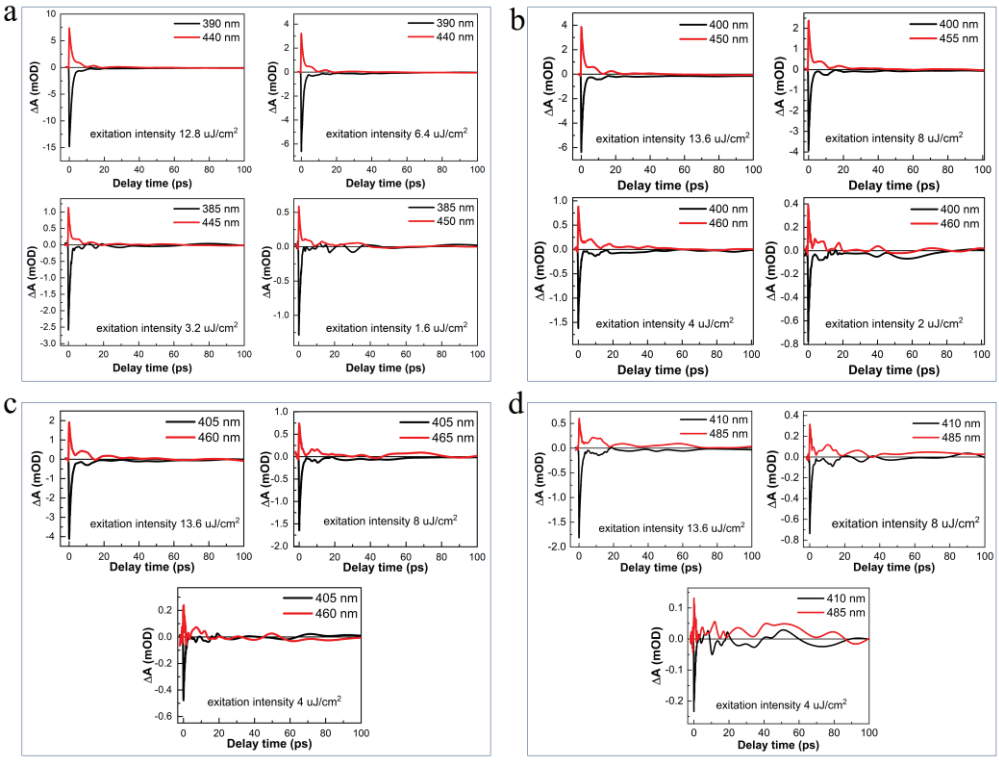

Figure 16 – TAS traces of S1 (a), S2 (b), S3 (c), and S4 (d) samples under different excitation intensities [**A2**]

For the investigation of the coupling time constants, pump excitation intensity measurements were performed in **Figure 16**. The *e-ph* coupling time constant ($\tau_{e\text{-}ph}$) was extrapolated from τ_1 under the excitation intensity of 0 as in [129,132,133]. The extrapolated *e-ph* coupling time constants are shown in **Table 3**.

Damping of the excited state depends on *e-ph* coupling and decreases from 0.96 ps (Sample S1, D=27.8±4.1nm) to 0.69 ps (Sample S4, D=56.3±5.6 nm). A relatively weak TAS signal relaxation component that can be attributed to *ph-ph s*cattering was observed. The duration range changed from 10 to 206 ps (**Table 4**).

Polycrystalline AgNPs exhibit a decrease in the *e-ph* coupling time constant with an increasing mean diameter (**Figure 17a**), while monocrystalline AgNCs seem to be independent of the edge length. However, the grain boundaries of polycrystalline materials have been reported to play an important role in all modes of plasmon damping [130] and characterize the *e-ph* coupling time, which, in turn, depends on the crystallinity of the NPs [129]. To analyze the decay time constant of the *e-ph*

coupling behavior in dependence on crystallinity, we chose the ratio (Crystallite size / Linear dimension of AgNPs)^2, assuming that the higher ratio of the crystallite size to the size of NPs corresponds to a more pronounced monocrystalline structure and reduces the number of grain boundaries of the NPs.

Table 4 – Fitting parameters of the S1-S4 AgNPs TAS traces by using Eq. (8) under different excitation intensities and at different probe wavelengths [**A2**]

Sample	Excitation intensity (μJ/cm^2)	Probe wavelength (nm)	$\tau 1$ (ps)	$A1$	$\tau 2$ (ps)	$A2$	R^2
S1	12.8	390	1.44±0.02	1.04±0.01	206.3±466.7	0.02±0.02	0.9974
		440	1.32±0.03	0.91±0.01	12.9±2.1	0.13±0.01	0.9986
	6.4	390	1.15±0.02	0.99±0.01	144.7±192.0	0.03±0.01	0.9962
		440	0.93±0.02	0.86±0.01	10.8±1.4	0.17±0.01	0.9978
	3.2	385	1.09±0.02	1.02±0.01	-	-	0.9945
		445	0.91±0.03	0.91±0.01	19.2±4.1	0.15±0.02	0.9942
	1.6	385	1.03±0.03	0.98±0.01	-	-	0.9830
		450	0.78±0.03	0.96±0.02	29.3±10.4	0.13±0.02	0.9850
S2	13.6	400	1.12±0.02	0.91±0.01	133.6±162.2	0.03±0.02	0.9940
		450	1.14±0.03	0.90±0.01	21.4±4.2	0.16±0.01	0.9957
	8	400	1.03±0.02	0.92±0.01	72.7±71.3	0.03±0.01	0.9942
		455	0.96±0.03	0.85±0.01	24.3±4.1	0.17±0.01	0.9953
	4	400	0.96±0.02	0.91±0.01	177.9±301.0	0.04±0.03	0.9889
		460	0.83±0.04	0.89±0.02	59.7±18.5	0.18±0.02	0.9815
	2	400	0.93±0.03	0.85±0.02	189.0±279.6	0.07±0.04	0.9770
		460	0.74±0.06	0.91±0.03	49.5±22.9	0.21±0.03	0.9424
S3	13.6	405	1.15±0.02	0.99±0.01	109.6±57.0	0.05±0.01	0.9973
		460	0.98±0.05	0.92±0.02	27.9±7.0	0.20±0.02	0.9867
	8	405	0.99±0.02	0.97±0.01	97.8±79.0	0.04±0.01	0.9951
		465	0.99±0.06	0.90±0.02	34.3±26.3	0.10±0.02	0.9656
	4	405	0.88±0.03	0.96±0.02	-	-	0.9690
		460	0.52±0.08	1.10±0.09	52.1±53.5	0.18±0.06	0.7719
S4	13.6	410	1.10±0.02	0.96±0.01	102.5±56.5	0.06±0.01	0.9953
		485	0.84±0.07	0.88±0.04	72.5±25.3	0.28±0.03	0.9415
	8	410	0.91±0.03	0.98±0.01	60.8±45.9	0.06±0.01	0.9888
		485	0.81±0.06	0.93±0.04	206.8±188.7	0.30±0.14	0.9114
	4	410	0.84±0.05	0.90±0.03	-	-	0.9086
		485	0.65±0.09	0.80±0.06	-	-	0.6697

Figure 17b presents the linear dependence of the decay time constant on (Crystallite size / Linear dimension of AgNPs)^2 and shows that it increases for a higher ratio of the crystallite size to the size of NPs. These findings are in good agreement with the other reports where the increase of the coupling efficiency of hot electrons with phonons due to grain boundaries in polycrystalline gold NCs makes the *e-ph* coupling process faster [129,130]. The present results of polycrystalline AgNPs were compared to the monocrystalline AgNCs (**Figure 17c**), where plasmon relaxation dynamics are indifferent to the size and don't show any clear dependence on the (Crystallite size / Linear dimension of AgNCs)^2 ratio. In **Figure 17a,c**, the red line shows the guide for the viewer's eyes which was chosen to demonstrate that the coupling time constant does not depend linearly on the size.

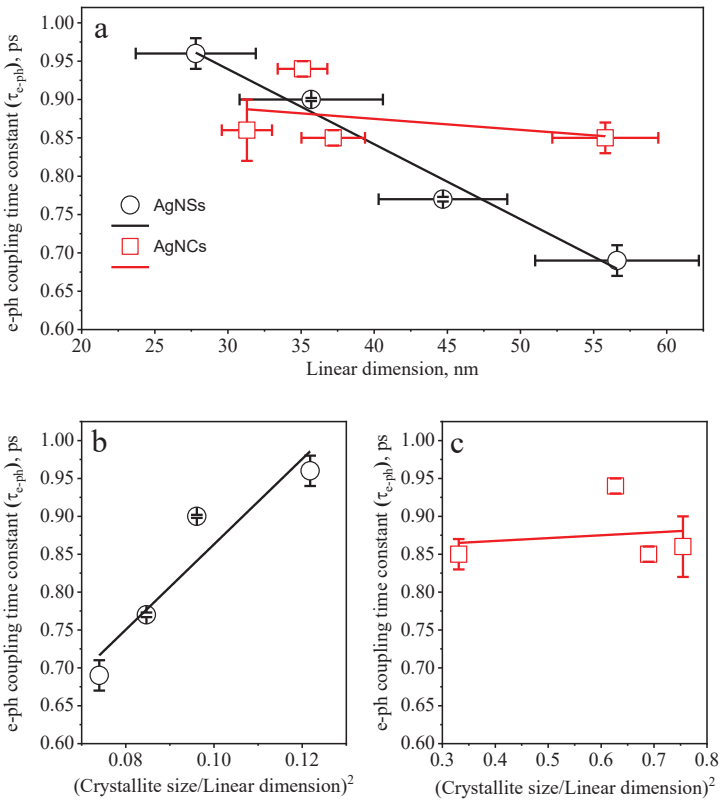

Figure 17 – Dependence of e-ph coupling time constant on the diameter of AgNPs (a). *e-ph* coupling time dependence on (Crystallite size / Linear dimension AgNPs)^2 (b). The red line shows the guide for eye [**A2**]

4.2. SERS Substrates Based on Unordered Particle Arrays in Dielectric Material

4.2.1. Fabrication and characterization of porous silicon

To fabricate a template with random traps for subsequent filling with NPs to create their array, porous silicon (PS) was chosen. Typically, PS formed by electrochemical anodization has a parasitic top layer, the so-called 'bottleneck' PS with little variation in pore sizes. The author of this thesis has demonstrated that reactive ion etching is an effective method for removing the parasitic layer (or 'open pores') [**A3**].

The surface morphology of the open pore PS was studied in dependence on the applied current density and concentration of HF. In **Figure 18**, the SEM images of one set of PS samples before and after RIE treatment, formed at j = 60 mA/cm^2 in 5 wt.%, 10 wt.% and 20 wt.% HF solutions, are shown.

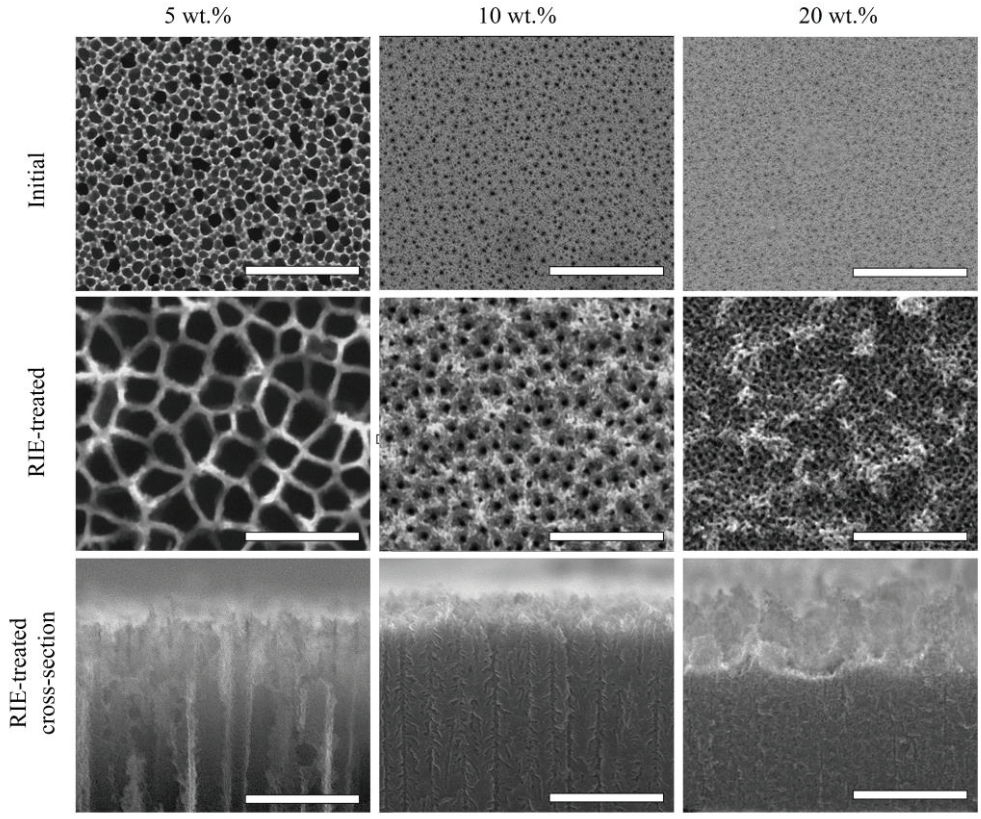

Figure 18 – Top view of initial PS (on top) formed at j = 60 mA/cm^2 in the electrolyte with HF concentration 5 wt.%, 10 wt.%, 20 wt.%. Top view and cross-section of the same samples after RIE treatment (at the bottom). Scale bar is 500 nm [**A3]**

The morphology of RIE-treated PS formed in the electrolyte with 5 wt.% (for all samples) and 10 wt.% HF (at a high current density) mostly looks smooth, and only a slight increase in the roughness of PS indicates isotropic etching of the top layer. The surface of the samples made at 10 wt.% HF at a low current density (20–60 mA/cm^2) and for all samples made with 20 wt.% HF is characterized by the formation of a porous layer consisting of islands which make the surface rough.

The mean pore diameter and the density of the pores are presented in **Figure 19**. One can see that the average diameter increases with an increase in the current density due to a larger number of holes which move to the Si/electrolyte interface as a continuous front and provide reactivity for a higher number of Si atoms in the vicinity of the surface defects. This linear dependence is followed until some critical value of the current density is reached, and then the pore size starts to decrease (**Figure 19a**). It should be noted that the critical current density value depends on the HF concentration, i.e., for a 5 wt.% HF solution, the maximum pore diameter of ~130 nm is reached at 60 mA/cm^2, while, for 10 wt.% HF solution, a 160 nm pore diameter is observed at 140 mA/cm^2. These trends can be explained by changes in the mechanism of PS formation by anodization [134]. At the current density higher than the critical value, the pores become spatially irregular, and a sponge-like structure is formed. The Si skeleton becomes thinner, and the pore density increases. A further increase in the current density leads to the electropolishing process. Moreover, electropolishing can be predicted by the pore density value, e.g., we have experimentally confirmed that, in 5 wt.% HF solution, this process starts at 100 mA/cm^2, while, for 10 wt.% HF, the current density must be higher than 400 mA/cm^2.

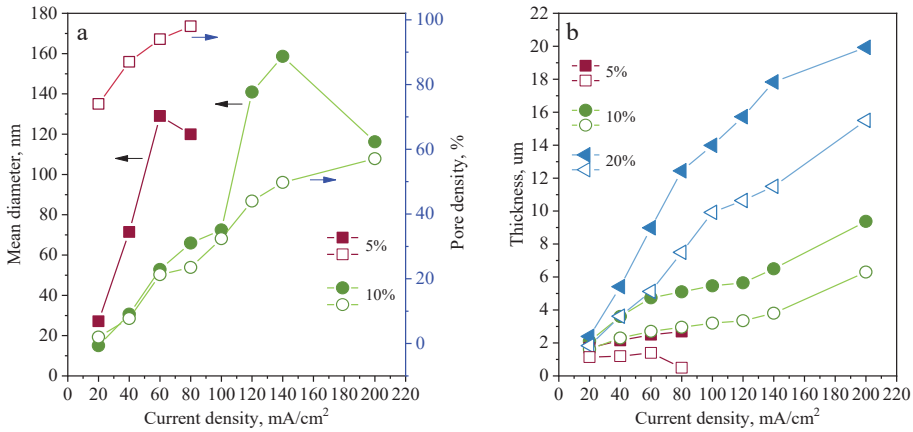

Figure 19 – Dependence of the mean pore diameter (filled symbols) and pore density (empty symbols) on the applied current density (a) and PS thickness (b) dependence (initial PS samples are marked with filled symbols; RIE-treated samples are marked with unfilled symbols) of PS samples formed at different HF concentrations [**A3**]

The PS thickness growth rate was determined from a cross-sectional analysis of SEM images. It was established that the growth rate of the layer thickness shows an almost linear dependence on the applied current density. At the same time, we can

observe that thicker layers were created at higher HF concentrations during the same process time (**Figure 19b**). The analysis of the thickness of the RIE-treated PS layers shows that the RIE-etch process runs slower for PS with a lower pore density. The RIE speed increases sharply for the samples fabricated in 5 wt.% HF and at j = 80 mA/cm^2 due to the high density of pores (which reaches up to 96%) and thin Si walls. After RIE, we observed that most of the moiety of the PS layer was removed, and the depth of the produced structure was approximately 500 nm, while the initial depth of PS was about 2.6 μm.

The optical properties of the PS layers, especially the refractive index, are important for the further development of photonic sensors where a porous material is used [135]. The surface layer consists of silicon crystallites and pores which contribute to diffuse light scattering and the final reflectivity. In **Figure 20**, the measured PS reflectance spectra of the samples formed at 5 wt.% HF and 10 wt.% HF exhibit a series of interference fringes related to the constructive and destructive interference of the reflected light from the air/PS and PS/Si interfaces corresponding to the Fabry-Pérot interference fringes. By applying the Fabry-Pérot interference principle [136], the *Effective Optical Thickness* (EOT) $2n_{PS}L$ was calculated. The value of the average refractive index of PS (n_{PS}) was evaluated from EOT by using the value of the PS layer thickness (L) (**Figure 19**). The calculated values are presented in **Table 5**. The frequency of the interference fringes strongly depends on the air fraction values (porosity) in the PS structure [137].

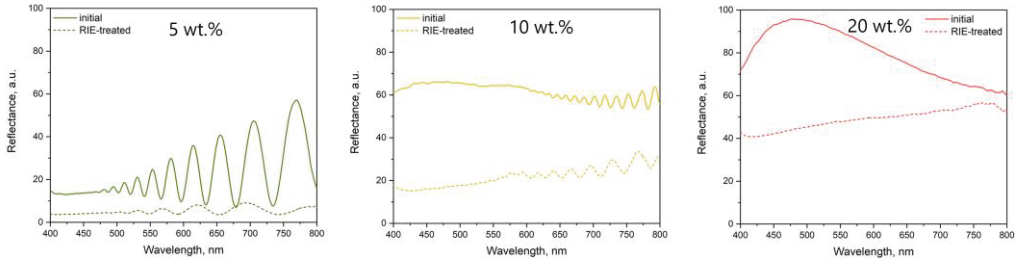

Figure 20 – Reflectance spectra of initial PS (solid line) and RIE-treated (dashed line) formed at j = 60 mA/cm^2 in electrolyte with HF concentration 5 wt.%, 10 wt.%, 20 wt.% [**A3**]

Table 5 – Average refractive index of initial and RIE-treated PS [**A3**]

HF concentration		Current density (mA/cm^2)							
		20	**40**	**60**	**80**	**100**	**120**	**140**	**200**
5 wt.%	initial	3.21	2.48	1.39	1.20	-	-	-	-
	RIE-treated	3.35	2.50	1.41	1.57	-	-	-	-
10 wt.%	initial	3.24	3.14	2.99	2.73	2.40	2.13	2.10	2.01
	RIE-treated	-	3.17	2.97	2.87	2.72	2.20	2.17	2.04

In general, the RIE-treated samples are considered as a one-layer structure, while the initial samples are considered to be multilayer structures having a different porosity. The calculated n_{PS} values for the samples made by using 5 wt.% and

10 wt.% HF electrolytes decrease with an increase of the applied current density, and it relates to an increase of the pore density (porosity) [138], which is in good agreement with the data presented in **Figure 19a**. An exception is observed for the PS sample formed in 5 wt.% at j = 80 mA/cm^2, where the refractive index increases. It can be attributed to the contribution of Si to the reflection spectrum as a result of the small amount of the remaining PS after etching. In most cases, the n_{PS} values of the non-treated PS samples are slightly lower than those of the RIE-treated samples because of the presence of a highly porous surface parasitic layer which contributes to n_{PS} and decreases its value. Only in one case (10 wt.% HF; j=60 mA/cm^2), the refractive index of the RIE-treated PS sample is lower than the value of the initial PS sample, but the difference is rather small, and it might relate to thickness estimation errors.

The reflectance spectrum of the initial PS samples prepared in 20 wt.% HF solution (**Figure 20**) looks similar to the spectrum of bare silicon. We assume that the porosity of these samples is so low that we cannot observe any major changes in their optical properties. The RIE-treated PS reflectivity is characterized by a lower intensity because of the scattering effect which occurs on a rough surface. In both cases, the reflectance spectra demonstrate fringes with a very low amplitude that are hardly distinguished and cannot be used for further determination of the optical parameters. The optical parameters were not set for the sample formed in 10 wt.% HF and j = 20 mA/cm^2 due to the same difficulties. It should be noted that the removal of the 'bottleneck' layer led to the opening of the structure which provided deposition of the highly ordered group of AgNPs divided by the silicon walls of the nanoscale thickness, as shown below.

4.2.2. *Nanoparticle deposition in the pore of nanostructured silicon and on flat surfaces*

Nanoparticle deposition was performed by using the CAPA method as it provides the most controlled distribution of colloidal NPs over a template's surface compared to the alternative techniques (e.g., drop deposition). AgNPs with a mean diameter of 62 nm with SD ~10% which coincide with the pore size of RIE treated PS formed in 10 wt.% HF solution and at j = 100 mA/cm^2 were chosen for the deposition process. The diameter of the NPs was selected based on the research showing the successful use of the size of such particles in sensing experiments [139], and the pore size of the developed PS sample was chosen to be fitted with NPs. In addition, the same AgNPs were deposited on nontreated PS formed at the same condition as the PS outlined above. The surface of PS after the AgNPs deposition is shown in **Figure 21**.

During the deposition process, several challenges were encountered. First, the surface of the template must be completely wetted by the solution [140], whereas the surface of PS is highly hydrophobic [**A2**]. Second, in spite of the fact that AgNPs being covered with hydrophilic PVP tended to aggregate more likely rather than pores penetration. Overcoming this challenge required careful optimization to provide a

successful integration of NPs onto the PS-based template. In this case, the mixture of ethanol, DMF, and additional PVP was used to maintain the good stability of NPs and to increase the wettability of the PS surface. As a result, the entrance filling factor of ~85% of AgNPs deposition into pores was achieved, by applying 0.1 μm/s stage speed of 0.1 m/s and maintaining the temperature at 12°C above the dew point (**Figure 21b**). Most of the deposited NPs are placed in pores. In rare cases, they occupied one pore or were displaced to the edge of the pore.

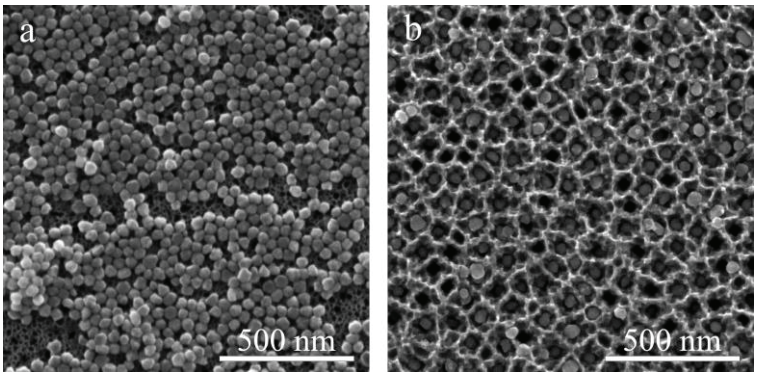

Figure 21 – Top view of the initial (a); and the RIE-treated PS (b) made in 10 wt.% HF solution and at j = 100 mA/cm^2 after AgNPs deposition [**A3**]

4.2.3. Modelling of nanoparticles on the surface and within pores

To investigate the structure, it is prospective that it has an extremely intensive EM field in the spots of contact between AgNP and the silicon wall; due to plasmonic coupling between MeNP and semiconductors [141], the modelling of AgNPs in pores of RIE-treated Si and on pores of non-treated Si was performed. Open-pore PS has randomly arranged pores, each of which borders with six others. The structure of NPs can be displayed as a hexagonal cell (if we somewhat idealize the structure) with a dimension r=92 nm, where the diameter of NPs is 62 nm separated with a 28 nm silicon wall, as shown in **Figure 22a**. The same unit cell can be used for closely packed NPs on the surface of PS with an *r* equal to 63 nm. In **Figure 22b,c**, the distribution of the EM field enhancement is presented. The highest enhancement of the EM field occurs in the vicinity of the metal surface when AgNPs are placed on PS. On the contrary, for AgNPs in pores, it is concentrated in the AgNPs-Si wall contact. As it is seen from the field enhancement distribution for NPs implemented in pores, the enhancement is 8 times stronger than for NPs on pores, which confirms the theory of the EM field enhancement in the metal-semiconductor interface. The simulated reflectance spectra presented in **Figure 22c,d** demonstrate the strong absorption near the 400 nm wavelength for AgNPs on PS and 375 nm for AgNPs in pores and exhibit a similar curve to the measured spectrum.

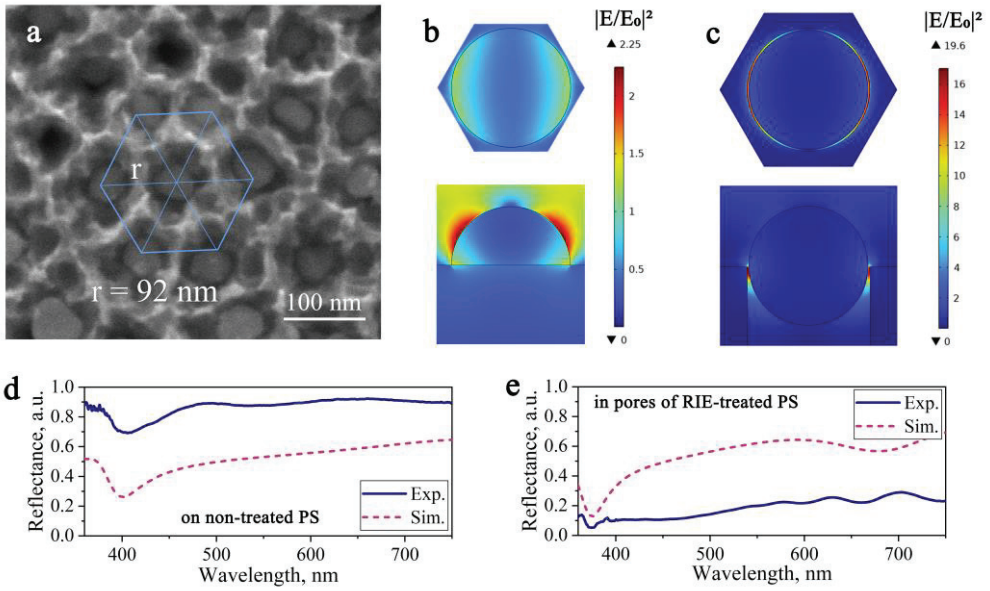

Figure 22 – SEM image of RIE-treated PS with implemented AgNPs into pores (a); top and cross-section view of enhancement of EM field of AgNPs on non-treated PS (b); top and cross-section view of enhancement of EM field of AgNPs implemented onto pores of RIE-treated PS (c); simulated and experimental reflectance spectra of AgNPs deposited on and into pores (d,e)

4.2.4. SERS sensitivity of unordered nanoparticle array

The SERS measurements were performed to evaluate *EF* by using 532-nm laser excitation. Despite the fact that both structures based on PS are characterized by absorption in the blue region, they are also sensitive at longer wavelengths. The recorded spectra of the 2NT molecule adsorbed on AgNPs from solution with 10^{-4} M concentration are presented in **Figure 23**. The peaks of the typical 2NT vibrational modes (764 cm^{-1}, 1067 cm^{-1}, 1377 cm^{-1}, 1583 cm^{-1}, 1621 cm^{-1}) are highlighted. By using the intensity of the most intense peak (1377 cm^{-1}), *EF* was calculated, and the values for NPs on non-treated PS and NPs within pores were 1.4×10^7 and 5.3×10^8, respectively, which indicates a significant enhancement of the Raman signal in the latter case, in agreement with the theoretically predicted results. This calculation was performed to provide a simple demonstration of the SERS enhancement for AgNPs in pores compared to them on PS. However, it cannot be considered as a fully correct evaluation. The difficulties in EF calculation for PS arise from the possibility of molecules being adsorbed onto the PS structures, and their amount can depend on the structure porosity. In the review article [**A1**], the issue of EF calculation is considered, and the comparison of SERS active substrates based on PS is suggested to be carried out based on the values of DL. The DL of the structure based on AgNPs in pores was set to 10^{-7} M for 2NT molecule at 532 nm wavelength excitation that is relatively high compared to the SERS substrates based on mesoporous silicon covered by AgNPs

which demonstrated the DL values in the range from 10^{-9} to 10^{-15} in dependence on the target molecule [**Table 1; A2**].

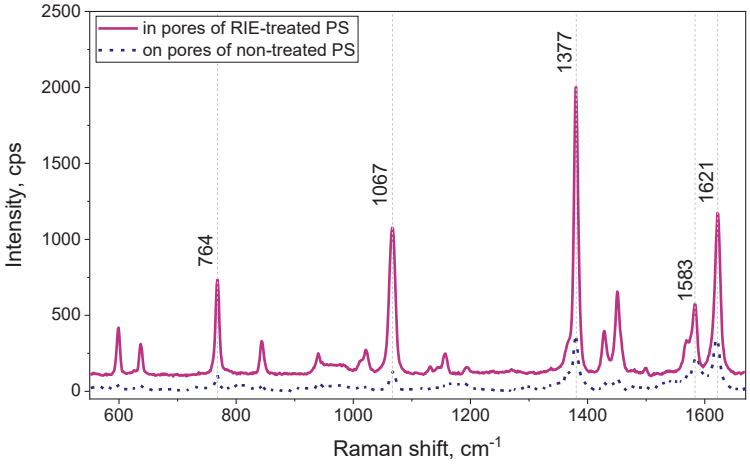

Figure 23 – SERS spectra of 2NT measured using PS-based substrates with NPs in and on pores

Due to the low SERS sensitivities of the open-pore PS substrate and difficulties in depositing NPs in the pores because of the rough surface, we have decided to shift our focus to SERS substrates based on arrays of NPs with tunable optical properties designed for targeted wavelength excitation.

4.3. SERS Substrates Based on an Ordered Array of Nanoparticles with Tunable Plasmonic Properties

4.3.1. Tailored plasmonic array for enhanced Raman excitation

Tailored plasmonic arrays were designed in a way to have an SLR peak (λ_{SLR}) closer to the target laser excitation wavelength (λ_{Ex}) of 532 nm. For this purpose, a square grating Λ = 330 nm (SQ330) with an RA wavelength (λ_{RA}) in PDMS at 470 nm was chosen based on the previously obtained results [119]. To show the tunability of the plasmonic properties of an array of NPs in dependence on their diameter, a simulation of the periodic structure was done by using a unit cell shown in **Figure 24**.

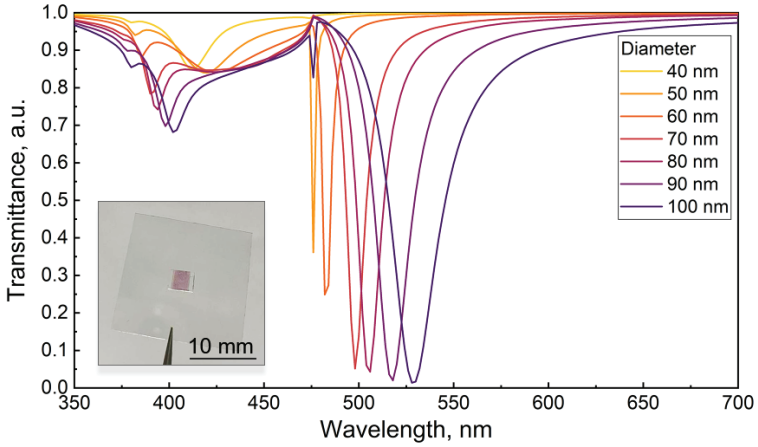

Figure 24 – Simulated transmittance spectra showing SLR peaks generated by arrays of single AgNPs from 40 to 100 nm in diameter [**A4**]

The simulated results (**Figure 24**) show that λ_{SLR} depends on the diameter of the NPs. The SLR peak redshifts, and its FWHM increases with an increasing NP diameter [142]. This behavior of SLR at a constant lattice period is attributed to changes in the LSPR properties of the particles, in which an increase in their diameter leads to a shift of the absorption peak to the red wave zone. The FWHM broadening is caused by λ_{SLR} moving away from λ_{RA}. NPs with a diameter of 90 to 100 nm show a λ_{SLR} value close to the target of 532 nm. AgNPs with a diameter of 88±5.2 nm that have a dipolar LSPR peak around 460 nm and which overlaps the λ_{RA} of the 330 nm square lattice (**Table 2**) were chosen to assemble into arrays.

Figure 25a presents an SEM image of the assembled plasmonic structure, where the traps in a structured PDMS substrate are filled primarily with single NPs (*monomer assemblies*). In **Figure 25b,c,** the simulated enhancement of the EM field by an isolated nanoparticle (perfectly matched boundary condition) and the particle in the array (periodic boundary conditions) are shown, respectively. A strong near-field is observed in both cases, with a 4.2- and 14.7-times enhanced field at the 532 nm wavelength in the isolated nanoparticle and array cases, respectively. The experimental and calculated values λ_{SLR} demonstrate good qualitative agreement (**Figure 25d**). The experimental dip in the transmittance spectrum is wider and slightly red-shifted because of the presence of the defects stemming from the self-assembly nature, which result in an empty trap, with random two or three NPs per trap. The difference in the spectral position between the experimental λ_{SLR} and λ_{Ex} in monomer assemblies is 9 nm.

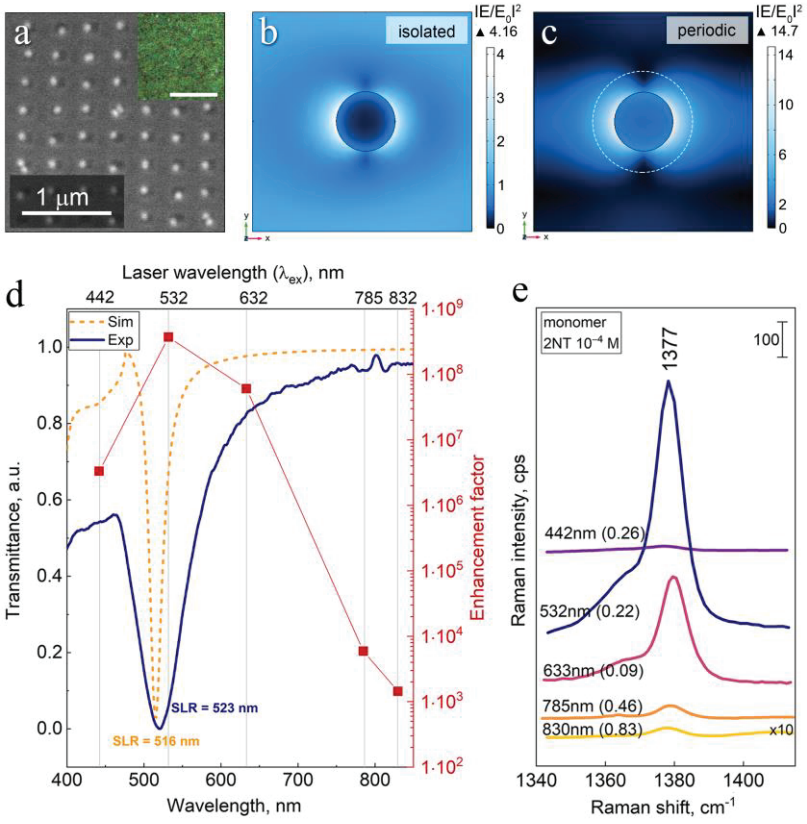

Figure 25 – Raman enhancement by resonant plasmonic arrays based on monomer and tetramer unit cells. (a) SEM micrograph of a monomer NP array and a dark field optical micrograph of the assembly as an inset (scale bar is 20 μm). EM field enhancement by (b) an isolated nanoparticle; and (c) a nanoparticle in Λ = 330 nm array (λ=532 nm, a dashed line indicates trap geometry). (d) Simulated and measured transmittance spectra of the monomer array; experimental values of the SERS *EF* of the monomer assembly (red squares), (the vertical line indicates λ_{Ex}). (e) Raman scattering spectra of 2NT (10^{-4} M), zoomed in on the 1377 cm^{-1} band versus excitation wavelengths (laser power in mW is indicated in parentheses) [**A4**]

The monomer-based SERS substrate was investigated at different excitation wavelengths for 2NT detection (**Figure 25e**). 10^{-4}M concentration for the initial evaluation was used. The most intense Raman band at 1377 cm^{-1} related to ring deformation was chosen to analyze the contribution of the SLR effect to the enhancement. The *EF* value was estimated by averaging the SERS signal intensity over the scanned area and comparing it to the SERS signal of a single molecule per unit of measurement. The data and a detailed description of the *EF* calculations are presented in the author's paper [**A4**]. The intensity of the 1377 cm^{-1} band and the corresponding *EF* showed a good correlation with the overlap of λ_{SLR} and λ_{Ex} (**Figure 25b**). The strongest intensity of the peak is observed at λ_{Ex}=532 nm, which resulted in

EF of $6.1 \cdot 10^8$. This value gradually decreased as the laser excitation was detuned from SLR.

4.3.2. Tailored plasmonic arrays with a multi-particle in unit cell

Usually, a strong SERS enhancement of non-SLR structures is observed in hot spots which are related to small gaps. To improve the *EF*-tailored plasmonic array substrates considered in Chapter 4.3.1, smaller NPs (77 nm in diameter) were assembled into the same PDMS template forming the tetramer structure (four particles per trap) and to keep the λ_{SLR} close to the target λ_{Ex} (**Figure 26**). We take into account that NPs were separated by a few nanometers due to the PVP layer as measured in TEM (Figure 13).

The author modeled this structure by using the same methods and parameters as those for the monomer-based structure. The EM field at λ_{Ex} is strongly localized in the gaps between the NPs and is enhanced 49.4 and 65.9 times in the isolated and periodic tetramer unit cell cases, respectively (**Figure 26b,c**), the latter is almost 4 times higher compared to the periodic monomer unit cell (**Figure 26b,c**). The simulated λ_{SLR} emerged at 579 nm and closely matched the experimental peak at 583 nm (**Figure 26d**). The experimental transmittance spectrum of the tetramer-based structure (**Figure 26d**) is slightly wider than the simulated result due to the non-ideal structure. The collective plasmonic behavior of the structure caused the redshift and widening of SLR. This follows the theory of plasmonic hybridization [143,144] where plasmonic NPs in close proximity act as a larger particle with red-shifted LSPR [**A4**].

Like the monomer assemblies examined before, the intensity of the Raman peak increases as the difference $|\lambda_{SLR} - \lambda_{Ex}|$ decreases for the tetramer structure in the same way as for monomer assemblies (**Figure 26d**). It is almost 4 times more intense compared to the monomer assembly measured under identical conditions (**Figure 26c**). The SERS *EF* for the tetramer structure demonstrates the same trend, by peaking at λ_{Ex}=532 nm with a value of $2.6 \cdot 10^9$, which is an order of magnitude higher compared to the monomer structure. Recently, *EF* of the wavelength-tunable nanoparticle arrays made by E-beam lithography [145] and template-assisted colloidal self-assembly technique [58,146] have been reported. SERS *EF* values in the range of 10^{-7} and 10^{-6} were reported when the SLR position, generated by the nanoparticles in arrays, was tuned to laser excitation. This tuning was achieved by changing the periodicity of the lattice with the nanoparticle size during the fabrication process [56], or the polymer substrate was stretched after the formation of the arrays [145]. These substrates demonstrate up to four and three orders of magnitude less enhancement in comparison to tetramer- and monomer-based structures.

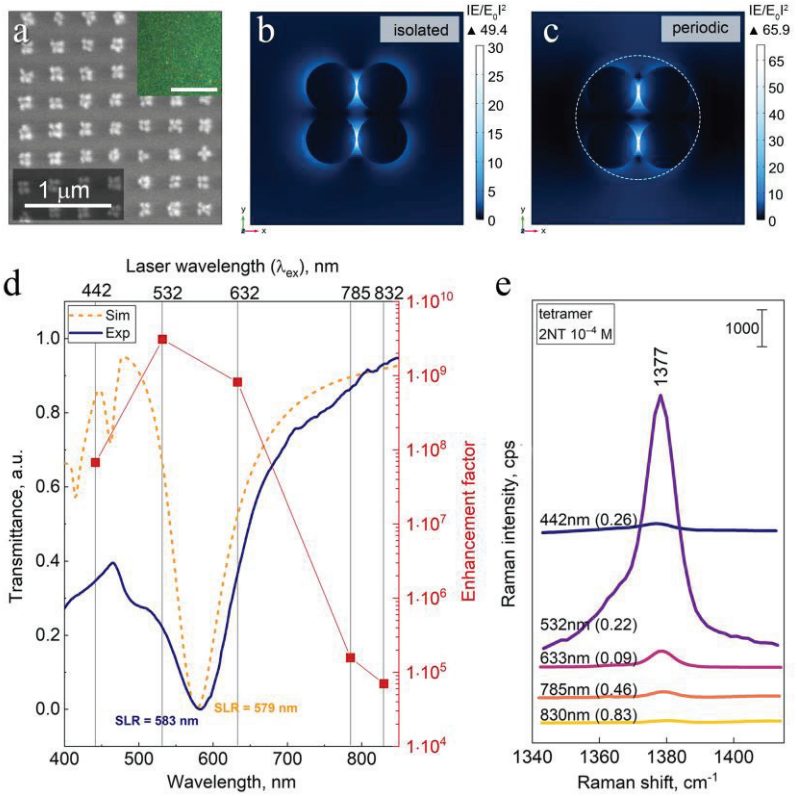

Figure 26 – (a) SEM of tetramer NP array and a dark field optical micrograph of the assembly as an inset (the scale bar is 20 μm). EM field enhancement by (b) an isolated tetramer; and (c) a tetramer in the array (λ=532 nm; the dashed line indicates trap geometry). (d) Simulated and measured transmittance spectra, and experimental values of SERS *EF* of the tetramer assembly (red squares); (vertical line indicates λ_{Ex}). (e) Raman scattering spectra of 2NT (10^{-4} M), zoomed in on the 1377 cm^{-1} band versus excitation wavelengths [**A4**]

4.3.3. Comparative analysis of SERS sensitivity of single and multi-ordered nanoparticles array

A comparison of *EF* of monomer and tetramer-based structures is supplemented by a plasmonic structure based on a monolayer of randomly arranged NPs (77±4.5 nm in diameter) on a flat PDMS substrate by using the SAM technique [147] [**A4**].

The SERS sensitivity of this monolayer was investigated in the same way at different laser wavelengths. The random monolayer substrate also shows a dependence on the excitation wavelength which peaks at λ_{Ex}=532 nm with the *EF* value of $1.6 \cdot 10^5$ [**A4**]. As reported, this dependence is typical for a single LSPR-based enhancement [148]. However, the normalized *EF* of monomer and tetramer to the *EF* of the monolayer peaked at λ_{Ex}=532 nm with 110- and 465-times higher values, respectively (**Figure 27**), which confirms the strong contribution of SLR to *EF* and

shows that it is possible to tailor the plasmonic properties of the structure based on the SLR effect to a particular excitation wavelength.

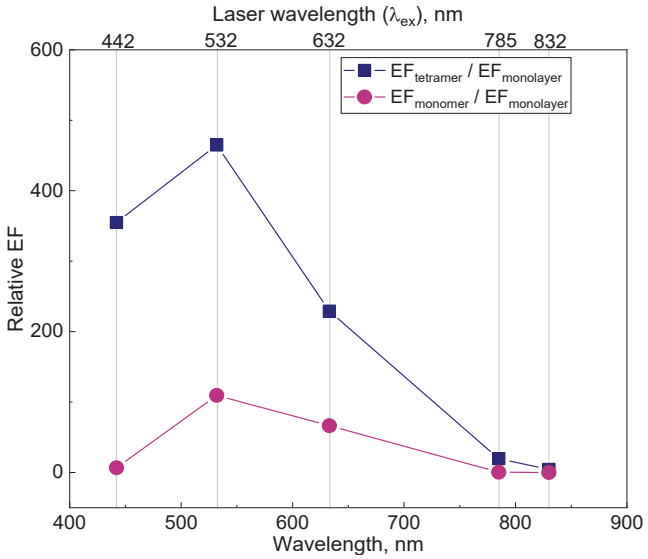

Figure 27 – Relative SERS *EF* of monomer and tetramer substrates versus wavelength of excitation (enhancement is normalized to SERS EF on a substrate with a monolayer of AgNPs) [**A4**]

The spatial enhancement homogeneity (i.e., the signal reproducibility) of the monomer-, tetramer-, and monolayer-base SERS substrate was investigated. Variation in intensity of the 1377 cm^{-1} band was recorded in a randomly chosen 20x20µm area of each structure in **Figure 28a**. The monolayer-based SERS substrate exhibits a large standard deviation value SD=37.35% due to the uncontrolled formation and positioning of the hot spots. The ordered arrangement of the NPs had a reduced deviation, but still a relatively high SD=31.81% was demonstrated. This relatively high signal variation is caused by 18% of defects [**Figure S5, A4**]. The tetramer SERS substrate showed more than two times lower SD (12.42%) due to the better control over the distribution and homogeneity of the hot spots and the reduction of lattice imperfections.

We used the excitation wavelength with the highest enhancement (532 nm) and investigated the SERS substrate *DL*. The registered spectra with the highlighted peaks of the typical 2NT vibrational modes are shown in **Figure 28b**. *DL* was determined at 10^{-8} M for monomer-based and 10^{-9} M for tetramer-based SERS substrates. In both cases, the intensity of the background increased at low concentrations because of the destruction of molecules and the increased contribution of impurities. The typical Raman peaks of PDMS (615 cm^{-1}; 708 cm^{-1}) can be seen in all measurements, but they do not overlap with the strong peaks attributed to the target molecule. In summary, the main peaks of the target molecule were able to be distinguished even at the lowest concentration investigated.

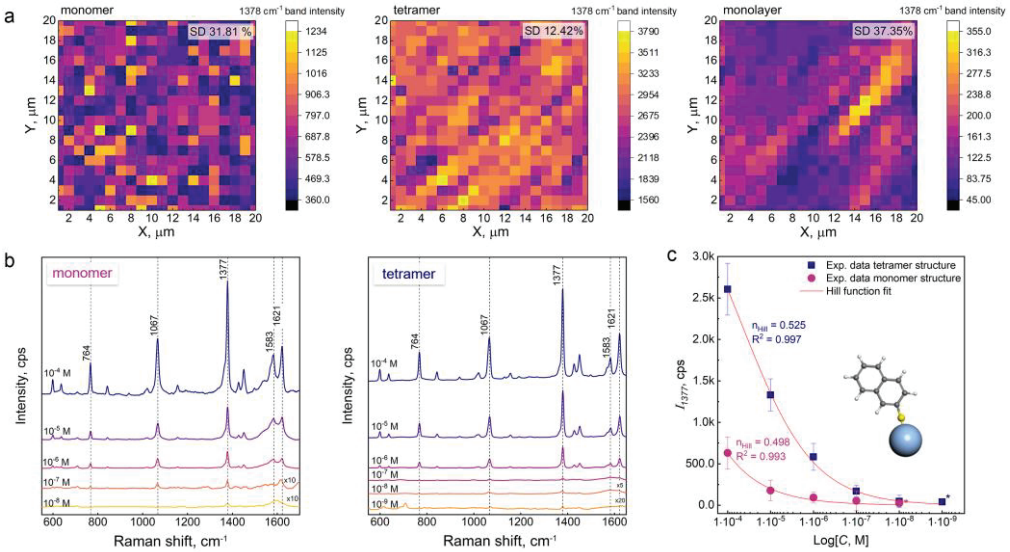

Figure 28 – Homogeneity of the SERS signal and Detection Limit of 2NT molecule. (a) 20x20 µm sized SERS maps of 1377 cm^{-1} band intensity of 2NT molecule adsorbed from a solution with a concentration of 10^{-4} M on Ag NPs monomer array (wavelength 532 nm, laser power 0.226 mW, integration time 1 s), tetramer array (0.0226 mW, 1 s), and monolayer (0.0226 mW, 3 s). (b) Raman scattering spectra of a range of 2NT concentrations were recorded by using monomer and tetramer-based SERS substrates at λ_{Ex}=532 nm. (c) The intensity of 1377 cm^{-1} band versus analyte molecule concentration [**A4**]

Figure 28c shows the plots of the intensity of the 1377 cm^{-1} peak versus the concentration indicating the SD of SERS signal fluctuation. SD is not indicated for small concentrations marked with an asterisk, as the SERS peaks of the target molecules were clearly distinguished from the noise only in two spectra. The experimental data are fitted by using the Hill function, assuming that the function can be applied to study the adsorption activity of 2NT molecules on our SERS substrates (bonding with AgNPs through the –SH moiety). Therefore, **Figure 28c** can be interpreted as the change in the reaction velocity between 2NT and AgNPs. In this way, n_{Hill} for the plasmonic array with a single NP is 0.498, and n_{Hill}=0.525 for four NPs. This suggests a higher efficiency of 2NT bonding to AgNPs since the surface area is more than 3 times higher compared to the substrate with monomers.

V. CONCLUSIONS

1. We have shown that, by applying the seed growth method, it is possible to produce uniform polycrystalline spherical silver nanoparticles with an average diameter ranging from 20 nm to 90 nm standard deviation in size of ±4 nm. The optimal concentration of tannic acid (0.0125 mM) in the seed solution was defined, while taking into account the ratio of tannic acid/trisodium citrate equal to 2.5×10^{-3}, and using 0.033 mM trisodium citrate, 0.008 mM tannic acid, and 0.083 mM silver nitrate in growth solutions.

2. The differences in the behavior of the *electron-phonon* (*e-ph*) relaxation time constants of chemically synthesized polycrystalline and monocrystalline silver nanoparticles with similar average linear sizes were discovered by transient absorption spectroscopy. The polycrystalline nanoparticles indicated a faster relaxation with an increasing size, while the decaying of monocrystalline counterparts was indifferent to the size. Further analysis showed that the *e-ph* coupling decay time constant depends linearly on the value of (Crystallite size / Linear dimension)^2 for polycrystalline silver nanoparticles, while monocrystalline nanoparticles do not show any clear dependence on this ratio, which can be explained by relaxation on crystallite boundaries.

3. According to the results of a study of porous silicon with open pores (~17–180 nm mean diameter) treated with reactive ion etching, the optimal hydrofluoric acid concentration for creating a homogeneous porous silicon substrate by electrochemical anodization of crystalline silicon is in the range of 5–10 wt.%. Additionally, the properties of porous silicon (the pore size and density, refractive index, and wettability) can be finely adjusted by changing the concentration of hydrofluoric acid and the applied current density.

4. The porous silicon structure created through reactive ion etching was found to be a favorable template for the deposition of an irregular array of silver nanoparticles by using capillary-assisted particle assembly. Within the pores, silver nanoparticles exhibited enhanced plasmonic properties compared to those on untreated porous silicon surfaces. This enhancement was marked by an increase of 19.6 times in the electromagnetic field and an SERS enhancement factor of 5.3×10^8 at a laser wavelength of 532 nm.

5. Tetramer- and monomer-based substrates demonstrated an excitation wavelength-dependent response where their SERS sensitivity gradually decreased with increasing differences between the surface lattice resonance and the target wavelength excitation.

6. The possibility of tuning the surface lattice resonance of the regular array of silver nanoparticles to the target wavelength of 532 nm by choosing the square lattice with the periodicity of 330 nm and the nanoparticle size of 88 nm in diameter followed by the increase in the substrate's SERS sensitivity has been shown. The SERS enhancement factor of the monomer-based substrate was found to equal to 6.2×10^8 at the target wavelength, and it was 110 times higher than that of the monolayer of silver nanoparticles. The detection limit for 2-naphthalene thiol was set at 10^{-8} M.

7. The implementation of hot spots within a regular array of silver nanoparticles demonstrated the significant enhancement in the SERS sensitivity of tailored surface lattice resonance-based substrates. The SERS enhancement factor values of the tetramer-based substrate reached $2.6x10^9$ values at the target wavelength, and it was 465 times higher than that of the monolayer of silver nanoparticles. The detection limit for 2-naphthalene thiol using such substrates was set at 10^{-9} M. Furthermore, the tetramer-based SERS substrate demonstrated the smallest variation (compared to monomer and monolayer silver nanoparticles) in the Raman signal over an area of 20x20 μm, as it reached a standard deviation of 12%.

VI. SANTRAUKA

6.1. Įvadas

Paviršiaus sustiprintos Ramano spektroskopijos (angl. Surface enhanced Raman spectroscopy, SERS) taikymo sritys yra labai įvairios, pradedant nuo aplinkosaugos tyrimų, teismo medicinos mokslo, farmakologijos ir kt. Biotechnologija šiuo metu yra sparčiai besivystanti sritis, kur vis didesnį mokslininkų bendruomenės susidomėjimą kelia nuolatinė mažesnių, efektyvesnių ir kompaktiškesnių prietaisų – biojutiklių paieška. Viena iš įdomių biologinių jutiklių taikymo sričių yra SERS, užtikrinanti kiekybinę ir kokybinę biologinių medžiagų analizę. Nanostruktūrinių medžiagų naudojimas biologinio jutiklio konstrukcijoje yra patrauklus dėl unikalių optinių, cheminių ir fizinių savybių. Šiuo metu yra atliekami moksliniai tyrimai, siekiant sukurti metalines nanomatmenų struktūras, kurios pasižymi plazmoninėmis savybėmis ir gali būti naudojamos kaip SERS aktyvūs padėklai. Deja, SERS spektroskopija kol kas nebuvo plačiai praktiškai taikoma kaip analitinis metodas. Nepaisant didelės pažangos formuojant ir tiriant nanostruktūras, esamų nebrangių technologijų, leidžiančių gaminti SERS aktyvius padėklus, pasižyminčius aukštu signalo stiprinimo faktoriumi ir dideliu atsikartojamumu, daugelis aktualių klausimų (registruojamo signalo dispersija padėklo plote, kiekybinė analizė ir pan.) išlieka neišspręsti. Šiuo atžvilgiu svarbu ne tik ištirti fizikinius SERS reiškinio aspektus, bet ir sukurti naujas medžiagas bei technologijas, skirtas SERS spektroskopijos padėklams formuoti. Šie tyrimai leistų praktiškai pritaikyti šį spektroskopijos metodą ir išspręsti jo platesnio pritaikomumo problemas.

Metalizuoto akytojo silicio struktūros yra plačiai naudojamos praktikoje kaip SERS padėklai. Metalizuoto akytojo silicio naudojimo perspektyvos paprastai siejamos su jo struktūros ypatybėmis, biologiniu suderinamumu, optinėmis, paviršiaus savybėmis, kurias galima nesunkiai keisti, parenkant pradinio monokristalinio silicio parametrus ir akytųjų sluoksnių formavimo būdus. Kita vertus, šiuo metu nėra sisteminių tyrimų, skirtų metalizuoto akytojo silicio susidarymui be paviršiaus sluoksnio, kuriame pastebimas „butelio kaklelio“ efektas. Tokių tyrimų rezultatai leistų naudoti akytąjį silicį kaip trafaretą formuojant nanometrinio storio silicio sienelėmis atskirtų sidabro nanodalelių masyvą. Tokia struktūra dėl plazmoninės jungties tarp metalinių nanodalelių ir puslaidininkio leidžia sukurti itin intensyvų elektromagnetinį lauką Ag nanodalelių ir silicio sienelės kontakto vietose.

Kitas būdas pasiekti maksimalų SERS signalo stiprinimo faktorių yra suderinti plazmono rezonansą su matavimams naudojamo lazerio bangos ilgiu. Tam galima panaudoti plazmoninių nanodalelių tvarkingą masyvą, kuriame dalelių išdėstymo geometrija turi įtakos struktūros absorbcijos smailės padėčiai ir jos intensyvumui. Absorbcijos smailės padėtis gali būti lengvai reguliuojama keičiant dalelių išdėstymo geometriją.

Šiuo metu tokioms struktūroms daryti plačiai naudojamos litografijos, suderintos su ėsdinimu, technologijos, leidžiančios gaminti daugybę nanodalelių su apibrėžtais dydžiais ir atstumais tarp jų. Antra vertus, metodą riboja skiriamoji geba,

brangios įrangos poreikis bei laiko sąnaudos. Šiuo požiūriu ypač efektyvus yra kapiliarinis nanodalelių išdėliojimo metodas (angl. Cappillary assisted particle assembly, CAPA). Jis leidžia pagaminti didelio ploto padėklus su tvarkingai išrikiuotomis nanodalelėmis ir gali būti laikomas alternatyva litografijai (ar panašiai).

Kita vertus, tokioms dvimatėms nanodalelių sistemoms labai svarbu yra ištirti nanodalelių optomechaninius režimus, nes jie gali turėti įtakos SERS rezultatams.

Šiame darbe daugiausia dėmesio skirsime SERS padėklų tyrimams ir taikymams, naudodami nanodalelių masyvus, įterptus į nanostruktūrinio silicio poras, kai SERS signalo stiprinimo faktorius gali būti pagerintas dėl plazmoninės jungties metalo ir puslaidininkio sąveikoje, bei tvarkingai surikiuotus nanodalelių masyvus, kurių jautrumą galima padidinti derinant dalelių sistemos plazmonines savybes pagal žadinimui naudojamo lazerio bangos ilgį.

6.1.1. *Tikslas*

Darbo tikslas – sukurti labai jautrius SERS aktyvius padėklus, naudojant chemiškai susintetintas sidabro nanodaleles, atsitiktinai arba tvarkingai nusodintas ant skirtingų padėklų, taikant kapiliarinio dalelių nusodinimo metodą.

6.1.2. *Uždaviniai*

1. Chemiškai susintetinti sferines Ag nanodaleles, ištirti paviršinio aktyvumo medžiagų koncentracijos įtaką nanodalelių dydžiui ir apibūdinti jų optomechanines savybes.
2. Sukurti ir ištirti akytuoju siliciu grįstų struktūrų, pagamintų elektrocheminio ėsdinimo būdu ir po jo atliekamu reaktyviuoju jonų ėsdinimu, morfologines, struktūrines ir optines savybes.
3. Pasitelkiant kapiliarinio nusodinimo techniką ir naudojant įvairaus periodiškumo trafaretus ir akytąjį silicį bei susintetintas sidabro nanodaleles, pagaminti tvarkingai išrikiuotų ir atsitiktinai išdėliotų nanodalelių SERS aktyvius padėklus.
4. Ištirti sukurtų SERS aktyvių padėklų SERS jautrumą, naudojant organinį sieros junginį kaip tikslinę molekulę.

6.1.3. *Naujumas*

1. Užuomazgų auginimo metodu susintetintos kontroliuojamo skersmens monodispersinės Ag nanodalelės.
2. Ultrasparti krūvininkų relaksacija polikristalinėse Ag nanodalelėse ištirta naudojant nepusiausvyrinės absorbcijos spektroskopijos metodą.
3. Elektrocheminis ėsdinimas, po kurio atliekamas reaktyvusis jonų ėsdinimas, panaudotas gaminant kontroliuojamų porų matmenų nanostruktūrinį akytąjį silicį.

4. Kapiliarinis dalelių nusodinimas panaudotas nanodalelėms surinkti į periodinę / neperiodinę gaudyklių sistemą, kontroliuojant jų skaičių gaudyklėje.
5. Parodyta, kad nanodalelių dydis keičia paviršiaus gardelės rezonanso (SLR) bangos ilgį.
6. SERS padėklai su sužadinimo bangos ilgiui pritaikytu SLR ir periodiniu karštųjų taškų užpildymu pasižymi itin dideliu jautrumu, viršijančiu esamus SERS padėklus su atsitiktiniu nanodalelių pasiskirstymu.

6.2. Metodika

Monodispersinės Ag nanodalelės buvo susintetintos taikant užuomazgų auginimo metodą [27], naudojant tanino rūgštį (angl. Tannic acid, TA) ($C_{76}H_{52}O_{46}$, „Sigma-Aldrich“, Kinija), trinatrio citratą (angl. Trisodium citrate, TC) ($C_6H_5Na_3O_7$*$2H_2O$, „Fluka“, Belgija) ir sidabro nitratą ($AgNO_3$, „Sigma-Aldrich“, JAV), po to funkcionalizuojant jas su PVP (polivinilpirolidonas, „Sigma-Aldrich“, JAV). Elektrocheminis kristalinio Si plokštelės (100) („Siegert Wafer“, Vokietija) ėsdinimas buvo atliktas naudojant nuolatinės srovės (DC) šaltinį B5-47, po to reaktyviuoju jonų ėsdinimo būdu („Vision LL-ICP“, Švedija) pašalintas parazitinis paviršiaus sluoksnis. Periodinės struktūros polimero trafaretas buvo pagamintas iš polidimetilsiloksano (PDMS), atkartojant Si trafareto formą ir naudojant minkštosios litografijos techniką. Si trafaretas buvo pagamintas pasitelkiant elektroninę litografiją („eLine plus“, „Raith“, Vokietija) ir reaktyvųjį jonų ėsdinimą („Vision LL-ICP“, „Plasma-Therm“, JAV) [116]. Kapiliarinis dalelių nusodinimas (CAPA) buvo atliktas naudojant originalią įrangą, aprūpintą motorizuotu didelio tikslumo transliatoriumi („LS-110“, „PI Micos“), temperatūros valdymo sistema („TEC-1090“, „Meerstetter Engineering GmbH“) bei optinio mikroskopo sistema (BX51, „Olympus“) su CCD kamera („QImaging“, „Micropublisher 3.3“) [117]. Absorbcijos / pralaidumo spektrai buvo užregistruoti naudojant *UV-Vis* šviesolaidinį spektrometrą „AvaSpec-2048“ („Avantes“, Nyderlandai). Ultrasparti Ag nanodalelių elektronų dinamika tirta nepusiausvyrinės absorbcijos spektroskopijos būdu, naudojant HARPIA spektrometrą („Light Conversion“, Lietuva) su Yb:KGW lazeriu „Pharos“ („Light Conversion“, LT). Koloidinių nanodalelių (NP) vaizdinimui buvo naudojamas skenuojamasis elektroninis mikroskopas („Quanta 200 FEG“, FEI) ir prašviečiantis elektronų mikroskopas („Philips“, CM200). Sintetintų Ag nanodalelių kristalinės struktūros analizė atlikta rentgeno spindulių difrakcijos (XRD) metodu, naudojant „Bruker AXS GmbH“ firmos difraktometrą „8 Discover“. Difrakcijos duomenų analizė buvo atlikta naudojant DIFFRAC.EVA bei „X'pert HighScore Plus“ programinę įrangą. SERS matavimai buvo atlikti naudojant daugiabangį Ramano mikroskopą („Renishaw“, „Wotton-under Edge“), kuriame integruotas termoelektriniu būdu aušinamas CCD detektorius. 2-naftalentiolio (2NT) („Sigma-Aldrich“, Belgija) organinė molekulė buvo pasirinkta kaip tikslinė molekulė SERS padėklo aktyvumo tyrimams. Stiprinimo faktoriaus apskaičiavimo metodas yra išsamiai aprašytas [118]. AgNP optinių savybių modeliavimas atliktas naudojant „COMSOL Multiphysics“, bangų optikos modulį ir baigtinių elementų metodą.

6.3. Rezultatai

6.3.1. Cheminė sidabro nanodalelių sintezė

Eksperimentiškai buvo ištirta Ag nanodalelių cheminei sintezei naudojamų komponentų įtaka. Darbe pasiūlyta metodika, leidžianti sintetinti reikiamo dydžio ir skirstinio Ag nanodaleles, naudojant užuomazgų auginimo techniką. Šis procesas susideda iš dviejų etapų, kuriuose naudotas trinatrio citrato bei tanino rūgšties derinys kaip reakcijos reduktorius ir stabilizatorius.

Komponentų, naudojamų nanodalelių dydžiui padidinti, koncentracijos sumažėjimas lemia nuoseklų augimo greičio sulėtėjimą viso ciklo metu, leidžiantį tiksliai kontroliuoti nanodalelių dydį. Nuoseklus Ag nanodalelių augimas buvo atliktas naudojant 0,033 mM TC, 0,008 mM TA ir 0,083 mM $AgNO_3$ auginimo tirpalus, kurių koncentracijos yra beveik tris kartus mažesnės už naudotas ankstesniuose eksperimentuose (0,347 mM TA, 0,1 mM TC ir 0,7 mM $AgNO_3$).

Po kiekvieno augimo etapo paviršiaus plazmonų rezonanso (angl. Surface plasmon resonance, SPR) smailė pasislinko per kelis nanometrus, o tai atitinka nedidelį nanodalelių dydžio padidėjimą (Figure 12). Po 21 nuoseklios augimo procedūros sidabro nanodalelių vidutinis skersmuo padidėjo nuo ~ 20 nm iki ~ 88 nm, o standartinis nuokrypis buvo apie 4–5 nm. Metodas pristato augimo procesą, kuris leidžia kontroliuoti užuomazgų susidarymo, augimo ir stabilizavimo procesus, kai suformuotos monodispersinės sferinės Ag dalelės.

6.3.2. *Ag nanodalelių kristalinė struktūra*

TEM vaizdai parodė nanodalelių polikristališkumą (Figure13), o kristalitų dydis buvo įvertintas iš XRD matavimų (Figure 14, apačioje). Analizuotos difrakcijos smailės ties 2Θ = 38,2°, 44,5°, 64,6° ir 77,6°, 81,7°, atitinkančios centruotojo paviršiaus gardeles (111), (200), (220), (311) ir (222) plokštumas.

Kristalitų dydis buvo apskaičiuotas pagal Scherrer formulę [121]. Ag nanodalelių kristalitų dydis didėjo kartu su skersmeniu, ir tai puikiai dera su taikomo sintezės metodo ypatumais.

6.3.3. Ag nanodalelių optomechaninis apibūdinimas

Išmatuotiems Ag nanodalelių tirpalams registruotos TAS signalo osciliacijos, kurios yra būdingos monodispersinių nanodalelių rinkiniui [122].

Iš TAS signalo laikinės priklausomybės (Figure 15) buvo apskaičiuotos elektrono-fonono sąveikos (*e-ph*, τ_1) ir fonono-fonono (*ph-ph*, τ_2) sklaidos laiko konstantos, Ag nanodalelių tyrimų rezultatai apibendrinti lentelėje (Table 4).

Būdingoms laiko konstantoms vertinti atlikti kintančio žadinimo intensyvumo matavimai (Figure 17). Ekstrapoliuotos *e-ph* sąveikos laiko konstantos pateiktos lentelėje (Table 3).

Nustatyta, kad sužadintos būsenos silpimas priklauso nuo *e-ph* sąveikos trukmės ir sumažėja nuo 0,96 ps (*pavyzdys S1*) iki 0,69 ps (*pavyzdys S4*). Taip pat pastebėtas

santykinai silpnas TAS signalo relaksacijos komponentas, kurį galima priskirti *ph-ph* sklaidai, kuriai būdingos trukmės buvo nuo 10 iki 206 ps (Table 4).

Didėjant polikristalinių Ag nanodalelių vidutiniam skersmeniui, *e-ph* sąveikos laiko konstantos mažėjo (Figure 17). Norėdami išanalizuoti *e-ph* sąveikos laiko konstantą priklausomai nuo dalelių kristališkumo, parodėme, kad šiam parametrui yra svarbus santykis (kristalito dydis / tiesinis Ag matmuo)^2. Paveiksle (Figure 17b) vaizduojama tiesinė *e-ph* sąveikos laiko konstantos priklausomybė nuo šio parametro rodo, kad konstanta tiesiškai didėja didėjant kristalitų dydžio ir nanodalelių dydžio santykiui. Autoriaus publikuotame darbe [A2] šie polikristalinių Ag nanodalelių rezultatai buvo lyginami su monokristalinių Ag nanokubų, kurių plazmonų relaksacijos dinamika nepriklausė nuo dalelių dydžio, nebuvo jokios aiškios priklausomybės nuo (kristalito dydžio / tiesinio Ag nanokubų matmens)^2 santykio.

6.3.4. Akytojo silicio gamyba ir apibūdinimas

Norint sukurti padėklą su atsitiktinai išdėstytomis gaudyklėmis, kurias vėliau būtų galima užpildyti nanodalelėmis, kad būtų sukurtas jų masyvas, buvo pasirinktas akytasis silicis. Paprastai elektrocheminio anodavimo būdu suformuotas akytasis silicis turi parazitinį viršutinį sluoksnį, vadinamąjį „butelio kaklelio“ akytąjį silicį, kurio porų dydis šiek tiek skiriasi nuo tūrinių verčių. Autorius įrodė, kad reaktyvusis jonų ėsdinimas (RIE) yra veiksmingas būdas, norint pašalinti parazitinį sluoksnį (arba „atviras poras“) [A3].

Ištirta atvirų porų akytojo silicio paviršiaus morfologija, priklausomai nuo naudojamos srovės tankio ir vandenilio fluorido rūgšties koncentracijos. Paveiksle (Figure 15) pavaizduoti vieno akytojo silicio mėginių rinkinio SEM vaizdai prieš ir po RIE apdorojimo, naudojant j = 60 mA/cm^2 5 proc. masės, 10 proc. masės ir 20 proc. masės fluorido rūgšties tirpalus.

RIE apdoroto akytojo silicio, susidariusio elektrolite su 5 proc. masės (visuose mėginiuose) ir 10 proc. masės fluorido rūgšties (esant dideliam srovės tankiui), morfologija dažniausiai atrodo lygi, o tik nedidelis akytojo silicio šiurkštumo padidėjimas rodo izotropinį viršutinio sluoksnio ėsdinimą. Mėginių, pagamintų naudojant 10 proc. masės vandenilio fluorido rūgštį esant mažam srovės tankiui (20–60 mA/cm^2), ir visų mėginių, pagamintų iš 20 proc. masės fluorido rūgšties, paviršius pasižymi akyto sluoksnio susidarymu, kurį sudaro grublėtą paviršių formuojančios salelės.

Vidutinis porų skersmuo ir porų tankis pateikti paveiksle (Figure 19). Matyti, kad vidutinis skersmuo didėja didėjant srovės tankiui. Ši tiesinė priklausomybė stebima tol, kol pasiekiama tam tikra kritinė srovės tankio vertė ir porų dydis pradeda mažėti. Esant dideliam srovės tankiui, susidarančios poros tampa erdviškai netaisyklingos, susidaro kempinę primenanti struktūra. Si skeletas tampa plonesnis, o porų tankis didėja. Tolesnis srovės tankio padidėjimas lemia elektropoliravimo procesą.

Paviršinis sluoksnis susideda iš silicio kristalitų ir porų, kurios daro įtaką šviesos sklaidai ir atspindžiui. Paveiksle (Figure 20) pateikti akytojo silicio mėginių,

susidariusių esant 5 proc. masės fluorido rūgšties ir 10 proc. masės fluorido rūgšties, atspindžio spektrai rodo oro / akytojo silicio ir akytojo silicio / Si riboje atspindėtos šviesos interferencinius maksimumus. Taikant Fabry-Pérot interferencijos lygtis [130] buvo įvertintos akytojo silicio vidutinio lūžio rodiklio (n_{PS}) reikšmės, jos pateiktos lentelėje (Table 5).

Apskaičiuotasis n_{PS} mėginiams, pagamintiems naudojant 5 proc. masės ir 10 proc. masės fluorido rūgšties elektrolitus, mažėjo didėjant srovės tankiui ir yra susijęs su porų tankio (poringumo) padidėjimu [132] bei gerai sutampa su paveiksle (Figure 19a) pateiktais duomenimis. Daugeliu atvejų neapdorotų akytojo silicio mėginių n_{PS} buvo šiek tiek mažesnis nei RIE apdorotų mėginių, nes yra labai akytas paviršinis parazitinis sluoksnis, kuris mažina n_{PS} vertę.

6.3.5. Nanodalelių nusodinimas nanostruktūrinio silicio porose ir ant plokščių paviršių

Nanodalelių nusodinimas buvo atliktas naudojant CAPA metodą, kadangi šis metodas užtikrina labiausiai kontroliuojamą koloidinių nanodalelių pasiskirstymą trafareto paviršiuje, palyginti su kitais metodais (pvz., lašelių nusodinimu). Eksperimentui buvo naudojamos Ag nanodalelės, kurių vidutinis skersmuo buvo 62 nm ir kurios sutapo su akytojo silicio RIE porų dydžiu (naudotas 10 % masės fluorido rūgšties tirpalas ir j = 100 mA/cm^2). Taip pat tokios pačios Ag nanodalelės buvo nusodintos ant neapdoroto akytojo silicio, susidariusio tokiomis pat sąlygomis, kaip ir anksčiau minėtasis akytasis silicis (Figure 21). Naudojant 0,1 μm/s bandinio judėjimo greitį ir palaikant 12 °C temperatūrą virš rasos taško buvo pasiektas Ag nanodalelių nusodinimo į poras ~85 % užpildymo koeficientas (Figure 21b). Galima matyti, kad dauguma nusėdusių nanodalelių susitelkia porose. Retais atvejais jos užimdavo vieną porą arba būdavo pasislinkusios į poros kraštą.

6.3.6. Nanodalelių modeliavimas paviršiuje ir porose

Atvirų porų akytasis silicis turi atsitiktinai išsidėsčiusias poras, kurių kiekviena ribojasi su šešiomis kitomis. Nanodalelių struktūra gali būti atvaizduojama kaip šešiakampė gardelė (idealizuojant struktūrą), kurios matmuo r = 92 nm, o nanodalelė, kurios skersmuo yra 62 nm, yra atskirta nuo kitos 28 nm silicio sienele (Figure 22a). Ta pati vienetinė gardelė gali būti naudojama glaudžiai suspaustoms nanodalelėms ant akytojo silicio paviršiaus, kurių r lygus 63 nm. Paveiksle (Figure 19b, c) yra parodytas elektromagnetinio lauko pasiskirstymas tokioje struktūroje. Didžiausias elektromagnetinio lauko stiprinimas pastebimas šalia metalinio paviršiaus, kai Ag nanodalelės yra ant akytojo silicio. Ir priešingai, kai Ag nanodalelės yra porose, jis koncentruojasi Ag nanodalelių ir Si sienelių kontakte. Kaip matyti iš nanodalelių porose lauko stiprumo pasiskirstymo, laukas sustiprinamas 8 kartus, palyginti su dalelėmis, kurios yra ant porų. Šis faktas patvirtina elektromagnetinio lauko stiprinimo teoriją metalo ir puslaidininkio riboje. Modeliuoti atspindžio spektrai, pateikti paveiksle (Figure 22c, d) rodo stiprią sugertį, esant 400 nm bangos ilgiui (Ag

nanodalelės ant akytojo silicio) ir 375 nm (Ag nanodalelės porose), kuri buvo pastebėta ir eksperimentiškai išmatuotuose spektruose.

6.3.7. SERS jautrumas nesurikiuotų nanodalelių masyvui

SERS matavimai buvo atlikti siekiant įvertinti analitinį stiprinimo faktorių, naudojant 532 nm bangos ilgio lazerio sužadinimą. Nepaisant to fakto, kad abi akytojo silicio struktūros pasižymi sugertimi mėlynojoje srityje, jos taip pat yra jautrios ilgesniems bangų ilgiams. 2NT molekulių, adsorbuotų ant Ag nanodalelių iš 10^{-4} M koncentracijos tirpalo, užregistruoti spektrai pateikiami paveiksle (Figure 23) Tipinės 2NT osciliacijų smailės (764 cm^{-1}, 1067 cm^{-1}, 1377 cm^{-1}, 1583 cm^{-1}, 1621 cm^{-1}) yra paryškintos. Naudojant intensyviausios smailės (1377 cm^{-1}) intensyvumą, buvo apskaičiuotas neapdoroto akytojo silicio ir nanodalelių bei porose esančių nanodalelių analitinis stiprinimo faktorius, kurių vertės buvo atitinkamai 1,4 x 10^7 ir 5,3 x 10^8. Rezultatai gerai sutampa su elektrinio lauko modeliavimo rezultatais.

6.3.8. Derinamas plazmoninis masyvas sustiprintai Ramano sklaidai

Parenkant periodinės gaudyklių struktūros periodą bei Ag nanodalelių dydį buvo suformuoti surikiuotų nanodalelių plazmoniniai masyvai taip, kad SLR smailė (λ_{SLR}) būtų artima žadinimui naudojamo lazerio bangos ilgiui 532 nm (λ_{Ex}). Šiam tikslui, remiantis anksčiau gautais rezultatais, pasirinkta kvadratinė gardelė Λ = 330 nm (SQ330) su RA bangos ilgiu (λ_{RA}) polidimetilsiloksanui esant 470 nm [116].

Modeliavimo rezultatai (Figure 24) rodo, kad λ_{SLR} priklauso nuo nanodalelių skersmens. SLR smailės raudonasis poslinkis ir jo spektrinės juostos pusplotis (FWHM) didėja, didėjant nanodalelių skersmeniui [135]. Nanodalelių, kurių skersmuo nuo 90 iki 100 nm, λ_{SLR} yra arti 532 nm tikslo. Eksperimentui buvo pasirinktos Ag nanodalelės, kurių skersmuo yra 88 nm ± 5,2 nm, o jų lokalizuoto paviršiaus plazmonų rezonanso smailė tirpale yra maždaug ties 460 nm (Table 2). Šios nanodalelės turi dipolinę LSPR smailę tirpale maždaug ties 470 nm po PVP funkcionalizacijos, ji persidengia su 330 nm kvadratinės gardelės λ_{RA}.

Paveiksle (Figure 25) pateiktas surikiuotos plazmoninės struktūros SEM vaizdas, kuriame struktūrinio polidimetilsiloksano padėklo gaudyklės yra užpildytos atskiromis nanodalelėmis (*monomerų rinkiniais*). Atitinkamai parodytas sumodeliuotas elektromagnetinio lauko stiprumas ties izoliuota nanodalele (puikiai suderinta ribinė sąlyga) ir dalele masyve (periodinės ribinės sąlygos). Abiem atvejais matomas stiprus artimasis laukas, sustiprintas atitinkamai 4,2 ir 14,7 karto 532 nm bangos ilgiui izoliuotų nanodalelių ir masyvo atvejais. Eksperimentinės ir apskaičiuotos λ_{SLR} reikšmės rodo gerą kokybinį sutapimą (Figure 25d). Eksperimentinis pralaidumo spektro plotis yra platesnis ir šiek tiek pasislinkęs į raudonųjų bangų intervalą dėl defektų, atsirandančių dėl naudoto metodo savitvarkio pobūdžio – neužpildytų tuščių gaudyklių, ir atsitiktinių dviejų trijų nanodalelių gaudyklėje. Spektrinės padėties skirtumas tarp eksperimentinių λ_{SLR} ir λ_{Ex} monomerų rinkiniuose yra 9 nm.

Monomerų pagrindu pagamintas SERS pagrindas buvo naudojamas esant skirtingiems sužadinimo bangos ilgiams, kad būtų galima aptikti 2NT (Figure 25e). Pirminiam vertinimui buvo naudojama 10^{-4}M koncentracija. Analitinis stiprinimo faktorius buvo įvertintas naudojant Ramano juostą ties 1377 cm^{-1}, apskaičiuojant SERS signalo intensyvumo vidurkį nuskaitytoje srityje ir palyginus jį su vienos molekulės SERS signalu matavimo vienete. Duomenys ir išsamus analitinių stiprinimo faktorių skaičiavimų aprašymas pateikti autoriaus darbe [A4]. 1377 cm^{-1} juostos intensyvumas ir atitinkamas analitinis stiprinimo faktorius gerai koreliavo su λ_{SLR} ir λ_{Ex} persidengimu (Figure 25b). Didžiausias smailės intensyvumas buvo, kai λ_{Ex} = 532 nm, o fiksuotas analitinis stiprinimo faktorius buvo $6{,}1 \cdot 10^8$. Jis laipsniškai mažėjo, kai žadinimo lazerio bangos ilgis nesutapo su SLR rezonansiniu bangos ilgiu.

6.3.9. *Surikiuotų nanodalelių plazmoniniai masyvai su daugeliu dalelių gaudyklėje*

Siekiant pagerinti surikiuotų nanodalelių plazmoninių masyvų padėklų monomerų pagrindu analitinius stiprinimo faktorius, mažesnės nanodalelės (77 nm skersmens) buvo nusodintos į tokią pačią polidimetilsiloksano kaukę, sudarant tetramero struktūrą (keturios dalelės vienoje gaudyklėje) ir siekiant išlaikyti λ_{SLR} arti tikslinio λ_{Ex} (Figure 28).

Modeliavimas parodė, kad elektromagnetinis laukas ties λ_{Ex} yra stipriai lokalizuotas tarpuose tarp nanodalelių ir atitinkamai sustiprėja 49,4 ir 65,9 karto izoliuotų ir periodinių tetramero vienetų ląstelių atvejais (Figure 28b, c), jis yra beveik 4 kartus didesnis, palyginti su periodinio monomero vieneto gaudykle (Figure 22b, c). Modeliuotas λ_{SLR} pastebėtas ties 579 nm ir gerai atitiko eksperimentinę smailę ties 583 nm (Figure 28d). Tetramerinės struktūros eksperimentinis pralaidumo spektras (Figure 28d) dėl neidealios struktūros yra taip pat šiek tiek platesnis nei modeliuojamas rezultatas. Kolektyviniam plazmoninio surikiuotų dalelių struktūros atsakui buvo būdingas SLR raudonasis poslinkis ir sugerties kreivės išplitimas. Tai atitinka plazmoninės hibridizacijos teoriją [136, 137], kai arti esančios plazmoninės nanodalelės veikia kaip didesnės dalelės, kurioms būdingas LSPR raudonasis poslinkis[A4].

Kaip ir anksčiau ištirtų monomerų rinkinių, Ramano smailės intensyvumas didėja, kai surikiuotų dalelių tetramero struktūros skirtumas $|\lambda_{SLR} - \lambda_{Ex}|$ mažėja (Figure 28d). Jis yra beveik 4 kartus intensyvesnis, palyginti su identiškomis sąlygomis išmatuotu monomerų rinkiniu (Figure 28c). Analitinis tetramerų struktūros SERS stiprinimo faktorius rodo tą pačią tendenciją, pasiekiant aukščiausią tašką ties λ_{Ex} = 532 nm, o jo vertė yra $2{,}6 \cdot 10^9$, kuri pagal dydį yra daug didesnė nei monomerų atveju.

6.3.10. *Surikiuotų pavienių ir daugelio nanodalelių masyvų lyginamoji SERS jautrumo analizė*

Teoriškai apskaičiuotas SERS stiprinimo faktorius, kuris yra proporcingas $|E/E_0|^4$ [149,150], gautas iš modeliavimo rezultatų, ir analitinės stiprinamojo faktoriaus reikšmės yra palygintos paveiksle (Figure 24a). Monomerų ir tetramerų

pagrindu sukurtų surikiuotų nanodalelių struktūrų stiprinimo faktoriaus palyginimas papildytas plazmonine struktūra, kurioje naudotas atsitiktinai išdėstytų nanodalelių (77 nm ± 4,5 nm skersmens) monosluoksnis ant plokščio PDMS padėklo [140] [A4].

Šio monosluoksnio SERS jautrumas buvo tiriamas tokiu pačiu būdu, esant skirtingiems lazerio bangų ilgiams. Atsitiktinai išdėstytų nanodalelių monosluoksnio pagrindas taip pat rodo priklausomybę nuo žadinimui naudojamo bangos ilgio ir pasiekia aukščiausią tašką ties λ_{Ex} =532 nm, o analitinė stiprinimo faktoriaus vertė yra $1{,}6 \cdot 10^5$ [A4]. Normalizuotas monomerų ir tetramerų struktūrų analitinis stiprinimo faktorius taip pat pasiekė aukščiausią tašką ties λ_{Ex} = 532 nm, bet buvo atitinkamai 110 ir 465 kartus didesnis (Figure 24b). Tai patvirtina esminį SLR indėlį į stiprinimo faktorių ir rodo, kad naudojamam sužadinimo bangos ilgiui galima pritaikyti struktūros plazmonines savybes išnaudojant SLR efektą.

Ištirtas sidabro nanodalelių monomerų, tetramerų ir monosluoksnio SERS pagrindo erdvinis stiprinimo homogeniškumas (t. y. signalo atsikartojamumas dideliame plote). Atsitiktinai parinktame kiekvienos struktūros 20 x 20 μm plote buvo užfiksuotas 1377 cm^{-1} juostos intensyvumas (Figure 24a). Monosluoksnio SERS pagrindui dėl nekontroliuojamo karštųjų taškų susidarymo ir padėties buvo būdinga didelė standartinio nuokrypio vertė, kuri siekė 37,35 %. Mažesnė, tačiau vis tiek santykinai aukšta nustatyta išrikiuotų dalelių standartinio nuokrypio vertė 31,81 %. Matyt, šį santykinai didelį signalo pokytį sukelia 18 % defektų (Figure S5, A4). Tetramero SERS pagrindo signalo standartinis nuokrypis buvo beveik du kartus mažesnis (12,42 %), nes buvo geriau kontroliuojamas karštųjų taškų pasiskirstymas ir homogeniškumas bei sumažintas gaudyklių netobulumas.

Panaudoję sužadinimo bangos ilgį, kur buvo didžiausias stiprinimas (532 nm), nustatėme SERS pagrindų detektavimo ribų (DL) vertes. Paveiksle (Figure 24b) parodyti užfiksuoti spektrai su paryškintomis tipiškomis 2NT molekulių vibracinėmis smailėmis. Monomerų SERS pagrindų DL vertė buvo nustatyta 10^{-8} M, o tetramerų – 10^{-9} M. Tipiškos polidimetilsiloksano Ramano smailės (615 cm^{-1}, 708 cm^{-1}) gali būti matomos atliekant visus matavimus, tačiau jos nepersidengia su tikslinei molekulei būdingomis stipriomis smailėmis.

6.4. Išvados

1. Parodėme, kad taikytas užuomazgų auginimo metodas leidžia sintetinti monodispersines polikristalines sferines sidabro nanodaleles, kurių vidutinis skersmuo ~ 20 nm – 90 nm. Buvo nustatyta optimali tanino rūgšties koncentracija (0,0125 mM) užuomazgų tirpale, esant tanino rūgšties ir trinatrio citrato santykiui $2{,}5 \times 10^{-3}$ bei naudojant 0,033 mM trinatrio citratą, 0,008 mM tanino rūgštį ir 0,083 mM sidabro nitratą auginimo tirpaluose.
2. Sidabro nanodalelių trumpalaikės absorbcijos spektroskopijos matavimai leido sistemingai ištirti elektronų ir fononų sąveikos procesą plazmonų relaksacijos dinamikoje. Susintetintoms polikristalinio sidabro nanodalelėms buvo būdinga greitesnė relaksacija didėjant jų dydžiui ir buvo nustatyta, kad elektronų ir fononų

sąveikos laiko konstanta tiesiškai didėja didėjant (kristalito dydis / sidabro nanodalelės skersmuo)^2 santykiui.

3. Remiantis akytojo silicio su atviromis poromis (vidutinis skersmuo ~ 17–180 nm), apdoroto reaktyviuoju jonų ėsdinimu, tyrimų rezultatais, nustatyta optimali vandenilio fluorido koncentracija (5–10 masės %) homogeniškam akytam silicio pagrindui sukurti elektrochemiškai anoduojant kristalinį silicį. Be to, akytojo silicio savybes (porų dydį ir tankį, lūžio rodiklį ir drėkinamumą) galima tiksliai sureguliuoti keičiant vandenilio fluorido rūgšties koncentraciją ir naudojamą srovės tankį.

4. Parodyta, kad reaktyviojo joninio ėsdinimo būdu gauta akytojo silicio struktūra yra tinkamas trafaretas silicio sienelėmis atskirtų sidabro nanodalelių savitvarkio masyvo nusodinimui kapiliariniu būdu. Sidabro nanodalelės porose pasižymėjo ryškesnėmis plazmoninėmis savybėmis nei ant neapdorotų akytojo silicio paviršių ir joms buvo būdingas elektromagnetinio lauko stiprinimas 19,6 karto, o analitinis SERS stiprinimo faktorius siekė 5,3 x 10^8 naudotam 532 nm lazerio bangos ilgiui.

5. Sidabro nanodalelių tetramerų ir monomerų SERS pagrindams buvo būdinga atsako priklausomybė nuo sužadinimo bangos ilgio, jų SERS jautrumas laipsniškai mažėjo, didėjant paviršiaus gardelės rezonanso ir sužadinimui naudoto bangos ilgio skirtumui.

6. Parodyta galimybė suderinti surikiuotų sidabro nanodalelių masyvo paviršiaus gardelės rezonansą iki naudoto 532 nm bangos ilgio, tam parenkant tinkamą nanodalelės dydį ir taip padidinant SERS pagrindo jautrumą. Nustatyta, kad monomerų SERS pagrindo analitinis stiprinimo faktorius siekė $6{,}2 \times 10^8$, esant tiksliniam bangos ilgiui, ir jis buvo 110 kartų didesnis nei sidabro nanodalelių monosluoksnio atveju. Tokiam pagrindui buvo nustatyta 10^{-8}M 2-naftalentiolio detektavimo riba.

7. Karštųjų taškų panaudojimas išrikiuotų sidabro nanodalelių masyve smarkiai padidino SERS padėklų, kuriuose naudojamas paviršiaus gardelės rezonansas, jautrumą. Tetramerų SERS pagrindo analitinės stiprinimo faktoriaus vertės siekė $2{,}6 \times 10^9$ reikšmes, esant tiksliniam bangos ilgiui, ir buvo 465 kartus didesnės nei sidabro nanodalelių monosluoksnio atveju. Naudojant tokius pagrindus buvo nustatyta 10^{-9}M 2-naftalentiolio detektavimo riba. Be to, tetramerų SERS padėkle registruotas mažiausias Ramano signalo kitimas (palyginti su monomerais ir monosluoksnėmis sidabro nanodalelėmis) 20 μm x 20 μm plote, ir standartinis nuokrypis siekė 12 %.

LITERATURE

[1] C. V. RAMAN, K.S. KRISHNAN, A New Type of Secondary Radiation, *Nature* **1928**, 121, 501–502. https://doi.org/10.1038/121501c0.

[2] E. SMITH, G. DENT, Modern raman spectroscopy: A practical approach, **2019**. https://doi.org/10.1002/0470011831.

[3] A.I. PÉREZ-JIMÉNEZ, D. LYU, Z. LU, G. LIU, B. REN, Surface-enhanced Raman spectroscopy: benefits, trade-offs and future developments, *Chem. Sci.* **2020**, 11, 4563–4577. https://doi.org/10.1039/D0SC00809E.

[4] M.E. ABDELSALAM, S. MAHAJAN, P.N. BARTLETT, J.J. BAUMBERG, A.E. RUSSELL, SERS at Structured Palladium and Platinum Surfaces, *J. Am. Chem. Soc.* **2007**, 129, 7399–7406. https://doi.org/10.1021/ja071269m.

[5] J. CEJKOVA, V. PROKOPEC, S. BRAZDOVA, A. KOKAISLOVA, P. MATEJKA, F. STEPANEK, Characterization of copper SERS-active substrates prepared by electrochemical deposition, *Appl. Surf. Sci.* **2009**, 255, 7864–7870. https://doi.org/10.1016/j.apsusc.2009.04.152.

[6] R. BUKASOV, Z. KUNUSHPAYEVA, A. RAPIKOV, S. ZHUNUSSOVA, A. SULTANGAZIYEV, O. FILCHAKOVA, High Contrast Surface Enhanced Fluorescence of Carbon Dot Labeled Bacteria Cells on Aluminum Foil, *J. Fluoresc.* **2020**, 30, 1477–1482. https://doi.org/10.1007/s10895-020-02610-2.

[7] C. ROPERS, C.C. NEACSU, T. ELSAESSER, M. ALBRECHT, M.B. RASCHKE, C. LIENAU, Grating-Coupling of Surface Plasmons onto Metallic Tips: A Nanoconfined Light Source, *Nano Lett.* **2007**, 7, 2784–2788. https://doi.org/10.1021/nl071340m.

[8] M.D. SALIK, P. CHAVEL, Resonant excitation analysis of waveguide grating couplers, *Opt. Commun.* **2001**, 193, 127–131. https://doi.org/10.1016/S0030-4018(01)01234-2.

[9] G. SHALEM, O. EREZ-COHEN, D. MAHALU, I. BAR-JOSEPH, Light Emission in Metal–Semiconductor Tunnel Junctions: Direct Evidence for Electron Heating by Plasmon Decay, *Nano Lett.* **2021**, 21, 1282–1287. https://doi.org/10.1021/acs.nanolett.0c03945.

[10] Y. SUZUKI, M. KOBAYASHI, A.H. OTTO, Anomalous IR Absorption of the System Gold Island Film in Water or Methanol, *Jpn. J. Appl. Phys.* **1997**, 36, 4446. https://doi.org/10.1143/JJAP.36.4446.

[11] X. WANG, Y. DENG, Q. LI, Y. HUANG, Z. GONG, K.B. TOM, J. YAO, Excitation and propagation of surface plasmon polaritons on a non-structured surface with a permittivity gradient, *Light Sci. Appl.* **2016**, 5, 1–6. https://doi.org/10.1038/lsa.2016.179.

[12] L. JENSEN, C.M. AIKENS, G.C. SCHATZ, Electronic structure methods for studying surface-enhanced Raman scattering, *Chem. Soc. Rev.* **2008**, 37, 1061. https://doi.org/10.1039/b706023h.

[13] S. FATEIXA, H.I.S. NOGUEIRA, T. TRINDADE, Hybrid nanostructures for SERS: materials development and chemical detection, *Phys. Chem. Chem. Phys.* **2015**, 17,

21046–21071. https://doi.org/10.1039/C5CP01032B.

[14] C. LEE, C.S. ROBERTSON, A.H. NGUYEN, M. KAHRAMAN, S. WACHSMANN-HOGIU, Thickness of a metallic film, in addition to its roughness, plays a significant role in SERS activity, *Sci. Rep.* **2015**, 5, 1–10. https://doi.org/10.1038/srep11644.

[15] K.L. KELLY, E. CORONADO, L.L. ZHAO, G.C. SCHATZ, The optical properties of metal nanoparticles: The influence of size, shape, and dielectric environment, *J. Phys. Chem. B* **2003**, 107, 668–677. https://doi.org/10.1021/jp026731y.

[16] B. WU, N. MATHEWS, T.-C. SUM, Surface Plasmon Resonance, in: Plasmonic Org. Sol. Cells, Nanosci. Nanotechnol., Springer, Singapore, **2017**: pp. 25–31. https://doi.org/10.1007/978-981-10-2021-6_2.

[17] K. WATANABE, Photochemistry on Nanoparticles, in: Encycl. Interfacial Chem., Elsevier, **2018**: pp. 563–572. https://doi.org/10.1016/B978-0-12-409547-2.13211-1.

[18] C.G. KHOURY, T. VO-DINH, Plasmonic nanowave substrates for SERS: Fabrication and numerical analysis, *J. Phys. Chem. C* **2012**, 116, 7534–7545. https://doi.org/10.1021/jp2120669.

[19] G. KUMARI, J. KANDULA, C. NARAYANA, How Far Can We Probe by SERS?, *J. Phys. Chem. C* **2015**, 119, 20057–20064. https://doi.org/10.1021/acs.jpcc.5b07556.

[20] F. BENZ, R. CHIKKARADDY, A. SALMON, H. OHADI, B. DE NIJS, J. MERTENS, C. CARNEGIE, R.W. BOWMAN, J.J. BAUMBERG, SERS of Individual Nanoparticles on a Mirror: Size Does Matter, but so Does Shape, *J. Phys. Chem. Lett.* **2016**, 7, 2264–2269. https://doi.org/10.1021/acs.jpclett.6b00986.

[21] K. KARN-ORACHAI, Gap-Dependent Surface-Enhanced Raman Scattering (SERS) Enhancement Model of SERS Substrate-Probe Combination Using a Polyelectrolyte Nanodroplet as a Distance Controller, *Langmuir* **2021**, 37, 10776–10785. https://doi.org/10.1021/acs.langmuir.1c01556.

[22] K.M. MAYER, J.H. HAFNER, Localized Surface Plasmon Resonance Sensors, *Chem. Rev.* **2011**, 111, 3828–3857. https://doi.org/10.1021/cr100313v.

[23] T.R. JENSEN, M.L. DUVAL, K.L. KELLY, A.A. LAZARIDES, G.C. SCHATZ, R.P. VAN DUYNE, Nanosphere Lithography: Effect of the External Dielectric Medium on the Surface Plasmon Resonance Spectrum of a Periodic Array of Silver Nanoparticles, *J. Phys. Chem. B* **1999**, 103, 9846–9853. https://doi.org/10.1021/jp9926802.

[24] S. SUN, I.L. RASSKAZOV, P.S. CARNEY, T. ZHANG, A. MOROZ, Critical Role of Shell in Enhanced Fluorescence of Metal-Dielectric Core-Shell Nanoparticles, *J. Phys. Chem. C* **2020**, 124, 13365–13373. https://doi.org/10.1021/acs.jpcc.0c03415.

[25] X. KONG, Q. YU, X. ZHANG, X. DU, H. GONG, H. JIANG, Synthesis and application of surface enhanced Raman scattering (SERS) tags of Ag@SiO 2 core/shell nanoparticles in protein detection, *J. Mater. Chem.* **2012**, 22, 7767–7774. https://doi.org/10.1039/c2jm16397g.

[26] J. ZHU, J.J. LI, J.W. ZHAO, The Effect of Dielectric Coating on the Local Electric Field Enhancement of Au-Ag Core-Shell Nanoparticles, *Plasmonics* **2015**, 10, 1–8. https://doi.org/10.1007/s11468-014-9769-1.

[27] S.-Y. Ding, J. Yi, J.-F. Li, B. Ren, D.-Y. Wu, R. Panneerselvam, Z.-Q. Tian, Nanostructure-based plasmon-enhanced Raman spectroscopy for surface analysis of materials, *Nat. Rev. Mater.* **2016**, 1, 16021. https://doi.org/10.1038/natrevmats.2016.21.

[28] N.G. Bastús, F. Merkoçi, J. Piella, V. Puntes, Synthesis of Highly Monodisperse Citrate-Stabilized Silver Nanoparticles of up to 200 nm: Kinetic Control and Catalytic Properties, *Chem. Mater.* **2014**, 26, 2836–2846. https://doi.org/10.1021/cm500316k.

[29] N.G. Bastús, J. Comenge, V. Puntes, Kinetically controlled seeded growth synthesis of citrate-stabilized gold nanoparticles of up to 200 nm: Size focusing versus ostwald ripening, *Langmuir* **2011**, 27, 11098–11105. https://doi.org/10.1021/la201938u.

[30] L. Lin, X. Bi, Y. Gu, F. Wang, J. Ye, Surface-enhanced Raman scattering nanotags for bioimaging, *J. Appl. Phys.* **2021**, 129,. https://doi.org/10.1063/5.0047578.

[31] M. Hu, J. Chen, Z.Y. Li, L. Au, G. V. Hartland, X. Li, M. Marquez, Y. Xia, Gold nanostructures: Engineering their plasmonic properties for biomedical applications, *Chem. Soc. Rev.* **2006**, 35, 1084–1094. https://doi.org/10.1039/b517615h.

[32] R. Li, K. Liu, S. Pan, J.H. Ding, Localized surface plasmon resonance of single silver nano-hemisphere, *Adv. Mater. Res.* **2013**, 818, 137–140. https://doi.org/10.4028/www.scientific.net/AMR.818.137.

[33] K.M. Mayer, F. Hao, S. Lee, P. Nordlander, J.H. Hafner, A single molecule immunoassay by localized surface plasmon resonance., *Nanotechnology* **2010**, 21, 255503. https://doi.org/10.1088/0957-4484/21/25/255503.

[34] L.J. Sherry, S.-H. Chang, G.C. Schatz, R.P. Van Duyne, B.J. Wiley, Y. Xia, Localized Surface Plasmon Resonance Spectroscopy of Single Silver Nanocubes, *Nano Lett.* **2005**, 5, 2034–2038. https://doi.org/10.1021/nl0515753.

[35] B.J. Wiley, Y. Chen, J.M. McLellan, Y. Xiong, Z.-Y. Li, D. Ginger, Y. Xia, Synthesis and Optical Properties of Silver Nanobars and Nanorice, *Nano Lett.* **2007**, 7, 1032–1036. https://doi.org/10.1021/nl070214f.

[36] G.J. Nusz, S.M. Marinakos, A.C. Curry, A. Dahlin, F. Hook, A. Wax, A. Chilkoti, Label-free plasmonic detection of biomolecular binding by a single gold nanorod, *Anal. Chem.* **2008**, 80, 984–989. https://doi.org/10.1021/ac7017348.

[37] C.L. Nehl, H. Liao, J.H. Hafner, Optical Properties of Star-Shaped Gold Nanoparticles, *Nano Lett.* **2006**, 6, 683–688. https://doi.org/10.1021/nl052409y.

[38] R.E. Darienzo, O. Chen, M. Sullivan, T. Mironava, R. Tannenbaum, Au nanoparticles for SERS: Temperature-controlled nanoparticle morphologies and their Raman enhancing properties, *Mater. Chem. Phys.* **2020**, 240, 122143. https://doi.org/10.1016/j.matchemphys.2019.122143.

[39] M. Potara, T. Nagy-Simon, A.M. Craciun, S. Suarasan, E. Licarete, F. Imre-Lucaci, S. Astilean, Carboplatin-Loaded, Raman-Encoded, Chitosan-Coated Silver Nanotriangles as Multimodal Traceable Nanotherapeutic Delivery Systems and pH Reporters inside Human Ovarian Cancer Cells, *ACS Appl. Mater. Interfaces* **2017**, 9,

32565–32576. https://doi.org/10.1021/acsami.7b10075.

[40] T.Y. FU, C.L. DU, Y.X. CHEN, R.X. ZHANG, Y. ZHU, L. SUN, D.N. SHI, Enhanced RI Sensitivity and SERS Performances of Individual Au Nanobipyramid Dimers, *Plasmonics* **2021**, 16, 485–491. https://doi.org/10.1007/s11468-020-01302-8.

[41] X. LUO, L. QIAO, Z. XIA, J. YU, X. WANG, J. HUANG, C. SHU, C. WU, Y. HE, Shape- and Size-Dependent Refractive Index Sensing and SERS Performance of Gold Nanoplates, *Langmuir* **2022**,. https://doi.org/10.1021/acs.langmuir.2c00663.

[42] H. CHEN, X. KOU, Z. YANG, W. NI, J. WANG, Shape- and size-dependent refractive index sensitivity of gold nanoparticles, *Langmuir* **2008**, 24, 5233–5237. https://doi.org/10.1021/la800305j.

[43] H. ZHU, X. YUAN, Q. YAO, J. XIE, Shining photocatalysis by gold-based nanomaterials, *Nano Energy* **2021**, 88, 106306. https://doi.org/10.1016/j.nanoen.2021.106306.

[44] S. SARINA, E.R. WACLAWIK, H. ZHU, Photocatalysis on supported gold and silver nanoparticles under ultraviolet and visible light irradiation, *Green Chem.* **2013**, 15, 1814–1833. https://doi.org/10.1039/c3gc40450a.

[45] M.A. AL-AZAWI, N. BIDIN, M. BOUOUDINA, S.M. MOHAMMAD, Preparation of gold and gold–silver alloy nanoparticles for enhancement of plasmonic dye-sensitized solar cells performance, *Sol. Energy* **2016**, 126, 93–104. https://doi.org/10.1016/j.solener.2015.12.043.

[46] A. HAJJIAH, H. BADRAN, I. KANDAS, N. SHEHATA, Perovskite Solar Cell with Added Gold/Silver Nanoparticles: Enhanced Optical and Electrical Characteristics, *Energies* **2020**, 13, 3854. https://doi.org/10.3390/en13153854.

[47] N. IBRAHIM, N.D. JAMALUDDIN, L.L. TAN, N.Y. MOHD YUSOF, A Review on the Development of Gold and Silver Nanoparticles-Based Biosensor as a Detection Strategy of Emerging and Pathogenic RNA Virus, *Sensors* **2021**, 21, 5114. https://doi.org/10.3390/s21155114.

[48] J. LIANG, H. LIU, J. YU, L. ZHOU, J. ZHU, Plasmon-enhanced solar vapor generation, *Nanophotonics* **2019**, 8, 771–786. https://doi.org/10.1515/nanoph-2019-0039.

[49] V.A. MARKEL, Coupled-dipole Approach to Scattering of Light from a One-dimensional Periodic Dipole Structure, *J. Mod. Opt.* **1993**, 40, 2281–2291. https://doi.org/10.1080/09500349314552291.

[50] S. ZOU, N. JANEL, G.C. SCHATZ, Silver nanoparticle array structures that produce remarkably narrow plasmon lineshapes, *J. Chem. Phys.* **2004**, 120, 10871–10875. https://doi.org/10.1063/1.1760740.

[51] S. ZOU, G.C. SCHATZ, Narrow plasmonic/photonic extinction and scattering line shapes for one and two dimensional silver nanoparticle arrays, *J. Chem. Phys.* **2004**, 121, 12606–12612. https://doi.org/10.1063/1.1826036.

[52] Q. LE-VAN, E. ZOETHOUT, E. GELUK, M. RAMEZANI, M. BERGHUIS, J. GÓMEZ RIVAS, Enhanced Quality Factors of Surface Lattice Resonances in Plasmonic Arrays of Nanoparticles, *Adv. Opt. Mater.* **2019**, 7, 1801451.

https://doi.org/10.1002/adom.201801451.

[53] V.G. KRAVETS, F. SCHEDIN, A.N. GRIGORENKO, Extremely narrow plasmon resonances based on diffraction coupling of localized plasmons in arrays of metallic nanoparticles, *Phys. Rev. Lett.* **2008**, 101, 1–4. https://doi.org/10.1103/PhysRevLett.101.087403.

[54] S. DENG, R. LI, J.E. PARK, J. GUAN, P. CHOO, J. HU, P.J.M. SMEETS, T.W. ODOM, Ultranarrow plasmon resonances from annealed nanoparticle lattices, *Proc. Natl. Acad. Sci. U. S. A.* **2020**, 117, 23380–23384. https://doi.org/10.1073/pnas.2008818117.

[55] S. QIU, H. ZHANG, Z. SHI, H. LI, Z.K. ZHOU, Ultrasensitive Refractive Index Sensing Based on Hybrid High-Q Metasurfaces, *J. Phys. Chem. C* **2023**, 127, 8263–8270. https://doi.org/10.1021/acs.jpcc.3c00367.

[56] R. GUO, T.K. HAKALA, P. TÖRMÄ, Geometry dependence of surface lattice resonances in plasmonic nanoparticle arrays, *Phys. Rev. B* **2017**, 95, 155423. https://doi.org/10.1103/PhysRevB.95.155423.

[57] J. KELAVUORI, V. VANYUKOV, T. STOLT, P. KARVINEN, H. REKOLA, T.K. HAKALA, M.J. HUTTUNEN, Thermal Control of Plasmonic Surface Lattice Resonances, *Nano Lett.* **2022**, 22, 3879–3883. https://doi.org/10.1021/acs.nanolett.1c04898.

[58] M. CHARCONNET, M.T. KORSA, S. PETERSEN, J. PLOU, C. HANSKE, J. ADAM, A. SEIFERT, Generalization of Self-Assembly Toward Differently Shaped Colloidal Nanoparticles for Plasmonic Superlattices, *Small Methods* **2023**, 7,. https://doi.org/10.1002/smtd.202201546.

[59] W. WANG, M. RAMEZANI, A.I. VÄKEVÄINEN, P. TÖRMÄ, J.G. RIVAS, T.W. ODOM, The rich photonic world of plasmonic nanoparticle arrays, *Mater. Today* **2018**, 21, 303–314. https://doi.org/10.1016/j.mattod.2017.09.002.

[60] L. CHEN, C. HU, Y. DONG, Y. LI, Q. SHI, G. LIU, R. LONG, Y. XIONG, Tunable Layered Gold Nanochips for High Sensitivity and Uniformity in SERS Detection, *J. Phys. Chem. C* **2023**,. https://doi.org/10.1021/acs.jpcc.3c01359.

[61] N. MEINZER, W.L. BARNES, I.R. HOOPER, Plasmonic meta-atoms and metasurfaces, *Nat. Photonics* **2014**, 8, 889–898. https://doi.org/10.1038/nphoton.2014.247.

[62] P. ZILIO, M. MALERBA, A. TOMA, R.P. ZACCARIA, A. JACASSI, F. DE ANGELIS, Hybridization in Three Dimensions: A Novel Route toward Plasmonic Metamolecules, *Nano Lett.* **2015**, 15, 5200–5207. https://doi.org/10.1021/acs.nanolett.5b01437.

[63] V.G. KRAVETS, F. SCHEDIN, R. JALIL, L. BRITNELL, R. V. GORBACHEV, D. ANSELL, B. THACKRAY, K.S. NOVOSELOV, A.K. GEIM, A. V. KABASHIN, A.N. GRIGORENKO, Singular phase nano-optics in plasmonic metamaterials for label-free single-molecule detection, *Nat. Mater.* **2013**, 12, 304–309. https://doi.org/10.1038/nmat3537.

[64] K.T. CARRON, H.W. LEHMANN, W. FLUHR, M. MEIER, A. WOKAUN, Resonances of two-dimensional particle gratings in surface-enhanced Raman scattering, *J. Opt. Soc. Am. B* **1986**, 3, 430. https://doi.org/10.1364/josab.3.000430.

[65] T.K. Hakala, H.T. Rekola, A.I. Väkeväinen, J.P. Martikainen, M. Nečada, A.J. Moilanen, P. Törmä, Lasing in dark and bright modes of a finite-sized plasmonic lattice, *Nat. Commun.* **2017**, 8, 1–7. https://doi.org/10.1038/ncomms13687.

[66] P. Berini, I. De Leon, Surface plasmon-polariton amplifiers and lasers, *Nat. Photonics* **2012**, 6, 16–24. https://doi.org/10.1038/nphoton.2011.285.

[67] V. Gupta, P.T. Probst, F.R. Goßler, A.M. Steiner, J. Schubert, Y. Brasse, T.A.F. König, A. Fery, Mechanotunable Surface Lattice Resonances in the Visible Optical Range by Soft Lithography Templates and Directed Self-Assembly, *ACS Appl. Mater. Interfaces* **2019**, 11, 28189–28196. https://doi.org/10.1021/acsami.9b08871.

[68] K. Kneipp, M. Moskovits, H. Kneipp, Surface Enhanced Raman Scattering: Physics and Applications | Katrin Kneipp, Martin Moskovits, Harald Kneipp | download, **2006**. https://b-ok.cc/book/496360/1659ac.

[69] E. Smith, G. Dent, Modern raman spectroscopy: A practical approach, **2019**. https://doi.org/10.1002/0470011831.

[70] B. Wiley, Y. Sun, Y. Xia, Synthesis of silver nanostructures with controlled shapes and properties, *Acc. Chem. Res.* **2007**, 40, 1067–1076. https://doi.org/10.1021/ar7000974.

[71] M. Yang, R. Alvarez-Puebla, H.S. Kim, P. Aldeanueva-Potel, L.M. Liz-Marzán, N.A. Kotov, SERS-active gold lace nanoshells with built-in hotspots, *Nano Lett.* **2010**, 10, 4013–4019. https://doi.org/10.1021/nl101946c.

[72] A.J. Blanch, M. Döblinger, J. Rodríguez-Fernández, Simple and Rapid High-Yield Synthesis and Size Sorting of Multibranched Hollow Gold Nanoparticles with Highly Tunable NIR Plasmon Resonances, *Small* **2015**, 11, 4550–4559. https://doi.org/10.1002/smll.201500095.

[73] H. Marks, M. Schechinger, J. Garza, A. Locke, G. Coté, Surface enhanced Raman spectroscopy (SERS) for in vitro diagnostic testing at the point of care, *Nanophotonics* **2017**, 6, 681–701. https://doi.org/10.1515/nanoph-2016-0180.

[74] L. Yang, J. Feng, J.N. Wang, Z. Gao, J. Xu, Y. Mei, Y.Y. Song, Engineering large-scaled electrochromic semiconductor films as reproductive SERS substrates for operando investigation at the solid/liquid interfaces, *Chinese Chem. Lett.* **2022**, 33, 5169–5173. https://doi.org/10.1016/j.cclet.2022.03.011.

[75] Y. Wei, Q. Hao, X. Fan, M. Li, L. Yao, G. Li, X. Zhao, H. Huang, T. Qiu, Investigation of the Plasmon-Activated C-C Coupling Reactions by Liquid-State SERS Measurement, *ACS Appl. Mater. Interfaces* **2022**, 14, 54320–54327. https://doi.org/10.1021/acsami.2c15223.

[76] N.A. Hatab, G. Eres, P.B. Hatzinger, B. Gu, Detection and analysis of cyclotrimethylenetrinitramine (RDX) in environmental samples by surface-enhanced Raman spectroscopy, *J. Raman Spectrosc.* **2010**, 41, 1131–1136. https://doi.org/10.1002/jrs.2574.

[77] Y. Ma, H. Liu, Y. Chen, C. Gu, G. Wei, T. Jiang, Improved lateral flow strip based on hydrophilic−hydrophobic SERS substrate for ultra−sensitive and quantitative

immunoassay, *Appl. Surf. Sci.* **2020**, 529, 2–7. https://doi.org/10.1016/j.apsusc.2020.147121.

[78] N. YANG, T.T. YOU, Y.K. GAO, C.M. ZHANG, P.G. YIN, Fabrication of a Flexible Gold Nanorod Polymer Metafilm via a Phase Transfer Method as a SERS Substrate for Detecting Food Contaminants, *J. Agric. Food Chem.* **2018**, 66, 6889–6896. https://doi.org/10.1021/acs.jafc.8b01702.

[79] V. SHARMA, S. KUMAR, A. JAISWAL, V. KRISHNAN, Gold Deposited Plant Leaves for SERS: Role of Surface Morphology, Wettability and Deposition Technique in Determining the Enhancement Factor and Sensitivity of Detection, *ChemistrySelect* **2017**, 2, 165–174. https://doi.org/10.1002/slct.201601451.

[80] W. TANG, D.B. CHASE, J.F. RABOLT, Immobilization of gold nanorods onto electrospun polycaprolactone fibers via polyelectrolyte decoration - A 3D SERS substrate, *Anal. Chem.* **2013**, 85, 10702–10709. https://doi.org/10.1021/ac400241z.

[81] W. YE, D. WANG, H. ZHANG, F. ZHOU, W. LIU, Electrochemical growth of flowerlike gold nanoparticles on polydopamine modified ITO glass for SERS application, *Electrochim. Acta* **2010**, 55, 2004–2009. https://doi.org/10.1016/j.electacta.2009.11.022.

[82] M. CELIK, S. ALTUNTAS, F. BUYUKSERIN, Fabrication of nanocrater-decorated anodic aluminum oxide membranes as substrates for reproducibly enhanced SERS signals, *Sensors Actuators, B Chem.* **2018**, 255, 2871–2877. https://doi.org/10.1016/j.snb.2017.09.105.

[83] T. WANG, Z. ZHANG, F. LIAO, Q. CAI, Y. LI, S.-T. LEE, M. SHAO, The Effect of Dielectric Constants on Noble Metal/Semiconductor SERS Enhancement: FDTD Simulation and Experiment Validation of Ag/Ge and Ag/Si Substrates, *Sci. Rep.* **2015**, 4, 4052. https://doi.org/10.1038/srep04052.

[84] G. LU, G. WANG, H. LI, Effect of nanostructured silicon on surface enhanced Raman scattering, *RSC Adv.* **2018**, 8, 6629–6633. https://doi.org/10.1039/c8ra00014j.

[85] S. ZAVATSKI, N. KHINEVICH, K. GIREL, S. REDKO, N. KOVALCHUK, I. KOMISSAROV, V. LUKASHEVICH, I. SEMAK, K. MAMATKULOV, M. VOROBYEVA, G. ARZUMANYAN, H. BANDARENKA, Surface enhanced raman spectroscopy of lactoferrin adsorbed on silvered porous silicon covered with graphene, *Biosensors* **2019**, 9, 34. https://doi.org/10.3390/bios9010034.

[86] H. V. BANDARENKA, N. V. KHINEVICH, A.A. BURKO, S. V. REDKO, S.A. ZAVATSKI, U.A. SHAPEL, K.Z. MAMATKULOV, M.Y. VOROBYEVA, G.M. ARZUMANYAN, 3D Silver Dendrites for Single-molecule Imaging by Surface-enhanced Raman Spectroscopy, *ChemNanoMat* **2020**, 1–10. https://doi.org/10.1002/cnma.202000521.

[87] H. V. BANDARENKA, K. V. GIREL, S.A. ZAVATSKI, A. PANARIN, S.N. TEREKHOV, Progress in the development of SERS-active substrates based on metal-coated porous silicon, *Materials (Basel).* **2018**, 11, 1–20. https://doi.org/10.3390/ma11050852.

[88] D. QIN, Y. XIA, G.M. WHITESIDES, Soft lithography for micro- and nanoscale patterning, *Nat. Protoc.* **2010**, 5, 491–502. https://doi.org/10.1038/nprot.2009.234.

[89] H. Guo, J. Tang, K. Qian, D. Tsoukalas, M. Zhao, J. Yang, B. Zhang, X. Chou, J. Liu, C. Xue, W. Zhang, Vectorial strain gauge method using single flexible orthogonal polydimethylsiloxane gratings, *Sci. Rep.* **2016**, 6, 1–10. https://doi.org/10.1038/srep23606.

[90] M. Wu, C. Zhang, Y. Ji, Y. Tian, H. Wei, C. Li, Z. Li, T. Zhu, Q. Sun, B. Man, M. Liu, 3D ultrasensitive polymers-plasmonic hybrid flexible platform for in-situ detection, *Polymers (Basel).* **2020**, 12,. https://doi.org/10.3390/polym12020392.

[91] C. Zhang, P. Yi, L. Peng, X. Lai, J. Chen, M. Huang, J. Ni, Continuous fabrication of nanostructure arrays for flexible surface enhanced Raman scattering substrate, *Sci. Rep.* **2017**, 7,. https://doi.org/10.1038/srep39814.

[92] J. Plou, M. Charconnet, I. García, J. Calvo, L.M. Liz-Marzán, Preventing Memory Effects in Surface-Enhanced Raman Scattering Substrates by Polymer Coating and Laser-Activated Deprotection, *ACS Nano* **2021**, 15, 8984–8995. https://doi.org/10.1021/acsnano.1c01878.

[93] L. Malaquin, T. Kraus, H. Schmid, E. Delamarche, H. Wolf, Controlled particle placement through convective and capillary assembly, *Langmuir* **2007**, 23, 11513–11521. https://doi.org/10.1021/la700852c.

[94] A.M. Steiner, M. Mayer, M. Seuss, S. Nikolov, K.D. Harris, A. Alexeev, C. Kuttner, T.A.F. König, A. Fery, Macroscopic Strain-Induced Transition from Quasi-infinite Gold Nanoparticle Chains to Defined Plasmonic Oligomers, *ACS Nano* **2017**, 11, 8871–8880. https://doi.org/10.1021/acsnano.7b03087.

[95] A. Yang, A.J. Hryn, M.R. Bourgeois, W.K. Lee, J. Hu, G.C. Schatz, T.W. Odom, Programmable and reversible plasmon mode engineering, *Proc. Natl. Acad. Sci. U. S. A.* **2016**, 113, 14201–14206. https://doi.org/10.1073/pnas.1615281113.

[96] A. Mizuno, A. Ono, Dynamic Control of the Interparticle Distance in a Self-Assembled Ag Nanocube Monolayer for Plasmonic Color Modulation, *ACS Appl. Nano Mater.* **2021**, 4, 9721–9728. https://doi.org/10.1021/acsanm.1c02089.

[97] Z. Ye, C. Li, Q. Chen, Y. Xu, S.E.J. Bell, Ultra-Stable Plasmonic Colloidal Aggregates for Accurate and Reproducible Quantitative SE(R)RS in Protein-Rich Biomedia, *Angew. Chemie* **2019**, 131, 19230–19235. https://doi.org/10.1002/ange.201911608.

[98] K.J. Si, D. Sikdar, Y. Chen, F. Eftekhari, Z. Xu, Y. Tang, W. Xiong, P. Guo, S. Zhang, Y. Lu, Q. Bao, W. Zhu, M. Premaratne, W. Cheng, Giant Plasmene Nanosheets, Nanoribbons, and Origami, *ACS Nano* **2014**, 8, 11086–11093. https://doi.org/10.1021/nn504615a.

[99] S.J. Barcelo, A. Kim, W. Wu, Z. Li, Fabrication of deterministic nanostructure assemblies with sub-nanometer spacing using a nanoimprinting transfer technique, *ACS Nano* **2012**, 6, 6446–6452. https://doi.org/10.1021/nn3020807.

[100] S. Almaviva, S. Botti, L. Cantarini, R. Fantoni, S. Lecci, A. Palucci, A. Puiu, A. Rufoloni, Ultrasensitive RDX detection with commercial SERS substrates, *J. Raman Spectrosc.* **2014**, 45, 41–46. https://doi.org/10.1002/jrs.4413.

[101] M. Hu, F.S. Ou, W. Wu, I. Naumov, X. Li, A.M. Bratkovsky, R.S. Williams, Z. Li, Gold nanofingers for molecule trapping and detection, *J. Am. Chem. Soc.* **2010**, 132, 12820–12822. https://doi.org/10.1021/ja105248h.

[102] M.S. Schmidt, J. Hübner, A. Boisen, Large area fabrication of leaning silicon nanopillars for Surface Enhanced Raman Spectroscopy, *Adv. Mater.* **2012**, 24, 11–18. https://doi.org/10.1002/adma.201103496.

[103] K. Wu, T. Li, M.S. Schmidt, T. Rindzevicius, A. Boisen, S. Ndoni, Gold Nanoparticles Sliding on Recyclable Nanohoodoos—Engineered for Surface-Enhanced Raman Spectroscopy, *Adv. Funct. Mater.* **2018**, 28,. https://doi.org/10.1002/adfm.201704818.

[104] W.S. Chew, S. Pedireddy, Y.H. Lee, W.W. Tjiu, Y. Liu, Z. Yang, X.Y. Ling, Nanoporous Gold Nanoframes with Minimalistic Architectures: Lower Porosity Generates Stronger Surface-Enhanced Raman Scattering Capabilities, *Chem. Mater.* **2015**, 27, 7827–7834. https://doi.org/10.1021/acs.chemmater.5b03870.

[105] F. Zou, H. Zhou, T. Van Tan, J. Kim, K. Koh, J. Lee, Dual-Mode SERS-Fluorescence Immunoassay Using Graphene Quantum Dot Labeling on One-Dimensional Aligned Magnetoplasmonic Nanoparticles, *ACS Appl. Mater. Interfaces* **2015**, 7, 12168–12175. https://doi.org/10.1021/acsami.5b02523.

[106] R. Gao, X. Song, C. Zhan, C. Weng, S. Cheng, K. Guo, N. Ma, H. Chang, Z. Guo, L.B. Luo, L. Yu, Light trapping induced flexible wrinkled nanocone SERS substrate for highly sensitive explosive detection, *Sensors Actuators, B Chem.* **2020**, 314, 128081. https://doi.org/10.1016/j.snb.2020.128081.

[107] K.N. Kanipe, P.P.F. Chidester, G.D. Stucky, M. Moskovits, Large Format Surface-Enhanced Raman Spectroscopy Substrate Optimized for Enhancement and Uniformity, *ACS Nano* **2016**, 10, 7566–7571. https://doi.org/10.1021/acsnano.6b02564.

[108] P. Nielsen, S. Hassing, O. Albrektsen, S. Foghmoes, P. Morgen, Fabrication of large-area self-organizing gold nanostructures with sub-10 nm gaps on a porous Al2O3 template for application as a SERS-substrate, *J. Phys. Chem. C* **2009**, 113, 14165–14171. https://doi.org/10.1021/jp9039012.

[109] G. Das, M. Chirumamilla, A. Toma, A. Gopalakrishnan, R.P. Zaccaria, A. Alabastri, M. Leoncini, E. Di Fabrizio, Plasmon based biosensor for distinguishing different peptides mutation states, *Sci. Rep.* **2013**, 3, 1–6. https://doi.org/10.1038/srep01792.

[110] X. Li, H. Hu, D. Li, Z. Shen, Q. Xiong, S. Li, H.J. Fan, Ordered array of gold semishells on TiO 2 spheres: An ultrasensitive and recyclable SERS substrate, *ACS Appl. Mater. Interfaces* **2012**, 4, 2180–2185. https://doi.org/10.1021/am300189n.

[111] H.K. Lee, Y.H. Lee, Q. Zhang, I.Y. Phang, J.M.R. Tan, Y. Cui, X.Y. Ling, Superhydrophobic surface-enhanced Raman scattering platform fabricated by assembly of Ag nanocubes for trace molecular sensing, *ACS Appl. Mater. Interfaces* **2013**, 5, 11409–11418. https://doi.org/10.1021/am403655g.

[112] A.B. Serrano-Montes, D.J. De Aberasturi, J. Langer, J.J. Giner-Casares, L.

SCARABELLI, A. HERRERO, L.M. LIZ-MARZÁN, A General Method for Solvent Exchange of Plasmonic Nanoparticles and Self-Assembly into SERS-Active Monolayers, *Langmuir* **2015**, 31, 9205–9213. https://doi.org/10.1021/acs.langmuir.5b01838.

[113] F. QIAN, A.J. PASCALL, M. BORA, T.Y.J. HAN, S. GUO, S.S. LY, M.A. WORSLEY, J.D. KUNTZ, T.Y. OLSON, On-demand and location selective particle assembly via electrophoretic deposition for fabricating structures with particle-to-particle precision, *Langmuir* **2015**, 31, 3563–3568. https://doi.org/10.1021/la502724n.

[114] Y. MA, H. LIU, M. MAO, J. MENG, L. YANG, J. LIU, Surface-Enhanced Raman Spectroscopy on Liquid Interfacial Nanoparticle Arrays for Multiplex Detecting Drugs in Urine, *Anal. Chem.* **2016**, 88, 8145–8151. https://doi.org/10.1021/acs.analchem.6b01884.

[115] G. YANG, J. NANDA, B. WANG, G. CHEN, D.T. HALLINAN, Self-Assembly of Large Gold Nanoparticles for Surface-Enhanced Raman Spectroscopy, *ACS Appl. Mater. Interfaces* **2017**, 9, 13457–13470. https://doi.org/10.1021/acsami.7b01121.

[116] S. NI, J. LEEMANN, I. BUTTINONI, L. ISA, H. WOLF, Programmable colloidal molecules from sequential capillarity-assisted particle assembly, *Sci. Adv.* **2016**, 2, 1–8. https://doi.org/10.1126/sciadv.1501779.

[117] N.J. GREYBUSH, M. SABOKTAKIN, X. YE, C. DELLA GIOVAMPAOLA, S.J. OH, N.E. BERRY, N. ENGHETA, C.B. MURRAY, C.R. KAGAN, Plasmon-enhanced upconversion luminescence in single nanophosphor-nanorod heterodimers formed through template-assisted self-assembly, *ACS Nano* **2014**, 8, 9482–9491. https://doi.org/10.1021/nn503675a.

[118] S. NI, M.J.K. KLEIN, N.D. SPENCER, H. WOLF, Cascaded assembly of complex multiparticle patterns, *Langmuir* **2014**, 30, 90–95. https://doi.org/10.1021/la403956e.

[119] M. JUODENAS, T. TAMULEVIČIUS, J. HENZIE, D. ERTS, S. TAMULEVIČIUS, Surface Lattice Resonances in Self-Assembled Arrays of Monodisperse Ag Cuboctahedra, *ACS Nano* **2019**, 13, 9038–9047. https://doi.org/10.1021/acsnano.9b03191.

[120] D. VIRGANAVIČIUS, M. JUODĖNAS, T. TAMULEVIČIUS, H. SCHIFT, S. TAMULEVIČIUS, Investigation of transient dynamics of capillary assisted particle assembly yield, *Appl. Surf. Sci.* **2017**, 406, 136–143. https://doi.org/10.1016/j.apsusc.2017.02.100.

[121] I. ALEKNAVIČIENĖ, E. PABRĖŽA, M. TALAIKIS, M. JANKUNEC, G. RAČIUKAITIS, Low-cost SERS substrate featuring laser-ablated amorphous nanostructure, *Appl. Surf. Sci.* **2022**, 571, 151248. https://doi.org/10.1016/j.apsusc.2021.151248.

[122] P. JIANG, A. NION, A. MARCHENKO, L. PIOT, D. FICHOU, Rotational Polymorphism in 2-Naphthalenethiol SAMs on Au(111), *J. Am. Chem. Soc.* **2006**, 128, 12390–12391. https://doi.org/10.1021/ja063060z.

[123] A.D. RAKIĆ, A.B. DJURIŠIĆ, J.M. ELAZAR, M.L. MAJEWSKI, Optical properties of metallic films for vertical-cavity optoelectronic devices, *Appl. Opt.* **1998**, 37, 5271. https://doi.org/10.1364/AO.37.005271.

[124] J. GROBELNY, M. KRZYZOWSKA, P. ORLOWSKI, K. RANOSZEK-SOLIWODA, E. SOCHA,

P. KRZYCZMONIK, G. CELICHOWSKI, A. IGNACZAK, E. TOMASZEWSKA, The role of tannic acid and sodium citrate in the synthesis of silver nanoparticles, *J. Nanoparticle Res.* **2017**, 19,. https://doi.org/10.1007/s11051-017-3973-9.

[125] C. GANGWAR, B. YASEEN, I. KUMAR, N.K. SINGH, R.M. NAIK, Growth Kinetic Study of Tannic Acid Mediated Monodispersed Silver Nanoparticles Synthesized by Chemical Reduction Method and Its Characterization, *ACS Omega* **2021**, 6, 22344–22356. https://doi.org/10.1021/acsomega.1c03100.

[126] J. LIU, D.A. SONSHINE, S. SHERVANI, R.H. HURT, Controlled Release of Biologically Active Silver from Nanosilver Surfaces, *ACS Nano* **2010**, 4, 6903–6913. https://doi.org/10.1021/nn102272n.

[127] A.L. PATTERSON, The scherrer formula for X-ray particle size determination, *Phys. Rev.* **1939**, 56, 978–982. https://doi.org/10.1103/PhysRev.56.978.

[128] G. V. HARTLAND, Optical studies of dynamics in noble metal nanostructures, *Chem. Rev.* **2011**, 111, 3858–3887. https://doi.org/10.1021/cr1002547.

[129] W. HUANG, W. QIAN, M.A. EL-SAYED, Y. DING, Z.L. WANG, Effect of the Lattice Crystallinity on the Electron−Phonon Relaxation Rates in Gold Nanoparticles, *J. Phys. Chem. C* **2007**, 111, 10751–10757. https://doi.org/10.1021/jp0738917.

[130] Y.U. STAECHELIN, D. HOEING, F. SCHULZ, H. LANGE, Size-Dependent Electron–Phonon Coupling in Monocrystalline Gold Nanoparticles, *ACS Photonics* **2021**, 8, 752–757. https://doi.org/10.1021/acsphotonics.1c00078.

[131] D. PECKUS, Š. MEŠKINIS, A. VASILIAUSKAS, E. RAJACKAITĖ, M. ANDRULEVIČIUS, V. KOPUSTINSKAS, S. TAMULEVIČIUS, Structure and optical properties of diamond like carbon films containing aluminium and alumina, *Appl. Surf. Sci.* **2020**, 529, 147040. https://doi.org/10.1016/j.apsusc.2020.147040.

[132] Q. DARUGAR, W. QIAN, M.A. EL-SAYED, M.P. PILENI, Size-dependent ultrafast electronic energy relaxation and enhanced fluorescence of copper nanoparticles, *J. Phys. Chem. B* **2006**, 110, 143–149. https://doi.org/10.1021/jp0545445.

[133] P.K. JAIN, W. QIAN, M.A. EL-SAYED, Ultrafast electron relaxation dynamics in coupled metal nanoparticles in aggregates, *J. Phys. Chem. B* **2006**, 110, 136–142. https://doi.org/10.1021/jp055562p.

[134] M. ZHAO, A. MCCORMACK, M. KESWANI, The formation mechanism of gradient porous Si in a contactless electrochemical process, *J. Mater. Chem. C* **2016**, 4, 4204–4210. https://doi.org/10.1039/c6tc00309e.

[135] G. LAMMEL, S. SCHWEIZER, S. SCHIESSER, P. RENAUD, Tunable optical filter of porous silicon as key component for a MEMS spectrometer, *J. Microelectromechanical Syst.* **2002**, 11, 815–828. https://doi.org/10.1109/JMEMS.2002.803278.

[136] T.F. PAES, A.F. BELOTO, E.C.D.S. GALVÃO, L.A. BERNI, Simple method for measuring the porosity, thickness and refractive index of porous silicon, based on the Fabry-Pérot interference spectrum, *Rev. Bras. Apl. Vácuo* **2017**, 35, 117. https://doi.org/10.17563/rbav.v35i3.1044.

[137] N.H. MANIYA, S.R. PATEL, Z.V.P. MURTHY, Electrochemical preparation of

microstructured porous silicon layers for drug delivery applications, *Superlattices Microstruct.* **2013**, 55, 144–150. https://doi.org/10.1016/j.spmi.2012.12.005.

[138] H. SOHN, Handbook of Porous Silicon, Springer International Publishing, Cham, **2021**. https://doi.org/10.1007/978-3-319-04508-5.

[139] K.G. STAMPLECOSKIE, J.C. SCAIANO, V.S. TIWARI, H. ANIS, Optimal size of silver nanoparticles for surface-enhanced raman spectroscopy, *J. Phys. Chem. C* **2011**, 115, 1403–1409. https://doi.org/10.1021/jp106666t.

[140] R. REDÓN, A. VÁZQUEZ-OLMOS, M.E. MATA-ZAMORA, A. ORDÓÑEZ-MEDRANO, F. RIVERA-TORRES, J.M. SANIGER, Contact angle studies on anodic porous alumina, *J. Colloid Interface Sci.* **2005**, 287, 664–670. https://doi.org/10.1016/j.jcis.2005.02.036.

[141] A. CASADEI, E.F. PECORA, J. TREVINO, C. FORESTIERE, D. RÜFFER, E. RUSSO-AVERCHI, F. MATTEINI, G. TUTUNCUOGLU, M. HEISS, A. FONTCUBERTA I MORRAL, L. DAL NEGRO, Photonic-plasmonic coupling of GaAs single nanowires to optical nanoantennas, *Nano Lett.* **2014**, 14, 2271–2278. https://doi.org/10.1021/nl404253x.

[142] P. OFFERMANS, M.C. SCHAAFSMA, S.R.K. RODRIGUEZ, Y. ZHANG, M. CREGO-CALAMA, S.H. BRONGERSMA, J. GÓMEZ RIVAS, Universal scaling of the figure of merit of plasmonic sensors, *ACS Nano* **2011**, 5, 5151–5157. https://doi.org/10.1021/nn201227b.

[143] N. LIU, T. LIEDL, Europe PMC Funders Group DNA-assembled advanced plasmonic architectures, **2019**, 118, 3032–3053. https://doi.org/10.1021/acs.chemrev.7b00225.DNA-assembled.

[144] R. BORAH, S.W. VERBRUGGEN, Coupled Plasmon Modes in 2D Gold Nanoparticle Clusters and Their Effect on Local Temperature Control, *J. Phys. Chem. C* **2019**, 123, 30594–30603. https://doi.org/10.1021/acs.jpcc.9b09048.

[145] I. RAGHEB, M. BRAÏK, S. LAU-TRUONG, A. BELKHIR, A. RUMYANTSEVA, S. KOSTCHEEV, P.-M. ADAM, A. CHEVILLOT-BIRAUD, G. LÉVI, J. AUBARD, L. BOUBEKEUR-LECAQUE, N. FÉLIDJ, Surface Enhanced Raman Scattering on Regular Arrays of Gold Nanostructures: Impact of Long-Range Interactions and the Surrounding Medium, *Nanomaterials* **2020**, 10, 2201. https://doi.org/10.3390/nano10112201.

[146] M. CHARCONNET, C. KUTTNER, J. PLOU, J.L. GARCÍA-POMAR, A. MIHI, L.M. LIZ-MARZÁN, A. SEIFERT, Mechanically Tunable Lattice-Plasmon Resonances by Templated Self-Assembled Superlattices for Multi-Wavelength Surface-Enhanced Raman Spectroscopy, *Small Methods* **2021**, 5, 2100453. https://doi.org/10.1002/smtd.202100453.

[147] Q. GUO, M. XU, Y. YUAN, R. GU, J. YAO, Self-assembled large-scale monolayer of Au nanoparticles at the air/water interface used as a SERS substrate, *Langmuir* **2016**, 32, 4530–4537. https://doi.org/10.1021/acs.langmuir.5b04393.

[148] Y. HU, T. ZHAO, P. ZHU, Y. ZHU, X. LIANG, R. SUN, C.P. WONG, Tailoring Size and Coverage Density of Silver Nanoparticles on Monodispersed Polymer Spheres as Highly Sensitive SERS Substrates, *Chem. - An Asian J.* **2016**, 11, 2428–2435. https://doi.org/10.1002/asia.201600821.

[149] R.K. SAINI, A. KUMAR, V. GOYAL, A. AGARWAL, R. PRAJESH, Evaluating EM-field enhancement of different shapes of metallic nanoparticles using COMSOL multiphysics for SERS-based sensors, *Mater. Today Proc.* **2023**, 76, 383–387. https://doi.org/10.1016/j.matpr.2022.11.425.

[150] I. KNORR, J. IHLEMANN, G. MAROWSKY, Prediction and Optimization of Surface-Enhanced Raman Scattering Geometries, **2002**, 14, 2008.

SCIENTIFIC PAPERS

[**A1**] Khinevich Nadzeya; Bandarenka Hanna; Zavatski Siarhei; Girel Kseniya; Tamulevičienė Asta; Tamulevičius Tomas; Tamulevičius Sigitas. Porous silicon – a versatile platform for mass-production of ultrasensitive SERS-active substrates // Microporous and Mesoporous Materials. Amsterdam: Elsevier. ISSN 1387-1811. eISSN 1873-3093. 2021, vol. 323, art. No. 111204, p. 1–18. DOI: 10.1016/j.micromeso.2021.111204 [IF: 5.2].

[**A2**] Nadzeya Khinevich, Domantas Peckus, Asta Tamulevičienė, Gerda Klimaitė, Joel Henzie, Tomas Tamulevičius, Sigitas Tamulevičius. Size and Crystallinity Effect on the Ultrafast Optical Response of Chemically Synthesized Silver Nanoparticles // Journal of Materiomics (2023), DOI: 10.1016/j.jmat.2023.08.009 [IF: 9.4].

[**A3**] Khinevich Nadzeya; Juodėnas Mindaugas; Tamulevičienė Asta; Bandarenka Hanna; Tamulevičius Sigitas. Tailoring Mesoporous Silicon Surface to Form a Versatile Template for Nanoparticle Deposition // Coatings. Basel: MDPI. ISSN 2079-6412. 2021, vol. 11, iss. 6, art. No. 699, p. 1–10. DOI: 10.3390/coatings11060699 [IF: 3.4].

[**A4**] Khinevich Nadzeya; Juodėnas Mindaugas; Tamulevičienė Asta; Tamulevičius Tomas; Talaikis Martynas; Niaura Gediminas; Tamulevičius Sigitas. Wavelength-Tailored Enhancement of Raman Scattering on a Resonant Plasmonic Lattice // Sensors and actuators B: Chemical. Lausanne: Elsevier. ISSN 0925-4005. eISSN 1944-8201. 2023, vol. 394, art. No. 134418, p. 1–8. DOI: 10.1016/j.snb.2023.134418 [IF: 8.400].

CURRICULUM VITAE

Nadzeya Khinevich
nadzeya.khinevich@ktu.lt

Education:

2001 – 2012	High School, Gymnasium № 29, Minsk, Belarus
2012 – 2017	Diploma of Electrical Engineer (field: Micro and Nanoelectronics), Belarusian State University of Informatics and Radioelectronics, Minsk, Belarus.
2017 – 2018	Master's degree in Engineering Sciences (field: Solid-State Electronics, Radioelectronics, Micro- and Nanoelectronics, Quantum Effect Devices), Belarusian State University of Informatics and Radioelectronics, Minsk, Belarus.
2018 – now	PhD in Materials Science, Kaunas University of Technology, Kaunas, Lithuania (expected 2024–05–31)
2022 March – June	ERASMUS+ internship at Mads Clausen Institute of the University of Southern Denmark, Sønderborg, Denmark

Professional experience:

2016 – 2017	Engineer, laboratory *Materials and Structures of Nanoelectronics*, Micro- and Nanoelectronics Department, Belarusian State University of Informatics and Radioelectronics, Minsk, Belarus.
2017 – 2020	Junior Researcher, laboratory *Applied Plasmonics*, Micro- and Nanoelectronics Department, Belarusian State University of Informatics and Radioelectronics, Minsk, Belarus
2020 – 2021	Junior Researcher, *UAB Nanoversa*, Kaunas, Lithuania
2020 – present	Project Junior Researcher, laboratory *Nano and Microlithography*, Institute of Materials Science Kaunas University of Technology, Kaunas, Lithuania.
2022 – present	Technician, laboratory *Surface and Thin Films*, Institute of Materials Science, Kaunas University of Technology, Kaunas, Lithuania.

Scientific papers forming the basis of this dissertation:

1. Khinevich Nadzeya; Bandarenka Hanna; Zavatski Siarhei; Girel Kseniya; Tamulevičienė Asta; Tamulevičius Tomas; Tamulevičius Sigitas. Porous silicon – a versatile platform for mass-production of ultrasensitive SERS-active substrates // Microporous and mesoporous materials. Amsterdam: Elsevier. ISSN 1387-1811. eISSN 1873-3093. 2021, vol. 323, art. No. 111204, p. 1–18. DOI: 10.1016/j.micromeso.2021.111204 [IF: 5,876].
2. Nadzeya Khinevich, Domantas Peckus, Asta Tamulevičienė, Gerda Klimaitė, Joel Henzie, Tomas Tamulevičius, Sigitas Tamulevičius. Size and crystallinity effect on the ultrafast optical response of chemically synthesized silver nanoparticles // Journal of Materiomics (2023), DOI: 10.1016/j.jmat.2023.08.009 [IF: 9.4].
3. Khinevich Nadzeya; Juodėnas Mindaugas; Tamulevičienė Asta; Bandarenka Hanna; Tamulevičius Sigitas. Tailoring mesoporous silicon surface to form a versatile template for nanoparticle deposition // Coatings. Basel: MDPI. ISSN 2079-6412. 2021, vol. 11, iss. 6, art. No. 699, p. 1–10. DOI: 10.3390/coatings11060699 [IF: 3.236].
4. Khinevich Nadzeya; Juodėnas Mindaugas; TamulevičienėAsta; Tamulevičius Tomas; Talaikis Martynas; Niaura Gediminas; Tamulevičius Sigitas. Wavelength-tailored enhancement of Raman scattering on a resonant plasmonic lattice // Sensors and actuators B: Chemical. Lausanne: Elsevier. ISSN 0925-4005. eISSN 1944-8201. 2023, vol. 394, art. No. 134418, p. 1–8. DOI: 10.1016/j.snb.2023.134418 [IF: 8.400].

Peer-reviewed publications not related to this dissertation:

5. Bandarenka Hanna V.; Khinevich Nadzeya; Burko Aliaksandr; Redko Sergey; Zavatski Siarhei; Shapel Uladzislau; Mamatkulov Kahramon; Vorobyeva Maria; Arzumanyan Grigory. 3D NPsdendrites for single-molecule imaging by surface-enhanced Raman spectroscopy // ChemNanoMat. Weinheim: Wiley-VCH. ISSN 2199-692X. 2021, vol. 7, iss. 2, p. 141–149. DOI: 10.1002/cnma.202000521 [IF: 3.820].
6. Gorudko I.V.; Grigorieva D.V.; Shamova E.V.; Gorbunov N.P.; Kokhan, A.U.; Kostevich V.A.; Vasilyev V.B.; Panasenko O.M.; Khinevich N.V.; Bandarenka H.V.; Burko A.A.; Sokolov A.V. Structure-biological activity relationships of myeloperoxidase to effect on platelet activation // Archives of biochemistry and biophysics. New York: Academic Press. ISSN 0003-9861. eISSN 1096-0384. 2022, vol. 728, art. No. 109353, p. 1–12. DOI: 10.1016/j.abb.2022.109353 [IF: 3.900].

Scientific conferences:

1. Mikalkevičius, Mantas; Khinevich, Nadzeya; Tamulevičius, Tomas; Tamulevičienė, Asta. Investigation of stability of NPs nanoparticles under different storage conditions // Open Readings 2023: 66th international conference for students of physics and natural sciences, April 18–21, 2023, Vilnius, Lithuania: annual abstract book / editors: M. Keršys, Š. Mickus. Vilnius: Vilnius University Press, 2023. ISBN 9786090708835. p. 220.
2. Peckus, Domantas; Khinevich, Nadzeya; Tamulevičiene, Asta; Henzie, Joel; Mougin, Karine; Spangenberg, Arnaud; Tamulevičius, Tomas; Tamulevičius, Sigitas. The size, shape and crystal structure of metal nanoparticles influence on their ultrafast plasmonic properties // 3rd Baltic biophysics conference: October 6–7, 2022, Vilnius, Lithuania: abstract book. Vilnius: Center for Physical Sciences and Technology. 2022, O08, p. 27.
3. Juodėnas, Mindaugas; Mylnikov, Vasilii; Göbel, Sebastian; Käll, Mikael; Peckus, D.; Khinevich, N.; Henzie, J.; Tamulevicius, T.; Tamuleviciene, A.; Tamulevicius, S. Manipulating light by plasmonic and dielectric metasurfaces // Advanced materials and technologies: book of abstracts of 24rd international conference-school, 22–26 August 2022, Palanga, Lithuania. Kaunas: Kaunas University of Technology. ISSN 2669-1930. 2022, p. 31.
4. Khinevich, Nadzeya; Peckus, Domantas; Tamulevičienė, Asta; Tamulevičius, Tomas; Tamulevičius, Sigitas. Size effect on crystalline structure and dynamic optical properties of NPs nanoparticles // Advanced materials and technologies: book of abstracts of 24th international conference-school, 22–26 August 2022, Palanga, Lithuania. Kaunas: Kaunas University of Technology. ISSN 2669-1930. 2022, A-P43, p. 80.
5. Khinevich, Nadzeya; Juodėnas, Mindaugas; Tamulevičienė, Asta; Tamulevičius, Tomas; Talaikis, Martynas; Niaura, Gediminas; Tamulevičius, Sigitas. Surface lattice resonance in NPs nanoparticle array for surface-enhanced Raman scattering spectroscopy // Advanced materials and technologies: book of abstracts of 24th international conference-school, 22–26 August 2022, Palanga, Lithuania. Kaunas: Kaunas University of Technology. ISSN 2669-1930. 2022, B-P30, p. 66.
6. Juodenas, M.; Peckus, D.; Khinevich, N.; Henzie, J.; Tamulevicius, T.; Tamuleviciene, A.; Tamulevicius, S. Plasmonic surface lattice resonance and optomechanics for self-assembled nanolasers // META 2022: the 12th international conference on metamaterials, photonic crystals and plasmonics, 19–22 July, 2022, Torremolinos, Spain: proceedings / edited by Said Zouhd. Torremolinos: META conference. ISSN 2429-1390. 2022, p. 875–876.
7. Khinevich, N.; Juodėnas, M.; Tamulevičienė, A.; Tamulevičius, T.; Talaikis, M.; Niaura, G.; Tamulevičius, S. NPs nanoparticle arrays for

wavelength taylored enhancement of Raman scattering // META 2022: the 12th international conference on metamaterials, photonic crystals and plasmonics, 19–22 July, 2022, Torremolinos, Spain: proceedings / edited by Said Zouhd. Torremolinos: META conference. ISSN 2429-1390. 2022, p. 877–878.

8. Khinevich, Nadzeya; Tamulevičienė, Asta; Juodėnas, Mindaugas; Tamulevičius, Tomas; Tamulevičius, Sigitas. SERS-active substrates based on NPsnanoparticle array induced surface lattice resonance // Joint international conference *Functional materials and nanotechnologies* and *Nanotechnology and innovation in the Baltic Sea region*, FM&NT – NIBS 2022, Riga, Latvia, July 3–6, 2022: book of abstracts / edited by L. Grīnberga, A. Šarakovskis, G. Kunakova. Riga: University of Latvia, 2022, Po-86. ISBN 9789934236457. p. 220.
9. Tamulevičienė, A.; Jokšaitė, J.; Khinevich, N.; Juodėnas, M.; Tamulevičius, T.; Tamulevičius, S. SERS using self-assembled nano structures of different geometry. Special case of wires, spheres and triangles // Joint international conference *Functional materials and nanotechnologies* and *Nanotechnology and innovation in the Baltic Sea region*, FM&NT – NIBS 2022, Riga, Latvia, July 3–6, 2022: book of abstracts / edited by L. Grīnberga, A. Šarakovskis, G. Kunakova. Riga: University of Latvia, 2022, INV-23. ISBN 9789934236457. p. 84.
10. Tamulevicius, Tomas; Juodėnas, Mindaugas; Khinevich, Nadzeya; Klinavicius, Tomas; Tamuleviciene, Asta; Peckus, Domantas; Henzie, Joel; Tamulevicius, Sigitas. Self-assembled metasurfaces for functional nanophotonics // Proceedings of SPIE: SPIE OPTO: advanced fabrication technologies for micro/nano optics and photonics XV: 22 January – 28 February 2022, San Francisco, California, United States. Bellingham, WA: SPIE. ISSN 0277-786X. eISSN 1996-756X. 2022, vol. PC12012, p. 1. DOI: 10.1117/12.2614629.
11. Khinevich, Nadzeya; Tamulevičienė, Asta; Tamulevičius, Sigitas. Dependence of semimonodispersed NPs nanoparticles growth kinetics on tannic acid and trisodium citrate ratio = Tanino rūgšties ir trinatrio citrato santykio įtaka pusiau monodispersinių sidabro nanodalelių augimo kinetikai // 44-oji Lietuvos nacionalinė fizikos konferencija, 2021 m. spalio 6–8 d., Vilnius: programa ir pranešimų tezės. Vilnius: Fizinių ir technologijos mokslų centras, 2021, P57. ISBN 9786099551180. p. 160.
12. Khinevich, Nadzeya; Juodėnas, Mindaugas; Tamulevičienė, Asta; Bandarenka, Hanna; Tamulevičius, Sigitas. Fabrication of templates for nanoparticle deposition based on mesoporous silicon with open pores // Advanced materials and technologies: book of abstracts of 23rd international conference-school, 23–27 August 2021, Palanga, Lithuania. Kaunas: Kaunas University of Technology. ISSN 2669-1930. 2021, C-P53, p. 83.

13. Khinevich, Nadzeya; Juodėnas, Mindaugas; Tamulevičienė, Asta; Bandarenka, Hanna; Tamulevičius, Sigitas. Fabrication of the plasmonic structure based on 'bottle-neck' free porous silicon with embedded NPsnanoparticles // NIBS conference 2021: [4th conference *Nanotechnology and innovation in the Baltic Sea region* (NIBS 2021), 4–6 August 2021, virtual conference]: technical digest. [S.l.]: Norddeutsche Initiative Nanotechnologie Schleswig-Holstein e.V. (NINa SH). 2021, PB12, p. 28.
14. Khinevich, Nadzeya; Juodenas, Mindaugas; Tamulevicius, Tomas; Tamulevicius, Sigitas. Development of a porous silicon based guide mode resonator as a template for SERS-application // Open readings 2021: 64th international conference for students of physics and natural sciences, 16–19 March, Vilnius, Lithuania: abstract book / editors: Š. Mickus, R. Platakytė, S. Pūkienė. Vilnius: Vilnius University Press, 2021, P2-39. ISBN 9786090705902. p. 208.
15. Tamulevičienė, Asta; Khinevich, Nadzeya; Mikalkevičius, Mantas; Juodėnas, Mindaugas; Tamulevičius, Tomas; Tamulevičius, Sigitas. Sidabro nanodarinių sintezė, jų modifikavimas ir taikymas paviršiuje stiprinamos ramano sklaidos jutikliams // Fizinių ir technologijos mokslų tarpdalykiniai tyrimai: 10-oji jaunųjų mokslininkų konferencija: pranešimų santraukos / leidinį sudarė Silva Aukštinaitienė ir Bronius Jaskelevičius. [Vilnius]: [Lietuvos mokslų akademija]. 2020, p. 26.
16. Khinevich, Nadzeya; Zavatsky, Sergey; Bandarenka, Hanna; Tamulevičius, Sigitas; Bondarenko, Vitaly. New features of mesoporous silicon structure // Advanced materials and technologies: book of abstracts of 22nd international conference – school, 24–28 August 2020, Palanga, Lithuania. Kaunas: Kaunas University of Technology. ISSN 1822-7759. 2020, A-P34, p. 59.
17. Khinevich, Nadzeya; Bandarenka, Hanna; Zavatski, Sergey; Tamulevicius, Sigitas. NPs nanoparticles and nanoplates on porous silicon for SERS applications = Sidabro nanodalelės ir nanoplokštelės ant porėtojo silicio SERS taikymams // 43-ioji Lietuvos nacionalinė fizikos konferencija, 2019 m. spalio 3-5 d., Kaunas: pranešimų medžiaga. Kaunas: Kauno technologijos universitetas, 2019. eISBN 9786090216385. p. 157. DOI: 10.5755/e01.9786090216385.
18. Khinevich, Nadzeya; Tamulevičius, Sigitas; Tamulevičienė, Asta; Bandarenka, Hanna; Zavatski, Sergey. New approach to fabrication of SERS-active substrates based on colloidal nanoparticles: poster // Advanced materials and technologies: book of abstracts of 21st international conference – school, 19–23 August 2019, Palanga, Lithuania. Kaunas: Kaunas University of Technology. ISSN 1822-7759. 2019, P23, p. 55.

COPIES OF THE PUBLICATIONS

Paper I: Porous silicon – A Versatile Platform for Mass-Production of Ultrasensitive SERS-Active Substrates

Nadzeya Khinevich, Hanna Bandarenka, Siarhei Zavatski, Kseniya Girel, Asta Tamulevičienė, Tomas Tamulevičius, Sigitas Tamulevičius

Microporous and Mesoporous Materials 323 (2021) 111204

Microporous and Mesoporous Materials 323 (2021) 111204

Contents lists available at ScienceDirect

Microporous and Mesoporous Materials

journal homepage: www.elsevier.com/locate/micromeso

Porous silicon - A versatile platform for mass-production of ultrasensitive SERS-active substrates

Nadzeya Khinevich [a,*], Hanna Bandarenka [b,c,d,**], Siarhei Zavatski [b,e], Kseniya Girel [b], Asta Tamulevičienė [a], Tomas Tamulevičius [a,f], Sigitas Tamulevičius [a,f]

[a] Institute of Materials Science, Kaunas University of Technology, 59 K. Baršausko St., 51423, Kaunas, Lithuania
[b] Applied Plasmonics Laboratory, Belarusian State University of Informatics and Radioelectronics, 6 Brovka St., 220013, Minsk, Belarus
[c] The Polytechnic School, Ira A. Fulton Schools of Engineering, Arizona State University, 6075 S. Innovation Way W., Mesa, AZ, 85212, USA
[d] Institute of Advanced Materials and Technologies, National University of Electronic Technology, 1 Shokin Sq., Zelenograd, Moscow, 124498, Russia
[e] Swiss Federal Institute of Technology Lausanne, 11 Station St., CH-1015, Lausanne, Switzerland
[f] Department of Physics, Kaunas University of Technology, Studentų St. 50, Kaunas, 51368, Lithuania

ARTICLE INFO

Keywords:
SERS
Porous silicon
Plasmonic nanoparticles
Attomolar detection limit
Bragg structures
Commercial SERS-Active substrates

ABSTRACT

Surface-enhanced Raman scattering (SERS) spectroscopy is one of the most prospective methods combining state-of-the-art nanomaterials and optical techniques for highly sensitive express-analysis and detection of organic and bioorganic objects in liquids and gases. Special programs have been recently started all over the world to bring the SERS-spectroscopy closer to wide implementation in medical diagnostics, forensics, security, monitoring sanitary conditions, etc. Despite outstanding features of SERS-spectroscopy, its effective practical use has been particularly slowed down by moderate reproducibility, non-versatility, and restrictions imposed by commercially available SERS-active substrates to measurement and storage regimes. The present review reports SERS-active substrates constituted by noble metals' nanoparticles (NPs) and porous silicon (PS), which potentially can be a tool to overcome the above-mentioned limitations. The PS template acts as a highly ordered host nanomaterial for the formation of a variety of metallic nanostructures, which morphological and optical properties can be easily tuned for the best performance to meet the customer requirements via managing PS synthesis regimes. An indubitable advantage of PS is the compatibility of its fabrication process with basic microelectronics operations and micro-electromechanical systems (MEMS) that make it possible to integrate SERS-active areas in a silicon chip. In contrast to the previously published reviews in the field, this one covers the most recent results on formation, characterization, and application of PS-based substrates demonstrating prominent SERS-activity that have been achieved for the last decade including modifications with graphene or Bragg structures, detection of molecules at amount down to attomolar concentration, bacteria recognition, etc.

1. Introduction

Several reviews on the surface-enhanced Raman scattering (SERS) provided by metalized silicon nanostructures have already been published, where main methods of fabrication, properties, and applications of such nanomaterials can be found [1,2]. In the present work information on the recent progress of the SERS-active substrates based on porous silicon (PS) as well as some original results in the field achieved by the authors are reported. Here we concentrate on the most popular and effective methods of noble metal deposition on PS, new approaches to increase the SERS-activity of the substrates, and show the freshest applications of metalized PS for detection of different biomolecules and determination of their structure by SERS-spectroscopy. Moreover, the mechanism of increasing the SERS-activity of the PS-based substrates facilitated by their morphology is deeply considered, as lately such structures demonstrated an enormous Raman signal enhancement.

Since the very beginning of its discovery, SERS-spectroscopy has been considered as a highly sensitive method for label-free molecule detection that can be carried out with miniaturized nanostructured SERS-active substrates and both stationary and portable spectrometers.

* Corresponding author. Institute of Materials Science, Kaunas University of Technology, 59 K. Baršausko St., 51423, Kaunas, Lithuania.
** Corresponding author. Applied Plasmonics Laboratory, Belarusian State University of Informatics and Radioelectronics, 6 Brovka St., 220013, Minsk, Belarus.
E-mail addresses: nadzeya.khinevich@ktu.edu (N. Khinevich), h.bandarenka@bsuir.by (H. Bandarenka).

https://doi.org/10.1016/j.micromeso.2021.111204
Received 25 February 2021; Received in revised form 26 May 2021; Accepted 27 May 2021
Available online 2 June 2021

An interest in SERS-spectroscopy has increased almost threefold over the last decade as depicted in Fig. 1.

The SERS technique finds a place in a wide range of applications including but not limited to forensic science [3], bioanalytical chemistry [4,5], food quality control [6], pharmacy [7], and biomedicine [8]. Recently, a great number of various SERS-active substrates for the single- or multianalyte study have been developed. A SERS-active substrate is usually comprised of plasmonic metal nanostructures (e. g., Au, Ag, Cu) because the surface plasmon resonance (SPR), which amplifies the characteristic Raman signal of the analyte(s), arises from collective oscillations of free electrons in them [9,10]. The nanostructures, which facilitate an enhancement of the Raman signal from the molecules adsorbed on their surface, can be divided into two groups:

(i) liquid substrates – colloidal solutions of metallic NPs (MeNPs);
(ii) solid substrates – metallic nanostructures immobilized on a surface of the solid plates, membranes, etc.

In general, plasmonic NPs of metals in liquid solutions can be synthesized by chemical or physical methods. In the first case, a reduction of metal ions in presence of reducing and stabilizing agents and formation of MeNPs (silver and gold are the most popular, while palladium, platinum, and copper are also used in some cases) in solutions is used. Variation of the reagents composition enables the growth of the NPs of different shapes such as spheres, triangles, nanorods, nanoplates, sunflowers, nanocubes, and nanostars (Fig. 2). The diameters of spheres, edges of the cubes, and triangles can be managed in a wide range using different concentrations (or molar ratios) of components, temperature, and time of the synthesis process. The second approach is often associated with the formation of NPs by laser ablation of bulk metals and metallic ions formation on solid substrate initiated thermal or photoreduction processes [11–14]. The formation of NPs in absence of any reagent in a solution appears to be one of the main advantages of laser ablation. Ablation efficiency and characteristics of the produced NPs depend on many technological parameters, including the wavelength of laser impinging the metallic target, duration of the laser pulses (in the femto-, pico- and nanosecond regime), duration of ablation, effective liquid medium, etc. Although the diversity of NPs' shape is limited, the laser ablation showed efficiency in the photothermal reshaping of NPs [15,16].

In practical terms, solid bases for the ordered assembling of MeNPs, which provide good SERS-signal uniformity across a large area of a substrate surface, are more attractive in comparison with the colloidal solutions. During the last decade, a wide choice of the solid SERS-active substrates based on paper, polymers (polydimethylsiloxane (PDMS) [20], polystyrene – polyisoprene -polystyrene (SIS) [21]), plants [22], fibres [23], dielectrics (glass [24], porous aluminium oxide [25]) and semiconductors (Ge and Si-based templates [26]) have been described in the literature (Fig. 3). Despite the popularity of immobilization of plasmonic NPs on cheap paper and polymer substrates, they can be hardly implemented in practice due to their fast degradability. Therefore the dielectric and semiconducting templates have been also widely studied as they provide a greater contribution to the Raman signal enhancement and longer shelf-life. For example, ordered silicon nanostructures (e.g., silicon nanowires, porous silicon (PS), etc.) templates are the second most used after the paper ones.

In particular, interest in silicon nanostructures, especially in PS, has appeared due to its effective photoluminescence that is not typical for bulk silicon [27]. This had launched an era of intensive study of the silicon nanostructures, which resulted in the discovery of many unique properties of this porous material such as electroluminescence [28], biocompatibility [29], and biodegradability [30]. Considering the PS structural characteristics, this material with an extremely developed surface area can have a well-ordered Si skeleton and can be presented not only as a layer fixed on a crystalline Si wafer but also as a free PS membrane or powders of the PS particles. Currently, the PS structures are applied in different fields starting with microelectronics and finishing with biosensing and drug delivery [31]. The production of this material is relatively simple and cost-effective. Several companies providing large-scale production of different PS materials for a variety of applications have already been set up on the international market [https://www.poroussilicon.com/; www.silicon-membranes.com].

Photonic structures based on the PS have been implemented in biosensing [32]. The PS has also shown phenomenal effectiveness for *ex vivo* and *in vivo* cancer monitoring by photoluminescence spectroscopy [33]. Since 2003, different morphological types of the PS with or without additional surface chemical modification have been used as templates for the design of noble metal nanostructures that are successfully applied in the SERS-spectroscopy [34].

In the process of developing new SERS-active substrates, the researchers have pursued the goal of increasing their efficiency through optimization of their generally accepted parameters: enhancement fac-

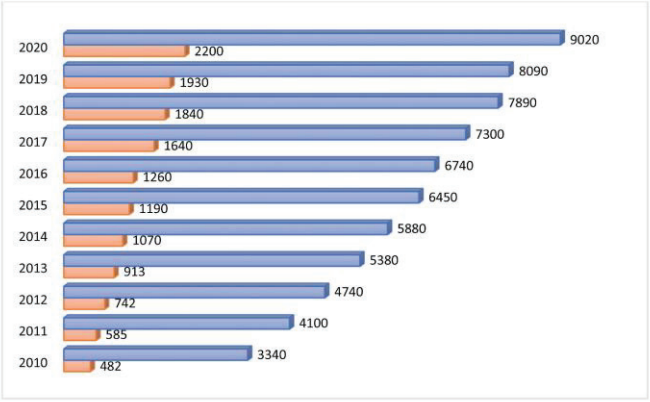

Fig. 1. The number of publications per year related to SERS-spectroscopy (blue charts) and PS-based SERS active substrates (red charts) (analysis was done by the authors using Google scholar database; the date of access – May 12, 2021). (For interpretation of the references to colour in this figure legend, the reader is referred to the Web version of this article.)

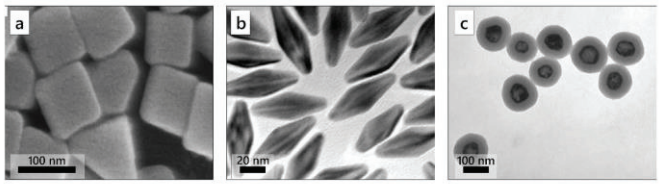

Fig. 2. Chemically synthesized MeNPs: (a) SEM image of silver nanocubes [17]; (b) TEM image of gold nanodipyramids [18]; (c) TEM image of Ag/Au nanoshells [19].

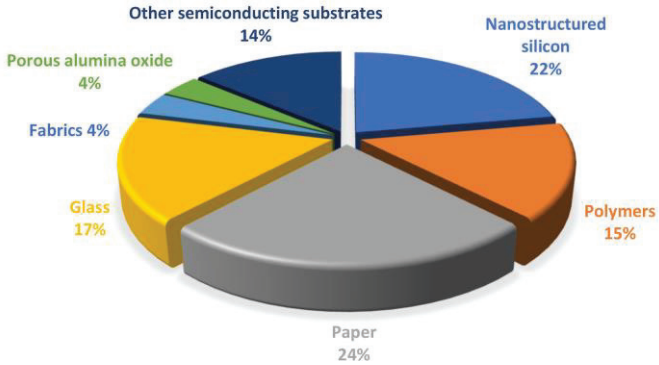

Fig. 3. Pie chart of the most useable solid templates in the SERS-spectroscopy for the last decade (analysis was done by the authors using Google scholar database; the date of access – May 12, 2021).

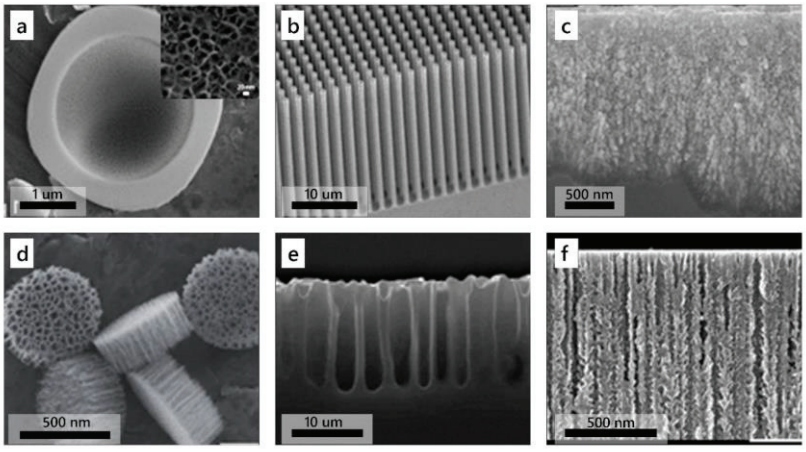

Fig. 4. SEM images of nanostructured silicon: (a) *meso*-PS silicon microparticles with 6 nm pore diameter [37]; (b) well-defined Si nanowire arrays synthesized via gas-phase etching [38]; (c) sponge-like *micro*-PS structure [39]; (d) cluster of monodisperse 600 nm × 200 nm discoidal PS particles with 30 nm pores [40]; (e) cross-sectional view of *macro*-PS with smoothed channels [41]; (f) cross-sectional view of *meso*-PS with branched channels (provided by the authors).

tor (EF) and detection limit (DL). The EF must be as high as possible and classically is calculated according to the following formula [35]:

$$EF = \frac{I_{SERS}/C_{SERS}}{I_{Raman}/C_{Raman}} \quad (1)$$

where C_{Raman} and C_{SERS} are the molecule concentrations in the Raman and SERS measurements; I_{Raman} and I_{SERS} are the normalized intensity values of the detected molecule characteristic band for the Raman and SERS measurements.

The DL can be defined as the smallest number of molecules (or their concentration) in a solution they are adsorbed from, which could be possible to detect and distinguish from baseline.

Since the SERS-active substrates based on the PS have recently shown outstanding performances (e.g. the DL can reach 10^{-18} M [36], the shelf life – up to 3 years [2]), there is a demand for a permanent renewal of the current data on its formation methods, properties, and further utilization as a template for the preparation of plasmonic metal nanostructures and a subsequent application for the SERS analysis, which are presented below.

2. Properties and fabrication of porous silicon

2.1. Properties of porous silicon

There are different kinds of nanostructured silicon layers and particles constituted by silicon nanowire ensembles, nanoporous silicon sponges, porous silicon nanoplates, quasi-ordered arrays of branched or smoothed nano- and micropore channels in silicon that have already found their application in the SERS-based biosensing (Fig. 4). However, apart from the description of the PS morphology by the shape of the pores and silicon nanocrystallites between them, this porous material is classified depending on its pore size.

It is generally accepted that porous silicon characterized by pore diameters in a range of 2–50 nm is called *meso*-PS. If the pore diameter is less than 2 nm or wider than 50 nm it is called *micro*-PS and *macro*-PS, respectively. In dependence on the type of initial silicon wafer, its conductivity (or resistivity), various morphologies, and different vertical ordered pore dimensions can be produced.

Furthermore, the crystallographic orientation of the initial silicon can contribute to the pores' growth direction. Varying a pores' morphology one can control the structural, mechanical, optical, electrical, and other properties of the PS that differ from those of the solid crystalline silicon [42]. All the PS types are characterized by high specific surface area. Apart from an extremely developed morphology, the PS is unique due to enrichment with surface states (e.g., broken Si bonds, Tamm states), which cause chemical activity of this material. The PS is also characterized by a void fraction per unit volume or, so-called porosity. The porosity directly relates to the pore volume of a porous material and its void content per unit weight (cm^3/g). This parameter plays an important role in many applications such as drug delivery (where it is necessary to set the maximum drug "payload" that can be delivered) and can vary from 1% to 97% depending on the PS formation method [43].

Due to tunable properties and surface chemical composition, provided by changing structural parameters that can be controlled by the appropriately chosen type of silicon and following fabrication process, the PS has found applications in biosensing [44], MEMS [45], microelectronics [46], catalysis [47], solar cells [48], optoelectronic and photonic devices [49], etc. *Micro*-PS is characterized by extremely high surface area (540–840 m^2/g) and has advantages over *meso*- and *macro*-PS for some applications. On the other hand, the poor mechanical strength of such a type of PS makes it difficult to use it as a template for the SERS-active substrates [2]. Consequently, the PS fabrication methods that are considered below include those resulting in the *meso*- and *macro*-PS.

2.2. Fabrication of porous silicon

Since the PS discovery over forty fabrication methods have been developed [50]. Two approaches (bottom-up and top-down) can be distinguished in the variety of nanostructures' synthesis techniques. The bottom-up ones consider the formation of the porous material by assembling the crystalline silicon clusters leaving a free space between them. This method is usually applied to produce a powder of the PS particles and can be carried out by magnetron sputtering [51], glancing angle deposition [52], laser-induced silane decomposition [53], or a combination of vapour deposition of multi-component alloy followed by dealloying [54]. The formation of well-defined porous structures via conventional bottom-up methods is complicated due to the fast oxidation and hydration of the silicon precursors. The top-down approach relies on the removal of silicon clusters from poly- or monocrystalline silicon wafers in a specific chemical environment (gaseous or liquid) that leads to the etching of voids and subsequent formation of a porous structure. This method is the most popular and can occur via chemical etching of bulk silicon with metal [55], photoelectrochemical etching [56–58], metal-assisted chemical etching [59], electrochemical etching (anodization) [60], laser-assisted etching process [61], deep reactive ion etching ultraviolet (DRIE-UV) lithography [62], etc. Thermal reduction of the porous silica particles in presence of magnesium or aluminium can be also considered as the top-down method [63].

2.2.1. Electrochemical etching (anodization)

The electrochemical etching is based on the removal of silicon clusters from the bulk silicon substrate in a solution containing hydrochloric acid (HF) as the main component. The etching of silicon atoms from the substrate occurs in presence of negatively charged fluorine ions and at applied external voltage. The silicon surface becomes more electrophilically charged, which provides an attack by F^- atoms. After four nucleophilic attacks, the generated SiF_4 reacts with two fluorides to form SiF_6^{2-}, which is a stable form in an aqueous electrolyte solution. These consecutive reactions partially remove the silicon atoms on the wafer surface, resulting in pore generation.

For the electrochemical etching, control of pore size and depth of porous layer can be provided by adjusting current density, time of anodization process, and concentration of HF acid in the electrolyte solution. The crystalline orientation, type and density of dopants, pH level, and temperature contribute to the morphology and formation speed of pores.

Chemical reactions describing the process can be presented as following [64]:

$$Si + 2HF + \lambda h^+ \rightarrow SiF_2 + 2H^+ + (2-\lambda)e^- \quad (2)$$

$$SiF_2 + 2HF \rightarrow SiF_4 + H_2 \quad (3)$$

$$SiF_4 + 2\,HF \rightarrow H_2SiF_6 \quad (4)$$

where h^+ is the hole, e^- is the electron, and λ is the number of charges exchanged.

Usually, the *meso*-PS can be created by anodization of highly-doped silicon of both n- and p-type conductivities and appear as vertical cylinders with a branched surface of silicon walls. Its porosity can reach 95% [31].

For the *macro*-PS formation, lightly doped silicon of both n- and p-type conductivities can be used, and a value of porosity barely reaches 20%. Pores of the *macro*-PS often have a cylindrical shape with a diameter of about several microns. As a rule, the surface of the *macro*-PS is usually covered with a thin layer of the *micro*-PS [65]. In the case of the n-type silicon wafer, generation of holes (h^+) is necessary, as it has a low hole density. To overcome such a limitation, the backside illumination is used as an external hole source [66]. Fig. 5 illustrates the most common ways of obtaining the different dimensions of pores fabricated by electrochemical etching depending on the most important

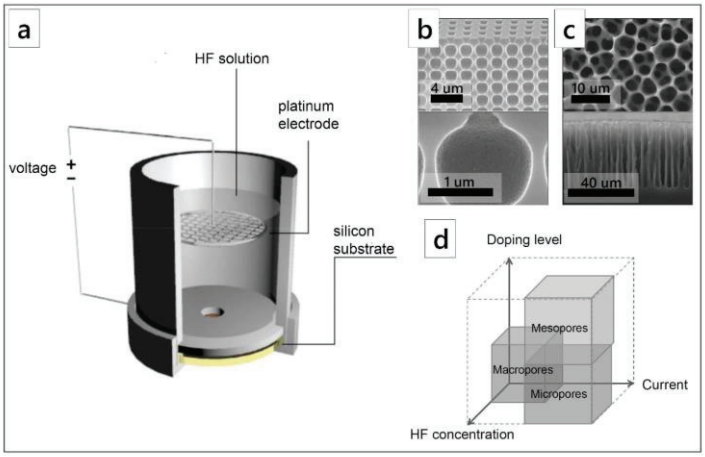

Fig. 5. (a) Electrochemical cell with Teflon mask [67]; (b) Bird's eye view of an etched sample with 2 μm interpore distance and cross section of a single modulated pore [68]; (c) top view and cross section view of the macroporous film [41]; (d) general phase diagram of pores [31].

parameters: HF concentration, doping level, and current density [31].

It should be mentioned that ethanol is typically added to the electrolyte during the anodic etching to reduce hydrogen bubble formation, improve pore wettability, and minimize strains in the resulting porous layer.

Changing the current density during the anodization process makes it possible to form a periodic structure of distinctive alternating the PS layers that could be called Bragg's reflectors [69].

2.2.2. *Metal-assisted chemical etching (MACE)*

Metal-assisted chemical etching (MACE) is the other popular formation method for the PS with porosity up to 90%, which advantage is an absence of the external voltage supply [70]. The MACE is a kind of self-catalytic silicon etching process based on local simultaneous oxidation-reduction and etching reactions providing the pores' formation (Fig. 6c–f). In this etching process, metal nanostructures are deposited on the silicon wafer surface and oxidized under the oxidizer reagent treatment. The generated holes injected from the metal into the Si substrate provide local substrate oxidation that is followed by the Si dissolution in presence of HF.

Chemical reactions of these processes can be divided into two types of reaction: (i) the cathode reaction, where metal plays a cathode role, and (ii) the anode reaction, where the Si atoms in the wafer act as an anode [71]:

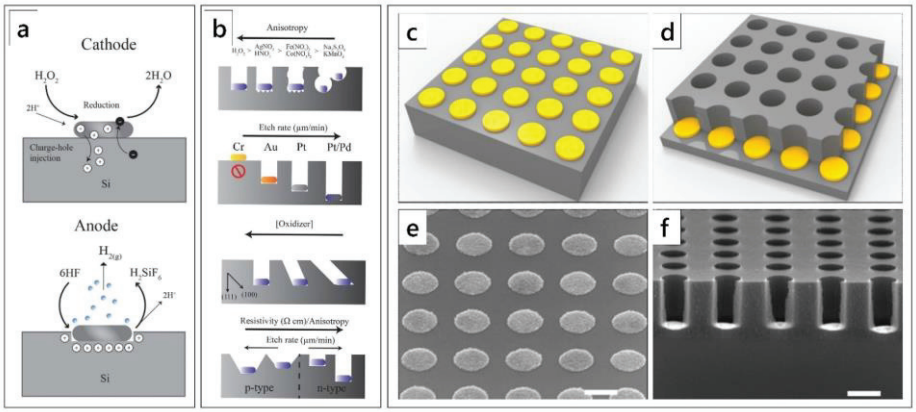

Fig. 6. (a) Schematic representing the MACE reaction at an isolated noble metal particle on flat silicon in a solution of HF/H_2O_2 and (b) schematic diagrams illustrating parameters affecting the anisotropy and etch rate in MACE [72]; (c–f) schematic showing the main steps of MACE process flow in the fabrication of Si nanoholes array: (c) array of a gold structure on flat silicon, (d) MACE to form silicon nanoholes array, (e) and (f) corresponding SEM pictures (scale bars are 500 nm) [73]. (For interpretation of the references to colour in this figure legend, the reader is referred to the Web version of this article.)

Cathode reaction $H_2O_2 + 2H^+ \rightarrow 2H_2O + 2h^+$ (5)

$2H^+ + 2e^- \rightarrow H_2\uparrow$ (6)

Anode reaction $Si + 4h^+ + 4HF \rightarrow SiF_4 + 4H^+$ (7)

$SiF_4 + 2HF \rightarrow H_2SiF_6$ (8)

Overall reaction $Si + H_2O_2 + 6HF \rightarrow {}_2H_2O + H_2SiF_6 + H_2\uparrow$ (9)

According to this reaction mechanism, H_2O_2 reacts with the metal nanostructure, and the formed holes (h^+) are injected at the metal/Si interface via diffusion into the Si valence band (Fig. 6a).

The etching rate is an important parameter in the MACE that influences not only the depth of the etched layer but also implies the morphology of the final structure. Fig. 6b presents the parameters affecting the rate and direction of the etching. For example, an increase in the etching rate induces a switch from the etching in the <100> direction to other directions, for the substrates having (100), (110), and (111) orientations. The etching rate usually depends on the [HF]/[oxidizer] ratio, where the role of the oxidizer is usually ascribed to the hydrogen peroxide (H_2O_2), nitrogen acid (HNO_3), or metal salt (Mn^+). $AgNO_3$, $HAuCl_4$, $KauCl_4$, $FeCl_3$ can also be used as metal oxidizer [70].

In the MACE process, the noble metal nanostructures such as discontinuous films, dendrites, or NPs deposited by electrochemical and electroless techniques, sputtering and evaporating methods can be used for the PS formation. Usually, for the fabrication of holes in silicon, noble metal NPs are used and an increase of their size may lead to the silicon nanowires fabrication instead of holes [74]. The electrical properties of the initial silicon wafer affect the shape of the vertical hole structure [70,75].

The MACE can promote the formation of the *meso*-PS with the smallest achieved hole diameter of 10 nm [76] and the *macro*-PS with pore size about several micrometres with the depth of holes up to 150 μm. Conducting the MACE after noble metal evaporation or combination with a particle-based patterning [77] can lead to highly ordered pores fabrication and deep, patterned, anisotropic, high-aspect-ratio silicon etching.

After the wet etching of silicon in the solutions based on the HF acid, the pore walls are coated with the dangling bonds or surface states which are passivated with hydrogen and fluorine ions. Freshly prepared PS contains SiH_x and SiF_x bonds. The air-storage leads to the PS oxidation and the formation of the Si-OH and Si-O-Si groups [78].

2.2.3. Dry etching

More accurate control of the pore size and their arrangement could be achieved by dry etching of silicon wafers. For example, DRIE - UV lithography [62] or template-assisted plasma etching [79] provide high-aspect-ratio pore formation (Fig. 7). However, the minimal resolution of porous structures is determined by the technique used. Usually, the dry etching is utilized for the *macro*-PS formation with the pore diameters about several micrometres and often these structures find application for biosensing or capacitors design because the PS morphology provides effective pore insulation. Nonetheless, photolithography can be combined with the anodization process [80] for producing the highly ordered *macro*-PS structure. In this case, the Si wafer is pre-patterned by photolithography and then etched in KOH followed by electrochemical etching. Etching in KOH is necessary to define the nucleation spots of pores.

3. Deposition of silver and gold nanostructures on porous silicon

The PS has been used as a template having developed active surface area and controllable morphology that can be easily produced and used for the formation of metallic nanostructures. Several technically simple methods of covering the PS by metals based on adsorption of NPs from colloidal solutions, wet deposition from the metal salt solution, or by using vacuum techniques have been reported [84–88].

3.1. Deposition of metallic nanoparticles from colloidal solutions

Considering the NPs deposition from colloidal solutions, two approaches that have been mostly used to fabricate NPs on top of PS surface should be mentioned: (i) in situ reduction of a metal salt solution by ultrafast laser ablation in liquids for the growth of NPs directly on a target surface [89] or (ii) self-assembling of previously synthesized NPs on a target substrate [84].

The self-assemble deposition is the most promising method because the NPs properties such as shape, size, and coating density can be easily

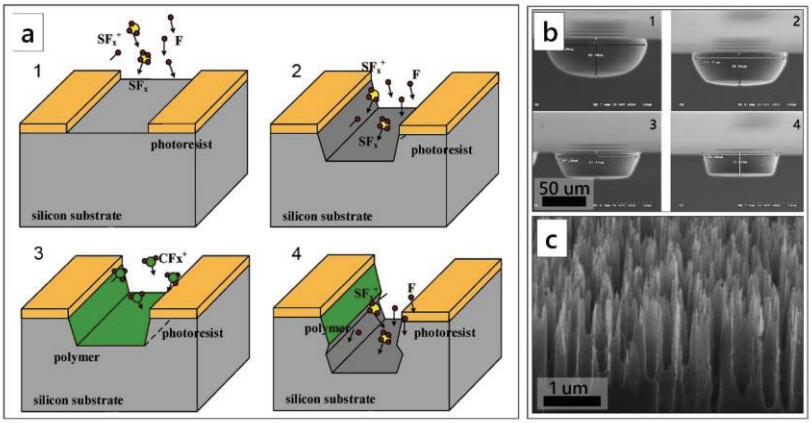

Fig. 7. (a) Schematics of the principle of the DRIE process: (1) the initial state, (2) the first etching process, (3) the upcoming passivation, (4) the second etching process [81]; (b) Profile changes with passivation contents (C_4F_8) balanced with SF_6 in DRIE silicon etching, 1 - 0% C_4F_8, 2–10% C_4F_8, 3–20% C_4F_8, 4–30% C_4F_8 [82]; (c) Black Silicon fabricated by RIE [83]. (For interpretation of the references to colour in this figure legend, the reader is referred to the Web version of this article.)

tuned during their synthesis before assembling. Usually, non-covalent chemistry takes part in the particles caption by surface, namely by electrostatic interaction between a charged surface (that can be modified by polyelectrolytes) and the charged NPs [90]. Langmuir-Schaefer, Langmuir-Blodgett, Layer-by-Layer (LbL) deposition are applied for producing a nano assembly covering the PS surface [91]. Spatially homogenously spread NPs create the number of "hot spots" that provide uniform distribution of the SERS signal from target molecules. "Hot Spot" is a tiny gap between the MeNPs where superimposed electromagnetic fields are observed.

Nonetheless, the immersion of the silanized PS substrates into the colloidal solution leads to the slow NPs aggregation onto the surface and appears as the simplest method of metal deposition [84,86,92]. Fig. 8 shows the differences in the deposition of gold NPs on *macro*-PS by LbL and substrate immersion in colloid solution techniques. The LbL technique provides a uniform monolayer of MeNPs over the PS surface unlike the immersion approach, which forms big clusters of the MeNPs.

Since naked MeNPs are unstable in organic solvents, some form of stabilizer is required to prevent their aggregation during (or after) the synthesis process. Moreover, the vibrational fingerprinting of the target molecules may be hampered by the overlapping with the Raman signals from the organic functionalized group. Additionally, the presence of functional end groups can have a profound influence on the physicochemical properties of the MeNPs and can influence the specific adsorption of the target molecules during the preparation of the substrates for the SERS analysis.

Often the freshly prepared PS is oxidized (thermally or in H_2O_2 solution), to stabilize its surface with silicon dioxide and impart a negative charge to the PS surface [93].

3.2. Spontaneous (immersion) deposition

Immersion or spontaneous deposition in presence of a reduction material surface is the most popular method used for the fabrication of metallic nanostructures on the external and internal surfaces of the PS [87,94] including the nano-PS pillar arrays [88], PS disks [95], etc. Therefore this deposition approach deserves a detailed consideration in the framework of the present review. An advantage of the immersion deposition is its simplicity. This process is self-induced and does not require any energy supply or use of vacuum technologies.

The PS possesses an active surface characterized by weak Si-H, Si-O, Si-OH bonds, and dangling Si bonds that can be easily oxidized. This feature can be used to reduce metallic ions to an atomic form on the top of and/or inside the PS from metal salt aqueous solution without specific reagents, which is required while ordinary chemical synthesis. In this case, the PS may act not only as mechanical support for the formation of the nanostructured films but also as a reducing agent. The formation process of the metallic nanostructures proceeds via a redox reaction between the substrate atoms and the metal ions in a solution. Immersion of the PS, which behaves as a source of electrons, in an aqueous solution containing metal ions (Me^+) leads to spontaneous metal cations reduction to atomic form by capturing electrons through the dangling bonds of the PS layer and to subsequent nucleation of metallic grains. The Si oxidation is the counter-reaction of Me^+ ion reduction and is usually observed during immersion plating of noble metals on the PS surface. Its redox process is given by the following equations [96]:

$$2Si_{(surf)} + H_2O \rightarrow Si\text{–}O\text{–}Si_{(surf)} + 2H^+_{(aq)} + 2e^- \quad (10)$$

$$2Si\text{–}H_{(surf)} + H_2O \rightarrow Si\text{–}O\text{–}Si_{(surf)} + 4H^+_{(aq)} + 4e^- \quad (11)$$

$$Me^+_{(aq)} + e^- \rightarrow Me_{(surf)} \quad (12)$$

In terms of immersion deposition of the specific metals, it is reasonable to review experimental results with silver, which is known as the strongest plasmonic substance. XPS spectra of the PS/Ag confirm the formation of the atomic silver by related peaks, appearing at 368.5 and 374.5 eV, which correspond to $Ag3d_{5/2}$ and $Ag3d_{5/2}$, respectively. Two peaks were also detected at 99.4 eV (assigned to Si^0) and 103.0 eV (assigned to SiO_2) justifying that the process of the silver ions' reduction is accompanied by the PS oxidation [97].

The immersion deposition process of metals on the PS has been studied by several research groups and a variety of morphological forms of metallic objects have been grown on the porous template (Fig. 9): polydispersive NPs [98], quasi-continuous layer [99]; highly branched dendrites [100]; nanovoids [101], nanothorns [102] and nanorods [60].

The immersion of the Si-based template into a metal ions solution leads to the spontaneous metal reduction that starts from the grains' nucleation across the whole surface of the porous substrate. An initial morphology of the grains negligibly depends on the PS structure, Si conductivity, or metal ion concentration in a solution and temperature. Certainly, these parameters influence the further formation of the metallic structures and have been already analyzed [2]. In this review, we would like to elucidate how the rate of the electron transfer from the volume to the surface of the PS affects the formation of metallic nanostructures.

In the considered process, the metallic structures deposited on the flat silicon surface have a morphology defined by the NPs with an almost perfect spherical shape (Fig. 9a and b). During prolonged exposure of the PS in aqueous solutions of metal ions, a continuous layer of silicon dioxide is formed on the surface, which prevents the direct interaction of ions from the solution and Si atoms, and finally leads to halting the metal reduction. In contrast to the bulk silicon, the developed PS surface is characterized by a high number of electrons on the surface and provides faster metal reduction. This ensures a higher density of the MeNPs, their wider distribution in diameter (related to the growth feature, as described earlier [103]), and the possibility of coalescence into

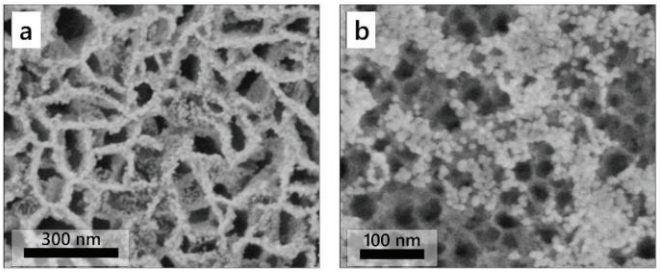

Fig. 8. SEM images of the PS decorated with gold NPs (a) via LbL nano-assembling of a positively charged polyelectrolyte and negatively charged citrate-capped gold NPs (GNPs) [91] and (b) by immersion of substrates into colloidal solution [86].

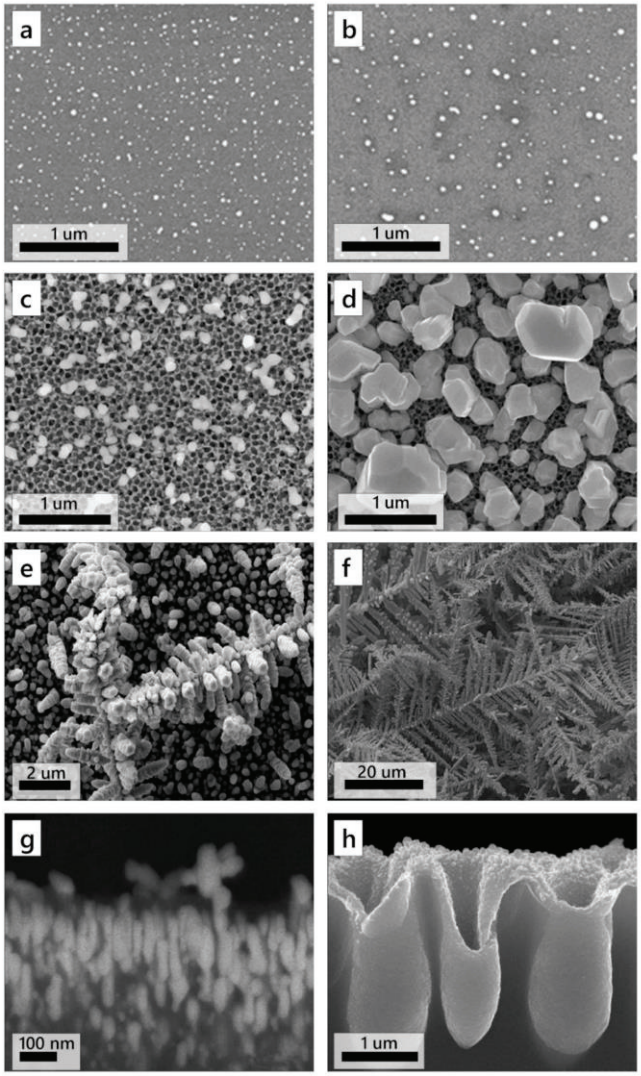

Fig. 9. SEM images of metallic structures formed by immersion deposition: (a, b) silver NPs deposited on monocrystalline silicon for 1 and 10 min, respectively (provided by authors); (c, d) silver NPs deposited on the *meso*-PS for 15 and 180 min, respectively [103]; (e, f) monocrystalline Si after silver deposition from solution with NH_4F for 5 and 60 min, respectively [100]; (g) *meso*-PS after gold deposition [60]; (h) *macro*-PS after electrochemical deposition of continuous Ni film and following immersion deposition of Ag NPs [105].

continuous film or large aggregates (Fig. 9c, d).

The presence of HF in the solution for metal deposition provides dissolution of the silicon dioxide and promotes the formation of the metallic nanostructures, producing a higher rate of electron transfer to the surface. The difference between the metal and silicon electronegativity is a driving force for the fast metal deposition on the silicon surface. The initially formed NPs grow isotropically at the beginning of the deposition process, penetrating in the silicon, displacing it, and covering all the surface. Due to the rapid growth and limited space, the particles then grow anisotropically, forming two layers of the metallic structures: NPs at the bottom of the whole metallic layer and dendrites or nanotorns in the top area (Fig. 9e and f) [100].

The rate of the metal ions reduction can be controlled by the concentration of reagents (HF and metal ions) in the solution and also by the variable PS porosity [104].

As an example, varying the depth of the PS layer one can control the rate of electrons transfer and, as the result, the metal morphology can be tuned.

Other external factors like an additional treatment by ultrasonication acceleration of the diffusion processes and enhancement of the mobility of the metal ions lead to deeper penetration of metal ions in the pores with the following reduction and metal nanorods formation (Fig. 9g) [60].

The immersion deposition technique provides metallic nanostructures with variable morphology that is characterized by specific plasmonic properties. It is known that the monodisperse MeNPs are characterized by only one transverse electromagnetic mode. But in the case of the polydispersed NPs obtained by an immersion deposition method, the sum of oscillation frequencies lays in a large region of the visible and near-infrared (NIR) ranges. This makes such nanostructures applicable for the SERS measurements under different excitation wavelengths [106]. The elongated structures (e.g., nanorods or dendrites) have two electromagnetics modes: transverse and longitudinal. The characteristic frequencies of such oscillations depend on the geometrical parameters of nanostructures and make them suitable for a wider range of excitation wavelengths, expanding in the NIR region [107].

3.3. Electrodeposition

Electrochemical deposition is a less popular but efficient method to produce metallic nanostructures on the PS surface. The method enables a decrease of the deposition time, avoiding chemical reductants or oxidants, surface activators that can cause undesired by-products, and gives an improved metal adhesion. Nonetheless, the electrochemical deposition provides the formation of the NPs and dendritic structures (Fig. 10b–f) [108–110]. The electrochemical deposition differs by its high efficiency of metal nanowires formation into pores with followed extrication (Fig. 10a) [111,112].

3.4. Vacuum methods

Vacuum deposition methods are usually applied for the formation of gold thin layers (rarely silver) on the external surface of the PS (see Fig. 11) [55]. For example, the influence of the thickness of gold nanofilms produced by the vapour deposition and depth of the PS has been studied, and the possibilities of the combination of these two parameters to achieve higher SERS-activity have been reported [59]. The effect of annealing on the morphology and SERS-activity of the metal layer have been examined. It has been shown that firstly, the annealing helps to solve the adhesion issues when metal-covered PS samples are immersed into an aqueous medium. Secondly, the annealing stimulates the formation of quasiperiodic metallic nanoisland arrays, which contribute to better SERS-intensity repeatability and enhancement. It has also been shown that the roughness of the PS surface increases the in-homogeneity of metal nanograins distribution, which occurs due to the greater amount of grain nucleation centres on the surface [113]. The in-homogeneity causes the appearance of "hot spots", improving the SERS-activity of the substrates. Nevertheless, the SERS-active substrates with metal covering, produced by vacuum methods of deposition with followed annealing, demonstrate a presentable SERS-activity for detection of organic molecules [114], albeit the metal morphology still stays limited.

4. Optimization of SERS-active substrates based on porous silicon

An improvement of the SERS-activity can be achieved by selection of the proper structural parameters of the template (e.g. periodic gratings [115–117], ring coupling metallic geometry [118]) or plasmonic NPs (e.g. combination of different metals [19,119,120] and their special arrangement [117]).

4.1. Porosity adjustment

In the case of the PS, a great increase of the SERS signal from the Rhodamine 6G (R6G) molecules adsorbed on the *meso*-PS/AgNPs substrate has been achieved through an adjustment of porosity [104]. To investigate the PS contribution to the Raman enhancement and the localized electromagnetic field distribution on the silver-coated

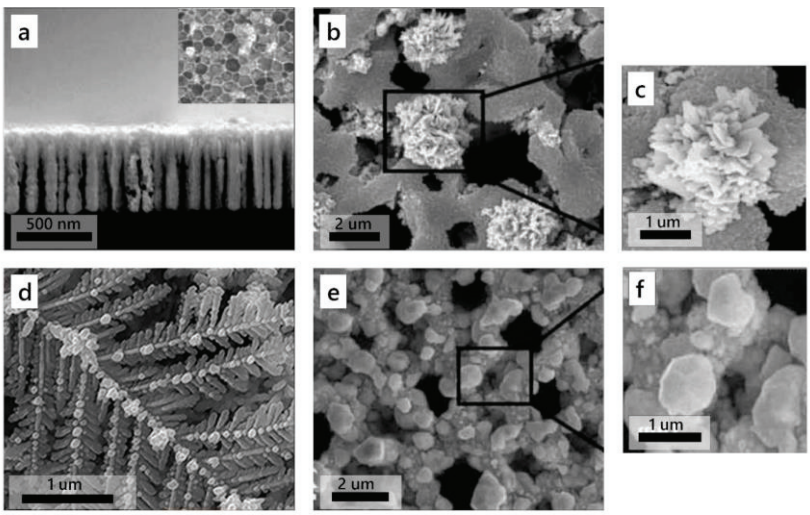

Fig. 10. SEM images of (a) Au nanorods in porous silicon matrix (inset top view) [111]; (b, c) GNPs on PS [109], (d) silver dendrites made by electroplating [110]; (e, f) silver NPs (AgNPs) on PS [109].

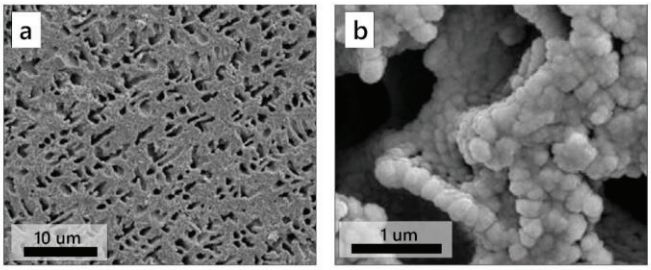

Fig. 11. (a, b) SEM image with different magnifications of 3D PS/Au architecture through sputtering Au film onto the 3D PS (sputtering time: 600 s) [55].

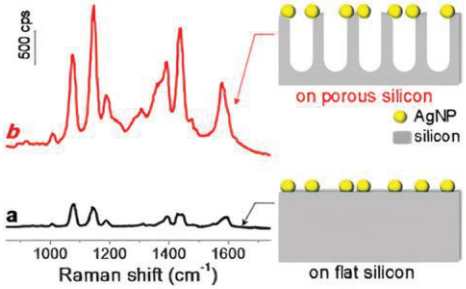

Fig. 12. Raman spectra of *p*-aminothiophenol (PATP) molecules adsorbed on the AgNPs coated (a) monocrystalline Si and (b) PS [115].

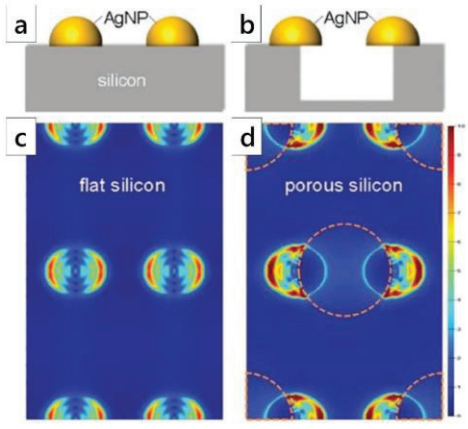

Fig. 13. Schemes (side views) and finite-difference time-domain (FDTD) simulations on the AgNPs coated (a, c) monocrystalline silicon and (b, d) PS. Dashed circles in (d) indicate the positions of silicon pores [115]. (For interpretation of the references to colour in this figure legend, the reader is referred to the Web version of this article.)

monocrystalline Si (flat) and the PS, the numerical simulation has been made (Figs. 12 and 13) [115]. It has been shown that the electromagnetic field is nearly 5 times stronger for the AgNPs/PS structure in contrast to the AgNPs/Si, but the exact mechanism of the PS influence on the Raman enhancement is still unclear.

It should be emphasized that during immersion metal deposition (which has been described above) on the PS some small NPs grow in pores and a huge specific surface area of the PS can improve the precipitation amount of R6G molecules in excitation volume, thus improving the SERS-spectroscopy sensitivity [121]. The excitation volume is the tiny focal volume, where molecules are exposed by the laser and can be calculated using Abby's equation [115]:

$$V = \pi d_{xy}^2 d_z \tag{13}$$

$$d_{xy} = \frac{\lambda}{2NA} \tag{14}$$

$$d_z = \frac{2\lambda}{NA^2} \tag{15}$$

where d_{xy} – the spot size in *xy* direction; d_z – in *z* direction, NA – the numerical aperture, λ – excitation wavelength.

However, it was reported that an improvement of the SERS activity relates to an increase in the porosity caused by the pore widening. This trend leads to rising number of the MeNPs located on the pore edges due to the better metal infiltration while its deposition. In addition, the pore widening provides a higher surface area for analyte molecule exposure, and consequently, the SERS signal intensity increases [121].

Concerning the pores' depth contribution to the SERS amplification, significant changes in the intensity of the SERS signal were not reported, except when the MeNPs are located on the bottom of the pore, forming "hot-spots". In this case, the intensity of the Raman signal stays stable when the depth is up to 450 nm. The further deepening results in a decrease of the SERS-activity that occurs as the Raman photons are trapped by the pores [115].

4.2. Modification of the porous silicon surface

Additional treatment of the PS surface is a way to manage the morphology of the further depositing plasmonic nanostructures pursuing goals of (i) new DL records, (ii) tuning position, intensity, and width of the SPR band, (iii) increasing the stability of metallic nanoobjects to oxidation, and so on. For instance, slight plasma etching of the *macro*-PS provided denser the 3D plasmonic coating of the silver dendrites grown on the plasma-treated external porous surface via immersion deposition [36]. Multiple crossing dendritic branches appeared to be a source of extremely effective 'hot spots", which facilitated a rather fast finding and identification of the single 2-nitro-5-thiobenzoic acid (TNB) molecule on their surface. In more detail, the TNB/5,

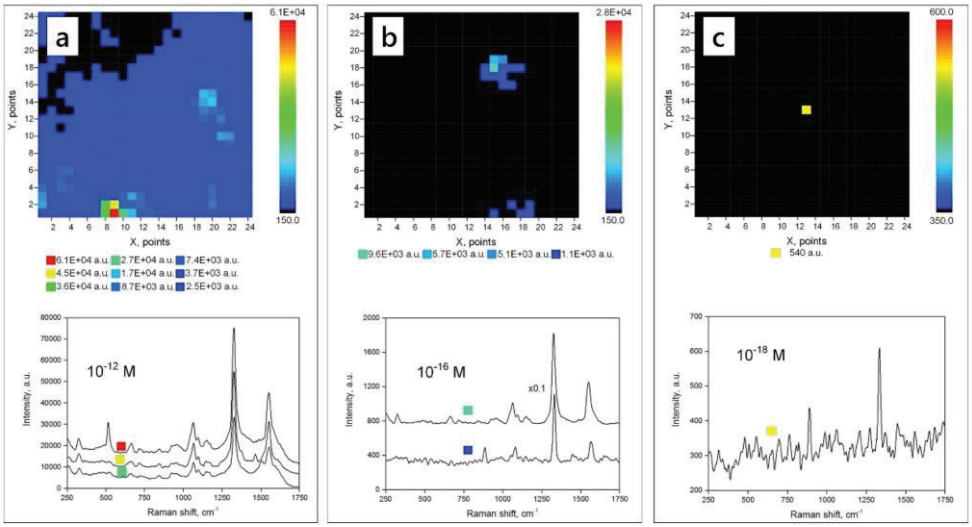

Fig. 14. SERS-imaging of the DTNB/TNB and TNB adsorbed on the silver dendrites on PS from DTNB solutions of (a) 10^{-12} M, (b) 10^{-16} M, and (c)10^{-18} M concentrations. SERS-intensity was measured at the 1335 cm^{-1} band [36].

5'-dithio-bis-(2-nitrobenzoic acid) (DTNB) molecules adsorbed on the 3D dendritic film on the plasma etched *macro*-PS from the 10^{-12} - 10^{-18} M DTNB solutions were detected and studied (Fig. 14).

4.3. Combination of porous silicon and Bragg's structures

A PS-based Bragg reflector (Bragg PS) represents a structure formed by multiple PS layers with different porosity, which correspond to different refractive indices [122,123]. Such layers act as a high-quality reflector with a characteristic photonic bandgap. The bandgap range, intensity, and position of the maximum reflectance on the wavelength scale can be set by changing the thickness and porosity of the layers. Often, the Bragg PS is fabricated by the electrochemical anodization and consists of 12–15 PS layers, having porosity, which is approximately two times different.

The first report about a combination of the Bragg PS and plasmonic metal was made in 2015 year [86]. However, the authors studied not the SERS-response but the fluorescence enhancement of R6G induced by gold NPs (GNPs) deposited on the Bragg PS. The mechanism of the enhancement by the Bragg PS was explained as follows. The excitation light at a wavelength of 500 nm was located outside the bandgap area of the reflection spectrum of Bragg PS (in that work Bragg's reflector with the centre of the bandgap 550 nm was used), where the reflectivity is lower, and most of the excitation light can be transmitted inside the multilayer of the PS and stimulate R6G fluorescence within the Bragg PS. The upward fluorescence was transmitted out of the Bragg PS, the downward fluorescence reflected from its surface. Thus, the fluorescence for the Bragg PS was stronger than for the single PS layer. The fluorescence intensity from the R6G molecules on the PS/GNPs was about two times higher compared to the PS, while the Bragg PS/GNPs also induced a stronger fluorescence response from the organic dye than the single-layered PS/GNPs. Later works have reported the combination of Bragg PS with noble NPs for the SERS application [91,124–128].

SERS-active substrates based on the Bragg PS was found to produce 5–8 times higher intensity of the Raman signal compared with that on the single-layer PS or monocrystalline Si substrate [125], leading to an

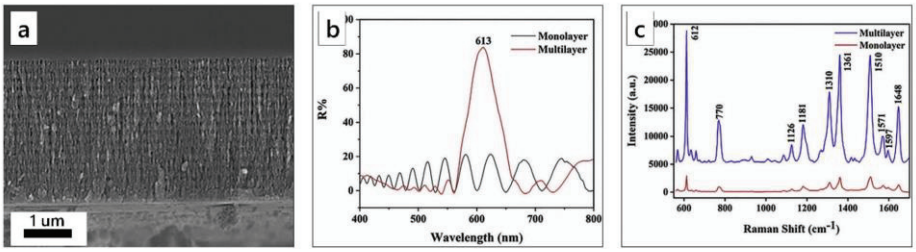

Fig. 15. (a) Cross-section image of Bragg PS; (b) reflectance spectra of the PS and Bragg PS; (c) the corresponding SERS spectra of R6G with a concentration of 10^{-5} M registered using PS and Bragg PS covered with AgNPS [129].

R6G detection limit from 1.0×10^{-13} M to 10^{-15} M. Related images of the Bragg PS and Ag NPs/Bragg PS structures along with their optical characteristics are shown in Fig. 15.

4.4. Diffraction gratings

Periodic arrays of gold or silver nanostructures can excite propagating surface plasmon polariton (PSPP) that have already shown their efficiency for SERS-spectroscopy [130–134].

When the localized surface plasmon polariton is considered as a non-propagating, characteristic excitation of electronic and electromagnetic field coupling, which generates a strong electromagnetic field enhancement only in the near-surface area of the nanostructures, PSPP is defined as polarized wave propagation along the metal grating surface, which enhances the electromagnetic field in a certain range area near the metal surface.

Changwu Lv. et al. [135] showed the potential of metalized periodic structure based on PS diffraction grating (DG) for the SERS-spectroscopy. The porosified DG covered with silver NPs demonstrated the amplification of the already strong SPR of the MeNPs adsorbed on the PS. The SERS-spectrum of the R6G molecules adsorbed on the PS/DG/AgNPs was two times more intensive than that collected with the use of the PS/AgNPs. The minimal concentration of the detected R6G molecules was 10^{-12} M under the 785 nm laser excitation.

4.5. Protection with graphene

Plasmonic structures characterized by a giant increase of electromagnetic field in the near-field, produce local heating that usually influences the molecular structure of the detected probe molecule. An important task during designing such high-sensitive SERS-substrates for biosensing application is preventing the destruction of the molecules during the SERS measurements. Recent papers reported covering the PS/Me nanostructure with graphene leads to decreasing in SERS-signal degradation for the adsorbed molecules [94,136].

Our research group was able to protect lactoferrin molecules adsorbed on the meso-PS/Ag SERS-active substrates from thermal denaturation by using graphene-containing coating shown in Fig. 16 [136]. The temperature of the lactoferrin denaturation is about 350 K. At this temperature the studied molecule starts to change its structure and amorphous carbon bonds appear on the SERS-spectra of the measured sample. According to provided simulations of substrate heating with the 473 nm laser, the graphene protective layer leads to a temperature decrease in the laser spot down to 340 K. The simulation data are in good agreement with the experimental results. The analyte molecules on the silvered PS protected with 1–8 graphene layers were detected after adsorption from the 10^{-18} M solution.

4.6. Substrate functionalization

Special attention should be paid to the molecules, which contain disulfide bonds R-S-S-R or free thiols groups R-S-H. Such molecules are widely used as functionalized agents for biosensing by SERS-spectroscopy. When metallic structures are immersed in the molecules' solution, they form a monolayer by attaching to the metallic surface through the formation of R-S-Me bonds [137–139]. The functionalization of a metallic surface by chosen molecular agent makes the SERS-active substrates specific to picking target molecules. This provides the capability to conduct the selective diagnostic of multicomponent substances at various concentrations [140]. For example, the PS disks covered with MeNPs showed the possibility for selective detection of glutathione in nanomolar concentration and their potential for *in vivo* biosensing application [95].

To improve the reproducibility and sensitivity of SERS-response Wand et al. proposed a new technology of functionalization to increase the selectivity of the SERS-active substrates [141]. They used magnetic ion liquid ($[C_6mim]FeCl_4$) as a reporter agent to modify the PS-based SERS-active substrate. The prepared substrates improved the loading capacity by taking advantage of the multiple ion adsorption sites, aggregation capacity, and specific adsorption capacity of ion liquid, to increase the number and density of the "hot spots".

To distinguish and illustrate the benefits of the metal-coated PS among the variety of the existing SERS-active substrates we summarized and systemized its most important parameters such as detection limit (DL), standard deviation (SD) of SERS signal intensity, and shelf life in dependence on the PS type and metal deposition technique (see Table 1).

It was reported that the lowest concentration 10^{-18} M of R6G can be achieved using colloidal nanoparticles [151] as well. But to reach this goal a special combination of metal and a dielectric material is needed, which provides a higher increase of electromagnetic field in "hot-spots". Such hybrid structure is so-called core-shell nanoparticles and their synthesis usually takes from several hours to several days [152,153]. In this case, PS material is considered to be a more attractive base for SERS-active substrates fabrication as it is characterized by simple, fast preparation (described in the *2* and *3* sections), high sensitivity, and good reproducibility (Table 1). In general colloidal solutions are characterized by low reproducibility of SERS spectra. Recently, the highest reproducibility was achieved by the arrangement of core-shells nanoparticles monolayer on the solid substrates [154]. Such structure demonstrated an SD of about 3%. However, to get this value of SD the size distribution of the used core-shell nanoparticles must be higher than 2%.

5. Application and commercialization of SERS-active substrates based on porous silicon

In recent years, SERS-spectroscopy has become widely used for the

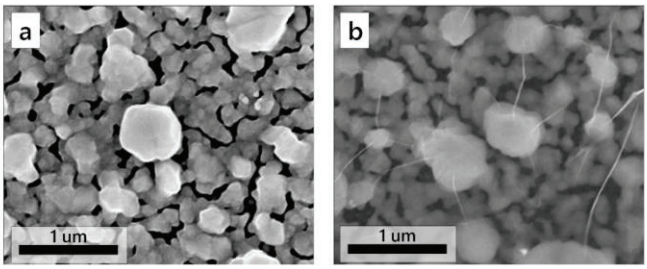

Fig. 16. SEM top-view images of the (a) silvered PS and (b) silvered PS covered with graphene [136].

Table 1
Structural parameters and characteristics of the PS-based SERS-active substrates.

Morphology of SERS-active substrate		Metal deposition technique	Detected Analytes	DL	SD	Shelf life	References
Meso-PS	AgNPs	Immersion	CuTMPyP4	10^{-11} M			[103]
			R6G	10^{-15} M	5%		[142]
			Phospholipid	10^{-12}M			
	AgNPs	Immersion	R6G	10^{-14} M	2–50%[a]		[106]
			Cyanine dye	10^{-14} M			
			p-mercapto-benzoic acid (*p*-MBA)	10^{-9} M	9%		[143]
			Micro RNA	10^{-9} M			[144]
	AgNPs/PS disk	Immersion	Glutathione Cysteine Homocysteine	10^{-9} M			[95]
	Ag dendrites	Immersion	DTNB/TNB	10^{-18} M			[36]
	AgNPS protected with graphene	Immersion	Lactoferrin	10^{-18} M	7%	Up to two years	[136]
	AgNPs/Bragg PS	Immersion	R6G Crystal violet	10^{-8} M			[127]
	AgNPs/Bragg PS	Immersion	R6G	10^{-15} M	9%		[129]
	AgNPS/Bragg PS	Immersion	R6G	10^{-13} M			[125]
	AgNPs/Bragg PS	Immersion	R6G Picric acid	10^{-10} M 10^{-8} M	8%		[126]
	AgNPs/DG	Immersion	R6G	10^{-12} M			[135]
	Ag dendrites	Electro-chemical	R6G	10^{-12} M			[110]
	Ag Layer	Sputtering	Cyclosarin 1,3,5-Trinitro-perhydro-1,3,5-triazine (RDX) Amphetamine Picric acid Ochratoxin A	10^{-9} M 10^{-12} M 10^{-12} M 10^{-13} M 10^{-6} M	 17–20%[a]		[145] [146]
	GNPs	Immersion	Peniciline	10^{-9} M	4.5%		[147]
	GNPs	Immersion	1,2-benzene-dithiol (BDT)	10^{-5} M	5%		[59]
	PdNPs	Immersion	Imidacloprid pesticide	10^{-9} M			[148]
	GNPs	Electro-chemical	BSA	10^{-8} M			[149]
	GNPs	Electro-chemical	R6G	10^{-6} M			[109]
	Gold nanorods	Electro-chemical	4-4′ bypiridine (BPY)	10^{-4} M			[111]
	GNPs	Sputtering	R6G	10^{-13} M	6%		[55]
Macro-PS	AgNPs	Immersion	CuTMpyP4	10^{-10} M		8 month	[94]
	AgNPs/Ni	Immersion	R6G	10^{-11} M			[105]
	AgNPs/Si Nanopillars	Immersion	R6G	10^{-15} M			[88]
	GNPs	Immersion	Cyanine	10^{-10} M			[150]
	Gold nano-thorns	Electro-chemical	Crystal violet	10^{-12} M			[102]

[a] The standard deviation of the Raman signal intensity depends on the concentration of the detected analyte.

detection and structural characterization of molecules in different liquids and gases. Ultra-low detection of small organic molecules by SERS-spectroscopy has been easily achieved using AgNPs/PS or GNPs/PS substrates [106,124–126,135,155,156]. Identification and analysis of organic objects such as tetrapyrrolic molecules [157], peptides [138, 139], proteins [108,114,149], enzymes [158], nucleic acids [106,159], antibiotics [58,147], DNA [160], microRNA [161], serum blood [114, 162,163], physiological fluids [164], bacteria [165], cells [166], antioxidant [95] and aflatoxins [108] has been already reported. It should be noticed that single-molecule detection is not always required for the analysis of multicomponent substances. In some cases, the detection of one component at the concentration of the maximum residue limit (MRL) is enough, e.g. for food quality control. In the recent reports [58, 147], a great potential of antibiotics detection in a food has been shown. Wali et al. detected penicillin G and ampicillin residue in a milk using GNPs/PS hybrid structure. The detection limit of 10^{-9} M (equal to 0.33 μg/kg and 0.35 μg/kg, respectively) was reached for these components, which is much lower than the MRL of penicillin in the milk (4 μg/kg) established by the European Union.

Also, the detection of a multicomponent analyte such as serum blood was reported [163]. Yue et al. demonstrated perspectives of the rapid and non-destructive diagnosis of echinococcosis by SERS-spectroscopy. In their study, the serum samples were clearly distinguished from the health human's controls samples and patient's samples via analysis of assignments of the bands in the measured serum blood SERS-spectra. It was shown that such biomolecular difference occurs because of metabolic changes in the patient' body. The authors provided a systematic analysis of three groups of the serum SERS spectra detected with the Ag/PS substrates.

Besides, the SERS-active substrates Bragg PS/Ag efficiency for early breast cancer detection patient serum was reported [162]. The SERS response of the serum for 30 normal people and 30 early breast cancer patients was measured and then statistically analyzed. The analysis results showed that the diagnostic sensitivity is 93.3%, the specificity is 96.7%, and the total accuracy rate is 95%.

In addition to the fact that the solid PS-based substrates demonstrate high sensitivity, several works have studied their time stability and reproducibility (Fig. 17) [2,97,165,167]. Usually, the standard deviation of SERS-signal intensity of about 30–40 recorded spectra using PS/MeNPs substrate does not exceed 10% [56,124]. This makes these substrates to be widely used for high-precision analysis in biosensing.

Chiral molecule structure studies are getting popular nowadays [168,169]. Despite the all PS-based substrates' advantages and wide applications in SERS-spectroscopy, there aren't any reports about its use for chiral molecule structure determination by Raman spectroscopy to the present moment.

The application examples of the substrates based on the PS considered above have been done with the SERS-active materials prepared at the research laboratory conditions. However, nowadays commercial SERS-active substrates formed on the PS templates are available [https://www.silmeco.com/, https://science.bsuir.by/en/microelectronics-and-nanotechnology/sers-active-substrates-for-increasing-sensitivity-of-

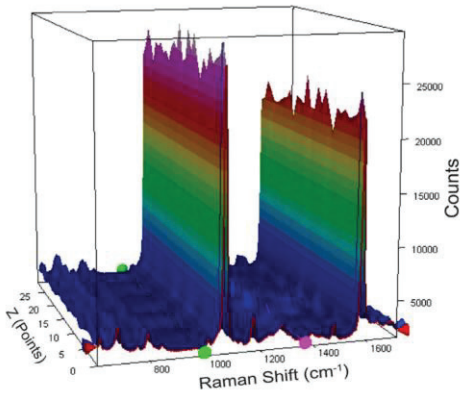

Fig. 17. The representative two-dimensional SERS spectra of *p*-MBA (10^{-6} M) have been recorded from 40 different spots on the SERS surface using mapping mode. The spectra have been collected over a distance of 1 mm with 10 μm steps (40 spectra are shown) [164].

raman-spectroscopy]. For instance, Silmeco substrates [https://www.silmeco.com/] represent silicon nanowires covered by silver or gold coating, which showed their efficiency in forensic detection of Cyclosarin, RDX, Amphetamine, and Picric acid in sample volume down to femtograms [145]. They also were utilized in food quality control for detection of mycotoxin [146] and therapeutic drug monitoring for anticancer drug imatinib [170]. The other commercial product (BelSERS substrates [https://science.bsuir.by/en/microelectronics-and-nanotechnology/sers-active-substrates-for-increasing-sensitivity-of-raman-spectroscopy] that is based on the silvered *meso*- or *macro*-PS have demonstrated its applicability for detection of peptides [143] and proteins [134], meldonium [171], DNA [148], phospholipids [142], fullerenes [172] and other organic molecules [36,103,105].

6. Conclusions

The data collected for the present review has demonstrated undoubted advantages of the PS template to be a proper host material for fabrication of the ultrasensitive, reliable, user-friendly and cost-effective SERS-active substrates that have confidently proved themselves as highly efficient tools for accurate molecular analysis. The PS layers or particles (e.g. microdisks) play a role of not only a mechanical support, which fabrication is affordable due to compatibility with the main steps of the Si technology, but of an agent precisely determinating the shape and size of plasmonic nanostructures which electrodynamic properties can be easily tuned to meet specific requirements of the SERS-analysis. The best DL for the small [38] and macromolecules [134] of the organic analytes achieved with the SERS-active substrates based on the PS templates is equal to attomolar concentration which is an absolute record for both solid and liquid SERS-active substrates, i.e. this is the smallest amount of the organic molecules at which they can be currently detected. The spot-to-spot and sample-to-sample reproducibility of the SERS intensity and shelf life provided by the PS-hosted substrates meet the strictest requirements for the commercial SERS-active materials.

Considering the discovery that the PS structure can contribute to the Raman signal enhancement itself we expect future increase in the number of the fundamental studies of this effect.

The other aspect of the evolution of the metalized PS substrates can potentially be an adaptation of Raman spectroscopy laboratories to quick fabrication of their own SERS-active materials. In practical terms this can be easily achieved through purchasing the PS chips and deposition of the metallic nanostructures immediately before the SERS-analysis. Table 1 has shown that the most SERS-active substrates are formed by affordable immersion deposition of metals on PS, which can be performed on site of the SERS-analysis.

However, some issues should be taken into account while analyzing the SERS-active substrates formed on the PS. Although the PS possesses the biocompatibility property, which is very valuable to provide biosensing in the different application fields, this porous material may easily degrade in a solution with high pH (>8), i.e. detection of molecules soluble in only alkaline solutions is hardly achievable with the PS-based substrates. It may be possible to obtain higher resistance to dissolution of the PS by specific biofunctionalization of its surface [30]. The next open question is the EF calculation and the number of detecting molecules. As it was proved in Refs. [36,137] the molecules tend to coalesce in the clusters on the SERS-active surface, so this is hard to confidently claim about their certain amount in the laser spot even if one can estimate the specific surface area of the plasmonic coating on/in the PS. In addition, there are not any reported techniques of the separation of the products from PS-based substrates after measurements and their reuse without degradation and losing plasmonic properties. This opens a new area of the study to make the SERS-spectroscopy more environmentally friendly decreasing the number of fabricated substrates.

Enclosing SERS-spectroscopy with the PS-based plasmonic nanomaterials can be potentially considered as an additional analytical technique for noninvasive cancer screening, diagnosis of the human immunodeficiency virus (HIV) or Alzheimer's disease, and there is a trail to extend its application area to food and drug quality control, forensics, security, monitoring sanitary conditions of the personal environment and public places and other spheres of human life. Moreover, the compatibility of porous silicon with the silicon technologies opens new prospects in the elaboration of novel sophisticated devices, like lab on chip enabling different types of diagnostics to be quicker and more specific.

CRediT authorship contribution statement

Nadzeya Khinevich: Formal analysis, Writing – original draft, Writing – review & editing. **Hanna Bandarenka:** Conceptualization, Supervision, Writing – original draft, Writing – review & editing. **Siarhei Zavatski:** Writing – original draft, Writing – review & editing. **Kseniya Girel:** Conceptualization, Writing – review & editing. **Asta Tamulevičienė:** Conceptualization, Writing – review & editing. **Tomas Tamulevičius:** Conceptualization, Writing – review & editing. **Sigitas Tamulevičius:** Conceptualization, Supervision, Writing – review & editing.

Declaration of competing interest

The authors declare that they have no known competing financial interests or personal relationships that could have appeared to influence the work reported in this paper.

Acknowledgments

This work was supported by funding from the Research Council of Lithuania (LMTLT) (Agreement No.P-LZ-21-1) and Russian Science Foundation (Project # 21-19-00761).

References

[1] H.V. Bandarenka, SERS analysis with porous silicon, in: Handbook of Porous Silicon, second ed., vols. 2–2, 2018, pp. 1315–1335, https://doi.org/10.1007/978-3-319-71381-6_107.

[2] H.V. Bandarenka, K.V. Girel, S.A. Zavatski, A. Panarin, S.N. Terekhov, Progress in the development of SERS-active substrates based on metal-coated porous silicon, Materials 11 (2018) 1–20, https://doi.org/10.3390/ma11050852.

[3] C. Muehlethaler, M. Leona, J.R. Lombardi, Towards a validation of surface-enhanced Raman scattering (SERS) for use in forensic science: repeatability and reproducibility experiments, Forensic Sci. Int. 268 (2016) 1–13, https://doi.org/10.1016/j.forsciint.2016.09.005.

[4] M. Kahraman, E.R. Mullen, A. Korkmaz, S. Wachsmann-Hogiu, Fundamentals and applications of SERS-based bioanalytical sensing, Nanophotonics 6 (2017) 831–852, https://doi.org/10.1515/nanoph-2016-0174.

[5] L.E. Jamieson, S.M. Asiala, K. Gracie, K. Faulds, D. Graham, Bioanalytical measurements enabled by Surface-Enhanced Raman Scattering (SERS) probes, Annu. Rev. Anal. Chem. 10 (2017) 415–437, https://doi.org/10.1146/annurev-anchem-071015-041557.

[6] Y. Jiang, D.W. Sun, H. Pu, Q. Wei, Surface enhanced Raman spectroscopy (SERS): a novel reliable technique for rapid detection of common harmful chemical residues, Trends Food Sci. Technol. 75 (2018) 10–22, https://doi.org/10.1016/j.tifs.2018.02.020.

[7] M.T. Alula, Z.T. Mengesha, E. Mwenesongole, Advances in surface-enhanced Raman spectroscopy for analysis of pharmaceuticals: a review, Vib. Spectrosc. 98 (2018) 50–63, https://doi.org/10.1016/j.vibspec.2018.06.013.

[8] I.Y. Stetciura, A.V. Markin, D.N. Bratashov, G.B. Sukhorukov, D.A. Gorin, Nanoencapsulated and microencapsulated SERS platforms for biomedical analysis, Curr. Opin. Pharmacol. 18 (2014) 149–158, https://doi.org/10.1016/j.coph.2014.10.002.

[9] J.H. Granger, M.C. Granger, M.A. Firpo, S.J. Mulvihill, M.D. Porter, Toward development of a surface-enhanced Raman scattering (SERS)-based cancer diagnostic immunoassay panel, Analyst 138 (2013) 410–416, https://doi.org/10.1039/c2an36128k.

[10] A. Shiohara, Y. Wang, L.M. Liz-Marzán, Recent approaches toward creation of hot spots for SERS detection, J. Photochem. Photobiol. C Photochem. Rev. 21 (2014) 2–25, https://doi.org/10.1016/j.jphotochemrev.2014.09.001.

[11] F. Mafuné, J.Y. Kohno, Y. Takeda, T. Kondow, H. Sawabe, Formation of gold nanoparticles by laser ablation in aqueous solution of surfactant, J. Phys. Chem. B 105 (2001) 5114–5120, https://doi.org/10.1021/jp0037091.

[12] M. Kawasaki, N. Nishimura, 1064-nm laser fragmentation of thin Au and Ag flakes in acetone for highly productive pathway to stable metal nanoparticles, Appl. Surf. Sci. 253 (2006) 2208–2216, https://doi.org/10.1016/j.apsusc.2006.04.024.

[13] S.I. Dolgaev, A.V. Simakin, V.V. Voronov, G.A. Shafeev, F. Bozon-Verduraz, Nanoparticles produced by laser ablation of solids in liquid environment, Appl. Surf. Sci. 186 (2002) 546–551, https://doi.org/10.1016/S0169-4332(01)00634-1.

[14] P. Ran, L. Jiang, X. Li, B. Li, P. Zuo, Y. Lu, Femtosecond photon-mediated plasma enhances photosynthesis of plasmonic nanostructures and their SERS applications, Small 15 (2019), https://doi.org/10.1002/smll.201804899.

[15] S. Link, C. Burda, B. Nikoobakht, M.A. El-Sayed, Laser-induced shape changes of colloidal gold nanorods using femtosecond and nanosecond laser pulses, J. Phys. Chem. B 104 (2000) 6152–6163, https://doi.org/10.1021/jp000679t.

[16] C. Li, J. Hu, L. Jiang, C. Xu, X. Li, Y. Gao, L. Qu, Shaped femtosecond laser induced photoreduction for highly controllable Au nanoparticles based on localized field enhancement and their SERS applications, Nanophotonics 9 (2020) 691–702, https://doi.org/10.1515/nanoph-2019-0460.

[17] S. Ben-Jaber, W.J. Peveler, R. Quesada-Cabrera, C.W.O. Sol, I. Papakonstantinou, I.P. Parkin, Sensitive and specific detection of explosives in solution and vapour by surface-enhanced Raman spectroscopy on silver nanocubes, Nanoscale 9 (2017) 16459–16466, https://doi.org/10.1039/c7nr05057g.

[18] S. Lin, X. Lin, S. Han, L. He, H. Zhao, J. Zhang, W. Hasi, L. Wang, Width and length dependent SERS performance of core-shell Au@Ag nanorod self-assembled monolayers, J. Alloys Compd. 805 (2019) 318–326, https://doi.org/10.1016/j.jallcom.2019.07.060.

[19] B. Küstner, M. Gellner, M. Schütz, F. Schöppler, A. Marx, P. Ströbel, P. Adam, C. Schmuck, S. Schlücker, SERS labels for red laser excitation: silica-encapsulated SAMs on tunable gold/silver nanoshells, Angew. Chem. Int. Ed. 48 (2009) 1950–1953, https://doi.org/10.1002/anie.200804518.

[20] Y. Ma, H. Liu, Y. Chen, C. Gu, G. Wei, T. Jiang, Improved lateral flow strip based on hydrophilic–hydrophobic SERS substrate for ultra−sensitive and quantitative immunoassay, Appl. Surf. Sci. 529 (2020) 2–7, https://doi.org/10.1016/j.apsusc.2020.147121.

[21] N. Yang, T.T. You, Y.K. Gao, C.M. Zhang, P.G. Yin, Fabrication of a flexible gold nanorod polymer metafilm via a phase transfer method as a SERS substrate for detecting food contaminants, J. Agric. Food Chem. 66 (2018) 6889–6896, https://doi.org/10.1021/acs.jafc.8b01702.

[22] V. Sharma, S. Kumar, A. Jaiswal, V. Krishnan, Gold deposited plant leaves for SERS: role of surface morphology, wettability and deposition technique in determining the enhancement factor and sensitivity of detection, ChemistrySelect 2 (2017) 165–174, https://doi.org/10.1002/slct.201601451.

[23] W. Tang, D.B. Chase, J.F. Rabolt, Immobilization of gold nanorods onto electrospun polycaprolactone fibers via polyelectrolyte decoration - a 3D SERS substrate, Anal. Chem. 85 (2013) 10702–10709, https://doi.org/10.1021/ac400241z.

[24] W. Ye, D. Wang, H. Zhang, F. Zhou, W. Liu, Electrochemical growth of flowerlike gold nanoparticles on polydopamine modified ITO glass for SERS application, Electrochim. Acta 55 (2010) 2004–2009, https://doi.org/10.1016/j.electacta.2009.11.022.

[25] M. Celik, S. Altuntas, F. Buyukserin, Fabrication of nanocrater-decorated anodic aluminum oxide membranes as substrates for reproducibly enhanced SERS signals, Sensor. Actuator. B Chem. 255 (2018) 2871–2877, https://doi.org/10.1016/j.snb.2017.09.105.

[26] T. Wang, Z. Zhang, F. Liao, Q. Cai, Y. Li, S.-T. Lee, M. Shao, The effect of dielectric constants on noble metal/semiconductor SERS enhancement: FDTD simulation and experiment validation of Ag/Ge and Ag/Si substrates, Sci. Rep. 4 (2015) 4052, https://doi.org/10.1038/srep04052.

[27] A.G. Cullis, L.T. Canham, Visible light emission due to quantum size effects in highly porous crystalline silicon, Nature 353 (1991) 335–338, https://doi.org/10.1038/353335a0.

[28] A.G. Cullis, L.T. Canham, P.D.J. Calcott, The structural and luminescence properties of porous silicon, J. Appl. Phys. 82 (1997) 909–965, https://doi.org/10.1063/1.366536.

[29] S.P. Low, N.H. Voelcker, Biocompatibility of porous silicon, in: Handbook of Porous Silicon, Springer International Publishing, Cham, 2018, pp. 533–545, https://doi.org/10.1007/978-3-319-71381-6_38.

[30] Q. Shabir, Biodegradability of porous silicon, in: Handbook of Porous Silicon, Springer International Publishing, Cham, 2014, pp. 1–7, https://doi.org/10.1007/978-3-319-04508-5_39-1.

[31] G. Korotcenkov, Porous Silicon: from Formation to Application: Formation and Properties, Volume One, CRC Press, 2016, https://doi.org/10.1201/b19342.

[32] Y. Zhao, G.A. Rodriguez, Y.M. Graham, T. Cao, G. Gaur, S.M. Weiss, Resonant photonic structures in porous silicon for biosensing, in: Frontiers in Biological Detection: from Nanosensors to Systems IX, vol. 10081, 2017, p. 100810D, https://doi.org/10.1117/12.2256893.

[33] M. Terracciano, I. Rea, N. Borbone, R. Moretta, G. Oliviero, G. Piccialli, L. De Stefano, Porous silicon-based aptasensors: the next generation of label-free devices for health monitoring, Molecules 24 (2019), https://doi.org/10.3390/molecules24122216.

[34] S. Chan, A.A. Berlin, M. Yamakawa, Metal Coated Nanocrystalline Silicon as an Active Surface Enhanced Raman Spectroscopy (SERS) Substrate, US vol. 6, 2006, p. 989, 897 B2.

[35] W.B. Cai, B. Ren, X.Q. Li, C.X. She, F.M. Liu, X.W. Cai, Z.Q. Tian, Investigation of surface-enhanced Raman scattering from platinum electrodes using a confocal Raman microscope: dependence of surface roughening pretreatment, Surf. Sci. 406 (1998) 9–22, https://doi.org/10.1016/S0039-6028(97)01030-3.

[36] H.V. Bandarenka, N.V. Khinevich, A.A. Burko, S.V. Redko, S.A. Zavatski, U. A. Shapel, K.Z. Mamatkulov, M.Y. Vorobyeva, G.M. Arzumanyan, 3D silver dendrites for single-molecule imaging by surface-enhanced Raman spectroscopy, ChemNanoMat (2020) 1–10, https://doi.org/10.1002/cnma.202000521.

[37] D. Fan, E. De Rosa, M.B. Murphy, Y. Peng, C.A. Smid, C. Chiappini, X. Liu, P. Simmons, B.K. Weiner, M. Ferrari, E. Tasciotti, Mesoporous silicon-PLGA composite microspheres for the double controlled release of biomolecules for orthopedic tissue engineering, Adv. Funct. Mater. 22 (2012) 282–293, https://doi.org/10.1002/adfm.201100403.

[38] N.P. Dasgupta, C. Liu, S. Andrews, F.B. Prinz, P. Yang, Atomic layer deposition of platinum catalysts on nanowire surfaces for photoelectrochemical water reduction, J. Am. Chem. Soc. 135 (2013) 12932–12935, https://doi.org/10.1021/ja405680p.

[39] R. Koda, K. Fukami, T. Sakka, Y.H. Ogata, Electrodeposition of platinum and silver into chemically modified microporous silicon electrodes, Nanoscale Res. Lett. 7 (2012) 1, https://doi.org/10.1186/1556-276X-7-330.

[40] B. Godin, C. Chiappini, S. Srinivasan, J.F. Alexander, K. Yokoi, M. Ferrari, P. Decuzzi, X. Liu, Discoidal porous silicon particles: fabrication and biodistribution in breast cancer bearing mice, Adv. Funct. Mater. 22 (2012) 4225–4235, https://doi.org/10.1002/adfm.201200869.

[41] M. Zhao, A. McCormack, M. Keswani, The formation mechanism of gradient porous Si in a contactless electrochemical process, J. Mater. Chem. C 4 (2016) 4204–4210, https://doi.org/10.1039/c6tc00309e.

[42] L. Canham, Tunable properties of porous silicon, in: Handbook of Porous Silicon, Springer International Publishing, Cham, 2014, pp. 201–206, https://doi.org/10.1007/978-3-319-05744-6_19.

[43] J. Salonen, Drug delivery with porous silicon, in: L. Canham (Ed.), Handbook of Porous Silicon, Springer International Publishing, Cham, 2014, pp. 909–919, https://doi.org/10.1007/978-3-319-05744-6_91.

[44] Y. Zhao, G. Gaur, S.T. Retterer, P.E. Laibinis, S.M. Weiss, Flow-through porous silicon membranes for real-time label-free biosensing, Anal. Chem. 88 (2016) 10940–10948, https://doi.org/10.1021/acs.analchem.6b02521.

[45] G. Lammel, S. Schweizer, S. Schiesser, P. Renaud, Tunable optical filter of porous silicon as key component for a MEMS spectrometer, J. Microelectromech. Syst. 11 (2002) 815–828, https://doi.org/10.1109/JMEMS.2002.803278.

[46] W. Kronast, B. Müller, W. Siedel, A. Stoffel, Single-chip condenser microphone using porous silicon as sacrificial layer for the air gap, Sensor Actuator Phys. 87 (2001) 188–193, https://doi.org/10.1016/S0924-4247(00)00483-0.

[47] X. Liu, H. Cheng, P. Cui, Catalysis by silver nanoparticles/porous silicon for the reduction of nitroaromatics in the presence of sodium borohydride, Appl. Surf. Sci. 292 (2014) 695–701, https://doi.org/10.1016/j.apsusc.2013.12.036.

[48] R.R. Bilyalov, R. Lüdemann, W. Wettling, L. Stalmans, J. Poortmans, J. Nijs, L. Schirone, G. Sotgiu, S. Strehlke, C. Lévy-Clément, Multicrystalline silicon solar cells with porous silicon emitter, Sol. Energy Mater. Sol. Cell. 60 (2000) 391–420, https://doi.org/10.1016/S0927-0248(99)00102-6.

[49] V. Torres-Costa, R.J. Martín-Palma, Application of nanostructured porous silicon in the field of optics. A review, J. Mater. Sci. 45 (2010) 2823–2838, https://doi.org/10.1007/s10853-010-4251-8.

[50] L. Canham, Routes of formation for porous silicon, in: Handbook of Porous Silicon, second ed., vols. 1–2, 2018, pp. 3–11, https://doi.org/10.1007/978-3-319-71381-6_1.

[51] V. Godinho, J. Caballero-Hernández, D. Jamon, T.C. Rojas, R. Schierholz, J. García-López, F.J. Ferrer, A. Fernández, A new bottom-up methodology to

produce silicon layers with a closed porosity nanostructure and reduced refractive index, Nanotechnology 24 (2013), https://doi.org/10.1088/0957-4484/24/27/275604.
[52] G. Beydaghyan, K. Kaminska, T. Brown, K. Robbie, Enhanced birefringence in vacuum evaporated silicon thin films, Appl. Opt. 43 (2004) 5343–5349, https://doi.org/10.1364/AO.43.005343.
[53] F. Voigt, R. Brüggemann, T. Unold, F. Huisken, G.H. Bauer, Porous thin films grown from size-selected silicon nanocrystals, Mater. Sci. Eng. C 25 (2005) 584–589, https://doi.org/10.1016/j.msec.2005.06.035.
[54] K. Fukutani, Y. Ishida, T. Aiba, H. Miyata, T. Den, Characterization of nanoporous Si thin films obtained by Al-Si phase separation, Appl. Phys. Lett. 87 (2005) 1–3, https://doi.org/10.1063/1.2149292.
[55] T. Huang, L. Cao, X. Zhang, X. Xiong, J. Xu, R. Xiao, A facile method to fabricate a novel 3D porous silicon/gold architecture for surface enhanced Raman scattering, J. Alloys Compd. 790 (2019) 127–133, https://doi.org/10.1016/j.jallcom.2019.03.161.
[56] A.M. Alwan, L.A. Wali, K.K. Hasan, A new route for developing highly efficient nano biochemical sensors for detecting ultra-low concentrations of tetracycline antibiotic residue in water, Gold Bull. 53 (2020) 39–46, https://doi.org/10.1007/s13404-020-00272-3.
[57] A.M. Alwan, A.A. Yousif, L.A. Wali, A study on the morphology of the silver nanoparticles deposited on the n-type porous silicon prepared under different illumination types, Plasmonics 13 (2018) 1191–1199, https://doi.org/10.1007/s11468-017-0620-3.
[58] L.A. Wali, K.K. Hasan, A.M. Alwan, An investigation of efficient detection of ultra-low concentration of penicillins in milk using AuNPs/PSi hybrid structure, Plasmonics (2020), https://doi.org/10.1007/s11468-019-01096-4.
[59] X. Sun, N. Wang, H. Li, Deep etched porous Si decorated with Au nanoparticles for surface-enhanced Raman spectroscopy (SERS), Appl. Surf. Sci. 284 (2013) 549–555, https://doi.org/10.1016/j.apsusc.2013.07.132.
[60] E. Nativ-Roth, K. Rechav, Z. Porat, Deposition of gold and silver on porous silicon and inside the pores, Thin Solid Films 603 (2016) 88–96, https://doi.org/10.1016/j.tsf.2016.01.020.
[61] M.Q. Zayer, A.M. Alwan, A.S. Ahmed, A.B. Dheyab, Accurate controlled deposition of silver nanoparticles on porous silicon by drifted ions in electrolytic solution, Curr. Appl. Phys. 19 (2019) 1024–1030, https://doi.org/10.1016/j.cap.2019.05.010.
[62] L.A. Woldering, R. Willem Tjerkstra, H.V. Jansen, I.D. Setija, W.L. Vos, Periodic arrays of deep nanopores made in silicon with reactive ion etching and deep UV lithography, Nanotechnology 19 (2008), https://doi.org/10.1088/0957-4484/19/14/145304.
[63] C.D.S. Bernardo, R. Metropolitana, C.L.S. Infante, C. Ignacio, C. Nos, Method for Producing Silicon My Means of Magnesiothermal Reduction, 2017. WO 2017/072064 Al.
[64] R. Memming, G. Schwandt, Anodic dissolution of silicon in hydrofluoric acid solutions, Surf. Sci. 4 (1966) 109–124, https://doi.org/10.1016/0039-6028(66)90071-9.
[65] D.V. Bru, Á.R. Martínez, Macroporous Silicon: Technology and Applications, New Research on Silicon - Structure, Properties, Technology, 2017, https://doi.org/10.5772/67698.
[66] J. Jakubowicz, Nanoporous silicon fabricated at different illumination and electrochemical conditions, Superlattice. Microst. 41 (2007) 205–215, https://doi.org/10.1016/j.spmi.2006.12.003.
[67] M.L. Coluccio, V. Onesto, G. Marinaro, M. Dell'apa, S. De Vitis, A. Imbrogno, L. Tirinato, G. Perozziello, E. Di Fabrizio, P. Candeloro, N. Malara, F. Gentile, Cell theranostics on mesoporous silicon substrates, Pharmaceutics 12 (2020) 1–23, https://doi.org/10.3390/pharmaceutics12050481.
[68] A. Langner, M. Knez, F. Müller, U. Gösele, TiO2 microstructures by inversion of macroporous silicon using atomic layer deposition, Appl. Phys. Mater. Sci. Process 93 (2008) 399–403, https://doi.org/10.1007/s00339-008-4784-8.
[69] N. Massad-Ivanir, S.K. Bhunia, R. Jelinek, E. Segal, Porous Silicon Bragg reflector/Carbon dot hybrids: synthesis, nanostructure, and optical properties, Front. Chem. 6 (2018) 1–10, https://doi.org/10.3389/fchem.2018.00574.
[70] C. Chiappini, MACE silicon nanostructures, in: Handbook of Porous Silicon, second ed., vols. 1–2, 2018, pp. 247–267, https://doi.org/10.1007/978-3-319-71381-6_17.
[71] S. Li, W. Ma, Y. Zhou, X. Chen, Y. Xiao, M. Ma, W. Zhu, F. Wei, Fabrication of porous silicon nanowires by MACE method in HF/H2O2/AgNO3 system at room temperature, Nanoscale Res. Lett. 9 (2014) 1–8, https://doi.org/10.1186/1556-276X-9-196.
[72] H. Alhmoud, D. Brodoceanu, R. Elnathan, T. Kraus, N.H. Voelcker, A MACEing silicon: towards single-step etching of defined porous nanostructures for biomedicine, Prog. Mater. Sci. (2020) 100636, https://doi.org/10.1016/j.pmatsci.2019.100636.
[73] L. Kong, Y. Zhao, B. Dasgupta, Y. Ren, K. Hippalgaonkar, X. Li, W.K. Chim, S. Y. Chiam, Minimizing isolate catalyst motion in metal-assisted chemical etching for deep trenching of silicon nanohole array, ACS Appl. Mater. Interfaces 9 (2017), https://doi.org/10.1021/acsami.7b04565, 20981–20990.
[74] J. de Boor, U. Gösele, Z. Huang, N. Geyer, P. Werner, Metal-assisted chemical etching of silicon: a review, Adv. Mater. 23 (2010) 285–308, https://doi.org/10.1002/adma.201001784.
[75] R.A. Lai, T.M. Hymel, V.K. Narasimhan, Y. Cui, Schottky barrier catalysis mechanism in metal-assisted chemical etching of silicon, ACS Appl. Mater. Interfaces 8 (2016) 8875–8879, https://doi.org/10.1021/acsami.6b01020.
[76] L. Li, Y. Liu, X. Zhao, Z. Lin, C.P. Wong, L. Li, Y. Liu, X. Zhao, Z. Lin, C.P. Wong, Uniform vertical trench etching on silicon with high aspect ratio by metal-assisted chemical etching using nanoporous catalysts, ACS Appl. Mater. Interfaces 6 (2014) 575–584, https://doi.org/10.1021/am4046519. Uniform vertical trench etching on silicon with high aspect ratio by metal-assisted chemical etching using nanoporous catalysts, ACS Applied Materials and Interfaces1.
[77] D. Brodoceanu, R. Elnathan, B. Prieto-Simón, B. Delalat, T. Guinan, E. Kroner, N. H. Voelcker, T. Kraus, Dense arrays of uniform submicron pores in silicon and their applications, ACS Appl. Mater. Interfaces 7 (2015) 1160–1169, https://doi.org/10.1021/am506891d.
[78] N. Errien, L. Vellutini, G. Louarn, G. Froyer, Surface characterization of porous silicon after pore opening processes inducing chemical modifications, Appl. Surf. Sci. 253 (2007) 7265–7271, https://doi.org/10.1016/j.apsusc.2007.03.017.
[79] L. Tian, K.B. Ram, I. Ahmad, L. Menon, M. Holtz, Optical properties of a nanoporous array in silicon, J. Appl. Phys. 97 (2005), https://doi.org/10.1063/1.1831541.
[80] Y. Wang, S. Park, J.T.W. Yeow, A. Langner, F. Müller, A capacitive humidity sensor based on ordered macroporous silicon with thin film surface coating, Sensor. Actuator. B Chem. 149 (2010) 136–142, https://doi.org/10.1016/j.snb.2010.06.010.
[81] J.C. Yu, Z.F. Zhou, J. Le Su, C.F. Xia, X.W. Zhang, Z.Z. Wu, Q.A. Huang, Three-dimensional simulation of DRIE process based on the narrow band level set and Monte Carlo method, Micromachines 9 (2018), https://doi.org/10.3390/mi9020074.
[82] B. Wu, A. Kumar, S. Pamarthy, High aspect ratio silicon etch: a review, J. Appl. Phys. 108 (2010), https://doi.org/10.1063/1.3474652.
[83] M. Steglich, T. Käsebier, M. Zilk, T. Pertsch, E.B. Kley, A. Tünnermann, The structural and optical properties of black silicon by inductively coupled plasma reactive ion etching, J. Appl. Phys. 116 (2014), https://doi.org/10.1063/1.4900996.
[84] Y. Jiao, D.S. Koktysh, N. Phambu, S.M. Weiss, Dual-mode sensing platform based on colloidal gold functionalized porous silicon, Appl. Phys. Lett. 97 (2010) 2008–2011, https://doi.org/10.1063/1.3503608.
[85] S.M. Budy, D.J. Hamilton, Y. Cai, M.K. Knowles, S.M. Reed, Polymer mediated layer-by-layer assembly of different shaped gold nanoparticles, J. Colloid Interface Sci. (2017), https://doi.org/10.1016/j.jcis.2016.10.022.
[86] F. Shi, Z. Jia, X. Lv, H. Zhang, J. Zhou, Enhancement of the R6G fluorescence by gold nanoparticle depositions in porous silicon Bragg reflectors, Phys. Status Solidi A, Appl. Mater. Sci. 212 (2015) 662–665, https://doi.org/10.1002/pssa.201431817.
[87] A.M. Alwan, A.A. Yousif, L.A. Wali, The growth of the silver nanoparticles on the mesoporous silicon and macroporous silicon: a comparative study, Indian J. Pure Appl. Phys. 55 (2017) 813–820.
[88] Y.Q. Wang, S. Ma, Q.Q. Yang, X.J. Li, Size-dependent SERS detection of R6G by silver nanoparticles immersion-plated on silicon nanoporous pillar array, Appl. Surf. Sci. 258 (2012) 5881–5885, https://doi.org/10.1016/j.apsusc.2012.02.129.
[89] A.J. Fulton, V. Ozhukil Kollath, K. Karan, Y. Shi, Gold nanoparticle assembly on porous silicon by pulsed laser induced dewetting, Nanoscale Adv. 2 (2020) 896–905, https://doi.org/10.1039/d0na00043d.
[90] S.M. Budy, D.J. Hamilton, Y. Cai, M.K. Knowles, S.M. Reed, Polymer mediated layer-by-layer assembly of different shaped gold nanoparticles, J. Colloid Interface Sci. 487 (2017) 336–347, https://doi.org/10.1016/j.jcis.2016.10.022.
[91] S. Mariani, A. Paghi, A.A. La Mattina, A. Debrassi, L. Dähne, G. Barillaro, Decoration of porous silicon with gold nanoparticles via layer-by-layer nanoassembly for interferometric and hybrid photonic/plasmonic (Bio)sensing, ACS Appl. Mater. Interfaces 11 (2019) 43731–43740, https://doi.org/10.1021/acsami.9b15737.
[92] J.W. Jiajia Wang, Z.J. Zhenhong Jia, C.L. Changwu Lv, Y.L. Yanyu Li, Application of metal nanoparticles/porous silicon diffraction grating in rhodamine 6 G fluorescence signal enhancement, Chin. Opt Lett. 15 (2017) 110501, https://doi.org/10.3788/col201715.110501.
[93] M.J. Sailor, Chemistry of Porous Silicon, Porous Silicon in Practice, 2012, pp. 189–227, https://doi.org/10.1002/9783527641901.ch6.
[94] K.V. Girel, A.Y. Panarin, H.V. Bandarenka, G. Isic, V.P. Bondarenko, S. N. Terekhov, Plasmonic silvered nanostructures on macroporous silicon decorated with graphene oxide for SERS-spectroscopy, Nanotechnology 29 (2018) 1–7, https://doi.org/10.1088/1361-6528/aad250.
[95] Y. Bu, G. Zhu, S. Li, R. Qi, G. Bhave, D. Zhang, R. Han, D. Sun, X. Liu, Z. Hu, X. Liu, Silver-Nanoparticle-Embedded porous silicon disks enabled SERS signal amplification for selective glutathione detection, ACS Appl. Nano Mater. 1 (2018) 410–417, https://doi.org/10.1021/acsanm.7b00290.
[96] M.V. Chursanova, L.P. Germash, V.O. Yukhymchuk, V.M. Dzhagan, I. A. Khodasevich, D. Cojoc, Optimization of porous silicon preparation technology for SERS applications, Appl. Surf. Sci. 256 (2010) 3369–3373, https://doi.org/10.1016/j.apsusc.2009.12.036.
[97] F.A. Harraz, A.A. Ismail, H. Bouzid, S.A. Al-Sayari, A. Al-Hajry, M.S. Al-Assiri, Surface-enhanced Raman scattering (SERS)-active substrates from silver plated-porous silicon for detection of crystal violet, Appl. Surf. Sci. 331 (2015) 241–247, https://doi.org/10.1016/j.apsusc.2015.01.042.
[98] A. Virga, P. Rivolo, E. Descrovi, A. Chiolerio, G. Digregorio, F. Frascella, M. Soster, F. Bussolino, S. Marchiò, F. Geobaldo, F. Giorgis, SERS active Ag nanoparticles in mesoporous silicon: detection of organic molecules and peptide-antibody assays, J. Raman Spectrosc. 43 (2012) 730–736, https://doi.org/10.1002/jrs.3086.
[99] C.H. Kam, V.E. Borisenko, N. Khinevich, V. Bondarenko, V.S. Gurin, S. Zavatski, S. V Gaponenko, Structure and sers activity of gold nanoparticles formed by chemical deposition on porous silicon, Phys. Chem. Appl. Nanostruct. (2017) 240–243, https://doi.org/10.1142/9789813224537_0056.

[100] W. Ye, C. Shen, J. Tian, C. Wang, L. Bao, H. Gao, Self-assembled synthesis of SERS-active silver dendrites and photoluminescence properties of a thin porous silicon layer, Electrochem. Commun. 10 (2008) 625–629, https://doi.org/10.1016/j.elecom.2008.01.040.
[101] S. Redko, A. Dolgiy, D. Zhygulin, V. Khaliava, N. Khinevich, S. Zavatski, H. Bandarenka, Fabrication and simulation of silver nanostructures on different types of porous silicon for surface enhanced Raman spectroscopy, in: M. Osiński, Y. Arakawa, B. Witzigmann (Eds.), Physics and Simulation of Optoelectronic Devices XXVII, SPIE, 2019, p. 61, https://doi.org/10.1117/12.2511299.
[102] K.J. Khajehpour, T. Williams, L. Bourgeois, S. Adeloju, Gold nanothorns-macroporous silicon hybrid structure: a simple and ultrasensitive platform for SERS, Chem. Commun. 48 (2012) 5349–5351, https://doi.org/10.1039/c2cc17078g.
[103] I.A. Khodasevich, K.V. Girel, H.V. Bandarenka, V.P. Bondarenko, S.N. Terekhov, A.Y. Panarin, Formation regularities of plasmonic silver nanostructures on porous silicon for effective surface-enhanced Raman scattering, Nanoscale Res. Lett. 11 (2016), https://doi.org/10.1186/s11671-016-1473-y.
[104] A.Y. Panarin, S.N. Terekhov, K.I. Kholostov, V.P. Bondarenko, SERS-active substrates based on n-type porous silicon, Appl. Surf. Sci. 256 (2010) 6969–6976, https://doi.org/10.1016/j.apsusc.2010.05.008.
[105] I. Khodasevich, A. Panarin, S. Terekhov, K. Artsemyeva, A. Dolgiy, H. Bandarenka, V. Bondarenko, Fabrication of SERS-active substrates by electrochemical and electroless deposition of metals in macroporous silicon, ECS Transactions 53 (2013) 85–95, https://doi.org/10.1149/05311.0085ecst.
[106] A. Virga, P. Rivolo, F. Frascella, A. Angelini, E. Descrovi, F. Geobaldo, F. Giorgis, Silver nanoparticles on porous silicon: approaching single molecule detection in resonant SERS regime, J. Phys. Chem. C 117 (2013) 20139–20145, https://doi.org/10.1021/jp405117p.
[107] V. Myroshnychenko, J. Rodríguez-Fernández, I. Pastoriza-Santos, A.M. Funston, C. Novo, P. Mulvaney, L.M. Liz-Marzán, F.J. García de Abajo, Modelling the optical response of gold nanoparticles, Chem. Soc. Rev. 37 (2008) 1792–1805, https://doi.org/10.1039/b711486a.
[108] V. Myndrul, R. Viter, M. Savchuk, M. Koval, N. Starodub, V. Silamiķelis, V. Smyntyna, A. Ramanavicius, I. Iatsunskyi, Gold coated porous silicon nanocomposite as a substrate for photoluminescence-based immunosensor suitable for the determination of Aflatoxin B1, Talanta 175 (2017) 297–304, https://doi.org/10.1016/j.talanta.2017.07.054.
[109] E. Ko, J. Hwang, J.H. Kim, J.H. Lee, S.H. Lee, V.K. Tran, W.S. Chung, C.H. Park, J. Choo, G.H. Seong, Electrochemical fabrication of nanostructures on porous silicon for biochemical sensing platforms, Anal. Sci. 32 (2016) 681–686, https://doi.org/10.2116/analsci.32.681.
[110] D. Ge, J. Wei, J. Ding, J. Zhang, C. Ma, M. Wang, L. Zhang, S. Zhu, Silver nano-dendrite-plated porous silicon substrates formed by single-step electrochemical synthesis for surface-enhanced Raman scattering, ACS Appl. Nano Mater. (2020), https://doi.org/10.1021/acsanm.0c00296.
[111] K. Fukami, M.L. Chourou, R. Miyagawa, Á.M. Noval, T. Sakka, M. Manso-Silván, R.J. Martín-Palma, Y.H. Ogata, Gold nanostructures for surface-enhanced Raman spectroscopy, Prepared by electrodeposition in porous silicon, Materials 4 (2010) 791–800, https://doi.org/10.3390/ma4040791.
[112] Á. Muñoz-Noval, K. Fukami, R.J. Martín-Palma, T. Sakka, M. Manso-Silván, Y. H. Ogata, Surface plasmon resonance study of Au nanorod structures templated in mesoporous silicon, Plasmonics 8 (2013) 35–40, https://doi.org/10.1007/s11468-012-9399-4.
[113] H. Dridi, L. Haji, A. Moadhen, Rough SERS substrate based on gold coated porous silicon layer prepared on the silicon backside surface, Superlattice. Microst. 104 (2017) 266–270, https://doi.org/10.1016/j.spmi.2017.02.002.
[114] X. Yue, X. Zheng, G. Lv, J. Mo, X. Yu, J. Liu, Z. Jia, X. Lv, J. Tang, Synthesis of a low-cost, stable, silicon-based SERS substrate for rapid, nondestructive biosensing, Optik 192 (2019) 162959, https://doi.org/10.1016/j.ijleo.2019.162959.
[115] G. Lu, G. Wang, H. Li, Effect of nanostructured silicon on surface enhanced Raman scattering, RSC Adv. 8 (2018) 6629–6633, https://doi.org/10.1039/c8ra00014j.
[116] Y. Shen, X. Cheng, G. Li, Q. Zhu, Z. Chi, J. Wang, C. Jin, Highly sensitive and uniform surface-enhanced Raman spectroscopy from grating-integrated plasmonic nanograss, Nanoscale Horizons 1 (2016) 290–297, https://doi.org/10.1039/c6nh00059b.
[117] S. Daniel, A. Matikainen, J. Turunen, P. Vahimaa, T. Nuutinen, Uniform distribution of Ag particles upon imprinted polymer grating for Raman signal enhancement, J. Colloid Interface Sci. 437 (2015) 119–123, https://doi.org/10.1016/j.jcis.2014.09.037.
[118] A. Gopalakrishnan, M. Chirumamilla, F. De Angelis, A. Toma, R.P. Zaccaria, R. Krahne, Bimetallic 3D nanostar dimers in ring cavities: recyclable and robust surface-enhanced Raman scattering substrates for signal detection from few molecules, ACS Nano 8 (2014) 7986–7994, https://doi.org/10.1021/nn5020038.
[119] J.M. Montgomery, A. Imre, U. Welp, V. Vlasko-Vlasov, S.K. Gray, SERS enhancements via periodic arrays of gold nanoparticles on silver film structures, Opt Express 17 (2009) 8669, https://doi.org/10.1364/oe.17.008669.
[120] G.K. Podagatlapalli, S. Hamad, S.V. Rao, Trace-level detection of secondary explosives using hybrid silver-gold nanoparticles and nanostructures achieved with femtosecond laser ablation, J. Phys. Chem. C 119 (2015) 16972–16983, https://doi.org/10.1021/acs.jpcc.5b03958.
[121] S. Chan, S. Kwon, T.W. Koo, L.P. Lee, A.A. Berlin, Surface-enhanced Raman scattering of small molecules from silver-coated silicon nanopores, Adv. Mater. 15 (2003) 1595–1598, https://doi.org/10.1002/adma.200305149.
[122] L. Canham, Handbook of Porous Silicon, Springer International Publishing, Cham, 2018, https://doi.org/10.1007/978-3-319-71381-6_19.
[123] F. Zhong, J. Mo, Y. Li, B. Sun, Z. Wu, Optical characteristics of porous silicon photonic crystals prepared on the back surface of silicon wafers, Optik 201 (2020) 163486, https://doi.org/10.1016/j.ijleo.2019.163486.
[124] X. Yue, H. Li, X. Lv, J. Tang, Porous silicon photonic crystal/silver composite produced by microwave-assisted reduction: applications to surface-enhanced Raman scattering, Opt. Mater. X 2 (2019) 100027, https://doi.org/10.1016/j.omx.2019.100027.
[125] J. Wang, Z. Jia, Y. Liu, Improvement of SERS by the optical modulation of photonic crystal, IEEE Sensor. J. 19 (2019) 11221–11227, https://doi.org/10.1109/JSEN.2019.2937092.
[126] F. Zhong, Z. Wu, J. Guo, D. Jia, Porous silicon photonic crystals coated with Ag nanoparticles as efficient substrates for detecting trace explosives using SERS, Nanomaterials 8 (2018), https://doi.org/10.3390/nano8110872.
[127] M. Škrabić, M. Kosović, M. Gotić, L. Mikac, M. Ivanda, O. Gamulin, Near-infrared surface-enhanced Raman scattering on silver-coated porous silicon photonic crystals, Nanomaterials 9 (2019), https://doi.org/10.3390/nano9030421.
[128] J. Wang, Z. Jia, Metal nanoparticles/porous silicon microcavity enhanced surface plasmon resonance fluorescence for the detection of DNA, Sensors (2018) 18, https://doi.org/10.3390/s18020661.
[129] X. Yue, H. Li, X. Lv, J. Tang, Porous silicon photonic crystal/silver composite produced by microwave-assisted reduction: applications to surface-enhanced Raman scattering, Opt. Mater. X 2 (2019) 100027, https://doi.org/10.1016/j.omx.2019.100027.
[130] Y. Kalachyova, D. Mares, O. Lyutakov, M. Kostejn, L. Lapcak, V. Švorčík, Surface plasmon polaritons on silver gratings for optimal SERS response, J. Phys. Chem. C 119 (2015) 9506–9512, https://doi.org/10.1021/acs.jpcc.5b01793.
[131] X. Xu, D. Hasan, L. Wang, S. Chakravarty, R.T. Chen, D.L. Fan, A.X. Wang, Guided-mode-resonance-coupled plasmonic-active SiO 2 nanotubes for surface enhanced Raman spectroscopy, Appl. Phys. Lett. 100 (2012) 191114, https://doi.org/10.1063/1.4714710.
[132] Y. Hou, J. Xu, W. Li, X. Wang, Coupled subwavelength gratings for surface-enhanced Raman spectroscopy, Phys. Chem. Chem. Phys. 13 (2011) 10946–10951, https://doi.org/10.1039/c0cp03002c.
[133] V.G. Kravets, A.V. Kabashin, W.L. Barnes, A.N. Grigorenko, Plasmonic surface lattice resonances: a review of properties and applications, Chem. Rev. (2018), https://doi.org/10.1021/acs.chemrev.8b00243.
[134] M. Saini, S. Augustine, M. Ranjan, T. Som, In-plane optical anisotropy and SERS detection efficiency of self-organized gold nanoparticles on silicon nanoripples: roles of growth angle and postgrowth annealing, Appl. Surf. Sci. 512 (2020) 145703, https://doi.org/10.1016/j.apsusc.2020.145703.
[135] J. Wang, Z. Jia, C. Lv, Enhanced Raman scattering in porous silicon grating, Opt Express 26 (2018) 6507, https://doi.org/10.1364/oe.26.006507.
[136] S. Zavatski, N. Khinevich, K. Girel, S. Redko, N. Kovalchuk, I. Komissarov, V. Lukashevich, I. Semak, K. Mamatkulov, M. Vorobyeva, G. Arzumanyan, H. Bandarenka, Surface enhanced Raman spectroscopy of lactoferrin adsorbed on silvered porous silicon covered with graphene, Biosensors 9 (2019) 34, https://doi.org/10.3390/bios9010034.
[137] S. Marchiò, A. Virga, F. Frascella, P. Rivolo, M. Soster, F. Geobaldo, F. Giorgis, E. Descrovi, F. Bussolino, G. Digregorio, A. Chiolerio, SERS active Ag nanoparticles in mesoporous silicon: detection of organic molecules and peptide-antibody assays, J. Raman Spectrosc. 43 (2011) 730–736, https://doi.org/10.1002/jrs.3086.
[138] F. Sun, D.D. Galvan, P. Jain, Q. Yu, Multi-functional, thiophenol-based surface chemistry for surface-enhanced Raman spectroscopy, Chem. Commun. 53 (2017) 4550–4561, https://doi.org/10.1039/c7cc01577a.
[139] S. Li, Q. Zhou, W. Chu, W. Zhao, J. Zheng, Surface-enhanced Raman scattering behaviour of 4-mercaptophenyl boronic acid on assembled silver nanoparticles, Phys. Chem. Chem. Phys. 17 (2015) 17638–17645, https://doi.org/10.1039/c5cp02409a.
[140] A. Ouhibi, A. Raouafi, N. Lorrain, M. Guendouz, N. Raouafi, A. Moadhen, Functionalized SERS substrate based on silicon nanowires for rapid detection of prostate specific antigen, Sensor. Actuator. B Chem. 330 (2021) 129352, https://doi.org/10.1016/j.snb.2020.129352.
[141] H. Li, Q. Wang, N. Gao, J. Fu, X. Yue, X. Lv, F.R. Zhong, J. Tang, T. Wang, Facile synthesis of magnetic ionic liquids/gold nanoparticles/porous silicon composite SERS substrate for ultra-sensitive detection of arsenic, Appl. Surf. Sci. 545 (2021) 148992, https://doi.org/10.1016/j.apsusc.2021.148992.
[142] G. Arzumanyan, N. Doroshkevich, K. Mamatkulov, S. Shashkov, K. Girel, H. Bandarenka, V. Borisenko, Phospholipid detection by surface-enhanced Raman scattering using silvered porous silicon substrates, Phys. Status Solidi 214 (2017) 1600915, https://doi.org/10.1002/pssa.201600915.
[143] C. Novara, S. Dalla Marta, A. Virga, A. Lamberti, A. Angelini, A. Chiadò, P. Rivolo, F. Geobaldo, V. Sergo, A. Bonifacio, F. Giorgis, SERS-active Ag nanoparticles on porous silicon and PDMS substrates: a comparative study of uniformity and Raman efficiency, J. Phys. Chem. C 120 (2016) 16946–16953, https://doi.org/10.1021/acs.jpcc.6b03852.
[144] C. Novara, A. Chiadò, N. Paccotti, S. Catuogno, C.L. Esposito, G. Condorelli, V. De Franciscis, F. Geobaldo, P. Rivolo, F. Giorgis, SERS-active metal-dielectric nanostructures integrated in microfluidic devices for label-free quantitative detection of miRNA, Faraday Discuss 205 (2017) 271–289, https://doi.org/10.1039/c7fd00140a.
[145] A. Hakonen, K. Wu, M. Stenbæk Schmidt, P.O. Andersson, A. Boisen, T. Rindzevicius, Detecting forensic substances using commercially available SERS substrates and handheld Raman spectrometers, Talanta 189 (2018) 649–652, https://doi.org/10.1016/j.talanta.2018.07.009.

[146] S. Rostami, K. Zór, D.S. Zhai, M. Viehrig, L. Morelli, A. Mehdinia, J. Smedsgaard, T. Rindzevicius, A. Boisen, High-throughput label-free detection of Ochratoxin A in wine using supported liquid membrane extraction and Ag-capped silicon nanopillar SERS substrates, Food Contr. 113 (2020) 107183, https://doi.org/10.1016/j.foodcont.2020.107183.
[147] L.A. Wali, K.K. Hasan, A.M. Alwan, Rapid and highly efficient detection of ultra-low concentration of penicillin G by gold nanoparticles/porous silicon SERS active substrate, Spectrochim. Acta Mol. Biomol. Spectrosc. 206 (2019) 31–36, https://doi.org/10.1016/j.saa.2018.07.103.
[148] A.M. Al Syadi, M. Faisal, F.A. Harraz, M. Jalalah, Immersion - plated palladium nanoparticles onto meso - porous silicon layer as novel SERS substrate for sensitive detection of imidacloprid pesticide, Sci. Rep. (2021) 1–14, https://doi.org/10.1038/s41598-021-88326-0.
[149] H. Dridi, A. Moadhen, L. Haji, Comparative SERS study carried out on unsilanized and silanized oxidized porous silicon surface coated by small gold nanoparticles, J. Porous Mater. 22 (2014) 239–245, https://doi.org/10.1007/s10934-014-9890-8.
[150] A.M. Alwan, I.A. Naseef, A.B. Dheyab, Well controlling of plasmonic features of gold nanoparticles on macro porous silicon substrate by HF acid concentration, Plasmonics 13 (2018) 2037–2045, https://doi.org/10.1007/s11468-018-0720-8.
[151] K.S. Anju, R. Gayathri, P.P. Subha, K.R. Kumar, M.K. Jayaraj, Optimally distributed Ag over SiO 2 nanoparticles as colloidal SERS substrate, Microchem. J. 147 (2019) 349–355, https://doi.org/10.1016/j.microc.2019.03.027.
[152] L.M. Liz-marza, M. Giersig, P. Mulvaney, Synthesis of nanosized gold - silica, Core - Shell Part. 7463 (1996) 4329–4335.
[153] C.D. Jones, L.A. Lyon, Synthesis and characterization of multiresponsive core-shell microgels, Macromolecules 33 (2000) 8301–8306, https://doi.org/10.1021/ma001398m.
[154] Z. Yi, G. Niu, J. Luo, X. Kang, W. Yao, W. Zhang, Y. Yi, Y. Yi, X. Ye, T. Duan, Y. Tang, Ordered array of Ag semishells on different diameter monolayer polystyrene colloidal crystals: an ultrasensitive and reproducible SERS substrate, Sci. Rep. 6 (2016) 1–11, https://doi.org/10.1038/srep32314.
[155] A.A. Jabbar, A.M. Alwan, A.J. Haider, Modifying and fine controlling of silver nanoparticle nucleation sites and SERS performance by double silicon etching process, Plasmonics 13 (2018) 1171–1182, https://doi.org/10.1007/s11468-017-0618-x.
[156] M. Ivanda, M. Ristić, M. Marciuš, M. Balarin, M. Kosović, O. Gamulin, V. Đerek, Porous silicon covered with silver nanoparticles as surface-enhanced Raman scattering (SERS) substrate for ultra-low concentration detection, Appl. Spectrosc. 69 (2015) 1417–1424, https://doi.org/10.1366/14-07729.
[157] A.Y. Panarin, S.N. Terekhov, I.A. Khodasevich, P.-Y. Turpin, Silver-coated nanoporous silicon as SERS-active substrate for investigation of tetrapyrrolic molecules, ICONO 2007: novel Photonics Materials, Optics Opt. Diagn. Nanostruct. 6728 (2007) 672828, https://doi.org/10.1117/12.752423.
[158] F. Giorgis, E. Descrovi, A. Chiodoni, E. Froner, M. Scarpa, A. Venturello, F. Geobaldo, Porous silicon as efficient surface enhanced Raman scattering (SERS) substrate, Appl. Surf. Sci. 254 (2008) 7494–7497, https://doi.org/10.1016/j.apsusc.2008.06.029.
[159] C. Novara, A. Lamberti, A. Chiadò, A. Virga, P. Rivolo, F. Geobaldo, F. Giorgis, Surface-enhanced Raman spectroscopy on porous silicon membranes decorated with Ag nanoparticles integrated in elastomeric microfluidic chips, RSC Adv. 6 (2016) 21865–21870, https://doi.org/10.1039/c5ra26746c.
[160] K. Girel, E. Yantcevich, G. Arzumanyan, N. Doroshkevich, H. Bandarenka, Detection of DNA molecules by SERS spectroscopy with silvered porous silicon as an active substrate, Phys. Status Solidi A, Appl. Mater. Sci. 213 (2016) 2911–2915, https://doi.org/10.1002/pssa.201600432.
[161] A. Chiadò, C. Novara, A. Lamberti, F. Geobaldo, F. Giorgis, P. Rivolo, Immobilization of oligonucleotides on metal-dielectric nanostructures for miRNA detection, Anal. Chem. 88 (2016) 9554–9563, https://doi.org/10.1021/acs.analchem.6b02186.
[162] X. Ma, H. Cheng, J. Hou, Z. Jia, G. Wu, X. Lv, H. Li, X. Zheng, C. Chen, Detection of breast cancer based on novel porous silicon Bragg reflector SERS-active structure, Spectroscopy (2019) 215.
[163] X. Yue, H. Li, J. Tang, J. Liu, J. Jiao, Rapid and label-free screening of echinococcosis serum profiles through surface-enhanced Raman spectroscopy, Anal. Bioanal. Chem. 412 (2020) 279–288, https://doi.org/10.1007/s00216-019-02234-x.
[164] A. Kamińska, T. Szymborski, T. Jaroch, A. Zmysłowski, A. Szterk, Gold-capped silicon for ultrasensitive SERS-biosensing: towards human biofluids analysis, Mater. Sci. Eng. C 84 (2018) 208–217, https://doi.org/10.1016/j.msec.2017.11.029.
[165] A.A. Jabbar, A.M. Alwan, M.Q. Zayer, A.J. Bohan, Efficient single cell monitoring of pathogenic bacteria using bimetallic nanostructures embedded in gradient porous silicon, Mater. Chem. Phys. 241 (2020) 122359, https://doi.org/10.1016/j.matchemphys.2019.122359.
[166] M.L. Coluccio, S. De Vitis, G. Strumbo, P. Candeloro, G. Perozziello, E. Di Fabrizio, F. Gentile, Inclusion of gold nanoparticles in meso-porous silicon for the SERS analysis of cell adhesion on nano-structured surfaces, Microelectron. Eng. 158 (2016) 102–106, https://doi.org/10.1016/j.mee.2016.03.045.
[167] H. Bandarenka, K. Artsemyeva, S. Redko, A. Panarin, S. Terekhov, V. Bondarenko, Effect of swirl-like resistivity striations in n+-type Sb doped Si wafers on the properties of Ag/porous silicon SERS substrates, Phys. Status Solidi Corr. Topic Solid state Phys. 10 (2013) 624–627, https://doi.org/10.1002/pssc.201200731.
[168] W. Ma, M. Sun, P. Fu, S. Li, L. Xu, H. Kuang, C. Xu, A chiral-nanoassemblies-enabled strategy for simultaneously profiling surface glycoprotein and MicroRNA in living cells, Adv. Mater. 29 (2017) 1–9, https://doi.org/10.1002/adma.201703410.
[169] W. Ma, C. Hao, M. Sun, L. Xu, C. Xu, H. Kuang, Tuning of chiral construction, structural diversity, scale transformation and chiroptical applications, Mater. Horiz. 5 (2018) 141–161, https://doi.org/10.1039/c7mh00966f.
[170] S. Fornasaro, A. Bonifacio, E. Marangon, M. Buzzo, G. Toffoli, T. Rindzevicius, M. S. Schmidt, V. Sergo, Label-free quantification of anticancer drug imatinib in human plasma with surface enhanced Raman spectroscopy, Anal. Chem. 90 (2018) 12670–12677, https://doi.org/10.1021/acs.analchem.8b02901.
[171] N. Khinevich, S. Zavatski, H. Bandarenka, V. Belyatsky, E. Galyuk, O. Ryneiskaya, Study of diluted meldonium solutions by surface enhanced Raman scattering spectroscopy, Int. J. Nanosci. 18 (2019) 1940054, https://doi.org/10.1142/S0219581X19400544.
[172] N. Khinevich, K. Girel, H. Bandarenka, V. Salo, A. Mosunov, Surface enhanced Raman spectroscopy of fullerene C60 drop-deposited on the silvered porous silicon, J. Phys. Conf. 917 (2017), https://doi.org/10.1088/1742-6596/917/6/062052.

Paper II: Size and Crystallinity Effect on the Ultrafast Optical Response of Chemically Synthesized Silver Nanoparticles

Nadzeya Khinevich, Domantas Peckus, Asta Tamulevičienė, Gerda Klimaite, Joel Henzie, Tomas Tamulevičius, Sigitas Tamulevičius

Journal of Materiomics 10 (3), (2024)

Journal of Materiomics xxx (xxxx) xxx

Contents lists available at ScienceDirect

Journal of Materiomics

journal homepage: www.journals.elsevier.com/journal-of-materiomics/

Research paper

Size and crystallinity effect on the ultrafast optical response of chemically synthesized silver nanoparticles

Nadzeya Khinevich [a], Domantas Peckus [a, b, *], Asta Tamulevičienė [a, b], Gerda Klimaitė [b], Joel Henzie [c], Tomas Tamulevičius [a, b], Sigitas Tamulevičius [a, b, **]

[a] Institute of Materials Science of Kaunas University of Technology, K. Baršausko St. 59, LT-51423, Kaunas, Lithuania
[b] Department of Physics, Kaunas University of Technology, Studentų St. 50, LT-51368, Kaunas, Lithuania
[c] International Center for Materials Nanoarchitectonics (WPI-MANA), National Institute for Materials Science (NIMS), Tsukuba, 305-0044, Japan

ARTICLE INFO

Article history:
Received 3 July 2023
Received in revised form
21 August 2023
Accepted 22 August 2023
Available online xxx

Keywords:
Silver nanospheres
Silver nanocubes
Electron-phonon coupling
Transient absorption spectroscopy
Crystallite size
Polycrystalline structure

ABSTRACT

The excited localized surface plasmon (LSP) in metallic nanoparticles is known to relax through several processes such as electron-electron scattering, electron-phonon coupling, and phonon-phonon scattering. In the current research, the ultrafast electron-phonon (e-ph) coupling relaxation processes for different average sizes and crystallinity of chemically synthesized silver nanoparticles were evaluated utilizing transient absorption spectroscopy. The nanoparticle size and crystallinity of similar linear dimension polycrystalline spherical and monocrystalline cubic nanoparticles ranging from *ca.* 30–60 nm was related to their electron relaxation time constants and revealed very different dependencies. For the monocrystalline nanocubes, the electron-phonon coupling was not dependent on the cube edge length, while for the polycrystalline nanospheres, it was linearly decreasing with diameter. We demonstrate that the e-ph coupling time constant could be used to evaluate crystallinity and crystallite size in plasmonic metal nanoparticles when the size (surface area) of the nanoparticle is known.

1. Introduction

Metal nanoparticle synthesis and optical characterization have become an important focus in diverse fields from catalysis to sensing and medicine. Special attention is paid to noble metal (Au, Ag, and Pt) nanostructures because they support plasmon resonance. Due to their unique physicochemical properties, Ag NPs are used as biosensor material, additives to composite fibres, cosmetic products, and electronic and optical components [1]. Ag NPs have been one of the most attractive nanomaterials in biomedicine, where they are used for antimicrobial and anticancer therapy, promote wound repair and bone healing, or as an adjuvant to vaccines as an antidiabetic agent [2]. Ag NPs also find multiple applications ranging from heterogeneous catalysis [3] to gas sensing and nonlinear optics [4,5]. Metallic nanoparticles act as a functional base component of nanoscale devices or sensors with high selectivity and sensitivity in these applications. These nanoparticles can also be applied in spectroscopic systems to enhance Raman scattering spectroscopy signal [6]. Nanoscale metal features support localized surface plasmon resonances (LSPs) associated with strong electromagnetic (EM) hotspots. These EM fields enhance the Raman scattering of adsorbed molecules and can be used for chemical sensing [4].

One of the key issues to consider during a variety of applications of metallic NPs includes developments and novel applications in photovoltaics, photodetection, photocatalysis, *etc.* where the LSP excitation of NPs is employed, is their ultrafast optical user-designed response. Currently, there is knowledge of the temporal evolution of hot electrons excited by light and its dependence on the size, composition, and morphology of metal NPs. The excited LSP in metallic NPs is known to relax through several processes such as electron-electron scattering (e-e, typical time scale *ca.* 100 fs), electron-phonon coupling (e-ph, 1–5 ps), and phonon-phonon scattering (ph-ph, 10–100 ps) [7]. When the excitation source is faster than the expansion/contraction period, the light-heated particles can form coherent vibrations called optomechanical

* Corresponding author. Institute of Materials Science of Kaunas University of Technology, K. Baršausko St. 59, LT-51423, Kaunas, Lithuania.
** Corresponding author. Institute of Materials Science of Kaunas University of Technology, K. Baršausko St. 59, LT-51423, Kaunas, Lithuania.
E-mail addresses: domantas.peckus@ktu.lt (D. Peckus), sigitas.tamulevicius@ktu.lt (S. Tamulevičius).
Peer review under responsibility of The Chinese Ceramic Society.

https://doi.org/10.1016/j.jmat.2023.08.009

Please cite this article as: N. Khinevich, D. Peckus, A. Tamulevičienė *et al.*, Size and crystallinity effect on the ultrafast optical response of chemically synthesized silver nanoparticles, Journal of Materiomics, https://doi.org/10.1016/j.jmat.2023.08.009

oscillations that decay together with ph-ph [7–9]. One of the pump-probe spectroscopy variants, transient absorption spectroscopy (TAS) is a primary choice for studying the kinetics of the LSP effect of different processes taking place in femto – to picosecond time scales. Despite intensive research in this field, the thermalization effect of hot electrons in metal NPs with the lattice via electron-phonon coupling, especially the NPs size and shape dependency of the process, has been controversially discussed in recent literature [8,10]. For example, theoretical studies [11] done on the temporal evolution of optically excited conduction electrons in small plasmon-supporting gold and silver NSs predict that the contribution of surface states (and the effect of the size of the NPs) to hot electron dynamics should be relatively small, as surface electrons only make a small fraction of the total conduction electrons for the particle sizes under consideration. In Refs. [8,12] it was experimentally shown that gold and silver NPs do not demonstrate a dependence of hot electron dynamics on size and shape, while copper NPs have shown some dependence on size [13]. Other studies indicated that the e-ph coupling time constants of Ag and Au NPs stop depending on size and shape if the diameter of the NPs becomes greater than 10 nm [8,14,15]. The importance of bulk phonons dependence on the degree of crystallinity of gold NPs was revealed – it was demonstrated that the e-ph coupling time constant increases when polycrystalline gold nanoprisms are annealed and transformed into nearly single-crystal nanospheres (NSs). On the other hand, a size-dependent e-ph coupling time constant was experimentally demonstrated in gold monocrystalline NSs [10]. The larger monocrystalline gold NPs have demonstrated a lower e-ph coupling time constant, which was explained as a result of the decreasing effect of electron-surface scattering and e-ph coupling constants approaching the values reported for bulk gold. Furthermore, the size dependences were outweighed by the effective scattering at grain boundaries [10]. Similar results were reported for gold NPs in Ref. [16] showing no influence of crystallinity on electron-phonon equilibration dynamics. It was suggested that the crystal twins present in the polycrystalline gold NPs do not significantly enhance the e-ph scattering.

Despite the manifold plasmonics-related applications of Ag NPs, the dependence of the e-ph interaction on crystallinity are almost not considered in the literature for Ag NPs in comparison to Au NPs. Studies of the dependence of e-ph coupling on size have been done for a long time [13,17,18] and in most cases no significant size effect was found [13,17–20]. This indicates that e-ph coupling dependence on size is very unlikely in Ag NPs. Nevertheless, in these articles, the crystalline structure was not examined; therefore, it is hard to discriminate between the size and crystallinity influence, which is being tackled in this work. In our studies, the difference in Ag NPs crystallinity was implied by the use of two different wet chemistry methods (reduction of silver salt and polyol synthesis).

Different preparation methods have been reported for the production of Ag NPs, including physical (laser ablation, sputtering, *etc.*), chemical (chemical reduction, green synthesis), photochemical methods, and microwave processing [1]. One of the popular methods used to produce silver nanospheres (Ag NSs) is the reduction of silver salt. In this method, monodisperse Ag NSs are synthesized via the reduction of silver nitrate using a mixture of two chemical agents: sodium citrate (SC) and tannic acid (TA). Combining SC and TA forms a complex with better reducing and stabilizing properties than SC and TA alone [21–23]. Whereas the polyol synthesis method is frequently utilized when non-spherical geometries are preferred, such as nanocubes (NCs), nanowires [24], *etc.* The method provides better control of the crystallinity and geometry of monocrystalline nanocubes (NC) and various polyhedrons were obtained [25,26].

In the current research, we have performed a systematic analysis of ultrafast processes taking place in highly monodispersed polycrystalline and monocrystalline Ag NPs colloids, investigating their LSP relaxation kinetics empowering TAS as a perspective tool for nanomaterial characterization. We explored the dependence of Ag nanoparticle shape, average size, and crystallinity on e-ph coupling. The e-ph coupling of single-crystal Ag NCs was size-invariant while e-ph coupling in polycrystalline Ag NSs had a linear size dependence.

2. Experimental section

2.1. Materials

Silver salt ($AgNO_3$), tannic acid (TA, $C_{76}H_{52}O_{46}$), and trisodium citrate (TC, $Na_3C_6H_5O_7$), 1,5-pentanediol, copper (II) chloride dihydrate ($CuCl_2{\cdot}2H_2O$), poly (vinylpyrrolidone) (PVP, M_w = 55,000 amu) were purchased from Sigma Aldrich and used without further purification. All solutions were prepared with Milli-Q water.

The synthesis of silver nanospheres (sequence a) was carried out according to the procedure developed by N. Bastus [23], where a complex of TA and TC is used and allows control over the nucleation, growth, and stabilization processes, leading to reproducible monodisperse Ag NSs. The method consists of two preparation steps: synthesis of silver seeds followed by growth of Ag NSs.

Synthesis of silver seeds. An aqueous solution (100 mL) containing 5 mmol/L TC and 0.012,5 mmol/L of TA was heated at 100 °C degrees for about 15 min under vigorous stirring. Subsequently, 1 mL of the silver salt solution (25 mmol/L) was injected. The synthesis lasted for 70 min.

Growth of Ag NSs. 19.5 mL of seeds were mixed with 16.5 mL of water and heated under 90 °C, 250 μL of 2.5 mmol/L TA, 100 μL of 25 mmol/L TC, and 250 μL of 25 mmol/L $AgNO_3$ were sequentially injected. After 30 min of heating, 1 mL of aliquots was extracted for further characterization. The solution produced was used as the seed solution for the subsequent synthesis step. The growth process was repeated four times. Aliquots were centrifuged at 7,000 r/min.

Monodisperse solutions of Ag nanocubes (sequence b) were prepared using a modified procedure based on the polyol synthesis method described in Refs. [26,27]. A copper chloride solution was prepared by dissolving 80 mg of $CuCl_2$ in 10 g of 1,5-pentanediol (PD; Acros). Then the two precursor solutions were prepared by dissolving 0.4 g of polyvinylpyrrolidone (PVP; Sigma-Aldrich) in 20 g of PD, and dissolving 35 μL of the above $CuCl_2$ solution and 0.4 g of $AgNO_3$ into 20 g of PD. Next, a 100 mL round bottom flask (RBF) was filled with 20 g of PD and heated to an internal temperature of 130 °C. Once the PD reached this temperature, 500 μL of the $AgNO_3$ solution was added to the RBF, then 30 s later 500 μL of the PVP solution was added to the RBF. This process was repeated every minute (*i.e.* Add the Ag^+ solution at 0:00, the PVP solution at 0:30, then Ag^+ at 1:00 and so on) until the desired nanocube size was achieved.

2.2. Analysis methods

UV–Vis absorbance spectra of the studied nanoparticles were recorded using a fibre-optic spectrometer AvaSpec-2048 (Avantes, The Netherlands) with a resolution of 1.2 nm in the 400–800 nm spectral range.

Transmission electron microscope (TEM) Tecnai G2 F20 X-TWIN (FEI, The Netherlands) with an FE source operated at 200 kV was used for the visualization of Ag NSs. 20 μL of the precipitates after centrifugation were dropped onto a TEM copper mesh and left to dry at room temperature. While Ag NCs were inspected with 2100F (JEOL) TEM operating at 200 kV.

The images were analyzed with ImageJ software and used for the estimation of the mean diameter/edge length and size distribution. For each sample, at least 50 NPs were measured to evaluate the mean diameter (D_M) and standard deviation (SD) - dispersity of the ensemble.

The X-ray diffraction method was used to study the crystalline structure of synthesized Ag NPs. The D8 Discover (Bruker AXS GmbH) diffractometer with a Cu $K_{\alpha 1}$ (λ = 0.154 nm) radiation source and parallel beam focusing geometry was used. Peak intensities were measured in the 30°–90° 2θ–θ with 0.012° step size. The DIFFRAC.EVA software was used to process the diffractograms. Considering that in all cases single-phase compounds were obtained, we performed the Rietveld refinement using X'pert HighScore Plus software to calculate crystallite sizes and lattice parameters based on Scherrer formula.

Transient absorption spectroscopy was used to study the ultrafast electron dynamics of Ag NPs. The HARPIA spectrometer (Light Conversion, Lithuania) was used for the TAS measurements. For the sample excitation with an ultrafast 290 fs pulse length and 1,030 nm wavelength Yb:KGW laser Pharos (Light Conversion, LT) with a regenerative amplifier at a 66.7 kHz repetition rate was used. Collinear optical parametric generator Orpheus and harmonic generator Lyra (Light Conversion, LT) were used to tune the pump beam wavelength to 350 nm with an excitation intensity of 0.6–13.6 μJ/cm^2, and a pulse width of about 290 fs. The samples of Ag NPs were probed with a white-light supercontinuum generated using a 2 mm thickness sapphire plate excited with the second harmonic (515 nm) of fundamental laser wavelength. The spectral range of the supercontinuum probe, as well as the detection range of the TAS signal relaxation dynamics, spanned wavelengths from 370 nm to 674 nm. The excitation beam was focused on a *ca.* 700 μm diameter spot, while the diameter of the spatially overlapped supercontinuum probe was *ca.* 500 μm [28].

3. Results and discussion

3.1. Properties of synthesized Ag NPs

The process of seeded growth chemical synthesis was repeated and after each growth cycle, Ag nanospheres of different sizes were obtained. The method based on a seed-growth approach allowed us the production of long-term stable aqueous colloidal Ag NS dispersions with narrow size distribution. The homogeneous growth of Ag seeds was kinetically controlled by adjusting the reaction parameters: concentrations of reducing agents, temperature, a silver precursor-to-seed ratio, and pH value as it was proposed in Ref. [23]. From the TEM analysis (Fig. 1) it was determined that Ag NSs diameters after the 1st growth process were 27.8 nm (noted as sample a1) and ranged to 56.6 nm (a4) after the 4th cycle. TEM microscopy analysis also revealed the polycrystalline structure of the Ag NSs (Fig. 1: a–d), while Ag nanocubes are monocrystalline structures (Fig. 1: e–h).

The increasing linear dimension was accompanied by the expected redshift of the absorbance peak (Fig. 2 a, c) related to the dipolar LSP resonance mode and the emergence of the second peak in the UV region associated with the quadrupole mode in larger Ag NSs (Fig. 2a) and Ag NCs (Fig. 2c). The mean diameter (D_M) and standard deviation (SD) of the synthesized Ag NSs, Ag NCs along with their size distribution are depicted in Fig. 2b and d, respectively.

3.2. Crystallinity analysis of Ag NPs

For each sample, the crystallite size and its standard deviation of the NPs were evaluated from the XRD patterns (Fig. 3) which show the diffraction peaks at $2\theta = 38.2°, 44.5°, 64.6°$, and $77.6°, 81.7°$ that correspond to the planes (111), (200), (220), (311), and (222) respectively of the face-centered cubic (FCC) silver structure, according to the standard powder diffraction card Joint Committee on Powder Diffraction Standards (JCPDS 04–0783).

The crystallite size was calculated using the Scherrer formula [29], and the results are presented in Table 1. The table includes the mean diameter of NSs and mean edge length of NCs with standard deviations defined from TEM analysis. One can see that for Ag NSs, the Ag NSs crystallite size increases together with the diameter (Table 1) and this is in good agreement with the applied synthesis approach where during the seeds-growth process, Ag ions reduce on the surface of Ag NPs avoiding new nucleation or agglomeration [23]. The growth mechanism enabled the formation of NPs with a controlled crystallite size, which is important in the quantitative studies of electron-phonon scattering, elucidating the effects of electron scattering in grain boundaries. The crystallite size of Ag NCs was bigger than their spherical counterparts and much closer to the linear dimension of the nanoparticles, a similar result was obtained for the monocrystalline silver nanocubes in Ref. [30] and gold nanospheres in Ref. [31].

3.3. Nonlinear optical spectroscopy

3.3.1. Excited-state relaxation dynamics

TAS measurements were employed to characterize Ag NPs, including defectiveness and structure. The TAS measurement data for Ag NSs at different probe wavelengths and different pump excitation intensities are shown in Figs. S1–S5. Electron-phonon coupling (e-ph, τ_1) and phonon-phonon (ph-ph, τ_2) scattering time constants were calculated from the TAS signal decay traces (Figs. S2–S5) by fitting traces at the negative and positive peaks of the TAS spectra using the exponential decay function with one or two components (1) [26,32].

$$I(t) = A_1 e^{-\frac{t}{\tau_1}} + A_2 e^{-\frac{t}{\tau_2}} + I_0 \quad (1)$$

where A_1; A_2 and τ_1; τ_2 are the amplitudes and time constants of decay, respectively, while I_0 represents the background of the TAS signal [32]. The fitting results for Ag NSs are summarized in Table S1, while the Ag NCs data analysis depicted in Figs. S7–S10 are compiled in Table S2.

For the investigation of coupling time constants, pump excitation intensity measurements were performed (Fig. S6 and Fig. S11). From these measurements, the e-ph coupling time constant ($\tau_{e\text{-}ph}$) was extrapolated from τ_1 under 0 excitation intensity as [13,33,34]. The extrapolated e-ph coupling time constants are shown in Table 1.

Damping of the excited state depends on e-ph couping. It varied from 0.69 ps to 0.96 ps for Ag NSs and from 0.85 ps to 1.05 ps for Ag NCs (Table S1). A relatively weak TAS signal relaxation component was observed and that can be attributed to ph-ph scattering whose durations ranged from 10 ps to 206 ps for Ag NSs (Table S1) and 22–73 ps for Ag NCs (Table S2).

The two-temperature model was used for the calculation of the electron-phonon coupling constant [8] and the electron-phonon coupling constant G was found based on the equation [13,33,35]:

$$G = \gamma T_0 / \tau_{e\text{-}ph} \quad (2)$$

where γ equals 65 J·m^{-3}·K^{-2} [36]; T_0 is the ambient temperature (293 K); $\tau_{e\text{-}ph}$ is hot-electron lifetimes (provided in Table 1).

The polycrystalline Ag NSs indicated a decrease in the e-ph coupling time constant with increasing mean diameter (Fig. 4a)

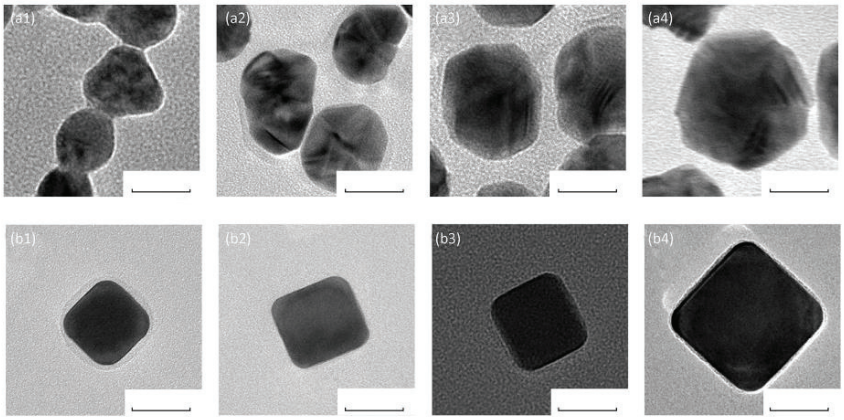

Fig. 1. TEM analysis of the Ag NPs. Top row: Ag nanospheres after 1st process of growth (a1); after 2nd (a2); after 3rd (a3), and after 4th (a4). Bottom row: Ag nanocubes with edge lengths of 32 nm (b1), 35 nm (b2), 37 nm (b3), and 55 nm (b4). The scale bar is 25 nm.

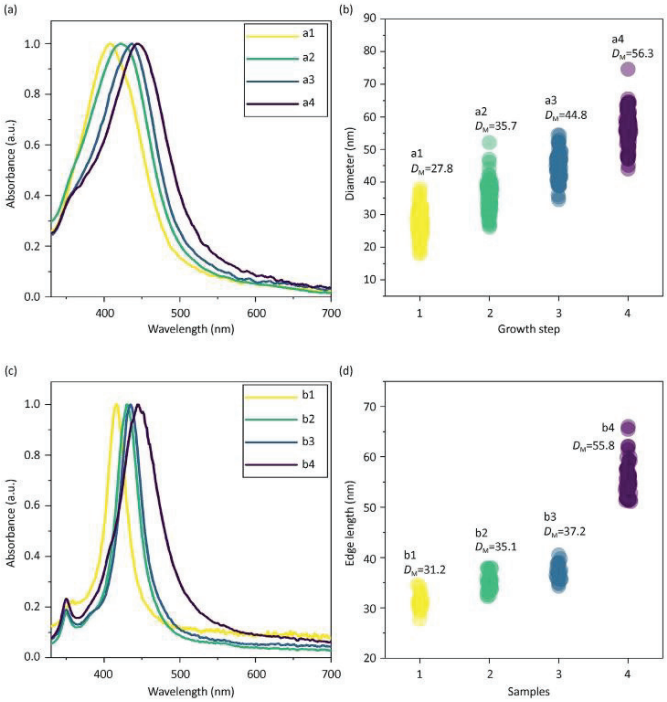

Fig. 2. UV–Vis absorbance spectra (a, c) and size distribution (b, d) of Ag NSs (a, b) and Ag NCs (c, d).

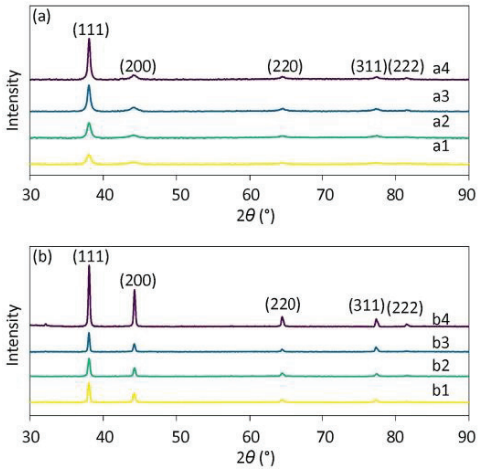

Fig. 3. XRD patterns of Ag NPs: nanospheres (a) and nanocubes (b). The peaks are assigned to diffraction from the planes (100), (200), (220), and (311) of silver (spectra are offset for clarity).

while the monocrystalline Ag NCs seem to be independent of the edge length (Fig. 4a). We also calculated the e-ph coupling time constant dependence on volume of Ag NSs and Ag NCs that corresponds well with data in Fig. 4a (Fig. S12). According to theoretical predictions, the absence of size-dependent e-ph coupling in Au and Ag NPs is due to the relatively small contributions of surface phonon modes to the e-ph coupling process [13] (in case they have a polycrystalline structure [31]). On the other hand, the dependence of the time constant of e-ph coupling on the NPs size has been reported for Cu NPs [13,37] and monocrystalline Au NPs [31]. In these cases, the dependence of the e-ph time constant was attributed to the stronger influence of surface phonon modes on the e-ph coupling process, and the increase in the size of NP has led to longer e-ph coupling time constants. However, this contradicts our obtained dependencies presented in Fig. 4 a. It is also known that the e-ph coupling time depends on the crystallinity of the NPs [33], and the grain boundaries are important to consider in all modes of plasmon damping [31]. To verify this hypothesis, we chose the ratio (Crystallite size/Linear dimension of Ag NPs)^2 (Table 1) for the analysis of the decay time constant of the e-ph coupling, assuming that the higher ratio of crystallite size to the size of NPs corresponds to a more pronounced monocrystalline structure and fewer grain boundaries of the NPs. In this ratio:

$$(\text{Crystallite size/Linear dimension of Ag NPs})^2 \quad (3)$$

Crystallite size – parameter calculated with Scherrer formula from Ag NPs sample XRD data; Linear dimension of Ag NPs – linear dimension is the length picked to evaluate size of Ag NPs. It is diameter for Ag NSs and edge length for Ag NCs. We use Eq. (3) to describe generally both types Ag NPs – for Ag NSs we use eq. (Crystallite size/Diameter of Ag NSs)^2 while for Ag NCs - (Crystallite size/Edge Length of Ag NCs)^2.

The linear dependence of the e-ph coupling decay time constant on (Crystallite size/Diameter of Ag NSs)^2 (Fig. 4b) shows that the e-ph coupling time constant for NSs is size-dependent, and this dependence correlates with the crystallinity of the NP. These findings support the results of other researchers who have shown that the grain boundaries in polycrystalline Au NCs increase the efficiency of coupling of hot electrons with phonons, making the e-ph coupling process faster [12,31]. In this way, the reviled dependence on the time constant e-ph coupling on (Crystallite size/Linear dimension of Ag NP)^2 could in the future be used for control of the crystalline structure of plasmonic metal NPs.

The analysis of e-ph coupling time constants was done for the Ag nanoparticles with sizes that provided us with the most reliable TAS data and therefore the most reliable e-ph coupling time constants. The extension of the range of sizes of samples becomes problematic, because smaller nanoparticles absorb more and scatter less light leading to a strong TAS signal but the smallest samples (below linear size 28 nm) are unstable therefore their time resolved spectroscopy becomes complicated. Investigation of sizes above 60 nm is also challenging because both the absorption and scattering from the nanoparticles prevail and lead to a decrease in TAS signal amplitude and larger noises which makes the calculation of e-ph coupling with huge error margins especially for Ag NSs samples. For comparison we used only Ag NCs that have most similar sizes/volume to Ag NSs. All in all, in our studies we chose to investigate the most reliable results demonstrating Ag nanoparticle sizes for the e-ph coupling time constant analysis. Although we believe that the size range could be extended in the study but some improvements to the synthesis and stability of Ag NSs need to be improved in the future.

4. Conclusion

The chemical synthesis method based on a seed-growth approach applied for the production of long-term stable aqueous colloidal dispersions of spherical silver nanoparticles with narrow, controlled size distribution (mean diameter 28–57 nm), and variable crystallinity proven by TEM, XRD and TAS measurements, allowed systematic studies of the e-ph coupling process in plasmon relaxation dynamics. Comparing similar mean linear dimensions of

Table 1
The mean sizes of Ag NSs (a1–a4) and Ag NCs (b1–b4) based on TEM analysis, crystallite size based on XRD data, electron-phonon coupling time constant $\tau_{e\text{-}ph}$ calculated from TAS data (eq (1)), e-ph coupling constant G based on eq. (2).

Sample	Linear dimension (Diameter/Edge length) (nm)	Crystallite size (nm)	Ratio (Crystallite size/Linear dimension)	Ratio (Crystallite size/Linear dimension)^2	$\tau_{e\text{-}ph}$ (ps)	$G \times 10^{16}$ (W/(m^3·K))
a1	27.8 ± 4.1	9.8 ± 3.1	0.349	0.122	0.96 ± 0.020	1.98
a2	35.7 ± 4.9	10.5 ± 3.8	0.310	0.096	0.90 ± 0.002	2.12
a3	44.7 ± 4.4	13.0 ± 4.8	0.291	0.085	0.77 ± 0.003	2.47
a4	56.6 ± 5.6	15.0 ± 6.6	0.272	0.074	0.69 ± 0.020	2.76
b1	31.3 ± 1.7	27.1 ± 1.4	0.869	0.755	0.86 ± 0.040	2.21
b2	35.1 ± 1.7	27.8 ± 1.9	0.792	0.627	0.94 ± 0.010	2.03
b3	37.2 ± 2.2	30.9 ± 4.5	0.831	0.690	0.85 ± 0.010	2.24
b4	55.8 ± 3.6	32.1 ± 3.8	0.575	0.331	0.85 ± 0.020	2.24

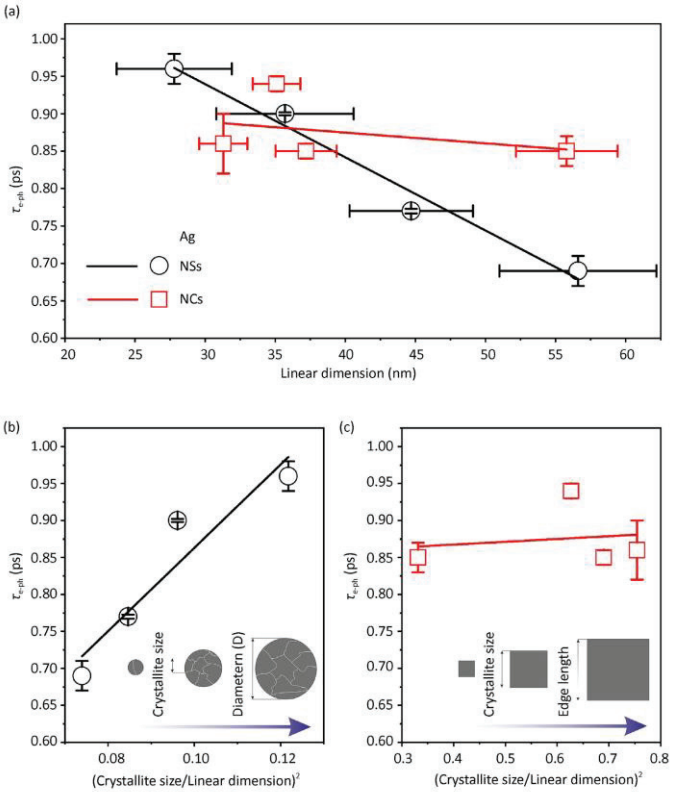

Fig. 4. Dependence of the e-ph coupling time constant ($\tau_{e\text{-}ph}$) on the diameter of Ag NSs and the edge length of the NCs (a). Estimated based on the negative TAS signal, (a), e-ph coupling time constant dependence on (Crystallite size/diameter of Ag NSs)^2 (b); (Crystallite size/edge length of Ag NCs)^2 (c). The black and red lines show the guide for eyes. D – diameter of Ag NSs, EL – edge length of Ag NCs. The insets show schematic image of Ag NSs samples (b) and Ag NCs samples (c).

chemically synthesized polycrystalline and monocrystalline silver particles it was obtained that their electron-phonon relaxation time constants follow different dependencies. The polycrystalline nanoparticles indicated faster relaxation with increasing size, while the decaying of monocrystalline counterparts was indifferent to the size. We have demonstrated that the e-ph coupling decay time constant depends linearly on (Crystallite size/Linear dimension of Ag NPs)^2 for polycrystalline Ag nanospheres, while monocrystalline Ag nanocubes do not show any clear dependence on this ratio. This fact illustrates that e-ph coupling time could be used to evaluate crystallinity and crystallite size in plasmonic metal nanoparticles when the size (surface area) of the nanoparticle is known.

Declaration of competing interest

The authors declare that they have no known competing financial interests or personal relationships that could have appeared to influence the work reported in this paper.

Acknowledgments

The studies were performed within the LaSensA project carried out under the M-ERA.NET 2 scheme (European Union's Horizon 2020 Research and Innovation Program, grant No. 685451) and co-funded by the Research Council of Lithuania (LMTLT), agreement No. S-M-ERA.NET-21-2, the National Science Centre of Poland, project No. 2020/02/Y/ST5/00086, and the Saxon State Ministry for Science, Culture and Tourism (Germany), grant No. 100577922, as well as from the tax funds on the basis of the budget passed by the Saxon state parliament.

Appendix A. Supplementary data

Supplementary data to this article can be found online at https://doi.org/10.1016/j.jmat.2023.08.009.

References

[1] Güzel R, Erdal G. Synthesis of silver nanoparticles. Silver Nanoparticles - Fabr.

Charact. Appl 2018;32:137–44. InTech.
[2] Xu L, Wang Y-Y, Huang J, Chen C-Y, Wang Z-X, Xie H. Silver nanoparticles: synthesis, medical applications and biosafety. Theranostics 2020;10:8996–9031.
[3] Yang Q, Hu M, Guo J, Ge Z, Feng J. Synthesis and enhanced photocatalytic performance of Ag/AgCl/TiO_2 nanocomposites prepared by ion exchange method. J Mater 2018;4:402–11.
[4] Mukherji S, Bharti S, Shukla G, Mukherji S. Synthesis and characterization of size- and shape-controlled silver nanoparticles. Phys. Sci. Rev. 2019;4:20170082.
[5] Zhang J, Zhang B, Yao S, Li H, Chen C, Bala H, et al. Improved triethylamine sensing properties of fish-scale-like porous SnO_2 nanosheets by decorating with Ag nanoparticles. J Mater 2022;8:518–25.
[6] Schlücker S. Surface-Enhanced Raman spectroscopy: concepts and chemical applications. Angew Chem Int Ed 2014;53:4756–95.
[7] Mahmoud MA, O'Neil D, El-Sayed MA. Shape- and symmetry-dependent mechanical properties of metallic gold and silver on the nanoscale. Nano Lett 2015;15. 2764–2764.
[8] Hartland GV. Optical studies of dynamics in noble metal nanostructures. Chem Rev 2011;111:3858–87.
[9] Su M-N, Ostovar B, Gross N, Sader JE, Chang W-S, Link S. Acoustic vibrations and energy dissipation mechanisms for lithographically fabricated plasmonic nanostructures revealed by single-particle transient extinction spectroscopy. J Phys Chem C 2021;125:1621–36.
[10] Staechelin YU, Hoeing D, Schulz F, Lange H. Size-dependent electron–phonon coupling in monocrystalline gold nanoparticles. ACS Photonics 2021;8:752–7.
[11] Saavedra JRM, Asenjo-Garcia A, García De Abajo FJ. Hot-electron dynamics and thermalization in small metallic nanoparticles. ACS Photonics 2016;3:1637–46.
[12] Huang W, Qian W, El-Sayed MA, Ding Y, Wang ZL. Effect of the lattice crystallinity on the Electron–Phonon relaxation rates in gold nanoparticles. J Phys Chem C 2007;111:10751–7.
[13] Darugar Q, Qian W, El-Sayed MA, Pileni MP. Size-dependent ultrafast electronic energy relaxation and enhanced fluorescence of copper nanoparticles. J Phys Chem B 2006;110:143–9.
[14] Arbouet A, Voisin C, Christofilos D, Langot P, Fatti N Del, Vallée F, et al. Electron-phonon scattering in metal clusters. Phys Rev Lett 2003;90:4.
[15] Beane G, Devkota T, Brown BS, Hartland GV. Ultrafast measurements of the dynamics of single nanostructures: a review. Rep Prog Phys 2019;82:016401.
[16] Goubet N, Tempra I, Yang J, Soavi G, Polli D, Cerullo G, et al. Size and nanocrystallinity controlled gold nanocrystals: synthesis, electronic and mechanical properties. Nanoscale 2015;7:3237–46.
[17] Roberti TW, Smith BA, Zhang JZ. Ultrafast electron dynamics at the liquid-metal interface: femtosecond studies using surface plasmons in aqueous silver colloid. J Chem Phys 1995;102:3860–6.
[18] Hodak JH, Martini I, Hartland GV. Spectroscopy and dynamics of nanometer-sized noble metal particles. J Phys Chem B 1998;102:6958–67.
[19] Jiang J, Miao F, Wu W, Kong D, Ridi B, Gao Y. Size effect on nonlinear optical properties and ultrafast dynamics of silver nanoparticles. Opt Express 2022;30:19533.
[20] Maurya SK, Rout A, Ganeev RA, Guo C. Effect of size on the saturable absorption and reverse saturable absorption in silver nanoparticle and ultrafast dynamics at 400 nm. J Nanomater 2019;2019:1–12.
[21] Ranoszek-Soliwoda K, Tomaszewska E, Socha E, Krzyczmonik P, Ignaczak A, Orlowski P, et al. The role of tannic acid and sodium citrate in the synthesis of silver nanoparticles. J Nanoparticle Res 2017;19:273.
[22] Restrepo CV, Villa CC. Synthesis of silver nanoparticles, influence of capping agents, and dependence on size and shape: a review. Environ Nanotechnol Monit Manag 2021;15:100428.
[23] Bastús NG, Merkoçi F, Piella J, Puntes V. Synthesis of highly monodisperse citrate-stabilized silver nanoparticles of up to 200 nm: kinetic control and catalytic properties. Chem Mater 2014;26:2836–46.
[24] Sun Y, Yin Y, Mayers BT, Herricks T, Xia Y. Uniform silver nanowires synthesis by reducing $AgNO_3$ with ethylene glycol in the presence of seeds and poly(-Vinyl pyrrolidone). Chem Mater 2002;14:4736–45.
[25] Henzie J, Grünwald M, Widmer-Cooper A, Geissler PL, Yang P. Self-assembly of uniform polyhedral silver nanocrystals into densest packings and exotic superlattices. Nat Mater 2012;11:131–7.
[26] Peckus D, Rong H, Stankevičius L, Juodenas M, Tamulevičius S, Tamulevičius T, et al. Hot electron emission can lead to damping of optomechanical modes in core-shell Ag@TiO_2 nanocubes. J Phys Chem C 2017;121:24159–67.
[27] Tao A, Sinsermsuksakul P, Yang P. Polyhedral silver nanocrystals with distinct scattering signatures. Angew Chem Int Ed 2006;45:4597–601.
[28] Peckus D, Tamuleviciene A, Mougin K, Spangenberg A, Vidal L, Bauerlin Q, et al. Shape influence on the ultrafast plasmonic properties of gold nanoparticles. Opt Express 2022;30:27730–45.
[29] Patterson AL. The scherrer formula for X-ray particle size determination. Phys Rev 1939;56:978–82.
[30] Helmlinger J, Prymak O, Loza K, Gocyla M, Heggen M, Epple M. On the crystallography of silver nanoparticles with different shapes. Cryst Growth Des 2016;16:3677–87.
[31] Staechelin YU, Hoeing D, Schulz F, Lange H. Size-dependent electron-phonon coupling in monocrystalline gold nanoparticles. ACS Photonics 2021;8:752–7.
[32] Peckus D, Meškinis Š, Vasiliauskas A, Rajackaitė E, Andrulevičius M, Kopustinskas V, et al. Structure and optical properties of diamond like carbon films containing aluminium and alumina. Appl Surf Sci 2020;529:147040.
[33] Huang W, Qian W, El-Sayed MA, Ding Y, Wang ZL. Effect of the lattice crystallinity on the electron-phonon relaxation rates in gold nanoparticles. J Phys Chem C 2007;111:10751–7.
[34] Jain PK, Qian W, El-Sayed MA. Ultrafast electron relaxation dynamics in coupled metal nanoparticles in aggregates. J Phys Chem B 2006;110:136–42.
[35] Lysenko S, Jimenez J, Zhang G, Liu H. Nonlinear optical dynamics of glass-embedded silver nanoparticles. J Electron Mater 2006;35:1715–21.
[36] Bigot J-Y, Halté V, Merle J-C, Daunois A. Electron dynamics in metallic nanoparticles. Chem Phys 2000;251:181–203.
[37] Peckus D, Tamulevičius T, Meškinis Š, Tamulevičienė A, Vasiliauskas A, Ulčinas O, et al. Linear and nonlinear absorption properties of diamond-like carbon doped with Cu nanoparticles. Plasmonics 2016;12:47–58.

Supplementary material

Size and crystallinity effect on the ultrafast optical response of the chemically synthesized silver nanoparticles

Nadzeya Khinevich[a], Domantas Peckus[a,b]*, Asta Tamulevičienė[a,b], Gerda Klimaitė[b], Joel Henzie[c], Tomas Tamulevičius[a,b], Sigitas Tamulevičius[a,b]*

[a]Institute of Materials Science of Kaunas University of Technology, K. Baršausko St. 59, LT-51423, Kaunas, Lithuania

[b]Department of Physics, Kaunas University of Technology, Studentų st. 50, LT-51368, Kaunas, Lithuania

[c]International Center for Materials Nanoarchitectonics (WPI-MANA), National Institute for Materials Science (NIMS), Tsukuba, 305-0044, Japan

*Corresponding authors. Tel: +370 (37) 313432. D. Peckus: domantas.peckus@ktu.lt; S. Tamulevičius: sigitas.tamulevicius@ktu.lt.

1. Silver nanospheres

Transient absorption spectroscopy data

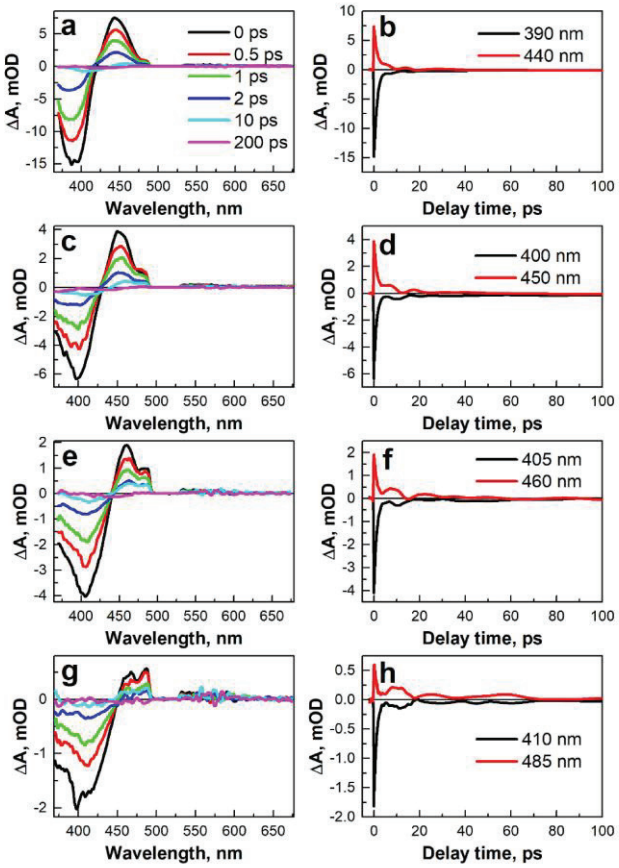

Fig. S1. TAS spectra and traces of samples *a1* (**a, b**), *a2* (**c, d**), *a3* (**e, f**), *a4* (**g, h**).

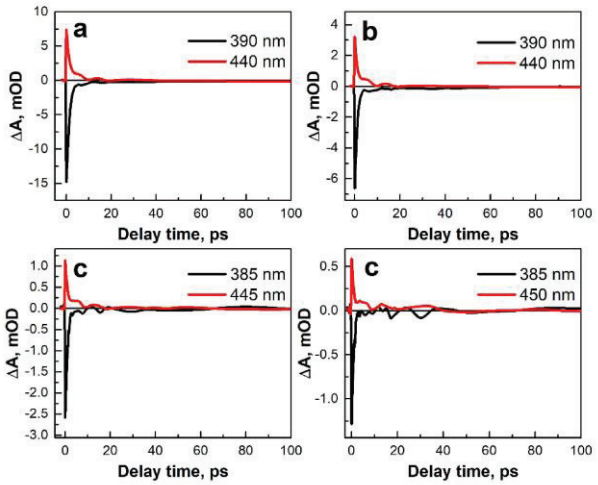

Fig. S2. TAS traces of *a1* sample under excitation at 12.8 (**a**), 6.4 (**b**), 3.2 (**c**), and 1.6 μJ/cm^2 (**d**).

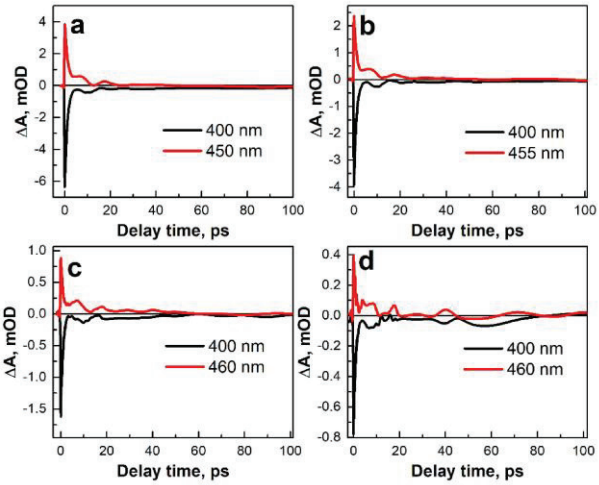

Fig. S3. TAS traces of *a2* sample under excitation at 13.6 (**a**), 8 (**b**), 4 (**c**), and 2 μJ/cm^2 (**d**).

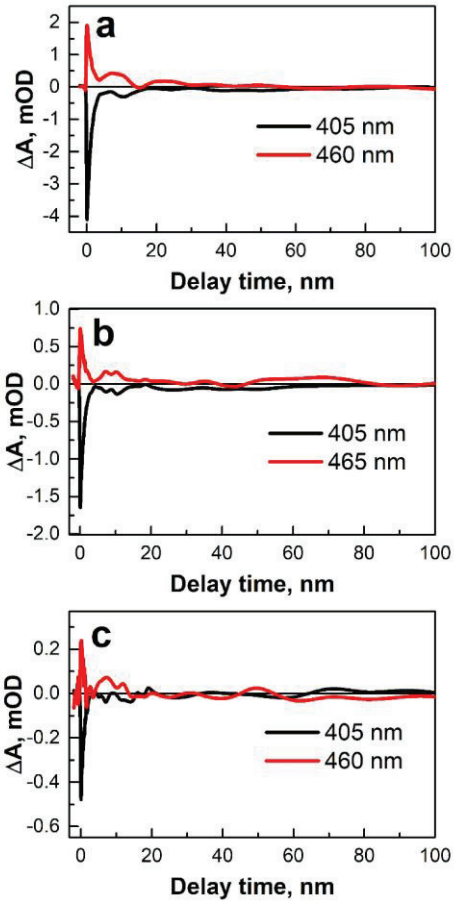

Fig. S4. TAS traces of *a3* sample under excitation at 13.6 (**a**), 8 (**b**), and 4 μJ/cm^2 (**c**).

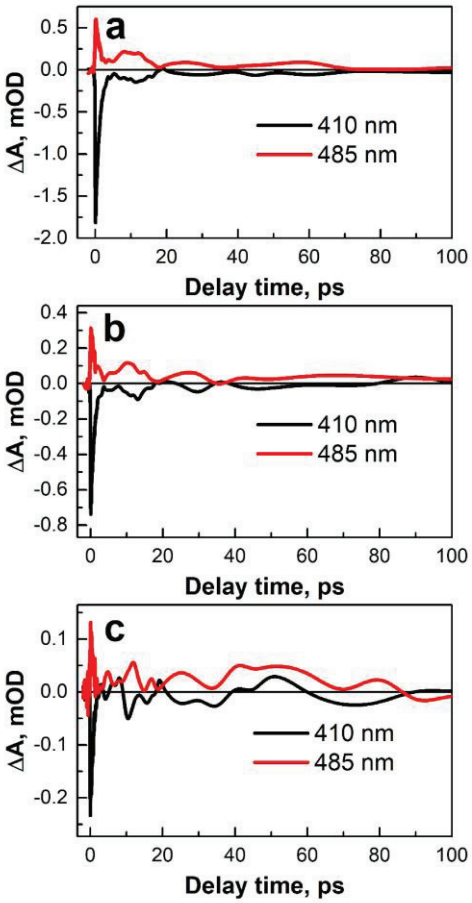

Fig. S5. TAS traces of *a4* sample under excitation at 13.6 (**a**), 8 (**b**), and 4 μJ/cm^2 (**c**).

Table S1. Fitting parameters of the *a1-a4* Ag NSs TAS traces using eq. (1) under different excitation intensities and at different probe wavelengths.

Sample	Excitation intensity ($\mu J/cm^2$)	Probe wavelength (nm)	τ_1 (ps)	A_1	τ_2 (ps)	A_2	R^2
a1	12.8	390	1.44±0.02	1.04±0.01	206.3±466.7	0.02±0.02	0.9974
		440	1.32±0.03	0.91±0.01	12.9±2.1	0.13±0.01	0.9986
	6.4	390	1.15±0.02	0.99±0.01	144.7±192.0	0.03±0.01	0.9962
		440	0.93±0.02	0.86±0.01	10.8±1.4	0.17±0.01	0.9978
	3.2	385	1.09±0.02	1.02±0.01	-	-	0.9945
		445	0.91±0.03	0.91±0.01	19.2±4.1	0.15±0.02	0.9942
	1.6	385	1.03±0.03	0.98±0.01	-	-	0.9830
		450	0.78±0.03	0.96±0.02	29.3±10.4	0.13±0.02	0.9850
a2	13.6	400	1.12±0.02	0.91±0.01	133.6±162.2	0.03±0.02	0.9940
		450	1.14±0.03	0.90±0.01	21.4±4.2	0.16±0.01	0.9957
	8	400	1.03±0.02	0.92±0.01	72.7±71.3	0.03±0.01	0.9942
		455	0.96±0.03	0.85±0.01	24.3±4.1	0.17±0.01	0.9953
	4	400	0.96±0.02	0.91±0.01	177.9±301.0	0.04±0.03	0.9889
		460	0.83±0.04	0.89±0.02	59.7±18.5	0.18±0.02	0.9815
	2	400	0.93±0.03	0.85±0.02	189.0±279.6	0.07±0.04	0.9770
		460	0.74±0.06	0.91±0.03	49.5±22.9	0.21±0.03	0.9424
a3	13.6	405	1.15±0.02	0.99±0.01	109.6±57.0	0.05±0.01	0.9973
		460	0.98±0.05	0.92±0.02	27.9±7.0	0.20±0.02	0.9867
	8	405	0.99±0.02	0.97±0.01	97.8±79.0	0.04±0.01	0.9951
		465	0.99±0.06	0.90±0.02	34.3±26.3	0.10±0.02	0.9656
	4	405	0.88±0.03	0.96±0.02	-	-	0.9690
		460	0.52±0.08	1.10±0.09	52.1±53.5	0.18±0.06	0.7719
a4	13.6	410	1.10±0.02	0.96±0.01	102.5±56.5	0.06±0.01	0.9953
		485	0.84±0.07	0.88±0.04	72.5±25.3	0.28±0.03	0.9415
	8	410	0.91±0.03	0.98±0.01	60.8±45.9	0.06±0.01	0.9888
		485	0.81±0.06	0.93±0.04	206.8±188.7	0.30±0.14	0.9114
	4	410	0.84±0.05	0.90±0.03	-	-	0.9086
		485	0.65±0.09	0.80±0.06	-	-	0.6697

Fig. S6 was prepared based on Table S1.

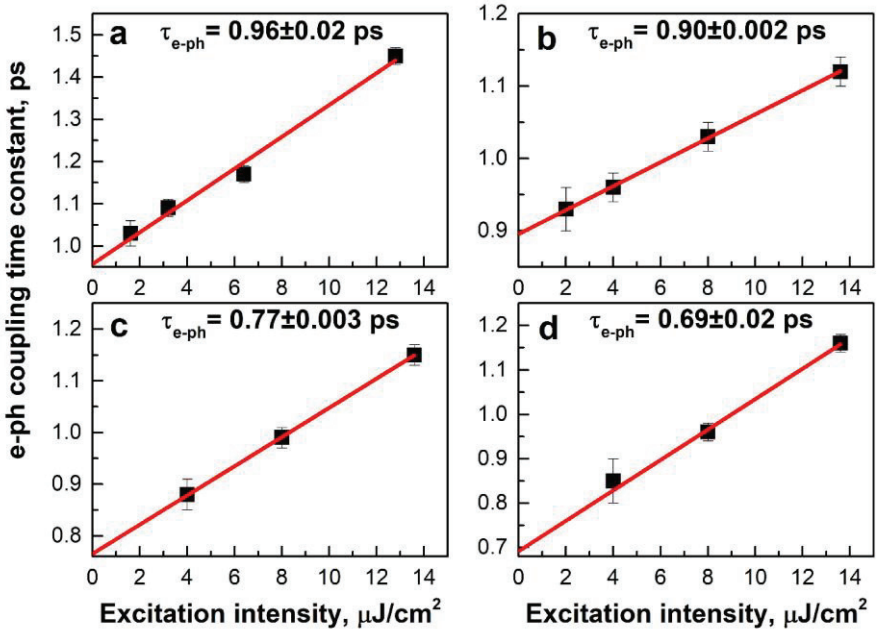

Fig. S6. Electron-phonon coupling time constant $\tau_{e\text{-}ph}$ dependence on excitation intensity for samples *a1* (**a**), *a2* (**b**), *a3* (**c**), *a4* (**d**) based on negative TAS signal. The data were fitted with linear function and extrapolated to 0 excitation intensity. The numbers indicate obtained *e-ph* coupling time constants.

2. Silver nanocubes

Transient absorption spectroscopy data

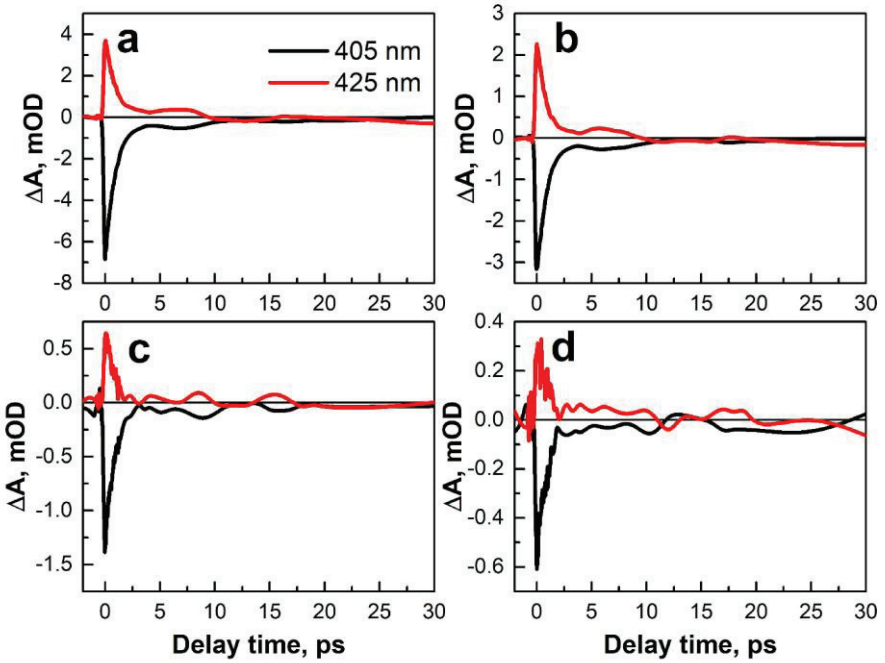

Fig. S7. TAS traces of *b1* sample under excitation at 11.2 (**a**), 8.8 (**b**), 4 (**c**), and 2 μJ/cm^2 (**d**).

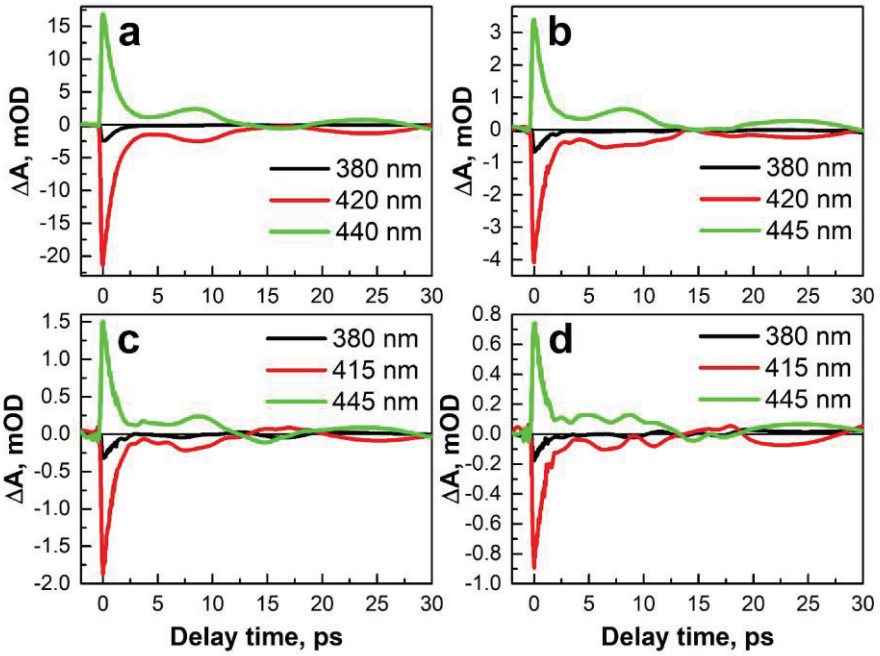

Fig. S8. TAS traces of *b2* sample under excitation at 9.6 (**a**), 2.4 (**b**), 1.2 (**c**), and 0.6 μJ/cm^2 (**d**).

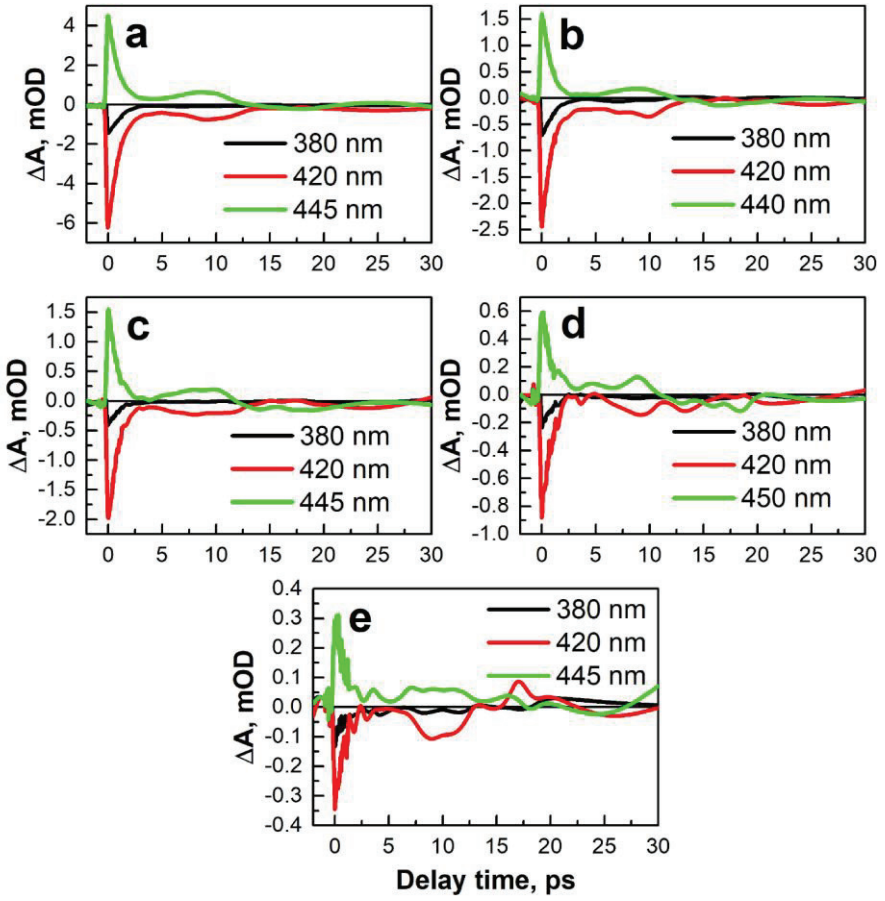

Fig. S9. TAS traces of *b3* sample under excitation at 9.6 (**a**), 4.8 (**b**), 2.4 (**c**), 1.2 (**d**), and 0.64 μJ/cm^2 (**e**).

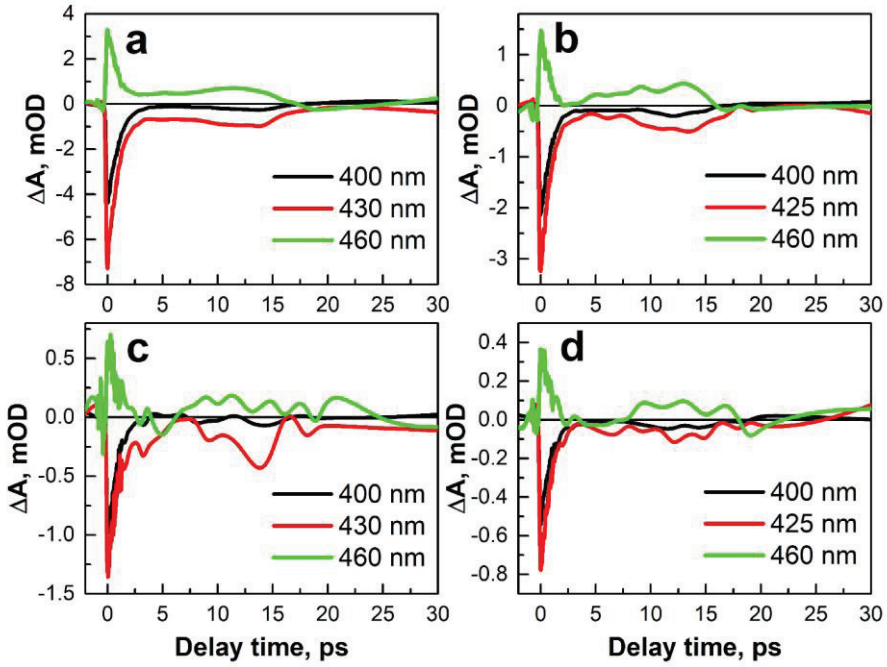

Fig. S10. TAS traces of *b4* sample under excitation at 9.6 (**a**), 4.8 (**b**), 2.4 (**c**), and 1.2 μJ/cm^2 (**d**).

Table S2. Fitting parameters of the *b1-b4* Ag NCs TAS traces using eq. (1) under different excitation intensities and at different probe wavelengths.

Sample	Excitation intensity ($\mu J/cm^2$)	Probe wavelength (nm)	τ_1 (ps)	A_1	τ_2 (ps)	A_2	R^2
b1	11.2	405 nm	0.96±0.01	0.95±0.01	72.7±16.3	0.10±0.01	0.9948
		430 nm	0.94±0.02	0.94±0.02	46.1±3.6	0.22±0.01	0.9960
	8.8	405 nm	1.01±0.02	0.97±0.01	-	-	0.9946
		425 nm	0.87±0.04	1.02±0.02	22.1±13.0	0.20±0.04	0.9880
	4	405 nm	0.91±0.02	1.02±0.01	-	-	0.991
		425 nm	0.90±0.03	1.06±0.02	-	-	0.977
	2	405 nm	0.87±0.02	0.90±0.01	-	-	0.9872
		425 nm	0.80±0.05	1.12±0.03	-	-	0.9358
b2	9.6	420 nm	1.05±0.02	0.95±0.01	-	-	0.9951
		440 nm	1.04±0.02	1.02±0.01	-	-	0.9894
	2.4	420 nm	0.96±0.02	0.93±0.01	-	-	0.9900
		445 nm	0.92±0.03	0.95±0.01	-	-	0.98
	1.2	415 nm	0.97±0.03	1.01±0.01	-	-	0.986
		445 nm	0.90±0.03	0.99±0.02	-	-	0.980
	0.6	415 nm	0.94±0.03	0.97±0.02	-	-	0.977
		445 nm	0.81±0.03	1.00±0.02	-	-	0.969
b3	9.6	420 nm	1.01±0.02	0.94±0.01	-	-	0.9951
		445 nm	0.97±0.02	0.96±0.01	-	-	0.9889
	4.8	420 nm	0.94±0.02	0.93±0.01	-	-	0.9899
		440 nm	0.89±0.02	1.04±0.01	-	-	0.9851
	2.4	420 nm	0.87±0.02	1.03±0.01	-	-	0.986
		445 nm	0.81±0.03	1.05±0.02	-	-	0.977
	1.2	420 nm	0.89±0.04	0.92±0.01	-	-	0.963
		450 nm	0.84±0.06	1.06±0.04	-	-	0.914
	0.64	420 nm	0.85±0.07	0.91±0.04	-	-	0.8711
		445 nm	0.82±0.10	0.86±0.06	-	-	0.778
b4	9.6	430 nm	0.98±0.02	0.90±0.01	-	-	0.9915
		460 nm	0.91±0.04	0.94±0.02	-	-	0.9567
	4.8	425 nm	0.88±0.02	0.96±0.01	-	-	0.9853
		460 nm	0.70±0.05	0.96±0.03	-	-	0.9060

	2.4	430 nm	0.89±0.06	0.88±0.03	-	-	0.908
		460 nm	0.72±0.10	1.02±0.09	-	-	0.709
	1.2	425 nm	0.88±0.03	1.00±0.02	-	-	0.977
		460 nm	0.82±0.08	1.01±0.05	-	-	0.848

Fig. S11 was prepared based on Table S2.

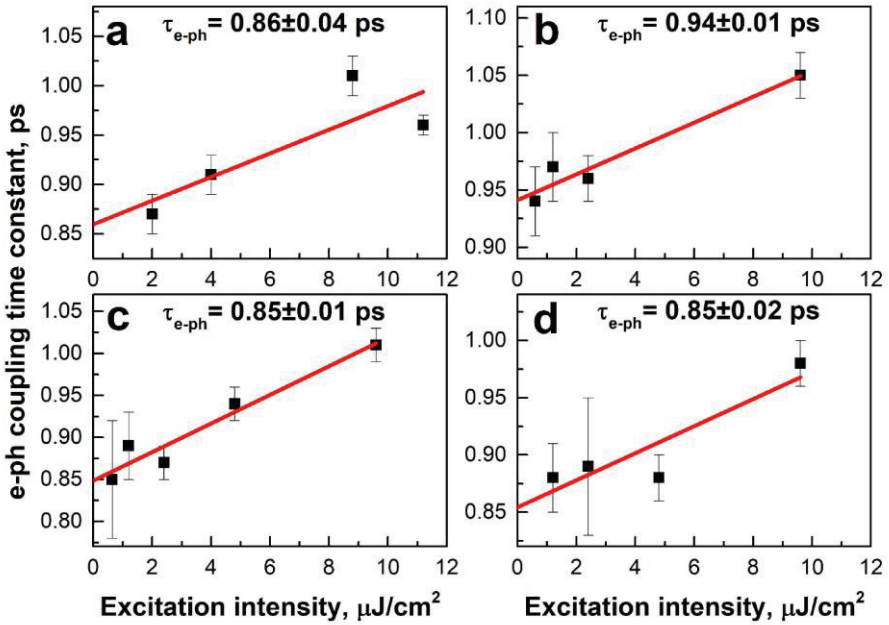

Fig. S11. Electron-phonon coupling time constant $\tau_{e\text{-}ph}$ dependence on excitation intensity for samples *b1* (**a**), *b2* (**b**), *b3* (**c**), *b4* (**d**) based on negative TAS signal. The data were fitted with linear function and extrapolated to 0 excitation intensity. The numbers indicate obtained *e-ph* coupling time constants.

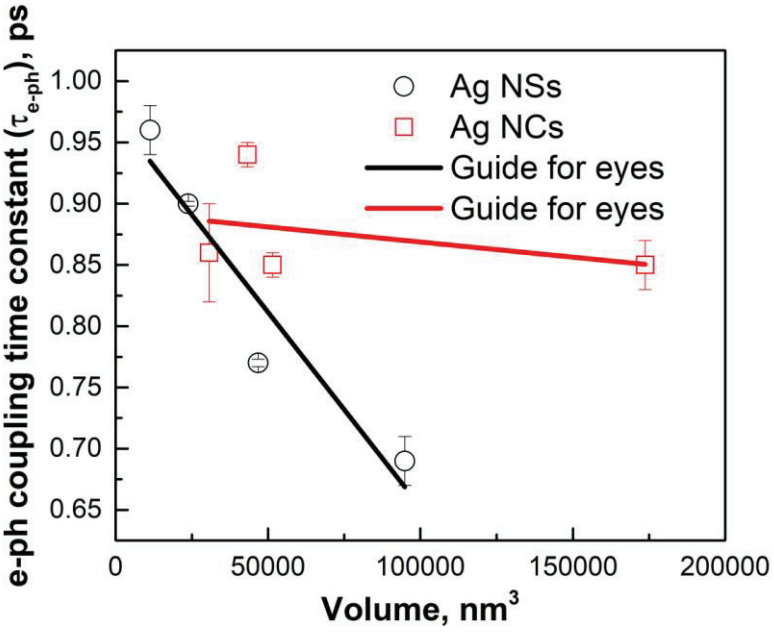

Fig. S12. Dependence of the *e-ph* coupling time constant on the volume of Ag NSs and NCs.

Paper III: Tailoring Mesoporous Silicon Surface to Form a Versatile Template for Nanoparticle Deposition

Nadzeya Khinevich, Mindaugas Juodėnas, Asta Tamulevičienė, Hanna Bandarenka, Sigitas Tamulevičius

Coatings 11 (6), 699 (2021).

coatings

MDPI

Article

Tailoring Mesoporous Silicon Surface to Form a Versatile Template for Nanoparticle Deposition

Nadzeya Khinevich [1,*], Mindaugas Juodėnas [1], Asta Tamulevičienė [1,2], Hanna Bandarenka [3,4] and Sigitas Tamulevičius [1,2,*]

[1] Institute of Materials Science, Kaunas University of Technology, 59 K. Baršausko St., 51423 Kaunas, Lithuania; mindaugas.juodenas@ktu.lt (M.J.); asta.tamuleviciene@ktu.lt (A.T.)
[2] Department of Physics, Kaunas University of Technology, 50 Studentu St., 51368 Kaunas, Lithuania
[3] Applied Plasmonics Laboratory, Belarusian State University of Informatics and Radioelectronics, 6 Brovka St., 220013 Minsk, Belarus; h.bandarenka@bsuir.by
[4] The Polytechnic School, Ira A. Fulton Schools of Engineering, Arizona State University, 6075 S. Innovation Way West, Mesa, AZ 85212, USA
* Correspondence: nadzeya.khinevich@ktu.edu (N.K.); sigitas.tamulevicius@ktu.lt (S.T.)

Abstract: Porous silicon (PS) can be used as a loading template in sensing or as a matrix to develop nanoparticle arrays. We present a comprehensive study of PS morphology and optical properties before and after the pore opening process, including the determination of thickness, pore size, and pore density of PS layers, its surface wettability, and reflectivity. The PS samples were fabricated by electrochemical anodization of monocrystalline silicon wafer in 5–20 wt.% hydrofluoric acid (HF) solution at a current density in the range of 20–200 mA/cm^2. Anodization was followed by the pore opening process, i.e., the removal of a parasitic superficial layer with a "bottleneck" structure by reactive ion etching (RIE). The results illustrate that "bottleneck"-free PS allows to achieve a high pore density using a low HF concentration and a reduced current density. We established that this structure demonstrates higher hydrophobicity in comparison to the samples before RIE. The applicability of the developed "bottleneck"-free PS was tested via filling the pores with silver nanoparticles, indicating its potential use as a template for the fabrication of nanoparticle arrays.

Keywords: porous silicon; electrochemical etching; parasitic layer; reactive ion etching; nanoparticle array

Citation: Khinevich, N.; Juodėnas, M.; Tamulevičienė, A.; Bandarenka, H.; Tamulevičius, S. Tailoring Mesoporous Silicon Surface to Form a Versatile Template for Nanoparticle Deposition. *Coatings* **2021**, *11*, 699. https://doi.org/10.3390/coatings11060699

Academic Editor: Charafeddine Jama

Received: 10 May 2021
Accepted: 8 June 2021
Published: 10 June 2021

1. Introduction

Porous silicon (PS) represents an intriguing platform to engineer miniature sensors compatible with Si technology that provide accurate and reliable detection of various organic molecules in a liquid or gaseous environment. The unique structural and optical properties of this porous material are easily tuned via the variation of regimes of its formation during the electrochemical anodization of monocrystalline silicon, which is the most convenient and affordable method to be used in both a research laboratory and industrial facilities [1,2].

The anodization of silicon wafers is usually accompanied by the growth of a thin parasitic layer caused by surface defects (e.g., surface roughness or uneven distribution of doping atoms) on the initial monocrystalline substrate. This surface layer usually consists of pores with a lower diameter compared to the pores distributed in the deeper layer, resulting in the so-called "bottleneck" effect. Therefore, it can strongly affect the morphology, mechanical, and electrical properties of the final PS-based device [3]. Such an effect is critical for the mesoporous silicon used to host or to capture nanostructures of other materials. Many applications imply the full filling of mesopores, which cannot be achieved due to the presence of the "bottleneck" layer [4]. For instance, mesoporous silicon is a suitable material for sensing elements because the pore diameters are equal or easily

adjustable to the size of organic molecules of the analyzed media. However, the parasitic layer can hamper their incorporation and diffusion within the porous matrix. Therefore, there is a need for the removal of the parasitic layer or prevention of its occurrence to provide a high loading effect of the PS sensing components [5]. Various methods to achieve this objective through the destruction of the "bottleneck" are reported. Among them, such methods as chemical dissolution [6,7], oxidation of PS followed by silicon dioxide removal in hydrofluoric acid (HF) [8], electropolishing, and plasma etching [9] have been demonstrated. Plasma etching is characterized by several advantages in comparison to other techniques [9]. The structural, chemical, electrical, and optical properties of the PS samples not subjected to the "bottleneck" layer removal have been thoroughly characterized and reported in [2,10,11]. However, the features of the final porous material free of the parasitic layer have not been sufficiently studied, despite their strong influence on the efficiency and reliability of the final devices containing PS components.

In the present work, PS was fabricated by electrochemical anodization at different formation conditions (HF concentration in the electrolyte and current density), and the parasitic layer was removed by reactive ion etching (RIE).

We present a comprehensive study of PS morphology and optical properties before and after the pore opening process provided via the removal of the parasitic layer. This work included the determination of the thickness, pore size, and pore density of the PS layers, its surface wettability, and reflectivity. The reflectance spectra of the PS layers were used to calculate the average refractive index. The influence of the HF concentration in the electrolyte and current density on the original size of pores was studied to define optimal conditions to produce nanostructures that can be used as templates for metal nanoparticles' (NPs) deposition.

2. Materials and Methods

Antimony-doped Si (100) wafer (Siegert Wafer, Aachen, Germany) with the resistivity of 0.008–0.02 ohm·cm was used for the PS formation. Before etching, the native silicon dioxide was removed in a low concentration (4 wt.%) hydrofluoric acid (Fluka, Seezle, Germany) solution. The electrochemical etching for the PS formation was carried out in an aqueous HF solution at different concentrations (5, 10, and 20 wt.%) for 90 s. Current density (j) was varied from 20 mA/cm^2 to 200 mA/cm^2. The removal of the parasitic surface layer was performed using RIE for 5 min in a 50 sccm gas flow of SF_6 at 20 mT pressure, 40 V bias voltage, and 500 W ICP (inductively coupled plasma) coil power (Vision LL-ICP, Plasma-Therm, Lomma, Sweden). After the RIE process, all the PS samples were cleaned in an ultrasonic bath in chloroform for 5 min to remove the oil that was used to bond them to a carrier wafer. Just before the characterization, the PS layers were treated with the diluted HF solution for a few seconds to remove oxidized areas.

The morphology and thickness of the PS samples were investigated using a scanning electron microscope FEI Quanta 200 FEG (FEI, Hillsboro, OR, USA) and analyzed using ImageJ software [12]. A drop shape analyzer DSA 25 (Kruss GmbH, Hamburg, Germany) was used for determining the water contact angle of the samples. The sessile drop method was applied for the contact angle determination.

Optical reflectance spectra of the PS layers were collected in the 400–800 nm spectral range with an optical microscope Olympus equipped with a fiber-optic spectrometer AvaSpec-2048 (Avantes, Apeldoorn, Netherlands) with 1.4 nm resolution.

To check the possibility to use PS as a template for the metal nanoparticles' deposition, spherical silver nanoparticles of 62 nm diameter with ~10% standard deviation in size were synthesized according to a previously described method [13]. In brief, the procedure of nanoparticles' synthesis consisted of two typical steps. At first, 100 mL of seed solution was prepared using 0.05 mM of tannic acid (TA) (Sigma-Aldrich, China), 5 mM of trisodium citrate (TC) (Lach-Ner, Neratovice, Czech Republic) and 0.025 mM silver nitrate ($AgNO_3$) (Girochem, Teplička nad Váhom, Slovenia) in Milli-Q water (Merck, Massachusetts, USA). Afterwards, the particles' size was tuned in the second synthesis step-growth of the seeds.

For this procedure 19.5 mL of seed solution was mixed with 16.5 mL of water and heated under the 90 °C. Then 500 mL of TC (25 mM), 1.5 mL of TA (2.5 mM) and 1 mL of $AgNO_3$ (25 mM) were added and kept heated and stirred for 30 min. The second step was repeated three times until the required nanoparticles' size was achieved. Synthesized silver NPs were deposited on PS by a capillary-assisted particle assembly (CAPA) procedure [14,15].

3. Results and Discussion

3.1. Surface Morphology

Scanning electron microscopy (SEM) top views and the pore diameter distribution of the standard, pre-polished, and RIE-treated PS samples are shown in Figure 1. The "standard" PS was fabricated using 10 wt.% HF solution at 100 mA/cm^2, whereas the "pre-polished" PS sample was additionally subjected to primary surface electropolishing at a current density of 3 A/cm^2 for 1 min.

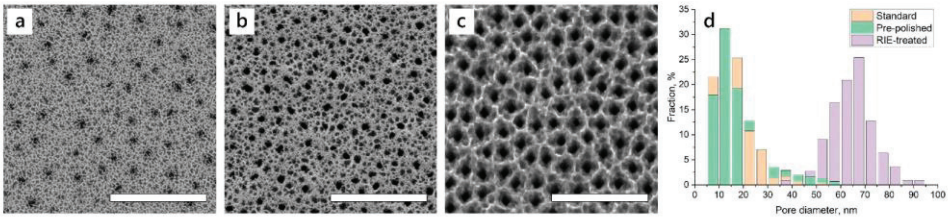

Figure 1. Scanning electron microscopy (SEM) top views of porous silicon (PS) formed in 10 wt.% hydrofluoric acid (HF) solution at 100 mA/cm^2 current density: (**a**) standard, (**b**) pre-polished, and (**c**) standard after reactive ion etching (RIE). The scale bar is 500 nm. (**d**) Pore size (diameter) distribution of the corresponding samples.

According to the SEM top-view images of the PS surface, one can see that the single-step electrochemical anodization process produces at least two different layers. The first layer is composed of small pores with a diameter of 15–20 nm that are irregularly shaped and randomly arranged. These pores are separated by silicon walls of the nanoscaled thickness (Figure 1a). A similar layer is observed on the pre-polished sample (Figure 1b). This layer has nearly the same surface morphology, but the size distribution of pore diameters becomes broader, and the number of "black" pores increases in comparison to the standard PS sample morphology (Figure 1a). It seems that the polishing procedure before the electrochemical anodization minimizes the number of defects on the surface, but some of them are still present and contribute to further PS formation. The pore size distribution determined for the sample after RIE (Figure 1c) indicates that the parasitic "bottleneck" layer was removed and the second layer with a mean pore size of 60–70 nm was uncovered (Figure 1d).

Figure 2 shows the SEM images of one set of the PS samples before and after RIE, formed at j = 60 mA/cm^2 in 5 wt.%, 10 wt.%, and 20 wt.% HF solutions. The morphology of the RIE-treated PS formed in the electrolyte with 5 wt.% (for all samples) and 10 wt.% HF (at high current density) mostly looks smooth, and only a slight increase in the roughness of the PS indicates isotropic etching of the top layer. The surface of the samples made at 10 wt.% HF at a low current density (20–60 mA/cm^2) and for all samples made in 20 wt.% HF is characterized by the formation of a porous layer, which consists of islands that make the surface rough. These substrates seem to be much less sensitive to liquid substances or nanoparticles loading into PS than the others with higher pore density.

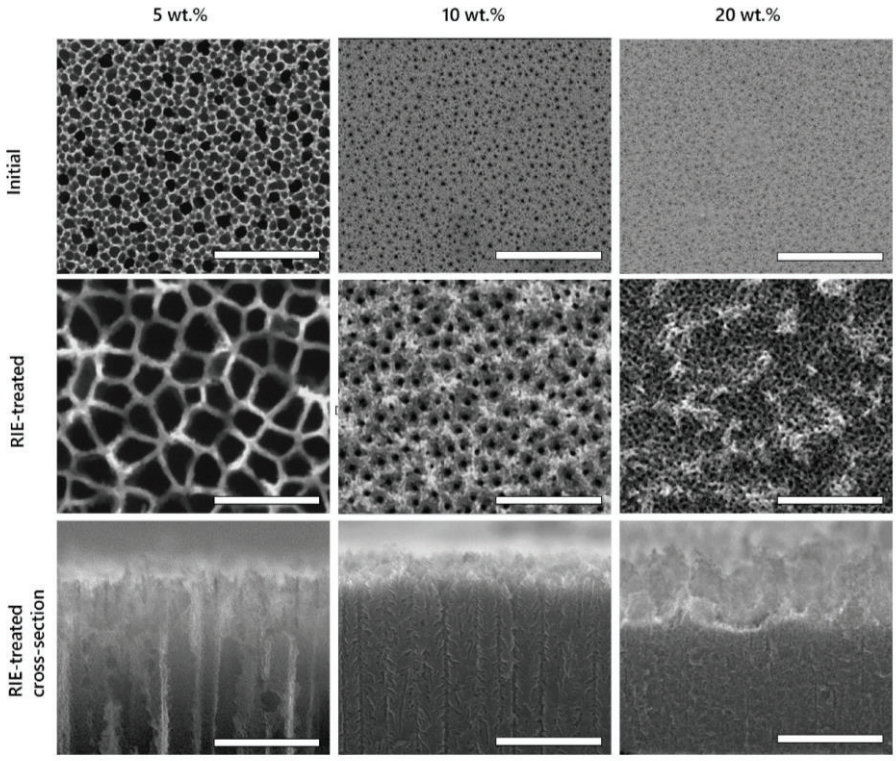

Figure 2. Top view of initial PS (on top) formed at j = 60 mA/cm^2 in the electrolyte with HF concentration 5 wt.%, 10 wt.%, 20 wt.%. Top view and cross-section of the same samples after RIE treatment (at the bottom). The scale bar is 500 nm.

In addition, these results demonstrate that RIE is a suitable method to remove the surface layer without damaging the inner morphology of the formed PS layers (Figure 2).

In general, the pores look uniform throughout the analyzed areas. The mean pore diameter and the density of the pores are presented in Figure 3. One can see that the mean diameter increases with the rise of current density. This linear dependence is followed until some critical value of current density is reached and the pore size starts to decrease. It should be noted that the critical current density value depends on the HF concentration, i.e., for 5 wt.% HF solution, the maximum pore diameter of ~130 nm is reached at 60 mA/cm^2, whereas for 10 wt.% HF solution a 160 nm pore diameter is observed at 140 mA/cm^2. These regularities can be explained by changes in the mechanism of PS formation by anodization [16]. At high current densities, the produced pores become spatially irregular, and a sponge-like structure is formed. The Si skeleton becomes thinner, and the pore density increases. Further increase in the current density leads to the electropolishing process. Moreover, the electropolishing can be predicted by the pore density value, e.g., we have experimentally confirmed that in 5 wt.% HF solution this process starts at 100 mA/cm^2, and for 10 wt.% HF, current density must be higher than 400 mA/cm^2.

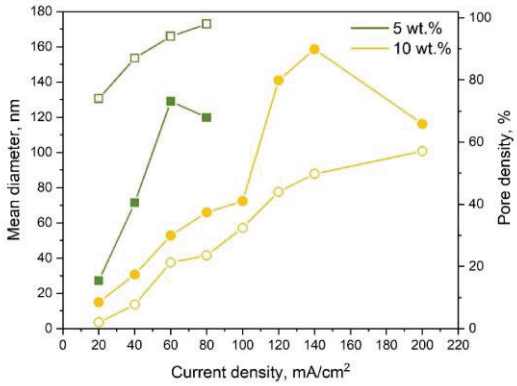

Figure 3. Dependence of the mean diameter (filled symbols) and pore density (empty symbols) on the applied current density of the PS samples formed at different HF concentrations.

The PS thickness growth rate was determined from the cross-section analysis of SEM images. It was established that the rate of the layer thickening is in direct dependence on the applied current density. At the same time, we can observe that thicker layers were created at higher HF concentrations during the same process time (Figure 4). The analysis of the thickness of the RIE-treated PS layers shows that the RIE process runs slower for PS with lower pore density. The RIE speed sharply increases for the samples fabricated in 5 wt.% HF at $j = 80$ mA/cm^2 due to the high density of pores (which reaches up to 96%) and thin Si walls. After the RIE, we observed that the most moiety of the PS layer was removed and the thickness of the produced structure was about 500 nm, whereas the initial thickness was about 2.6 µm.

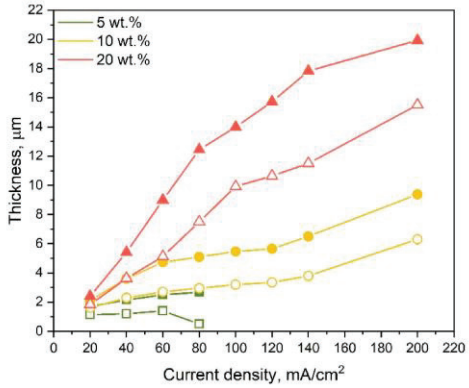

Figure 4. The PS thickness dependence on applied current density during electrochemical anodization in different concentration HF solutions. Initial PS samples are marked with filled symbols, RIE-treated samples with unfilled symbols.

3.2. Surface Wettability

The surface wettability is an essential surface characteristic in the case when the PS is designed to be used as a component of a sensor. Figure 5 shows that the PS hydropho-

bicity is much higher than that of the monocrystalline Si, for which the contact angle was measured to be 91° (Figure 5b).

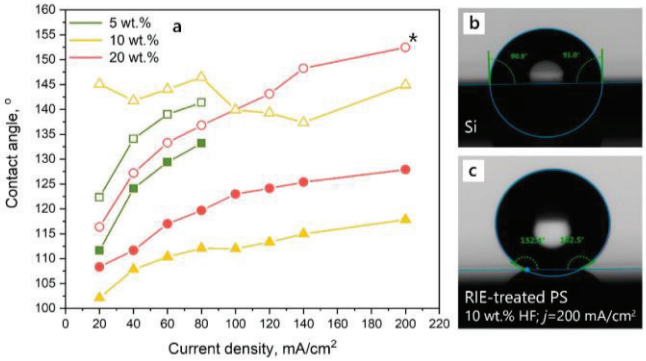

Figure 5. The contact angle of the PS samples before and after RIE. (**a**) the dependence of water contact angle on the current density applied during the anodization process of porous silicon. Initial PS samples are marked with filled symbols, RIE-treated samples with unfilled symbols; (**b**) water contact angle measured on bare Si and (**c**) on RIE-treated PS formed in 10 wt.% HF solution at j = 200 mA/cm^2 (contact angle value is indicated with the "*" mark in the graph).

The contact angle of the standard PS samples looks to be smaller than the contact angle of RIE-treated samples, but it shows the same behavior in dependence on the current density, i.e., the PS hydrophobicity increases with the increase of current density. The contact angle value changed from 112° to 133°, from 108° to 127°, and from 102° to 118° for the PS samples formed in 5 wt.%, 10 wt.%, and 20 wt.% HF solutions, respectively. The contact angle of the RIE-treated PS samples formed in 5 wt.% and 10 wt.% HF solution increased from 122° to 141°, and from 116° to 152° respectively (Figure 5a). In the final case, the PS layer formed in 10 wt.% HF and at j = 200 mA/cm^2 (marked in the graph) demonstrates the superhydrophobic effect as the contact angle is greater than 150° (Figure 5c).

In the case of the RIE-treated PS substrate formed in 20 wt.% HF solution, no clear dependence of the contact angle on the current density was observed. Such an effect is interplayed with the rough surface morphology that was found to be almost independent on the applied current density.

The results illustrate that in all the cases when the PS was produced using the HF concentrations lower than 20 wt. %, the contact angle (or wettability of the surface) can be easily adjusted using different current densities applied in a course of the anodization. Moreover, RIE contributes to an additional increase in the contact angle.

To successfully use the PS as a template for nanoparticles' assembly by CAPA, the contact angle of a suspension of nanoparticles and the substrate must be properly tuned to achieve a high assembly yield. According to several studies [17–19], the value of the contact angle ensuring a successful assembly is in the range from 30° to 75°. In the PS case, such conditions can be set by reducing the free surface energy using surfactants [20] or changing the template wetting behavior by oxidation [21], oxygen plasma treatment [22], or functionalization [23].

3.3. Optical Properties

Optical characterization of the PS layers, especially the investigation of the refractive index, is the most important task for further development of photonic sensors based on this porous material [24]. It is known that the PS surface layer consists of silicon crystallites and pores that contribute to diffuse scattering and final reflectivity.

The measured PS reflectance spectra (for samples formed at 5 wt.% and 10 wt.% HF) show a series of interference fringes that correspond to the constructive and destructive interference of the reflected light from air/PS and PS/Si interfaces that are also called Fabry–Pérot interference fringes (Figure 6). Using the Fabry–Pérot interference principle [25], the effective optical thickness (EOT) $2n_{PS}L$ was evaluated and then the value of the average refractive index (n_{PS}) was extracted from EOT using the value of PS layer thickness (L values were taken from Figure 4). The results obtained are presented in Table 1. The frequency of the interference fringes strongly depends on the air fraction values in the PS structure [26].

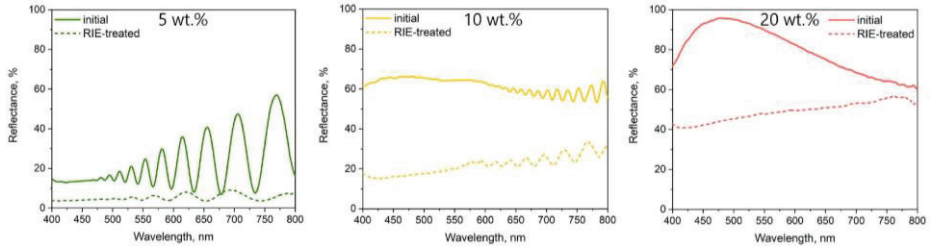

Figure 6. Reflectance spectra of initial PS (solid line) and RIE-treated (dashed line) formed at $j = 60$ mA/cm^2 in the electrolyte with HF concentration of 5 wt.%, 10 wt.%, 20 wt.%.

Table 1. The Average Refractive Index of Initial and RIE-treated PS.

HF Conc.		Current Density (mA/cm^2)							
		20	**40**	**60**	**80**	**100**	**120**	**140**	**200**
5 wt.%	initial	3.21	2.48	1.39	1.20	-	-	-	-
	RIE-treated	3.35	2.50	1.41	1.57	-	-	-	-
10 wt.%	initial	3.24	3.14	2.99	2.73	2.40	2.13	2.10	2.01
	RIE-treated	-	3.17	2.97	2.87	2.72	2.20	2.17	2.04

The refractive index was calculated for the samples made using 5 wt.% and 10 wt.% HF electrolytes. According to Table 1, the refractive index decreases with the increase of the applied current density, and this is usually related to the increase of pore density (porosity) [27]. The exception is observed for the PS sample formed in 5 wt.% at $j = 80$ mA/cm^2, where the refractive index increases sharply. We attribute this to the contribution of Si to the reflection spectra due to the small amount of the remaining PS after etching (see Section 3.1). In general, the RIE-treated samples are regarded as a single-layer structure, whereas the initial samples are considered to be multi-layer consisting of the layers with different porosity. In most cases, the refractive index value of the initial PS samples is slightly lower than that of RIE-treated samples. This can be explained by the presence of a highly porous surface parasitic layer that contributes to the refractive index and decreases its value. Only in a single case (10 wt.% HF; $j = 60$ mA/cm^2), the refractive index of the RIE-treated PS sample is smaller than the value of the initial PS sample, but the difference is rather small, and it could be attributed to the thickness estimation errors.

The reflectance spectra of the initial PS samples prepared in 20 wt.% HF solution (Figure 6) look similar to the spectrum of the bare silicon. We assume that the porosity of these samples is so low that we cannot observe any major changes in their optical properties. The RIE-treated PS reflectivity is characterized by a lower intensity due to the scattering effect that occurs on a rough surface. In both cases, the reflectance spectra demonstrate fringes with a very low amplitude that are hardly distinguished and cannot be used for

further determination of optical parameters. The optical parameters were not determined for the sample formed in 10 wt.% HF and j = 20 mA/cm^2 due to the same difficulties.

3.4. Reactive Ion Etching (RIE) Etched Porous Silicon Templates for the Nanoparticles' Deposition

The "bottleneck"-free PS substrate has great potential as a template, which provides a precise definition of shape, size, and spatial location of different nanostructures for the development of radically new metamaterials with outstanding magnetic, optical, catalytic, and other features. As a proof of concept of this work, we demonstrated how the mesoporous silicon with pores opened by the RIE treatment can be used for ordered embedding of spherical silver nanoparticles possessing the prominent surface plasmon resonance (SPR) in the blue range of the optical spectrum. In particular, this property is in high demand to design and engineer components of Si-based devices for photovoltaic and sensing applications.

In our work, we deposited silver nanoparticles on the PS samples made in 10 wt.% HF solution and at j = 100 mA/cm^2. Silver nanoparticles with a mean diameter of 62 nm with ~10% standard deviation in size were used. The diameter of the spherical silver nanoparticles was selected in accordance to the pore size of the developed PS sample and based on the research showing the successful use of such particles' size in sensing experiments [28]. The CAPA method [14] was selected for the silver nanoparticles' deposition. Namely this approach provides the most controlled distribution of the colloidal nanoparticles over a template's surface compared to other techniques (e.g., drop deposition). The PS surface after the silver nanoparticles' deposition is shown in Figure 7 (the top view of the RIE-treated PS sample before NPs implementation is presented in Figure 1c). To show the importance of surface morphology on the deposition yield the particles were applied on the initial sample and on RIE-treated sample in the same conditions (Figure 7). In both cases similar silver nanoparticles were used. The PS sample not subjected to the RIE treatment provided anchoring of the silver nanostructures in some places around the sample surface but their distribution was uneven (Figure 7a). Due to a mismatch of pore and silver nanoparticle diameter, all the particles were distributed on the top of the surface. On the other hand, when the surface layer was etched away, the silver nanoparticles penetrated nearly all the pores (pore entrance filling factor was ~85%). It should be noted that in rare cases, a few nanoparticles occupied one pore or were displaced to the edge of the pore. It should be highlighted that the removal of the "bottleneck" layer led to opening the structure that provided deposition of the highly ordered ensemble of the silver nanoparticles divided by the silicon walls of the nano scaled thickness. The final structure had the prospect of possessing an extremely intensive electromagnetic field in the spots of silver nanoparticle and silicon wall contact, due to plasmonic coupling between metallic nanoparticles and semiconductor [29]. What is also important, the distance between the nanoparticles can be tuned as well as the pore size and particle diameter by varying anodization and synthesis conditions, respectively.

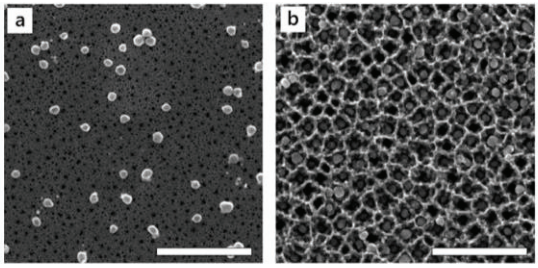

Figure 7. Top view of the initial (**a**) and the RIE-etched PS (**b**) made in 10 wt.% HF solution and at j = 100 mA/cm^2 after Ag nanoparticles deposition. The scale bar is 500 nm.

4. Conclusions

We demonstrated that RIE is an efficient method for the removal of the parasitic surface layer without damaging the morphology of the PS. The analysis of the electrochemical anodization conditions revealed that the properties of the PS (pore size and density, refractive index, wettability) can be tuned in a wide range. Changing the current density and HF concentration during the electrochemical etching process enables the pore size to be managed in a range from 10 nm up to 160 nm. We showed that the surface wettability is in a good dependence on current density and by selecting proper conditions we can create hydrophobic (100°) or superhydrophobic (152°) structures. The optimal HF concentration for the creation of porous structures was determined to be in the range of 5–10 wt.%, whereas PS formed at 20 wt.% HF concentration comprised of islands that reduce the flatness of the surface. The RIE-etched PS sample formed at 10 wt.% HF solution was shown to be a favorable template for the CAPA deposition of the highly ordered array of the 62 nm size silver nanoparticles divided by silicon walls with the filling factor of ~85%, which are expected to possess prominent plasmonic properties and present the object of a future study. The selection of the described electrochemical etching conditions allows us to create templates with a variable pore size and to adapt the surface morphology to nanoparticle deposition.

Author Contributions: Conceptualization, N.K., A.T., S.T. and H.B.; methodology, N.K. and M.J.; investigation, N.K.; resources, N.K., A.T.; writing—original draft preparation, N.K., A.T. and H.B.; writing—review and editing, all authors. All authors have read and agreed to the published version of the manuscript.

Funding: N.K: M.J, A.T., and S.T. acknowledge funding from the Research Council of Lithuania (LMTLT) (Agreement No.P-LZ-21-1).

Institutional Review Board Statement: Not applicable.

Informed Consent Statement: Not applicable.

Data Availability Statement: Not applicable.

Conflicts of Interest: The authors declare no conflict of interest.

References

1. Jane, A.; Dronov, R.; Hodges, A.; Voelcker, N.H. Porous silicon biosensors on the advance. *Trends Biotechnol.* **2009**, *27*, 230–239. [CrossRef]
2. Canham, L. *Handbook of Porous Silicon*; Springer International Publishing: Berlin, Germany, 2018; Volume 1–2, ISBN 9783319713816.
3. Redko, S.V.; Bondarenko, V.P.; Petrovich, V.A.; Kotov, D.A.; Chubenko, E.B.; Sherstnyov, A.I. Influence of the Surface Layer on the Electrochemical Deposition of Metals and Semiconductors into Mesoporous Silicon. *Semiconductors* **2016**, *50*, 372–376. [CrossRef]
4. Mariani, S.; Pino, L.; Strambini, L.M.; Tedeschi, L.; Barillaro, G. 10 000-Fold Improvement in Protein Detection Using Nanostructured Porous Silicon Interferometric Aptasensors. *ACS Sens.* **2016**, *1*, 1471–1479. [CrossRef]
5. Mariani, S.; Strambini, L.M.; Barillaro, G. Electrical Double Layer-Induced Ion Surface Accumulation for Ultrasensitive Refractive Index Sensing with Nanostructured Porous Silicon Interferometers. *ACS Sens.* **2018**, *3*, 595–605. [CrossRef]
6. Chamard, V.; Dolino, G.; Muller, F. Origin of a parasitic surface film on p+ type porous silicon. *J. Appl. Phys.* **1998**, *84*, 6659–6666. [CrossRef]
7. Harraz, F.A.; El-Sheikh, S.M.; Sakka, T.; Ogata, Y.H. Cylindrical pore arrays in silicon with intermediate nano-sizes: A template for nanofabrication and multilayer applications. *Electrochim. Acta* **2008**, *53*, 6444–6451. [CrossRef]
8. Sciacca, B.; Secret, E.; Pace, S.; Gonzalez, P.; Geobaldo, F.; Quignard, F.; Cunin, F. Chitosan-functionalized porous silicon optical transducer for the detection of carboxylic acid-containing drugs in water. *J. Mater. Chem.* **2011**, *21*, 2294–2302. [CrossRef]
9. Errien, N.; Vellutini, L.; Louarn, G.; Froyer, G. Surface characterization of porous silicon after pore opening processes inducing chemical modifications. *Appl. Surf. Sci.* **2007**, *253*, 7265–7271. [CrossRef]
10. Korotcenkov, G. *Porous Silicon: From Formation to Application: Formation and Properties, Volume One*; Korotcenkov, G., Ed.; CRC Press: Boca Raton, FL, USA, 2016; ISBN 9780429076503.
11. Torres-Costa, V.; Martín-Palma, R.J. Application of nanostructured porous silicon in the field of optics. A review. *J. Mater. Sci.* **2010**, *45*, 2823–2838. [CrossRef]
12. ImageJ Software. Available online: https://imagej.nih.gov/ij/index.html (accessed on 4 June 2021).
13. Bastús, N.G.; Merkoçi, F.; Piella, J.; Puntes, V. Synthesis of highly monodisperse citrate-stabilized silver nanoparticles of up to 200 nm: Kinetic control and catalytic properties. *Chem. Mater.* **2014**, *26*, 2836–2846. [CrossRef]

14. Juodenas, M.; Tamulevičius, T.; Henzie, J.; Erts, D.; Tamulevičius, S. Surface Lattice Resonances in Self-Assembled Arrays of Monodisperse Ag Cuboctahedra. *ACS Nano* **2019**, *13*, 9038–9047. [CrossRef]
15. Juodėnas, M.; Peckus, D.; Tamulevičius, T.; Yamauchi, Y.; Tamulevičius, S.; Henzie, J. Effect of Ag Nanocube Optomechanical Modes on Plasmonic Surface Lattice Resonances. *ACS Photonics* **2020**. [CrossRef]
16. Zhao, M.; McCormack, A.; Keswani, M. The formation mechanism of gradient porous Si in a contactless electrochemical process. *J. Mater. Chem. C* **2016**, *4*, 4204–4210. [CrossRef]
17. Ni, S.; Isa, L.; Wolf, H. Capillary assembly as a tool for the heterogeneous integration of micro- and nanoscale objects. *Soft Matter* **2018**, *14*, 2978–2995. [CrossRef]
18. Malaquin, L.; Kraus, T.; Schmid, H.; Delamarche, E.; Wolf, H. Controlled particle placement through convective and capillary assembly. *Langmuir* **2007**, *23*, 11513–11521. [CrossRef]
19. Kang, J.; Park, C.G.; Lee, S.H.; Cho, C.; Choi, D.G.; Lee, J.Y. Fabrication of high aspect ratio nanogrid transparent electrodes: Via capillary assembly of Ag nanoparticles. *Nanoscale* **2016**, *8*, 11217–11223. [CrossRef]
20. Spencer, S.J.; Andrews, G.T.; Deacon, C.G. Contact angle of ethanol-water solutions on crystalline and mesoporous silicon. *Semicond. Sci. Technol.* **2013**, *28*. [CrossRef]
21. Muñoz, E.C.; Díaz, C.; Navarrete, E.; Henríquez, R.; Schrebler, R.; Córdova, R.; Marotti, R.; Heyser, C. Characterization of surface changes on silicon and porous silicon after interaction with hydroxyl radicals. *Arab. J. Chem.* **2019**, *12*, 5125–5133. [CrossRef]
22. Jiang, L.; Li, S.; Wang, J.; Yang, L.; Sun, Q.; Li, Z. Surface wettability of oxygen plasma treated porous silicon. *J. Nanomater.* **2014**, *2014*. [CrossRef]
23. Dattilo, D.; Armelao, L.; Maggini, M.; Fois, G.; Mistura, G. Wetting behavior of porous silicon surfaces functionalized with a fulleropyrrolidine. *Langmuir* **2006**, *22*, 8764–8769. [CrossRef]
24. Lammel, G.; Schweizer, S.; Schiesser, S.; Renaud, P. Tunable optical filter of porous silicon as key component for a MEMS spectrometer. *J. Microelectromech. Syst.* **2002**, *11*, 815–828. [CrossRef]
25. Paes, T.F.; Beloto, A.F.; Galvão, E.C.D.S.; Berni, L.A. Simple method for measuring the porosity, thickness and refractive index of porous silicon, based on the Fabry-Pérot interference spectrum. *Rev. Bras. Apl. Vácuo* **2017**, *35*, 117. [CrossRef]
26. Maniya, N.H.; Patel, S.R.; Murthy, Z.V.P. Electrochemical preparation of microstructured porous silicon layers for drug delivery applications. *Superlattices Microstruct.* **2013**, *55*, 144–150. [CrossRef]
27. Sohn, H. Refractive Index of Porous Silicon Refractive Index of Porous Silicon. In *Handbook of Porous Silicon*; Canham, L., Ed.; Springer: Cham, Switzerland, 2018; pp. 241–352. [CrossRef]
28. Stamplecoskie, K.G.; Scaiano, J.C.; Tiwari, V.S.; Anis, H. Optimal size of silver nanoparticles for surface-enhanced raman spectroscopy. *J. Phys. Chem. C* **2011**, *115*, 1403–1409. [CrossRef]
29. Casadei, A.; Pecora, E.F.; Trevino, J.; Forestiere, C.; Rüffer, D.; Russo-Averchi, E.; Matteini, F.; Tutuncuoglu, G.; Heiss, M.; Fontcuberta I Morral, A.; et al. Photonic-plasmonic coupling of GaAs single nanowires to optical nanoantennas. *Nano Lett.* **2014**, *14*, 2271–2278. [CrossRef] [PubMed]

Paper IV: Wavelength-Tailored Enhancement of Raman Scattering on a Resonant Plasmonic Lattice

Nadzeya Khinevich, Mindaugas Juodėnas, Asta Tamulevičienė, Tomas Tamulevičius, Martynas Talaikis, Gediminas Niaura, Sigitas Tamulevičius

Sensors and Actuators: B. Chemical 394 (2023) 134418

Sensors & Actuators: B. Chemical 394 (2023) 134418

Contents lists available at ScienceDirect

Sensors and Actuators: B. Chemical

journal homepage: www.elsevier.com/locate/snb

Wavelength-tailored enhancement of Raman scattering on a resonant plasmonic lattice

Nadzeya Khinevich [a,*], Mindaugas Juodėnas [a,b], Asta Tamulevičienė [a,c], Tomas Tamulevičius [a,c,d], Martynas Talaikis [e], Gediminas Niaura [e], Sigitas Tamulevičius [a,c,**]

[a] Institute of Materials Science, Kaunas University of Technology, 51423 Kaunas, Lithuania
[b] Physics Department, Chalmers University of Technology, Gothenburg 41296, Sweden
[c] Department of Physics, Kaunas University of Technology, 51423 Kaunas, Lithuania
[d] UAB Nanoversa, 51423 Kaunas, Lithuania
[e] Department of Organic Chemistry, Center for Physical Sciences and Technology (FTMC), 10257 Vilnius, Lithuania

ARTICLE INFO

Keywords:
Surface plasmon resonance
Surface lattice resonance
Capillarity-assisted particle assembly
Surface-enhanced Raman scattering spectroscopy
Silver nanoparticles
Molecule detection

ABSTRACT

Routine single-molecule analysis using surface-enhanced Raman scattering (SERS) is still out of reach using conventional substrates based on corrugated metallic surfaces. Tailoring the substrate to a specific excitation wavelength is an effective way to improve the SERS enhancement factor. Here, we present a comprehensive theoretical and experimental study of wavelength-tailored SERS substrates with improved sensitivity, exploiting the surface lattice resonance (SLR) in a plasmonic lattice comprised of assembled Ag nanoparticles. We tuned the SLR close to 532 nm and evaluated its effect on SERS. We found that SLR-based substrates had 10 times overall higher sensitivity and 100 times higher sensitivity at the target wavelength compared to non-tuned counterparts. Furthermore, we compared monomer and tetramer unit cell cases and found that the combined effect of tuned SLR and hot spots further improves the enhancement factor more than 400 times over a substrate with a random layer of nanoparticles.

1. Introduction

Raman scattering spectroscopy is a powerful analytical method, but it is based on inefficient scattering of Stokes-shifted light. Therefore, it requires high-intensity laser illumination, especially to detect low analyte concentrations. This drawback can be partially circumvented by exploiting elaborated surface nanostructures that enhance the exciting electromagnetic field, *i.e.,* using surface-enhanced Raman spectroscopy (SERS) which has become an important field of study. It found multiple applications requiring high sensitivity to elemental surface composition, such as electrochemistry, catalysis, biology, medicine, art conservation, materials science, and others [1,2]. SERS achieves high sensitivity, resolving as little material as a single molecule, by exploiting (i) electromagnetic enhancement associated with localized surface plasmon excitation in metal nanoparticles (NPs) or nanostructures and/or (ii) chemical enhancement due to electron transfer to/from metal nanoparticles from/to target molecules [3]. Additional improvement can be achieved by employing electromagnetic hot spots – geometric configurations that can locally amplify the electromagnetic field up to 10 orders of magnitude [4,5], *e.g.*, sharp features on single nanostructures, nanogaps between nanostructures, *etc*.

Conventional SERS substrates are usually based on corrugated irregular metallic surfaces or aggregated colloidal nanoparticles [6,7] of noble metals, mainly silver, gold, or their alloys. Highly effective SERS substrates with various nanogaps were demonstrated using colloidal lithography and reactive ion etching [8]. In [9] it was demonstrated that monodisperse, atomically smooth Ag polyhedral with controlled interparticle gaps can result in reproducible SERS enhancement factors (EF) but required a careful alignment to small areas with nanoparticles. Industrial applications, where Raman spectroscopy is used as a routine process, need effective and low-cost SERS substrates that enable reproducible and stable measurements on a large area substrate.

The enhancement usually covers a certain wavelength band related to the localized surface plasmon resonance (LSPR) of the nanostructures and can vary across the substrate. Thus, commercially available SERS substrates are recommended to be used at different laser excitation from

* Corresponding author.
** Corresponding author at: Institute of Materials Science, Kaunas University of Technology, 51423 Kaunas, Lithuania.
E-mail addresses: nadzeya.khinevich@ktu.lt (N. Khinevich), sigitas.tamulevicius@ktu.lt (S. Tamulevičius).

https://doi.org/10.1016/j.snb.2023.134418
Received 23 June 2023; Received in revised form 16 July 2023; Accepted 5 August 2023
Available online 7 August 2023

514 nm to 782 nm (www.sersitive.eu/shop/silver-s/; www.oceaninsight.com/products/sampling-accessories/raman/sers/sers/). However, silver-based substrates demonstrate the highest sensitivity at shorter wavelengths and lower enhancement at longer. Besides tuning plasmon resonance to obtain the maximum sensitivity of the substrate at the required wavelength (for example 785 nm which is mainly used for biomolecules study) is difficult due to manufacturing limitations.

Light scattered by plasmonic nanoparticles arranged in a lattice can couple to photonic modes enabled by array [10]. This results in an extreme reduction of the spectral linewidth and an improvement of the resonance quality factor [11]. This resonant effect, called plasmonic lattice resonance (or surface lattice resonance – SLR), finds multiple applications [12] including nonlinear optics [13], photovoltaics [14], data storage [15], biosensing [11], plasmon-based lasers [16], and surface-enhanced fluorescence [17]. The wavelength of the SLR is tunable because it depends on the interplay between the LSPR and the Rayleigh anomaly. The former depends on the scatterer size, shape, and material, while the latter is related to the photonic structure parameters such as the lattice type and pitch. Therefore, the resonant properties of the structure can be tuned by varying the size of the nanoparticles, the lattice periodicity, and the refractive index of the surrounding medium [18]. Such nanoparticle arrays were recently demonstrated as very efficient SERS substrates [18–20]. A two-fold increase in SERS EF was reported when the SLR position generated by nanoparticle clusters in an array was tuned to the laser excitation by stretching the polymer substrate, resulting in 10^7 EF at the target wavelength [19,21].

Currently, a variety of different nanofabrication techniques, such as electron beam lithography, focused ion beam lithography, and nanoimprint lithography are used to produce high-quality factor SLR nanoparticle arrays [22,23]. Recently, we have presented a capillarity-assisted particle assembly method (CAPA) to deposit monodisperse single-crystal colloidal Ag nanocubes with a high level of long-range positional control at the single-particle level into nearly defect-free > 1 cm^2 hexagonal and square lattices [24,25]. In the latter, the SLR peak was tailored from 522 nm to 585 nm by depositing chemically synthesized monodisperse AgNPs in 300–400 nm lattices pitch [25]. It is possible to produce large-area nanoparticle arrays with a controllable number of particles per deposition site by matching the NP and trap sizes and using a templated assembly method such as CAPA [26]. The low-cost structures and the direct application as SERS substrates targeted for a specific excitation wavelength or Raman peak without the need for substrate deformation control like in [19] are important parameters for SERS substrate commercialization.

In this work, we present wavelength-tailored SERS substrates enabled by the SLR. We produced them using the CAPA method and tuned the resonant response to match the 532 nm excitation wavelength commonly used in Raman spectroscopy. We characterized our substrates using lasers covering the 442 nm, 533 nm, 632 nm, 785 nm, and 832 nm wavelength range and discuss the effect of the overlap between the excitation wavelength and the SLR peak on the EF and the detection limit of the 2-Naphthalenethiol (2NT) analyte. Our results indicate that the SERS activity of the substrates was enhanced when the SLR peak and excitation wavelength matched. In addition, we show the contribution of hot spots created by multiparticle unit cells. Four nanoparticles per unit cell demonstrated orders of magnitude stronger SERS enhancement compared to single particle assemblies and a uniform layer of nanoparticles. Our results pave the way for large-scale, efficient SERS substrates that can be tailored to target molecules or excitation wavelengths for superior sensitivity and reproducibility.

2. Materials and methods

2.1. Nanoparticle synthesis

The synthesis of silver nanoparticles was carried out using the seeded-growth method [27] in which a complex of tannic acid (TA) ($C_{76}H_{52}O_{46}$) and trisodium citrate (TC) ($C_6H_5Na_3O_7$ *2 H_2O) is used. The method enables control over the nucleation, growth, and stabilization processes, which leads to reproducible monodisperse silver nanoparticles (Ag NPs). Spherical nanoparticles with a diameter of 77 nm ± 4.5 nm and 88 nm ± 5.2 nm (Fig S1) were synthesized and functionalized by Polyvinylpyrrolidone (PVP, average MW ~ 55,000) for better stabilization during CAPA deposition. Before deposition, the concentration of the nanoparticles was increased by up to 10 times and the solvent was exchanged and mixed with ethanol and dimethylformamide (DMF) in a 1 / 2 ratio.

2.2. Polymer template fabrication

The templates for CAPA deposition were made of polydimethylsiloxane (PDMS) by replicating a 20 mm × 20 mm Si mold. The latter was fabricated using electron-beam lithography (eLine plus, Raith) and reactive ion etching (Vision LL-ICP, Plasma-Therm). The pattern consisted of a square array of 180 nm diameter, 100 nm tall, and 330 nm centre-to-centre spaced round pillars. The Si mold was functionalized with trichloro-(1 H,1 H,2 H,2 H-perfluorooctyl)-silane (Alfa Aesar) to prevent bonding with PDMS in subsequent soft-lithography replication cycles. 20 ml drop of 10:1 mixture of polymer base and curing agent (Sylgard 184, Dow-Corning) was dispensed on the Si mold and covered by a glass coverslip. The sample was cured at 100 °C for 35 min in the oven. After cross-linking, the glass coverslip with patterned PDMS film was separated from the mold [24].

2.3. Capillarity-assisted particle deposition

Capillarity-assisted particle deposition was performed using a custom-made setup equipped with a motorized linear precision translator (LS-110, PI Micos), a temperature control system (TEC-1090, Meerstetter Engineering GmbH), and an optical microscope system (BX51, Olympus) with a CCD camera (QImaging, Micropublisher 3.3) [28]. The PDMS template was placed on the moving stage, and 100 µl of Ag NPs solution was dispensed and confined by a fixed microscope slide. The speed of the stage was kept at 1 µm/s and the sample holder temperature controlled by the thermoelectric controller was set the 21 °C and 30 °C above the dew point for single- and multi-particle assembly, respectively.

2.4. Characterization techniques

Scanning electron microscopy (Quanta 200 FEG, FEI) at a low vacuum in a water vapor atmosphere was used for the imaging of NPs on insulating PDMS substrates and transmission electron microscope (Philips, CM200) at a high vacuum for imaging of colloidal nanoparticles after PVP functionalization. The UV–vis transmittance and absorbance spectra of the fabricated array of nanoparticles on the PDMS substrate were recorded using an optical fibre-coupled spectrometer (AvaSpec-2048, Avantes; resolution 1.2 nm) and a custom-made collimated light source covering the 400 – 800 nm spectral range [29]. SERS mapping was performed using a multiwavelength Raman microscope (Renishaw, Wotton-under Edge) equipped with a thermoelectrically cooled CCD detector. Samples were excited and spectra were collected using the following combinations of laser wavelengths and gratings: 442 nm (2400 lines/mm), 532 nm (1800 lines/mm), 633 nm (1800 lines/nm), 785 nm (1200 lines/nm), and 830 nm (830 lines/mm). The 20 µm × 20 µm surface area was mapped with a step size of 1.5 µm. A 50 × /0.75 NA (Leica) objective lens focused laser light to *ca.* 0.8–1.4 µm size spot on the surface depending on the wavelength used. Organic molecule 2-Naphthalenethiol (2NT) was chosen as the target molecule for the substrate's SERS-activity investigation because of its self-assembling monolayer ability.

2.5. The Raman scattering enhancement factor

The Raman scattering enhancement factor (*EF*) was calculated according to the following equation:

$$EF = \frac{I_{SERS} \times N_R}{I_R \times N_{SERS}}, \quad (1)$$

where I_{SERS} is the measured integrated SERS intensity of the substrate adsorbed 2NT monolayer; I_R is the measured integrated intensity of the Raman scattering from a bulk sample; N_{SERS} is the number of molecules under laser illumination at the surface; N_R is the number of molecules under laser illumination in a bulk compound solution.

SERS intensity was determined by averaging all acquired spectra on a selected map followed by background extraction and then calculating the intensity at 1377 cm^{-1} by fitting the obtained spectrum with the Gaussian-Lorentzian shape component. To determine the enhanced Raman intensity, 2.5 mM of 2NT solution in ethanol was measured in a 1 cm thick quartz cell by using the 5 × /0.12 NA (Leica) objective lens. The method to calculate *EF* is detailed in the reference [30]. We assumed that the surface of the Ag NP array was fully covered by a monolayer of 2NT when one 2NT molecule occupies 21.6 A^2 surface area ($Å^2$/molecule) [31]. The instrumental response at different laser wavelengths was taken into account and all the calculated data is present in Tables S2-S4.

2.6. Simulations

FEM modelling was performed using COMSOL Multiphysics using the wave optics module. A two-way periodic boundary condition was set to simulate the square pattern. First, a unit cell with a width of 330 nm with one nanoparticle per trap (monomer) was modelled and the diameter of the particles was varied from 40 nm to 100 nm, with a step of 10 nm. Real samples were modelled by building the unit cell based on SEM measurements using a monomer with 88 nm and a tetramer – four nanoparticles – with a diameter of 77 nm each. Finally, a spherical computational domain with perfectly matched layers (PML) was implemented for isolated monomer and tetramer structure calculations. The optical constants of Ag were taken from [32].

3. Results and discussion

Laser light in the green color range is considered less destructive when used for the detection of organic molecules by Raman spectroscopy. Therefore, we focused on developing a SERS-active substrate featuring an SLR peak (λ_{SLR}) close to 532 nm (λ_{Ex}). SLR manifests itself as a narrow dip in the transmittance spectrum of a plasmonic nanoparticle array and can appear when in-plane diffracted waves (Rayleigh anomaly (RA)) constructively interfere with light scattered by the nanoparticles (LSPR). The position and linewidth of the SLR depend on the spectral overlap between the LSPR and the RA and are observed most easily when the RA is redshifted from the LSPR. The relationship between the RA wavelength and the periodicity of a square array (Λ) at normal incidence is described by a simplified diffraction equation:

$$\lambda_{RA} = \Lambda n, \quad (2)$$

where λ_{RA} is the RA wavelength; Λ is the array pitch;*n* is the refractive index of the medium (for PDMS $n = 1.425$). Taking into account our previous results [24], we chose a square lattice $\Lambda = 330$ nm with λ_{RA} in PDMS at 470 nm (Fig. 1) to obtain a reasonably intense peak close to 532 nm.

The simulated results (Fig. 1c) show how λ_{SLR} depends on the diameter of the nanoparticles. The SLR peak redshifts and its FWHM increases with increasing NP diameter [33]. 90–100 nm diameter nanoparticles show λ_{SLR} close to the target of 532 nm. Based on this and our previous work [25] (the edge length of nanocubes used in our previous experiments was converted to the effective radius of spherical nanoparticles), we selected Ag NPs with a diameter of 88 nm ± 5.2 nm to assemble into arrays. These nanoparticles have a dipolar LSPR peak in solution at around 460 nm (Fig. S1a) that overlaps the λ_{RA} of the 330 nm

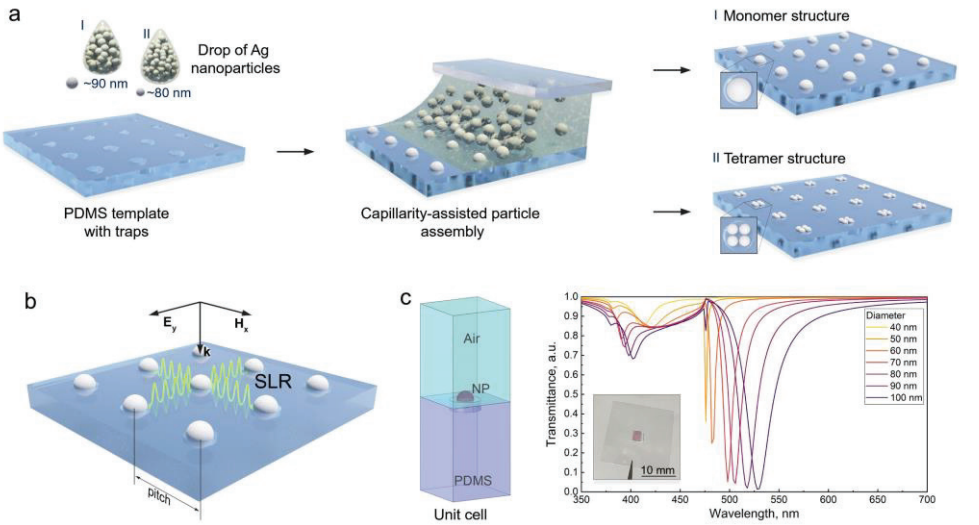

Fig. 1. Ag nanoparticle arrays produced using the capillarity-assisted particle assembly method feature the surface lattice resonance. (a) Assembly of Ag NPs into monomer and tetramer arrays using CAPA and a typical sample used for Raman analysis. (b) Structure of the plasmonic lattice on PDMS substrate with excited SLRs at a certain wavelength supported by AgNPs array. (c) 3D model of the unit cell used to simulate a square array of nanoparticles in traps; simulated transmittance spectra showing SLR peaks generated by arrays of single Ag NPs from 40 to 100 nm in diameter.

square lattice. An SEM micrograph of the assembled plasmonic structure is presented in Fig. 2a, where the traps in a structured PDMS substrate are filled primarily by single nanoparticles (we call these structures monomer assemblies). Fig. 2a depicts the simulated electromagnetic field enhancement by an isolated nanoparticle (perfectly matched boundary conditions) and the particle in the array (periodic boundary conditions). Strong near-field is observed in both cases, with 4.2 and 14.7 times enhanced field at 532 nm wavelength in the isolated nanoparticle and array cases respectively. The experimental and calculated λ_{SLR} are in good qualitative agreement (Fig. 2b). The experimental dip in the transmittance spectrum is wider and slightly red-shifted. It might be caused by the presence of the defects stemming from the self-assembly nature resulting in an empty trap, random two-three nanoparticles per trap. The dispersion of the nanoparticle size (Fig. S1), and their positioning inaccuracy as seen in the SEM image (Fig. 2a). Assemblies of several nanoparticles per trap using the CAPA method are possible because of the ratio between the trap diameter and nanoparticle size [26]. The spectral position difference between experimental λ_{SLR} and λ_{Ex} in monomer assemblies is 9 nm (Fig. 2b).

We used these substrates to detect 2NT with a few different excitation wavelengths (Fig. 2c). The concentration for the initial evaluation was 10^{-4} M because it produced a clear spectrum of the target molecule. We selected the most intense Raman band at 1377 cm^{-1} related to the ring deformation (Table S1) to analyze the contribution of SLR to the enhancement. The analytical EF was estimated by averaging SERS signal intensity over the scanned area and evaluating it to the SERS signal of single molecule per unit values of the measurement. The data and detailed description of the analytical EF calculations are presented in the Supplementary material. The intensity of the 1377 cm^{-1} band and the corresponding analytical EF showed a good correlation with the overlap of λ_{SLR} and λ_{Ex} (Fig. 2b). As expected, we observed the strongest intensity of the peak when excited by $\lambda_{Ex} = 532$ nm resulting in an analytical EF of $6.1{\cdot}10^8$ which gradually decreased as the laser excitation was detuned from the SLR.

SERS enhancement is often attributed to electromagnetic hot spots that form in small gaps or around sharp features. To investigate a possible improvement of the analytical EF in our substrates, we assembled 77 nm diameter nanoparticles on the same template but made sure that they formed multiparticle assemblies by careful tuning of the assembly process (Fig. 2d). Smaller nanoparticles were chosen to create the tetramer structure (four particles per trap) and to keep the λ_{SLR} close to the target λ_{Ex}. We assume that the nanoparticles were separated by a few nanometers due to the PVP layer as measured in the TEM images (Fig. S2).

We modelled this structure using the same methods and parameters as for the monomer structure. The electromagnetic field at λ_{Ex} is strongly localized in the gaps between the nanoparticles and is enhanced 49.4 and 65.9 times in isolated and periodic tetramer unit cell cases respectively (Fig. 2d). The latter is approximately 4 times higher compared to the monomer unit cell (Fig. 2a). The simulated λ_{SLR} emerged at 579 nm and closely matched the experimental peak at 583 nm (Fig. 2e). The collective plasmonic behaviour of the structure caused the red-shift and widening of the SLR. This follows the theory of plasmonic hybridization [34,35] where plasmonic nanoparticles in close proximity act as one larger particle with red-shifted LSPR. These results are in line with the previously reported effect of the cluster size on the SLR peak position in a periodic structure [36].

As seen in Fig. 2d, near-field coupling between nanoparticles is observed in both isolated and periodic tetramer structures, but the electromagnetic field is more intense in the latter case. The experimental transmittance spectrum of the tetramer-based structure (Fig. 2e) is a bit wider than the simulated result because of the non-ideal structure.

Like the monomer assemblies examined before, the intensity of the Raman peak increases as the difference $|\lambda_{SLR} - \lambda_{Ex}|$ decreases (Fig. 2f).

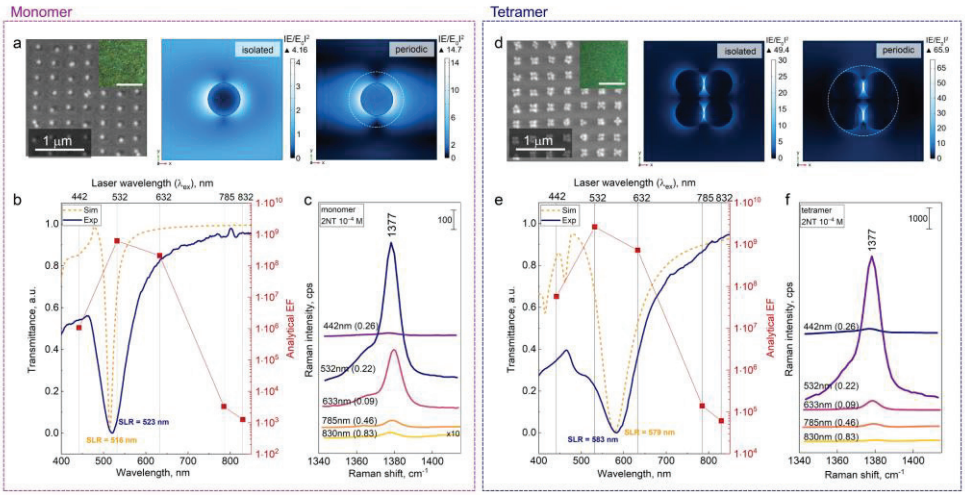

Fig. 2. Raman enhancement by resonant plasmonic arrays based on monomer and tetramer unit cells. (a) SEM micrograph of a monomer NP array and a dark field optical micrograph of the assembly as an inset (scale bar is 20 μm). Electromagnetic field enhancement by an isolated nanoparticle and a nanoparticle in Λ= 330 nm array (λ = 532 nm, a dashed line indicates the trap geometry). (b) Simulated and measured transmittance spectra of the monomer array; experimental values of the analytical SERS EF of the monomer assembly (red squares), (vertical line indicates λ_{Ex}). (c) Raman scattering spectra of 2NT (10^{-4} M), zoomed in on the 1377 cm^{-1} band *versus* excitation wavelengths (laser power in mW is indicated in parentheses). (d) SEM of a tetramer NP array and a dark field optical micrograph of the assembly as an inset (scale bar is 20 μm). Electromagnetic field enhancement by an isolated tetramer and a tetramer in the array (λ = 532 nm, the dashed line indicates the trap geometry). (e) Simulated and measured transmittance spectra, and experimental values of the analytical SERS EF of the tetramer assembly (red squares), (vertical line indicates λ_{Ex}). (f) Raman scattering spectra of 2NT (10^{-4} M), zoomed in on the 1377 cm^{-1} band *versus* excitation wavelengths.

Remarkably, it is almost 4 times more intense compared to the monomer assembly measured under identical conditions (Fig. 2c). The analytical SERS EF for the tetramer structure demonstrates the same trend, peaking at λ_{Ex}= 532 nm with the value of $2.6{\cdot}10^9$, which is an order of magnitude higher compared to the monomer structure. For clarity, the theoretically calculated SERS EF that is proportional $|E/E_0|^4$ [37,38] obtained from modeling results in Fig. 2a,d and experimentally determined analytical EF values are compared in Fig. 3a.

To understand the extremely high analytical EF measured using tetramers in the array, we formed a monolayer of randomly arranged NPs (77 nm ± 4.5 nm in diameter) on a flat PDMS substrate using the self-assembled monolayers (SAM) technique [39] (Fig. S4). The SERS sensitivity of this monolayer was verified in the same manner, using various laser wavelengths. We found that the random NP monolayer substrate also show excitation wavelengths dependance peaking at λ_{Ex}= 532 nm with analytical EF value of $1.6{\cdot}10^5$ (Fig. S4c). This dependence is typical for the LSPR alone based enhancement [40]. However, when we referenced the results of SLR-based substrates to these measurements, we found that the normalized analytical EF of monomer and tetramer peaked at λ_{Ex} = 532 nm with 110 and 465 times higher, respectively (Fig. 3b). This confirms the strong contribution of SLR to the EF and proves that it is possible to tailor these substrates to a specific excitation wavelength.

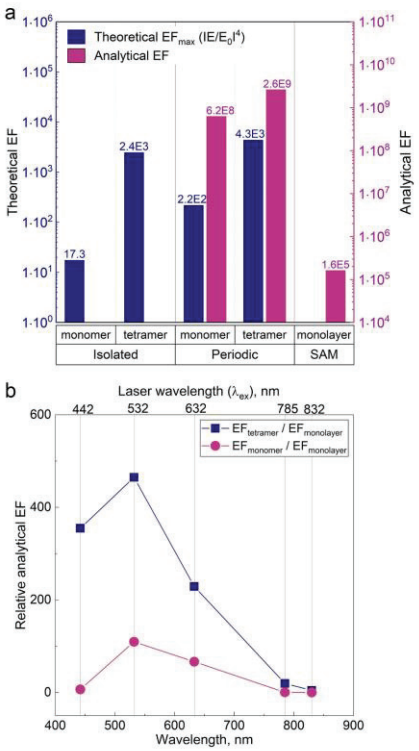

Fig. 3. SERS enhancement on a tailored plasmonic array *versus* a random plasmonic substrate. (a) The maximum value of the theoretical SERS EF ($|E/E_0|^4$) and analytical SERS EF on monomer, tetramer, and monolayer substrates. (b) Relative analytical SERS EF of monomer and tetramer substrates *versus* wavelength of excitation (enhancement is normalized to analytical SERS EF on a substrate with a monolayer of Ag nanoparticles).

After confirming that well-defined NP arrays provide a better performance, we investigated the spatial enhancement homogeneity (*i.e.,* reproducibility) of the three SERS substrate types. The variation of the intensity of the 1377 cm^{-1} band recorded in a randomly chosen 20 × 20 μm area of the monolayer-, monomer-, and tetramer-based SERS substrates is shown in Fig. 4a. The monolayer-based SERS substrate exhibits a large standard deviation value SD = 37.35 % due to the uncontrolled formation and positioning of the hot spots. The ordered arrangement of nanoparticles had a reduced deviation but still a comparatively high SD = 31.81 %. Such relatively high signal variation is caused due 18 % of defects obtained from a similar size area (Fig. S5) as analyzed in the Raman maps (Fig. 4a). The tetramer SERS substrate demonstrated an almost two times lower SD (12.42 %) because of better control over the distribution and homogeneity of hot spots and reduction of lattice imperfections.

The spatial Raman scattering intensity fluctuation over the scanned area evaluated on the tetramer-based structure is in the same range as other highly homogeneous SERS substrates. The ones made by electron beam lithography and nanotransfer printing on PDMS exhibited an SD value of 13 % [41] while template-guided self-assembly gold nanocluster arrays [42] and the layered gold nanochips produced by controllable electron-beam lithography [6] are characterized by SD≈ 12 %. The fact that arranged NPs demonstrate better reproducibility than randomly distributed NPs implies that even lower SERS signal intensity variations, comparable to a recent report [43], could be achieved *via* better Ag NPs size monodispersity.

Fig. 4b shows the full Raman scattering spectra of 2NT molecules adsorbed on the silver nanoparticles on the substrate that was already discussed in Fig. 2. We used the excitation wavelength with the highest enhancement (532 nm) and investigated concentrations from 10^{-4} M to 10^{-9} M. The spectra feature the typical 2NT vibrational modes listed in Supplementary material Table S1. The highlighted peaks (1377 cm^{-1}, 1583 cm^{-1}, 1621 cm^{-1}) are easily detectable at all concentrations tested. Therefore, the limit of detection (DL) was determined as 10^{-8} M. The intensity of the background increased at low concentrations because of the destruction of molecules and the increased contribution of impurities. The typical Raman peaks of PDMS listed in Table S1 can be seen in all measurements, but they do not overlap with the strong peaks attributed to the target molecule. In summary, the main peaks of the target molecule were able to be distinguished even at the lowest concentration investigated.

In Fig. 4c we plot the intensity of the 1377 cm^{-1} peak *versus* the concentration indicating the SD of SERS signal fluctuation. The SD is not indicated for small concentrations marked with an asterisk, as SERS peaks of target molecules were clearly distinguished from the noise only in two spectra. The experimental data can be fitted using the Hill function, which is usually used in biochemistry to describe processes that involve cooperative binding events [44]. The Hill coefficient n_{Hill} usually describes the number of bond ligands to macromolecules, *i.e.* their binding activity or concentration. In our case, we assume that the Hill function can be applied to study the adsorption activity of 2NT molecules on our SERS substrates (bonding with Ag NPs through the –SH moiety). Therefore, Fig. 4b can be interpreted as the change in reaction velocity between 2NT and Ag NPs. In this way, the n_{Hill} for the plasmonic array with single nanoparticles is 0.498.

Finally, we analyzed the detection limit of the tetramer assembly and showed the results in Fig. 4b. The typical 2NT Raman bands (Table S1) are easily visible in the spectra (PDMS peaks are better expressed at low 2NT concentrations). We found that the DL using the tetramer assembly is 10^{-9} M. Similarly, to the monomer assembly, the I_{1377} intensity *vs.* concentration plot obeys the Hill function and demonstrates n_{Hill} = 0.525. This suggests a higher efficiency of 2NT bonding to silver nanoparticles since the surface area is more than 3 times higher compared to the substrate with monomers. SERS measurements were

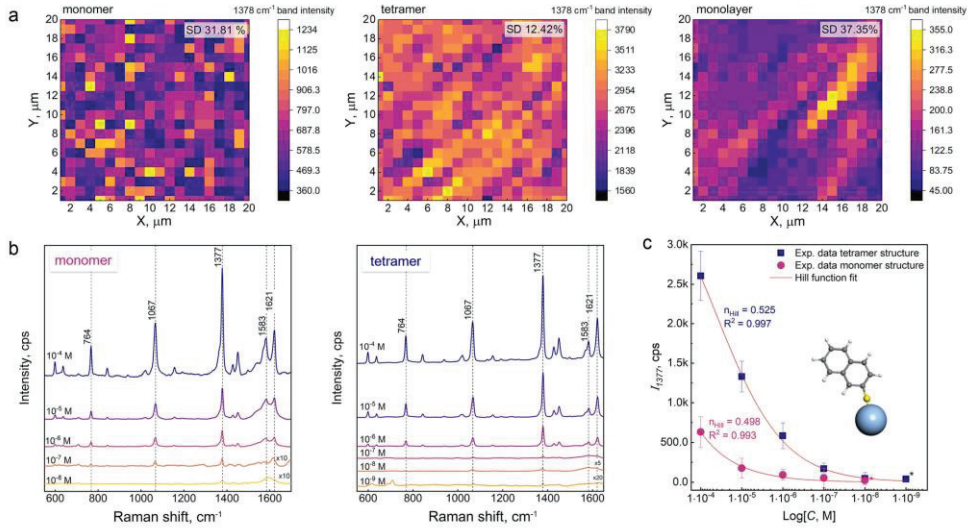

Fig. 4. Homogeneity of the SERS signal and Detection Limit of the 2NT molecule. (a) The 20 μm x 20 μm sized SERS maps of the 1377 cm^{-1} band intensity of the 2NT molecule adsorbed from a solution with a concentration of 10^{-4} M on Ag NPs monomer array (wavelength 532 nm, laser power 0.226 mW, integration time 1 s), tetramer array (0.0226 mW, 1 s), and monolayer (0.0226 mW, 3 s). (b) Raman scattering spectra of a range of 2NT concentrations were recorded using monomer and tetramer-based SERS substrates at $\lambda_{Ex} = 532$ nm. (c) The intensity of the 1377 cm^{-1} band *versus* analyte molecule concentration. [a]For 2NT concentration of 10^{-8} M measured with the monomer-based structure and 10^{-9} M measured with tetramer-base structure the SD of the SERS signal fluctuation is not indicated.

done within 2 months after NP deposition.

Tuning the SLR to the target wavelength by choosing the right nanoparticle size and lattice pitch increases the substrate's SERS sensitivity. Compared to the monomer in the unit cell, the tetramer exhibits a high electromagnetic field intensity in hot spots, which does not increase drastically, upon switching to a periodic structure, as in the case of the monomer. Basically, the SERS substrate based on randomly distributed hot spots is already showing relatively high analytical EF. However, the observed increase in analytical EF (Fig. 2) and the limit of detection in tetramer arrays indicate the importance of the spatially controlled hot spots. This is primarily attributed to the maximum closeness of nanoparticles to each other and secondly to photonic interaction.

4. Conclusions

In summary, we demonstrated SERS-active substrates with tunable enhancement properties that employ the surface lattice resonance in a regular structure of silver nanoparticles. Two-dimensional arrays of monomer and tetramer Ag NP assemblies were produced by capillarity-assisted particle assembly. The SLR properties were tuned to overlap the laser excitation wavelength at 532 nm. The fabricated substrates showed an excitation wavelength-dependent EF response. The highest enhancement was achieved using the designed laser wavelength close to the SLR peak position. We used 2-Naphthalenethiol (2NT) analyte molecule to demonstrate the detection limit which we found at a concentration of 10^{-8} M. This detection limit was further improved by implementing hot spots in the structure in the form of tetramers (four particles per trap). The tetramer structure showed more than an order of magnitude higher SERS EF and detected the 2NT down to 10^{-9} M concentration. The latter SERS substrate also showed the smallest Raman signal variation over an area of 20 μm x 20 μm, reaching a standard deviation of 12 %. On the basis of these results, reproducible Raman sensors can be designed for various wavelength regions and relieve the demand for different sources and detection systems.

CRediT authorship contribution statement

Nadzeya Khinevich: Writing – original draft, Methodology, Investigation, Data curation. **Mindaugas Juodėnas:** Investigation, Validation, Writing – review & editing. **Asta Tamulevičienė:** Investigation, Writing – review & editing. **Tomas Tamulevičius:** Investigation, Validation, Writing – review & editing. **Martynas Talaikis:** Investigation, Methodology, Formal analysis, Writing – review & editing. **Gediminas Niaura:** Investigation, Writing – review & editing. **Sigitas Tamulevičius:** Conceptualization, Investigation, Supervision, Writing – review & editing.

Declaration of Competing Interest

The authors declare that they have no known competing financial interests or personal relationships that could have appeared to influence the work reported in this paper.

Data availability

Data will be made available on request.

Acknowledgements

The studies were performed within the LaSensA project carried out under the M-ERA.NET 2 scheme (European Union's Horizon 2020 Research and Innovation Program, grant No. 685451) and co-funded by the Research Council of Lithuania (LMTLT), agreement No. S-M-ERA.NET-21-2, the National Science Centre of Poland, project No. 2020/02/Y/ST5/00086, and the Saxon State Ministry for Science, Culture and Tourism (Germany), grant No. 100577922, as well as from the tax funds

on the basis of the budget passed by the Saxon state parliament.

The authors thank Loic Vidal (Institut de Science des Matériaux) for the TEM images and Alexander Burko (Belarusian State University of Informatics and Radioelectronics) for access to custom-made software for the analysis of SERS spectra.

Appendix A. Supporting information

Supplementary data associated with this article can be found in the online version at doi:10.1016/j.snb.2023.134418.

References

[1] Z. Huang, A. Zhang, Q. Zhang, D. Cui, Nanomaterial-based SERS sensing technology for biomedical application, J. Mater. Chem. B 7 (2019) 3755–3774, https://doi.org/10.1039/c9tb00666d.

[2] Q. Tong, W. Wang, Y. Fan, L. Dong, Recent progressive preparations and applications of silver-based SERS substrates, TrAC Trends Anal. Chem. 106 (2018) 246–258, https://doi.org/10.1016/j.trac.2018.06.018.

[3] J. Langer, D. Jimenez de Aberasturi, J. Aizpurua, R.A. Alvarez-Puebla, B. Auguié, J. J. Baumberg, G.C. Bazan, S.E.J. Bell, A. Boisen, A.G. Brolo, J. Choo, D. Cialla-May, V. Deckert, L. Fabris, K. Faulds, F.J. García de Abajo, R. Goodacre, D. Graham, A. J. Haes, C.L. Haynes, C. Huck, T. Itoh, M. Käll, J. Kneipp, N.A. Kotov, H. Kuang, E. C. Le Ru, H.K. Lee, J.-F. Li, X.Y. Ling, S.A. Maier, T. Mayerhöfer, M. Moskovits, K. Murakoshi, J.-M. Nam, S. Nie, Y. Ozaki, I. Pastoriza-Santos, J. Perez-Juste, J. Popp, A. Pucci, S. Reich, B. Ren, G.C. Schatz, T. Shegai, S. Schlücker, L.-L. Tay, K. G. Thomas, Z.-Q. Tian, R.P. Van Duyne, T. Vo-Dinh, Y. Wang, K.A. Willets, C. Xu, H. Xu, Y. Xu, Y.S. Yamamoto, B. Zhao, L.M. Liz-Marzán, Present and future of surface-enhanced Raman scattering, ACS Nano 14 (2020) 28–117, https://doi.org/10.1021/acsnano.9b04224.

[4] E.C. Le Ru, P.G. Etchegoin, Quantifying SERS enhancements, MRS Bull. 38 (2013) 631–640, https://doi.org/10.1557/mrs.2013.158.

[5] M. Zhu, M. Li, M. Su, J. Liu, B. Liu, Y. Ge, H. Liu, J. Hu, Can "Hot Spots" be stable enough for surface-enhanced Raman scattering? J. Phys. Chem. C 125 (2021) 13443–13448, https://doi.org/10.1021/acs.jpcc.1c03321.

[6] L. Chen, C. Hu, Y. Dong, Y. Li, Q. Shi, G. Liu, R. Long, Y. Xiong, Tunable layered gold nanochips for high sensitivity and uniformity in SERS detection, J. Phys. Chem. C (2023), https://doi.org/10.1021/acs.jpcc.3c01359.

[7] K. Wang, M. Huang, J. Chen, L. Lin, L. Kong, X. Liu, H. Wang, M. Lin, A "drop-wipe-test" SERS method for rapid detection of pesticide residues in fruits, J. Raman Spectrosc. 49 (2018) 493–498, https://doi.org/10.1002/jrs.5308.

[8] Y. Chen, H. Li, J. Chen, D. Li, M. Zhang, G. Yu, L. Jiang, Y. Zong, B. Dong, Z. Zeng, Y. Wang, L. Chi, Self-generating nanogaps for highly effective surface-enhanced Raman spectroscopy, Nano Res. 15 (2022) 3496–3503, https://doi.org/10.1007/s12274-021-3924-8.

[9] J. Henzie, S.C. Andrews, X.Y. Ling, Z. Li, P. Yang, Oriented assembly of polyhedral plasmonic nanoparticle clusters, Proc. Natl. Acad. Sci. USA 110 (2013) 6640–6645, https://doi.org/10.1073/pnas.1218616110.

[10] V.A. Markel, Coupled-dipole approach to scattering of light from a onedimensional periodic dipole structure, J. Mod. Opt. 40 (1993) 2281–2291, https://doi.org/10.1080/09500349314552291.

[11] V.G. Kravets, A.V. Kabashin, W.L. Barnes, A.N. Grigorenko, Plasmonic surface lattice resonances: a review of properties and applications, Chem. Rev. 118 (2018) 5912–5951, https://doi.org/10.1021/acs.chemrev.8b00243.

[12] A.D. Utyushev, V.I. Zakomirnyi, I.L. Rasskazov, Collective lattice resonances: plasmonics and beyond, Rev. Phys. 6 (2021), 100051, https://doi.org/10.1016/j.revip.2021.100051.

[13] M.J. Huttunen, P. Rasekh, R.W. Boyd, K. Dolgaleva, Using surface lattice resonances to engineer nonlinear optical processes in metal nanoparticle arrays, Phys. Rev. A 97 (2018) 1–7, https://doi.org/10.1103/PhysRevA.97.053817.

[14] W. Wang, L. Qi, Light management with patterned micro- and nanostructure arrays for photocatalysis, photovoltaics, and optoelectronic and optical devices, Adv. Funct. Mater. 29 (2019) 1807275, https://doi.org/10.1002/adfm.201807275.

[15] B.C. Stipe, T.C. Strand, C.C. Poon, H. Balamane, T.D. Boone, J.A. Katine, J.L. Li, V. Rawat, H. Nemoto, A. Hirotsune, O. Hellwig, R. Ruiz, E. Dobisz, D.S. Kercher, N. Robertson, T.R. Albrecht, B.D. Terris, Magnetic recording at 1.5Pbm-2 using an integrated plasmonic antenna, Nat. Photonics 4 (2010) 484–488, https://doi.org/10.1038/nphoton.2010.90.

[16] A. Yang, T.B. Hoang, M. Dridi, C. Deeb, M.H. Mikkelsen, G.C. Schatz, T.W. Odom, Real-time tunable lasing from plasmonic nanocavity arrays, Nat. Commun. 6 (2015) 6939, https://doi.org/10.1038/ncomms7939.

[17] G. Vecchi, V. Giannini, J. Gómez Rivas, Shaping the fluorescent emission by lattice resonances in plasmonic crystals of nanoantennas, Phys. Rev. Lett. 102 (2009), 146807, https://doi.org/10.1103/PhysRevLett.102.146807.

[18] I. Ragheb, M. Braïk, S. Lau-Truong, A. Belkhir, A. Rumyantseva, S. Kostcheev, P.-M. Adam, A. Chevillot-Biraud, G. Lévi, J. Aubard, L. Boubekeur-Lecaque, N. Félidj, Surface enhanced Raman scattering on regular arrays of gold nanostructures: impact of long-range interactions and the surrounding medium, Nanomaterials 10 (2020) 2201, https://doi.org/10.3390/nano10112201.

[19] M. Charconnet, C. Kuttner, J. Plou, J.L. García-Pomar, A. Mihi, L.M. Liz-Marzán, A. Seifert, Mechanically tunable lattice-plasmon resonances by templated self-assembled superlattices for multi-wavelength surface-enhanced Raman spectroscopy, Small Methods 5 (2021) 2100453, https://doi.org/10.1002/smtd.202100453.

[20] M. Charconnet, M.T. Korsa, S. Petersen, J. Plou, C. Hanske, J. Adam, A. Seifert, Generalization of self-assembly toward differently shaped colloidal nanoparticles for plasmonic superlattices, Small Methods 2201546 (2023) 2201546, https://doi.org/10.1002/smtd.202201546.

[21] M. Charconnet, M.T. Korsa, S. Petersen, J. Plou, C. Hanske, J. Adam, A. Seifert, Generalization of self-assembly toward differently shaped colloidal nanoparticles for plasmonic superlattices, Small Methods 2201546 (2023) 2201546, https://doi.org/10.1002/smtd.202201546.

[22] H. Ko, S. Singamaneni, V.V. Tsukruk, Nanostructured surfaces and assemblies as SERS media, Small 4 (2008) 1576–1599, https://doi.org/10.1002/smll.200800337.

[23] J. Wang, Q. Zhang, Y. Yan, Y. Liu, Y. Geng, Fabrication of periodic nanostructures for SERS substrates using multi-tip probe-based nanomachining approach, Appl. Surf. Sci. 576 (2022), 151790, https://doi.org/10.1016/j.apsusc.2021.151790.

[24] M. Juodenas, T. Tamulevičius, J. Henzie, D. Erts, S. Tamulevičius, Surface lattice resonances in self-assembled arrays of monodisperse Ag cuboctahedra, ACS Nano 13 (2019) 9038–9047, https://doi.org/10.1021/acsnano.9b03191.

[25] M. Juodėnas, D. Peckus, T. Tamulevičius, Y. Yamauchi, S. Tamulevičius, J. Henzie, Effect of Ag nanocube optomechanical modes on plasmonic surface lattice resonances, ACS Photonics (2020), https://doi.org/10.1021/acsphotonics.0c01187.

[26] Y. Yin, Y. Lu, B. Gates, Y. Xia, Template-assisted self-assembly: a practical route to complex aggregates of monodispersed colloids with well-defined sizes, shapes, and structures, J. Am. Chem. Soc. 123 (2001) 8718–8729, https://doi.org/10.1021/ja011048v.

[27] N.G. Bastús, F. Merkoçi, J. Piella, V. Puntes, Synthesis of highly monodisperse citrate-stabilized silver nanoparticles of up to 200 nm: kinetic control and catalytic properties, Chem. Mater. 26 (2014) 2836–2846, https://doi.org/10.1021/cm500316k.

[28] D. Virganavicius, M. Juodėnas, T. Tamulevičius, H. Schift, S. Tamulevičius, Investigation of transient dynamics of capillary assisted particle assembly yield, Appl. Surf. Sci. 406 (2017) 136–143, https://doi.org/10.1016/j.apsusc.2017.02.100.

[29] T. Tamulevičius, R. Šeperys, M. Andrulevičius, V. Kopustinskas, Š. Meškinis, S. Tamulevičius, V. Mikalayeva, R. Daugelavičius, Application of holographic sub-wavelength diffraction gratings for monitoring of kinetics of bioprocesses, Appl. Surf. Sci. 258 (2012) 9292–9296, https://doi.org/10.1016/j.apsusc.2012.04.022.

[30] I. Aleknavičienė, E. Pabrėža, M. Talaikis, M. Jankunec, G. Račiukaitis, Low-cost SERS substrate featuring laser-ablated amorphous nanostructure, Appl. Surf. Sci. 571 (2022), 151248, https://doi.org/10.1016/j.apsusc.2021.151248.

[31] P. Jiang, A. Nion, A. Marchenko, L. Piot, D. Fichou, Rotational polymorphism in 2-naphthalenethiol sAMs on Au(111), J. Am. Chem. Soc. 128 (2006) 12390–12391, https://doi.org/10.1021/ja063060z.

[32] A.D. Rakić, A.B. Djurišić, J.M. Elazar, M.L. Majewski, Optical properties of metallic films for vertical-cavity optoelectronic devices, Appl. Opt. 37 (1998) 5271, https://doi.org/10.1364/AO.37.005271.

[33] P. Offermans, M.C. Schaafsma, S.R.K. Rodriguez, Y. Zhang, M. Crego-Calama, S. H. Brongersma, J. Gómez Rivas, Universal scaling of the figure of merit of plasmonic sensors, ACS Nano 5 (2011) 5151–5157, https://doi.org/10.1021/nn201227b.

[34] N. Liu, T. Liedl, DNA-assembled advanced plasmonic architectures, Chem Rev. 118 (2019) 3032–3053, https://doi.org/10.1021/acs.chemrev.7b00225.DNA-assembled.

[35] R. Borah, S.W. Verbruggen, Coupled plasmon modes in 2D gold nanoparticle clusters and their effect on local temperature control, J. Phys. Chem. C 123 (2019) 30594–30603, https://doi.org/10.1021/acs.jpcc.9b09048.

[36] C. Matricardi, C. Hanske, J.L. Garcia-Pomar, J. Langer, A. Mihi, L.M. Liz-Marzán, Gold nanoparticle plasmonic superlattices as surface-enhanced Raman spectroscopy substrates, ACS Nano 12 (2018) 8531–8539, https://doi.org/10.1021/acsnano.8b04073.

[37] I. Knorr, J. Ihlemann, G. Marowsky, Prediction and Optimization of Surface-Enhanced Raman Scattering Geometries, 14 (2002) 2008.

[38] R.K. Saini, A. Kumar, V. Goyal, A. Agarwal, R. Prajesh, Evaluating EM-field enhancement of different shapes of metallic nanoparticles using COMSOL multiphysics for SERS-based sensors, Mater. Today Proc. 76 (2023) 383–387, https://doi.org/10.1016/j.matpr.2022.11.425.

[39] Q. Guo, M. Xu, Y. Yuan, R. Gu, J. Yao, Self-assembled large-scale monolayer of Au nanoparticles at the air/water interface used as a SERS substrate, Langmuir 32 (2016) 4530–4537, https://doi.org/10.1021/acs.langmuir.5b04393.

[40] Y. Hu, T. Zhao, P. Zhu, Y. Zhu, X. Liang, R. Sun, C.P. Wong, Tailoring size and coverage density of silver nanoparticles on monodispersed polymer spheres as highly sensitive SERS substrates, Chem. Asian J. 11 (2016) 2428–2435, https://doi.org/10.1002/asia.201600821.

[41] N.A. Abu Hatab, J.M. Oran, M.J. Sepaniak, Surface-enhanced Raman spectroscopy substrates created via electron beam lithography and nanotransfer printing, ACS Nano 2 (2008) 377–385, https://doi.org/10.1021/nn7003487.

[42] B.M. Reinhard, Engineered SERS substrates with multiscale signal enhancement: nanoparticle cluster arrays, AIP Conf. Proc. 1267 (2010) 952–953, https://doi.org/10.1063/1.3482909.
[43] H. Wei, W. Leng, J. Song, M.R. Willner, L.C. Marr, W. Zhou, P.J. Vikesland, Improved quantitative SERS enabled by surface plasmon enhanced elastic light scattering, Anal. Chem. 90 (2018) 3227–3237, https://doi.org/10.1021/acs.analchem.7b04667.
[44] H. Prinz, Hill coefficients, dose–response curves and allosteric mechanisms, J. Chem. Biol. 3 (2010) 37–44, https://doi.org/10.1007/s12154-009-0029-3.

Nadzeya Khinevich obtained the M.Sc.Eng degree from the Belarusian State University of Informatics and Radioelectronics (BSUIR, Belarus) in 2018. She is currently working on her Ph.D. thesis (at Kaunas University of Technology, Lithuania) which is dedicated to the development of optical sensors for Surface-enhanced Raman scattering spectroscopy application (SERS). Her field of research is the fabrication of non-periodic and periodic plasmonic structures with tuned optical properties for biosensing using SERS.

Mindaugas Juodenas graduated from Kaunas University of Technology obtaining a Bachelor of Science degree in Mechatronics in 2014, followed by a Master of Science degree in Materials Science in 2016. He successfully defended his doctoral thesis in Materials Engineering from Kaunas University of Technology in 2021. Currently, he is a postdoctoral researcher at Chalmers University of Technology, where his research focuses on integrated metasurfaces for nanophotonics, bioimaging and biosensing.

Asta Tamulevičienė is currently a senior researcher at the Kaunas University of Technology (KTU). Her research through all the carriers was related to the light phenomena, either *via* the analysis of the optical properties of the materials or the application of light-based analytical methods to determine the structure of the materials. Currently, her interests are the synthesis of noble metal nanoparticles and the application of nanoparticles for sensors based on Surface Enhanced Raman Scattering (SERS).

Tomas Tamulevičius graduated from Kaunas University of Technology (KTU, Lithuania) with Ph.D. in Physics in 2012. Since the year 2019, he works as a Chief researcher at the Institute of Materials Science of KTU. He is also a Professor and Principal investigator of the research group "Applied Optics and Photonics" at the Physics Department of KTU since 2018. Since 2020 is a member of the Young Academy of the Lithuanian Academy of Sciences. He was visiting scientist at the University of Southern Denmark at Prof. Horst-Günter Rubahn's group NanoSYD and IBM Research Zurich (Switzerland) at Dr Heiko Wolf's group. His main fields of research are the formation of micro and nanostructures for optical and microfluidic applications. Modelling of the optical response of such structures as well as their practical applications for laser beam splitters, refractive index, and immune sensors, antiviral and antimicrobial surfaces, acoustic microscope calibration blocks, and templates for capillarity-assisted deposition (CAPA) of well-organized micro-/nano- particle arrays for the origination of plasmonic metasurfaces and surface-enhanced Raman scattering (SERS) substrates.

Martynas Talaikis is a researcher at Vilnius University Life Sciences Center, where he defended his Ph.D. in 2020, and he is a senior researcher at the State Research Institute Center for Physical Sciences and Technology. His current scientific interests are surface-enhanced vibrational spectroscopy, plasmonic and magneto-plasmonic nanoparticles, and spectroelectrochemistry.

Gediminas Niaura got his Ph.D. degree from Vilnius University (VU, Lithuania) in Electrochemistry in 1992. In 2002 got Habilitation in Physical Sciences (Chemistry). From 1982–2010 he worked at the Institute of Chemistry at VU as an engineer, junior researcher, researcher, senior researcher and chief researcher. 1993–2005 worked as a researcher at the US National Institute of Standards and Technology(total duration of work abroad - 3 years 8 months). Also from 1999 to 2010, he worked at the Institute of Biochemistry as a senior researcher. Since 2010 he is a professor in the Center for Physical Sciences and Technology at VU. His fields of interest include vibrational spectroscopy of biomolecules, surface vibrational spectroscopy, spectroelectrochemistry, Surface-enhanced Raman spectroscopy, sum frequency generation spectroscopy.

Sigitas Tamulevičius obtained his Ph.D. degree from the University of Vilnius (Lithuania) in 1984, and Doctor Habilitus degree from Kaunas University of Technology (KTU) in 1994. From 1990–1991, he was a postdoctoral researcher at the Royal Institute of Technology (Stockholm, Sweden). In 1994 he was a Research Scholar, Fulbright Scholarship, Department of Physics, Massachusetts Institute of Technology (USA). Since 1996 he is a full professor at the Physics Department and Research director of the Institute of Materials Science of KTU. Since 2010 he is a full Member of the Lithuanian Academy of Sciences. His research interests include physical aspects of micro and nanotechnologies, surface physics, plasmonics, plasma and laser irradiation-based technologies and applications, plasmonics, and biosensors.

Appendix A. Supplementary material

Wavelength-tailored enhancement of Raman scattering on a resonant plasmonic lattice.

Nadzeya Khinevich[a*], Mindaugas Juodėnas[a,b], Asta Tamulevičienė[a,c], Tomas Tamulevičius[a,c,d], Martynas Talaikis[e], Gediminas Niaura[e], and Sigitas Tamulevičius[a,c*]

[a]Institute of Materials Science, Kaunas University of Technology, 51423 Kaunas, Lithuania

[b]Physics Department, Chalmers University of Technology, Gothenburg 41296, Sweden

[c] Department of Physics, Kaunas University of Technology, 51423 Kaunas, Lithuania

[d]UAB Nanoversa, 51423 Kaunas, Lithuania

[e]Department of Organic Chemistry, Center for Physical Sciences and Technology (FTMC), 10257 Vilnius, Lithuania

Extinction spectra of the used NP colloids were obtained from the UV-Vis-NIR measurement (Fig. S1a). Information about the corresponding silver nanoparticle size distributions (Fig. S1b) was obtained from the SEM micrographs of NPs dispersed on a silicon substrate.

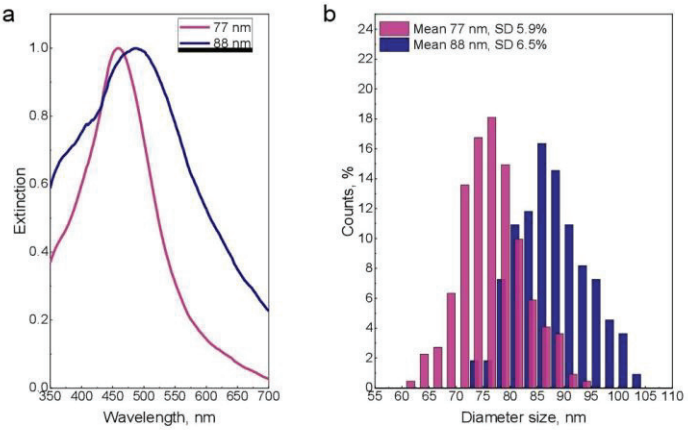

Fig. S1. Analysis of synthesized Ag NPs. (a) Extinction spectra of synthesized Ag NPs in solution. (b) The mean diameter and distribution (SD – standard deviation in %) were obtained from the SEM micrograph analysis.

The list of 2NT and PDMS Raman bonds seen in the experimental spectra referred from the literature [1,2] are summarized in Table S1.

Table S1 Observed vibrational wavenumbers of 2NT and PDMS measured using λ_{Ex} = 532 nm.

Peak position	**Assignments**
2NT [1]	
599 cm^{-1}	Ring deformation
637 cm^{-1}	Ring deformation
764 cm^{-1}	Ring deformation
842 cm^{-1}	C–H twist
940 cm^{-1}	C–H bend
1020 cm^{-1}	C–H bend
1067 cm^{-1}	C–H bend
1377 cm^{-1}	Ring stretch
1428 cm^{-1}	Ring stretch
1450 cm^{-1}	Ring stretch
1566 cm^{-1}	Ring stretch
1583 cm^{-1}	Ring stretch
1621 cm^{-1}	Ring stretch
PDMS [2]	
615 cm^{-1}	Si-C stretch
708 cm^{-1}	Si-C stretch

TEM micrograph of the nanoparticles functionalized with PVP is depicted in Fig. S2.

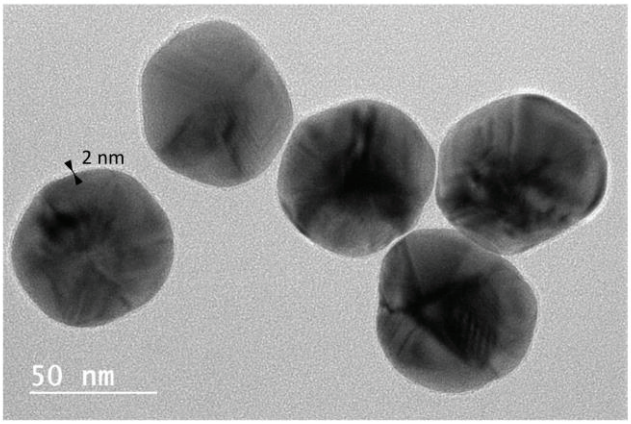

Fig. S2. TEM image of synthesized nanoparticles with a mean diameter of 77 nm. The arrows indicate the thickness of the PVP capping layer.

Data of 2NT reference Raman spectra acquisition conditions with multiwavelength Raman microscope (Renishaw, Wotton-under Edge) and SERS measurements are presented in Table S2.

Table S2 Raman Setting parameters.

Objective	**NA**	***f*, mm**	**Measurements**	**2NT contraction (c)**	**Number of measured molecules**
5x	0.12	14	Raman	2.5 mM (in solution)	Table S3
50x	0.75	0.4	SERS	Molecules absorbed on the surface of silver nanoparticles from 10^{-4}M concentration in solution.	calculated with the condition of formation of a molecule monolayer on the metal surface (Table S4)

To analyze the SERS EF of the studied SERS-active substrates, the Raman spectrum of 2NT molecule was registered and the Raman intensity of 1 molecule for unit values of the measurement parameters was calculated following the process:

I. Raman probe volume [3]:

The probed volume is the volume of the sample irradiated by laser and approximated as a cylinder (Fig. S3), where $2W_0$ is the diameter of the cylinder and $2z_0$ is its length.

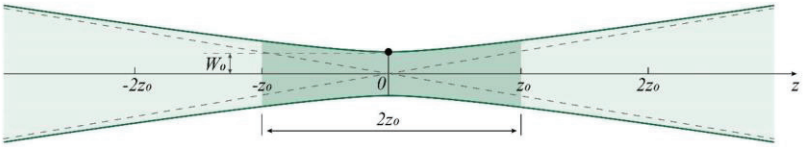

Fig. S3. The sampling volume in Raman measurements of liquid samples [3].

The $2W_0$ and $2z_0$ are determined using the equations (S1) and (S2) respectively:

$$2W_0 = \frac{4\lambda f}{\pi d}, \tag{S1}$$

$$2z_0 = \frac{16\lambda f^2}{\pi d^2}, \tag{S2}$$

where λ – laser wavelength, d – diameter of an unfocused laser beam, f – focal length of focusing lens.

Then the volume (V) is calculated as follows:

$$V = \left(\frac{\pi(2W_0)^2}{4}\right) 2z_0. \tag{S3}$$

II. Number of probed molecules:

$$N_{molecule} = N_A \times c \times V, \tag{S4}$$

where N_A – Avogadro constant (6.022×10^{23} mole^{-1}), c – concentration of molecules in solution.

III. Raman intensity of one 2NT molecule per unit values of the measurement parameters:

The Raman intensity of a single molecule is defined as the quotient of the measured intensity divided by the number of molecules. Also, to calculate the intensity of one molecule reached during the integration time of 1 s and the laser power of 1 mW, the obtained value must be divided by the given parameter during the analysis.

Obtained values of the probed volume, the number of probed molecules and the intensity of single molecules Raman signal per unit values of the measurement parameters are shown in Table S3.

Table S3 Input data and probed 2NT molecules in solution.

The spectrometer sensitivity drift at different measurements. The ratio of silicon's 520 cm^{-1} mode (I_{Si} prior SERS divided by I_{Si} prior Raman measurement).					
Laser wavelength, nm	*442*	*532*	*633*	*785*	*830*
Monolayer	*0.34*	*2.63*	*2.56*	*1.44*	*3.19*
Monomer	*0.27*	*1.01*	*2.16*	*1.00*	*0.96*
Tetramer	*0.41*	*2.51*	*2.33*	*1.39*	*2.33*
Raman probe volume					
Input beam diameter (d), mm	*1.20*	*0.70*	*0.95*	*7.75*	*7.75*
Beam waist diameter ($2W_0$), mm	*0.007*	*0.014*	*0.012*	*0.002*	*0.002*
Length of effective volume ($2z_0$), mm	*0.31*	*1.08*	*0.70*	*0.01*	*0.01*
Volume (V), mm^3	*1.E-05*	*2.E-04*	*8.E-05*	*3.E-08*	*4.E-08*
V, L	*1.0E-11*	*1.6E-10*	*7.8E-11*	*3.3E-14*	*4.0E-14*
Probed number of 2NT molecules ($N_{molecule}$)	*1.6E+10*	*2.4E+11*	*1.2E+11*	*5.0E+07*	*6.0E+07*
Raman intensity of 1380 cm^{-1} mode (2NT, solution, 2.5 mM)					
Raman band 1380 cm^{-1} intensity, cps	*39312*	*123553*	*13483*	*20333*	*5117*
Laser power, mW	*52.8*	*45.3*	*9.4*	*92*	*166*
Accumulation time, s	*600*	*1200*	*600*	*600*	*600*
Raman band 1380 cm^{-1} intensity at 1 mW and 1 s of accumulation time, cps	*1.24*	*2.27*	*2.39*	*0.37*	*0.05*
1 molecule brings Raman intensity per 1 s and 1 mW	*7.9E-11*	*9.7E-12*	*2.0E-11*	*7.3E-09*	*8.6E-10*

SERS measurements were done using dry substrates with adsorbed 2NT molecules on the surface of the silver nanoparticles. Analytical SERS EF was calculated taking into account that the molecules form a monolayer on the particle surface.

First of all, the probed surface area (A) was calculated:

$$A = \pi W_0^2, \tag{S5}$$

where W_0 is the laser beam waist.

The next step includes determining the number of traps (N_{tr}) that fall into the laser spot:

$$N_{tr} = \frac{A}{\Lambda^2} \tag{S6}$$

where Λ^2 is the area of the unit cell for the array with periodicity Λ = 330 nm.

For the monomer-based structure, the number of traps is equal to the number of silver nanoparticles (N_p), for the tetramers-based structure the number of particles is determined as the $N_p = N_{tr} \times 4$. In the case of monolayer-base structure N_p is found out as quotient from A divided by the square area of the circumscribed square:

$$N_{p\ (monolayer)} = \frac{A}{4R^2}, \tag{S7}$$

where R – radius of the nanoparticle. In the case of the monomer-based substrate, the radius of used nanoparticles is 44 nm, and for tetramer-based the radius is 38,5 nm.

Probed surface area (S_{probe}) of the silver nanoparticles is calculated by multiplying the surface of one nanoparticle by their number:

$$S = 4\pi R^2; \tag{S8}$$

$$S_{probe} = S \times N_p, \tag{S9}$$

where S – is the surface area of the spherical silver nanoparticle.

The number of probed molecules ($N_{molecule}$) is determined by $S_{probe}/S_{molecule}$ ($S_{molecule}$ – the area occupied by one molecule adsorbed on the surface).

The calculation of the SERS intensity of single molecule per unit values of the measurement parameters was carried out similarly to the calculation for Raman intensity described above.

The analytical SERS EF is defined as the ratio of the single molecule SERS intensity signal to the single molecule Raman intensity signal divided by silicon peak intensity ratio (Si signal intensity before SERS divided by Si signal intensity before Raman measurement). The values of the discussed calculation are presented in Table S4.

Table S4 SERS probe surface area, number of probed 2NT molecules and SERS EF for monomer-based structure.

					SERS probe surface area
Laser wavelength, nm	*442*	*532*	*633*	*785*	*830*
Beam waist (W_0), mm	*0.00036*	*0.00043*	*0.00051*	*0.00064*	*0.00068*
Surface area (A), mm^2	*4.1E-07*	*5.9E-07*	*8.3E-07*	*1.3E-06*	*1.4E-06*
Number of probed traps(N_{tr})	*3.7*	*5.3*	*7.5*	*11.5*	*12. 9*
					Number of probed particles (N_p)
Monolayer	*1.1E+02*	*1.5E+02*	*2.2E+02*	*3.3E+02*	*3.7E+02*
Monomer	*3.66E+00*	*5.30E+00*	*7.50E+00*	*1.15E+01*	*1.29E+01*
Tetramer	*1.46E+01*	*2.12E+01*	*3.00E+01*	*4.61E+01*	*5.16E+01*
					Probed surface area of nanoparticles (S_{probe}), mm^2
Monolayer	*1.97E-06*	*2.86E-06*	*4.05E-06*	*6.22E-06*	*6.96E-06*
Monomer	*9.30E-08*	*1.35E-07*	*1.91E-07*	*2.93E-07*	*3.28E-07*
Tetramer	*2.72E-07*	*3.94E-07*	*5.58E-07*	*8.59E-07*	*9.60E-07*
					Number of probed molecules ($N_{molecules}$)
Monolayer	*9.13E+06*	*1.32E+07*	*1.87E+07*	*2.88E+07*	*3.22E+07*
*Monomer**	*3.44E+05*	*4.99E+05*	*7.06E+05*	*1.09E+06*	*1.21E+06*
Tetramer	*1.26E+06*	*1.83E+06*	*2.59E+06*	*3.98E+06*	*4.45E+06*
					Average intensities extracted from SERS maps**
Laser power, mW	*0.264*	*0.2265*	*0.094*	*0.46*	*0.83*
Monolayer	*39*	*1902*	*3111*	*2143*	*1014*
Monomer	*8*	*3022*	*6577*	*26*	*1.26*
Tetramer	*2327*	*116370*	*89550*	*5565*	*544*
					1 molecule brings SERS intensity per 1 s and 1 mW
Monolayer	*4.E-06*	*1.E-04*	*2.E-04*	*7.E-05*	*4.E-05*
Monomer	*2.E-05*	*6.E-03*	*9.E-03*	*2.E-05*	*1.0E-06*

Tetramer	*2.E-03*	*6.E-02*	*3.E-02*	*1.E-03*	*1.2E-04*
					Analytical Enhancement factor
Monolayer	*1.6E+05*	*5.7E+06*	*3.2E+06*	*7.1E+03*	*1.4E+04*
Monomer	*1.1E+06*	*6.2E+08*	*2.1E+08*	*3.3E+03*	*1.2E+03*
Tetramer	*5.7E+07*	*2.6E+09*	*7.3E+08*	*1.4E+05*	*6.1E+04*

* Taken into account 20% of defects

** The intensity normalized to 1 s and 1 mW.

Fig. S5 depicts the typical situation of the mapping over a monomer substrate using a green wavelength laser.

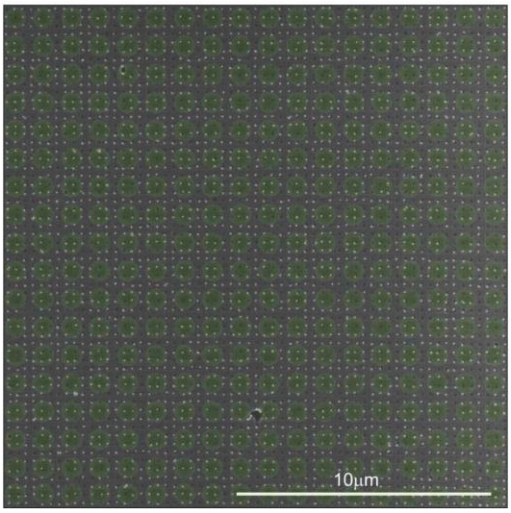

Fig. S5. The SEM image of the 20 μm x 20 μm area of the monomer-based SERS-active substrate overlaid with the XY scanned acquisition points for obtaining the SERS map (green circles indicate laser spots with a diameter of 0.86 μm arranged according to the scanning procedure with a 1.5 μm step).

References

[1] R.A. Alvarez-Puebla, D.S. Dos Santos Jr, R.F. Aroca, Surface-enhanced Raman scattering for ultrasensitive chemical analysis of 1 and 2-naphthalenethiols, Analyst. 129 (2004) 1251. https://doi.org/10.1039/b410488a.

[2] D. Cai, A. Neyer, R. Kuckuk, H.M. Heise, Raman, mid-infrared, near-infrared and ultraviolet-visible spectroscopy of PDMS silicone rubber for characterization of polymer optical waveguide materials, J. Mol. Struct. 976 (2010) 274–281.

https://doi.org/10.1016/j.molstruc.2010.03.054.

[3] B.E.A. Saleh, M.C. Teich, Fundamentals of Photonics, third edit, Wiley, 2013.

ACKNOWLEDGEMENTS

I would like to express my gratitude to my supervisor Prof. Sigitas Tamulevičius for the guidance and support. Special thanks are dedicated to Prof. Tomas Tamulevičius, Dr. Asta Tamulevičienė and Dr. Mindaugas Juodėnas whose guidance and willingness to impart their knowledge and experience have been invaluable throughout this study.

I am also grateful to each and every colleague from the Institute of Materials Science of the Kaunas University of Technology, Mads Clausen Institute of the University of Southern Denmark, Institut de Science des Matériaux de Mulhouse, and NanoBioMedical Centre Adam Mickiewicz University for fruitful cooperation, sincere sharing of knowledge and skills, and random interesting and supportive conversations that made my stay in these places unforgettable.

Thanks should also go to Dr. Hanna Bandarenka's and Prof. Vitaliy Bondarenko's research groups from my *alma mater* Belarusian State University of Informatics and Radioelectronics who impacted and inspired me and without whom my career as a researcher would not have begun.

Lastly, my deepest gratitude goes to my family, my lovely husband, and close friends for their support and belief in me which has kept my spirit and motivation not only during the compilation of this dissertation but also in life.

UDK 544.174.5+602.1:53.082.9+620.1-181.48](043.3)

SL344. 2024-04-10, 20,5 leidyb. apsk. l. Tiražas 14 egz. Užsakymas 58.
Išleido Kauno technologijos universitetas, K. Donelaičio g. 73, 44249 Kaunas
Spausdino leidyklos „Technologija“ spaustuvė, Studentų g. 54, 51424 Kaunas